

Copyright
by
Marcelino Mendes de Almeida Neto
2019

The Dissertation Committee for Marcelino Mendes de Almeida Neto certifies that this is the approved version of the following dissertation:

**Quaternion Regression and Finite-Time Controllers for
Attitude Dynamics**

Committee:

Maruthi Akella, Supervisor

Todd E. Humphreys

Renato Zanetti

Luis Sentis

Chris D'Souza

Brian Coltin

**Quaternion Regression and Finite-Time Controllers for
Attitude Dynamics**

by

Marcelino Mendes de Almeida Neto

DISSERTATION

Presented to the Faculty of the Graduate School of
The University of Texas at Austin
in Partial Fulfillment
of the Requirements
for the Degree of

DOCTOR OF PHILOSOPHY

THE UNIVERSITY OF TEXAS AT AUSTIN

December 2019

To my parents *Americo Almeida* and *Simone Teixeira*, for their support and source of pride, admiration and reference for my personal and professional growth.

To my siblings *Anna Laura Almeida*, *Americo Almeida* and *Pedro Arthur Almeida*: friends for an entire life.

Acknowledgments

Special thanks to Dr. *Maruthi Akella* for guiding and assisting me on this extraordinary experience for the achievement of a Ph.D. Degree.

I would like to thank the committee members for their availability in reviewing this Ph.D. manuscript and their contributions on this dissertation.

Thanks to my coauthors Dr. *Daniele Mortari*, Dr. *Renato Zanetti*, and *Rahul Moghe*. Your cooperation contributed to ensure the highest quality in our publications together.

To the members and cohabitants of the *Auto-GNC* laboratory throughout the last five years. It was great to work with every one of you towards developing and growing the lab. Special thanks to *Arjun Ram*, whose support was critical in the last year during the collaborative project with Lockheed Martin.

To the members at the *Radionavigation Laboratory* for the projects that we worked together. Special thanks to Dr. *Todd Humphreys* for the support and guidance in the development of the *Aerial Robotics* undergraduate/graduate course.

Thanks to my internship mentors at NASA Ames, Dr. *Trey Smith* and Dr. *Brian Coltin*. Thank you for the fun and fascinating experience at the Intelligent Robotics Group on the development of Astrobe. I would like

to acknowledge the *Agencia Espacial Brasileira* (Brazilian Space Agency) for enabling the internship opportunity at NASA Ames.

To all friends and colleagues within the *Aerospace Engineering* graduate program. You helped me endure all the hardships of a Ph.D., and for that I am thankful! Special thanks to those in the *qualifying exams study groups*: *Kirsten Tuggle*, *Emily Kollin*, Dr. *Jhanani Selvakumar*, and Dr. *Andrei Marchidan*.

To the *Aerospace Engineering faculty* at *The University of Texas at Austin* for their teaching excellency. They are able to expand one's conceptions about engineering, *life, the universe and everything* rather than just providing 42 as an answer.

I would like to acknowledge my sponsors throughout the achievement of this Ph.D. degree: the *Aerospace Engineering Department* at *The University of Texas at Austin*, *NASA Johnson Space Center* (with special thanks to Dr. *Chris D'Souza*), *Lockheed Martin Corporation*, and the *Coordenação de Aperfeiçoamento de Pessoal de Nível Superior*.

Quaternion Regression and Finite-Time Controllers for Attitude Dynamics

Marcelino Mendes de Almeida Neto, Ph.D.
The University of Texas at Austin, 2019

Supervisor: Maruthi Akella

This dissertation presents two major research contributions to the field of attitude dynamics and control. The first topic comprises of estimating the angular velocity of a rigid body purely with orientation measurements expressed in terms of the quaternion parameterization. At first, the object of interest is assumed to be in pure-spin, and a simple two-step algorithm is derived and analyzed as part of this dissertation. These results are further extended for the general case of angular velocity estimation by way of relaxing the pure-spin restriction. The proposed angular velocity estimator is particularly useful in the context of vision-based navigation, as demonstrated through simulations. The second major research contribution from this dissertation is represented through a pair of new Lyapunov-based controllers that steer a fully actuated rigid body attitude system from an arbitrary initial configuration to any desired one within prescribed finite-time. The stability and convergence properties owing to these two controllers are analyzed through Lyapunov analysis

and extensive numerical simulation studies. Finite-time attitude controllers, as opposed to asymptotic controllers, can be particularly useful in satellites that need to repeatedly reorient themselves with hard-deadline constraints.

Table of Contents

Acknowledgments	v
Abstract	vii
List of Tables	xii
List of Figures	xiii
Chapter 1. Introduction	1
Part I Angular Velocity Estimation from Orientation Measurements	1
Chapter 2. QuateRA: The Quaternion Regression Algorithm	2
2.1 Introduction	3
2.2 Motivation: Batch Estimation of Linear Velocity from Position Measurements	8
2.2.1 Analysis	14
2.3 Attitude Kinematics and Measurement Model	17
2.3.1 Attitude Kinematics	17
2.3.2 Measurement Model	19
2.4 Problem Formulation	23
2.5 The Quaternion Regression Algorithm	27
2.5.1 Estimation of the Axis of Rotation	27
2.5.2 Estimation of the Angular Velocity Magnitude	33
2.5.3 Covariance Estimate	37
2.5.4 Algorithm Summary	38
2.5.5 QuateRA Analysis	39

2.6	QuateRA Monte Carlo Analysis	41
2.7	Conclusions	50
Chapter 3. Real-time Angular Velocity Estimation of Non-cooperative Space Objects Using Camera Measurements		56
3.1	Introduction	57
3.2	Problem Formulation	61
3.3	The Quaternion Regression Algorithm	64
3.4	Consistency Test	67
3.5	Simulation Results	71
	3.5.1 Metrics for Analysis of Simulation Results	74
	3.5.2 Algorithm Comparison	81
3.6	Conclusions	82
Part II Finite-time Attitude Controllers		84
Chapter 4. New Class of Attitude Controllers Guaranteed to Converge within Specified Finite-Time		85
4.1	Introduction	85
4.2	Control Design	87
	4.2.1 MRP Stabilization	89
	4.2.2 Attitude Stabilization	93
	4.2.2.1 Disturbance-Free Analysis	96
	4.2.2.2 Disturbance Analysis	97
4.3	Tracking Control	98
4.4	Practical Considerations	101
4.5	Simulation Results	103
	4.5.1 Perfect measurements	103
	4.5.2 Noise corrupted measurements	108
4.6	Conclusion	110

Chapter 5. Time-varying feedback for attitude regulation in prescribed finite-time	111
5.1 Introduction	112
5.2 Control Design	114
5.2.1 Storage Function	115
5.2.2 Finite Time Proof	117
5.2.3 Summary of the Stability Proof	123
5.3 Simulation Results	124
5.4 Conclusions	128
Chapter 6. Conclusions	131
Appendices	133
Appendix A. Appendices for QuateRA	134
A.1 Total Least Squares Problem Formulation	134
A.2 Gaussian Marginal Covariance Along a Line	135
A.3 Statistics of the Spherical Uniform Distribution	139
A.4 Multiplicative Extended Kalman Filter Formulation	142
Appendix B. Appendices for Chapter 4	147
B.1 Boundedness of $\mu^{\alpha_1}\sigma$	147
B.2 Convergence proof for $\mu^\rho(t)\sigma(t)$	151
Appendix C. Appendices for Chapter 5	153
C.1 Finite Time Tracking Design	153
Bibliography	159

List of Tables

2.1	Percent deviation between MEKF and QuateRA for $dt = 0.1s$ and $\Omega = 0.1rad$	53
2.2	Percent deviation between MEKF and QuateRA for $dt = 1s$ and $\Omega = 0.1rad$	53
2.3	Percent deviation between MEKF and QuateRA for $dt = 1s$ and $\Omega = 1rad$	53
2.4	Number of times that <i>Fmincon</i> converged for $dt = 0.1s$ and $\Omega = 0.1rad$	54
2.5	Number of times that <i>Fmincon</i> converged for $dt = 1s$ and $\Omega = 0.1rad$	54
2.6	Number of times that <i>Fmincon</i> converged for $dt = 1s$ and $\Omega = 1rad$	54
2.7	Percent deviation between <i>Fmincon</i> and QuateRA for $dt = 0.1s$ and $\Omega = 0.1rad$ (there is no data for $n = 5$).	55
2.8	Percent deviation between <i>Fmincon</i> and QuateRA for $dt = 1s$ and $\Omega = 0.1rad$ (there is no data for $n = 5$).	55
2.9	Percent deviation between <i>Fmincon</i> and QuateRA for $dt = 1s$ and $\Omega = 1rad$ (there is no data for $n = 5$).	55
3.1	Performance comparison for the multiple simulations.	80
3.2	Performance comparison for the multiple simulations using linear Markov extension for the MEKF.	82

List of Figures

2.1	Sample Mean and Standard Deviation of the projection of the estimated AOR along a direction perpendicular to the true AOR. Measurements taken at 10Hz, with an AVM of $\Omega = 0.1\text{rad/s}$. Results are shown as a function of the number of measurements (x axis) and the standard deviations σ_θ (different plots).	43
2.2	Sample Mean and Standard Deviation of the estimated AVM error for measurements taken at 10Hz, and an AVM of $\Omega = 0.1\text{rad/s}$. Results are shown as a function of the number of measurements (x axis) and the standard deviations σ_θ (different plots).	44
2.3	Percentual deviation of the average estimated standard deviation for $\hat{\sigma}_\omega$ w.r.t. the sample standard deviation σ_ω , assuming sampling frequency of 10Hz, and an AVM of $\Omega = 0.1\text{rad/s}$. Results are shown as a function of the number of measurements (x axis) and the measurement noise standard deviations σ_θ (different plots).	45
2.4	Sample Mean and Standard Deviation of the projection of the estimated AOR along a direction perpendicular to the true AOR. Measurements taken at 1Hz, with an AVM of $\Omega = 0.1\text{rad/s}$. Results are shown as a function of the number of measurements (x axis) and the standard deviations σ_θ (different plots). . . .	46
2.5	Sample Mean and Standard Deviation of the estimated AVM error for measurements taken at 10Hz, and an AVM of $\Omega = 0.1\text{rad/s}$. Results are shown as a function of the number of measurements (x axis) and the standard deviations σ_θ (different plots).	47
2.6	Percentual deviation of the average estimated standard deviation for $\hat{\sigma}_\omega$ w.r.t. the sample standard deviation σ_ω , assuming sampling frequency of 10Hz, and an AVM of $\Omega = 0.1\text{rad/s}$. Results are shown as a function of the number of measurements (x axis) and the measurement noise standard deviations σ_θ (different plots).	48
3.1	Reference frames and rotational transformations.	61
3.2	Proposed Algorithm Pipeline.	63

3.3	Residual plot for planar motion (left) and quaternion motion with out-of-plane component (right). The index i represents the subscript for $\hat{e}_i \triangleq \hat{\mathbf{q}}_i^T \hat{\mathbf{u}}_3$	69
3.4	Itokawa rendering with different light sources.	72
3.5	Left: History of the camera's pose with respect to the asteroid's fixed frame determined from running the ORB-SLAM algorithm. The red and black dots are features on the asteroid surface. Right: Example of features taken from one frame in the image plane.	73
3.6	Simulation results for Itokawa's tumbling motion assuming initial angular velocity of $\boldsymbol{\omega}(0) = [0.025, 0.01, 0.005]^T$	75
3.7	Simulation results for Itokawa's tumbling motion with poor lighting conditions assuming initial angular velocity of $\boldsymbol{\omega}(0) = [0.01, 0.02, -0.005]^T$	76
3.8	Simulated view of the Cassini spacecraft.	77
3.9	Simulation results for Cassini's tumbling motion assuming initial angular velocity of $\boldsymbol{\omega}(0) = [0.01, 0.02, 0.005]^T$	78
3.10	Simulation results for Cassini's tumbling perturbed motion assuming initial angular velocity of $\boldsymbol{\omega}(0) = [0.0, -0.02, -0.035]^T$	79
4.1	Time histories of state trajectories for the set-point regulation case with perfect measurements. The plots on the left display the simulation outputs in a linear scale, whereas the plots on the right present the same outputs in logarithmic scale.	105
4.2	Time histories of state trajectories for the set-point regulation case with perfect measurements and applied disturbances. The plots on the left display the simulation outputs in a linear scale, whereas the plots on the right present the same outputs in logarithmic scale.	106
4.3	Time histories of state trajectory errors for the trajectory tracking case with perfect measurements. The plots on the left display the simulation outputs in a linear scale, whereas the plots on the right present the same outputs in logarithmic scale.	107
4.4	System convergence to the origin with noisy measurements. The blue plot shows the controller that caps $\mu(t)$ at $\kappa = 0.85$, while the red plot shows the controller that detects the switching time through the FFT method. The plots on the left display the simulation outputs in a linear scale, whereas the plots on the right present the same outputs in logarithmic scale.	109

5.1	Time histories of state trajectories for the set-point regulation case with $\phi_1 = \phi_2 = 20$	125
5.2	Time histories of state trajectories for the disturbed set-point regulation case with $\phi_1 = \phi_2 = 20$, and $\mathbf{d} = [0.5 \ 0.5 \ 0.5]^T$ N.m.	126
5.3	Time histories of state trajectories for the disturbed set-point regulation case with $\phi_1 = \phi_2 = 100$	127
5.4	Time histories of state trajectories for the disturbed set-point regulation case with $\phi_1 = \phi_2 = 1$	128
A.1	Illustration for the proof of marginal PDF along a line.	136
A.2	Illustration of Archimedes' Hat-Box Theorem.	140

Chapter 1

Introduction

Attitude estimation and control are fields of research with an extensive literature and set of applications. These domains are explicitly important in fixed-wing aircrafts [28], helicopters [66], multicopters [5, 33], space systems [15, 70], underwater vehicles [71], among many other applications. With the miniaturization of embedded computing and sensing within the last decade, many of those attitude systems are becoming fully autonomous for multiple applications, with little to no human intervention in their operation. Full automation of these systems allow for stricter requirements on their operations, as it eliminates human-related uncertain factors. As a consequence, autonomous systems rely increasingly more on algorithm robustness.

When it comes to attitude estimation, past researchers have developed excellent models for attitude tracking and estimation of tumbling rigid bodies with known inertia and actuation properties. However, there is a limited set of methods for dealing with systems whose inertia or actuation torques are unknown. This is one of the problems explored in the current dissertation, with the ultimate goal of developing an algorithm that is able to track a non-cooperative tumbling target using a visual sensor only (RGB camera).

In the field of rigid-body attitude control, two new formulations of finite-time controllers are introduced. The controllers are derived from Lyapunov-based formulations, and contrast with asymptotic controllers by guaranteeing convergence to a desired trajectory in finite-time, as opposed to asymptotically. These new control laws are feedback-based and are robust to unknown disturbance torques.

This dissertation is subdivided in two parts, with two chapters in each. Part I (Chapters 2 and 3) concerns of estimating the angular velocity of an attitude system based on sequential orientation measurements, whereas Part II (Chapters 4 and 5) presents new attitude controllers that steer a fully actuated rigid body towards any desired configuration within prescribed finite time. Each of these chapters is a standalone text with introduction, developments and conclusions, although some parts are reduced from the original publications to prevent redundancy in the current manuscript.

Chapter 2 proposes a batch solution to the problem of estimating constant angular velocity based on sequential orientation measurements, as presented in [6]. Provided that the angular velocity remains constant, the orientation quaternion belongs to a constant plane of rotation as time evolves. Motivated by this fundamental property, one can determine the angular velocity's direction by estimating the quaternion plane of rotation. Hence, the estimation of the quaternion plane of rotation leads to the determination of the axis of rotation. The angular velocity magnitude is estimated by projecting the measured quaternions onto the estimated plane of rotation, and then

computing the least squares evolution of the quaternion angle in the plane. Performance evaluation of the proposed algorithm is done through a Monte Carlo analysis, also being compared with a Multiplicative Extended Kalman Filter.

Chapter 3 concerns of estimating the angular velocity of a non-cooperative target using camera measurements. These results build upon the solutions of Chapter 2 by adapting the estimation algorithm for when the angular velocity is not constant, but rather evolving with unknown input torques. The new algorithm assumes that a fixed set of past orientation measurements evolve such that the angular velocity is approximately constant for the whole window of measurements. In order to determine the size of the window (such that the pure-spin assumption is reasonable), the estimator in Chapter 3 employs statistical consistency tests to determine whether or not a set of measurements seem to satisfy the assumption of “constant angular velocity”. The number of input measurements adapts itself with time based on the results of these consistency tests. The performance of the proposed angular velocity estimator is analyzed through a camera-target simulator, where the target is tracked using Simultaneous Localization and Mapping algorithms, providing relative orientation measurements. Preliminary results from Chapter 3 were presented in [7].

Chapter 4 introduces a new class of finite-time feedback controllers for rigid-body attitude dynamics subject to full actuation, as presented in [2]. The control structure is Lyapunov-based and is designed to regulate the con-

figuration from an arbitrary initial state to any prescribed final state within user-specified finite transfer-time. A salient feature is that the synthesis of the control structure is explicit, i.e., given the transfer-time time, the feedback-gains are explicitly stated to satisfy the convergence specifications. A major contrast between this work and others in the literature is that instead of resorting to feedback-linearization (to get to the so-called normal form), the new proposed approach approach efficiently marries the process of designing time-varying feedback gains with the logarithmic Lyapunov function for attitude kinematics based on the Modified Rodrigues Parameters representation. Saliently, this finite-time solution extends nicely for accommodating trajectory tracking objectives and possesses robustness with respect to bounded external disturbance torques. Numerical simulations are performed to test and validate the performance and robustness features of the new control designs.

Chapter 5 introduces an alternative control law to what is proposed in Chapter 4. In contrast with the previous solution, the stabilizing control law herein presented does not depend on any knowledge on the inertial properties of the controlled rigid body, and it does not require cancellation of the non-working gyroscopic terms present in attitude equations of motion. The new solution still guarantees limit convergence to the origin as time approaches the terminal time, but it can no longer be assured that the storage function decreases monotonically throughout the controlled period. As in Chapter 4, the new controller is also shown to be able to track trajectories, as well as being robust to bounded eternal disturbance torques. The results of Chapter 5 were

previously presented in [3].

The contributions in this dissertation are outlined below:

- Derivation and development of the Quaternion Regression Algorithm for attitude systems in pure spin, along with a Monte Carlo analysis on its performance (Chapter 2).
- Adaptation of QuateRA for estimating the tumbling rate of a target that is not in pure spin by introducing a self-tuning adaptive algorithm. The algorithm performance is analyzed by tracking a non-cooperative tumbling target using an RGB camera (Chapter 3).
- The derivation of a finite-time attitude controller for fully-actuated rigid bodies (possibly disturbed by unknown bounded torques) based on a backstepping formulation (Chapter 4).
- The derivation of a finite-time attitude controller for fully-actuated rigid bodies (possibly disturbed by unknown bounded torques) based on a Lyapunov-like formulation without resorting to backstepping (Chapter 5).

Part I

Angular Velocity Estimation from Orientation Measurements

Chapter 2

QuateRA: The Quaternion Regression Algorithm

2.1 Introduction

This chapter¹ presents a batch solution to the problem of angular velocity estimation using a time-sequence of orientation measurements in terms of the Euler quaternion parameterization. Our approach is motivated by the constant translational velocity estimation problem, whose solution is well known and has well-understood statistical properties [11]. Surprisingly, the rotational counterpart is significantly more challenging and has not yet been solved in a batch estimation sense (to the author’s best knowledge). Based on reasonable assumptions for the quaternion noise measurement model, we derive a simple two-step algorithm that establishes a closed-form solution for the constant angular velocity estimation problem without the need to use iterative algorithms.

The problem of estimating the angular velocity under pure spin is a specialized case to the general problem of estimating the angular velocity for a tumbling body. However, the understanding of the pure spin problem aids solving the generalized case assuming that the tumbling motion can be approximated to pure spin throughout a sufficiently short-duration finite sequence of measurements. A kinematic approach (such as the one proposed in the current work) can be particularly useful when estimating the angular velocity of a non-cooperative target whose inertia properties and external torques are

¹“Marcelino Almeida, Renato Zanetti, Daniele Mortari, and Maruthi Akella. Quatera: The quaternion regression algorithm. *Submitted to the Journal of Guidance, Control, and Dynamics*, 2019.” (Marcelino Almeida conducted the problem formulation, the mathematical proofs, simulation and analyses, and wrote the paper.)

unknown.

The lack of precise knowledge of the rigid-body’s inertia matrix and torque vector also poses a major challenge to standard angular velocity estimation techniques. Many of the existing angular velocity estimators [47, 53] rely on the knowledge of the target’s specific inertia and torque parameters. An exception can be made for the *derivative approach* described in Ref. [9], but as the author acknowledges, the angular velocity estimator can produce considerable error due to the presence of measurement noise. In Ref. [10], the authors present the Pseudolinear Kalman Filter (PSELIKA), which does not depend on knowledge of inertia matrix or input torques. However, PSELIKA is developed with the goal of “simplicity rather than accuracy” [10], serving as a relatively coarse angular velocity estimator for control loop damping purposes.

In Ref. [51], generalizations to Wahba’s problem are proposed by accepting sequential vector measurements instead of the traditional simultaneous ones (see Ref. [38] and the references therein). These generalizations imply the need to estimate for initial orientation and angular velocity (not only orientation, as in Wahba’s problem). The work of Ref. [51] proposes the following problems:

- First Generalized Wahba’s Problem (FGWP) - The system is in pure spin with known spin-axis but unknown spin rate. The author presents a closed-form solution to this problem based on two measurements. The work of Ref. [54] uses semidefinite optimization to solve FGWP for more

than two measurements.

- Second Generalized Wahba’s Problem (SGWP) - The system is tumbling (torque-free) with known inertia matrix. This system is shown to be observable with at least three vector measurements, but no solution is provided by Ref. [51]. A solution to the three-vector measurement problem is provided in Ref. [26] and a numerical solution is provided in Ref. [52] for four measurements or more.

An alternative solution to the pure spin angular velocity estimation problem is to use methods based on the Multiplicative Extended Kalman Filter (MEKF) [24, 34, 36], since these rely on kinematics only. These methods should usually converge if properly initialized and iterated through a backward smoothing process [50] or through some gradient descent method. Iterated nonlinear programming methods² present the drawback that these might converge to local minima, or not even converge. Our batch solution in this paper departs from filtering-based ones in that no iterations are necessary for the proposed algorithm.

The primary contribution of this work is the Quaternion Regression Algorithm (QateRA). Instead of solving the problem through well-established filtering approaches [24, 34, 36], we solve the problem through a geometrical standpoint. We provide an alternative to an attitude EKF by introducing an attitude regression algorithm. QateRA builds upon the work of Ref. [42], and

²Here we use the term *iterated* to denote *sequential* algorithms.

it is a batch solver (does not require iterations), even though the problem is nonlinear. QuateRA uses a sequence of orientation measurements to determine the system’s axis of rotation (AOR) through a Singular Value Decomposition (SVD) procedure, and then it uses the AOR to estimate for the angular velocity magnitude (AVM). We develop QuateRA’s AOR estimation with use of the Total Least Squares (TLS) cost function, and we are able to provide a solution under mild assumptions on the measurement noise. In fact, the AOR estimation algorithm herein presented shares important similarities with the problem of averaging quaternions [35, 37], but instead of finding an average quaternion, we search for an average quaternion plane. The quaternion average is actually a particular solution to our algorithm. In the current work, we also discuss some asymptotic statistical properties involving QuateRA, apart from validating those results with Monte Carlo simulations.

QuateRA’s AOR estimation was first introduced by Ref. [42], and experimental validation was presented in Ref. [4]. Ref. [7] used QuateRA’s AOR estimate in conjunction with a modified MEKF to estimate the relative angular velocity of a non-cooperative target. The current chapter presents an expanded version of the work in Ref. [6], which differs from the previous contributions within Refs. [4, 7, 42] in the following aspects:

- The previous works used QuateRA’s AOR estimation based on heuristics, instead of being a solution that formally minimizes a cost function. In the current work, we start from a constrained version of TLS (the constraints are a direct consequence of the quaternion unit-norm condition),

and reach the same solution suggested by Ref. [42] under the assumption of small angle approximation for the quaternion measurement noise.

- None of the previously reported results in this field (Refs. [4, 7, 42]) analyzed the statistical properties of QuateRA. In the current work, we explore the strong consistency properties of QuateRA, and we propose covariance matrices for the angular velocity estimation. We also present Monte Carlo analysis to validate the derived statistical properties.
- When estimating the AVM, Ref. [42] suggested the use of performing “*dirty*” derivatives on the most recently measured quaternions. In contrast, the work of [4] showed that one can often obtain better results by pre-filtering the measured quaternions before employing the derivative. The AVM estimation in Ref. [7] is performed by using a modified MEKF. The AVM estimation suggested by Ref. [42] is actually biased under mild measurement noise, while the solutions presented in Refs. [4] and [7] remedy the bias problem, but introduce tuning parameters. In contrast, this work reprojects the measured quaternions onto the plane of rotation estimated by QuateRA, and calculates the AVM as an average quaternion angular displacement over time.

The remainder of this chapter is organized as follows: Section 2.2 presents a motivation to the angular velocity estimation problem by introducing solutions to the simple problem of estimating constant linear velocity

from position measurements. Some of the insights therein are crucial for understanding QuateRA’s statistical properties. Section 2.3 introduces the rotational attitude kinematics, describing some notation and parametrizations, as well as the assumed measurement model. Section 2.4 presents the estimation problem formulation, introducing the optimization cost function and constraints of the problem. Section 2.5 presents QuateRA, and Section 2.6 introduces a Monte Carlo analysis of QuateRA, comparing it with an MEKF formulation, and a solution using a nonlinear solver for the same problem. Finally, Section 2.7 presents conclusions for this work.

2.2 Motivation: Batch Estimation of Linear Velocity from Position Measurements

The goal of this section is to explore a well known (and solved) problem through a different perspective. This section discusses the simple problem of estimating the linear velocity of a point mass whose position is measured through time. We introduce the traditional Least Squares solution to the problem, and compare it with a two-step solution in which the direction of velocity is estimated, then its estimate is used for further estimating the linear velocity’s magnitude. Because QuateRA splits the problem in two as in the latter case of this section, we draw insights on what to expect on QuateRA’s performance.

Assume a point mass moving on the xy plane with unknown constant velocity $\mathbf{v} = [v_x \ v_y]^T$. The position of the body is denoted as $\mathbf{p} = [x \ y]^T$.

The kinematics of the problem is described as:

$$\mathbf{p}(t) = \mathbf{p}_0 + \mathbf{v}t, \quad (2.1)$$

where t denotes time and $\mathbf{p}_0 \triangleq [x_0 \ y_0]^T$ is the position of the system at time $t = 0$. The goal of this section is to estimate the vector $\mathbf{X} = [\mathbf{p}_0^T \ \mathbf{v}^T]^T$ through LS and TLS, drawing parallels between the two approaches.

We denote an estimated variable as $\hat{(\cdot)}$ ($\hat{x}(t)$ is an estimate of $x(t)$ and $\hat{y}(t)$ is an estimate of $y(t)$), and a measured variable as $\bar{(\cdot)}$ ($\bar{\mathbf{p}}$ is a measurement of \mathbf{p} and $\bar{\mathbf{v}}$ is a measurement of \mathbf{v}). We use *star* notation $(\cdot)^*$ with variables with general covariance to distinguish them from their counterpart with normalized covariance ($\text{cov}[\mathbf{p}^*]$ is a positive-definite matrix, while $\text{cov}[\mathbf{p}] = \mathbf{I}$, where \mathbf{I} is an identity matrix). The notation $\vec{(\cdot)}$ is used to denote unit-norm vectors ($\vec{\mathbf{x}}$ satisfies $\|\vec{\mathbf{x}}\|_2 = 1$). In addition, for simplicity of notation, we denote $\mathbf{p}_i = \mathbf{p}(t_i)$.

Assume that we measure the position of this system at n different instants of time $t_i, i \in \{1, \dots, n\}$. The measurement model is given by:

$$\begin{cases} \bar{x}(t_i) = x(t_i) + \epsilon_x(t_i) \\ \bar{y}(t_i) = y(t_i) + \epsilon_y(t_i) \end{cases}, \quad (2.2)$$

where $\boldsymbol{\epsilon}_i^* \triangleq [\epsilon_x(t_i) \ \epsilon_y(t_i)]^T$ is assumed to be a normally distributed random variable with mean $\mathbb{E}[\boldsymbol{\epsilon}_i^*] = \mathbf{0}$ and covariance $\mathbf{P}_\epsilon \triangleq \text{cov}[\boldsymbol{\epsilon}_i^*] = \mathbb{E}[\boldsymbol{\epsilon}_i^* \boldsymbol{\epsilon}_i^{*T}]$, with $\mathbf{P}_\epsilon > 0$. We denote the measured position $\bar{\mathbf{p}}_i^* = \mathbf{p}_i + \boldsymbol{\epsilon}_i^*$, which is a random variable with mean $\mathbb{E}[\bar{\mathbf{p}}_i^*] = \mathbf{p}_i$ and covariance $\text{cov}[\bar{\mathbf{p}}_i^*] = \mathbf{P}_\epsilon$. Decomposing the covariance matrix as $\mathbf{P}_\epsilon = \mathbf{L}\mathbf{L}^T$, we define the normalized measurements

$\bar{\mathbf{p}}_i = \mathbf{L}^{-1}\bar{\mathbf{p}}_i^*$ such that $\bar{\mathbf{p}}_i = \mathbf{L}^{-1}\mathbf{p}_i + \mathbf{L}^{-1}\boldsymbol{\epsilon}_i^*$. Defining $\boldsymbol{\epsilon}_i = \mathbf{L}^{-1}\boldsymbol{\epsilon}_i^*$, we have that $\mathbb{E}[\boldsymbol{\epsilon}_i] = \mathbf{0}$ and $\text{cov}[\boldsymbol{\epsilon}_i] = \mathbb{E}[\boldsymbol{\epsilon}_i\boldsymbol{\epsilon}_i^T] = \mathbf{I}_2$, where \mathbf{I}_2 is the two-dimension identity matrix.

The vector of normalized measured positions is written as $\bar{\mathbf{P}} \triangleq [\bar{\mathbf{p}}_1^T \ \bar{\mathbf{p}}_2^T \ \cdots \ \bar{\mathbf{p}}_n^T]^T$, and the equivalent vector of normalized true positions is given by $\mathbf{P} \triangleq [(\mathbf{L}^{-1}\mathbf{p}_1)^T \ (\mathbf{L}^{-1}\mathbf{p}_2)^T \ \cdots \ (\mathbf{L}^{-1}\mathbf{p}_n)^T]^T$. The measurement error vector is written as $\boldsymbol{\varepsilon} \triangleq [\boldsymbol{\epsilon}_1^T \ \boldsymbol{\epsilon}_2^T \ \cdots \ \boldsymbol{\epsilon}_n^T]^T$, implying $\bar{\mathbf{P}} = \mathbf{P} + \boldsymbol{\varepsilon}$. Since $\mathbb{E}[\boldsymbol{\varepsilon}] = \mathbf{0}$, then we have that $\mathbb{E}[\bar{\mathbf{P}}] = \mathbf{P}$ and $\text{cov}[\bar{\mathbf{P}}] = \text{cov}[\boldsymbol{\varepsilon}] = \mathbf{I}_{2n}$.

Given the measurement vector $\bar{\mathbf{P}}$, we want to optimally estimate the system's initial position \mathbf{p}_0 and velocity \mathbf{v} . A common method to solve this problem is to use the least squares solution, which pursues to find optimal \mathbf{p}_0 and \mathbf{v} that minimizes the cost function:

$$J = \frac{1}{2}\boldsymbol{\varepsilon}^T\boldsymbol{\varepsilon} = \frac{1}{2}(\bar{\mathbf{P}} - \mathbf{P})^T(\bar{\mathbf{P}} - \mathbf{P}). \quad (2.3)$$

The solution to this problem is very well known in the literature. Constructing the matrix $\mathbf{H} \in \mathbb{R}^{2n \times 4}$:

$$\mathbf{H} = \begin{bmatrix} \mathbf{L}^{-1} & \mathbf{0} & \cdots & \mathbf{0} \\ \mathbf{0} & \mathbf{L}^{-1} & \cdots & \mathbf{0} \\ \vdots & \vdots & \ddots & \vdots \\ \mathbf{0} & \mathbf{0} & \cdots & \mathbf{L}^{-1} \end{bmatrix} \begin{bmatrix} \mathbf{I}_2 & t_1\mathbf{I}_2 \\ \mathbf{I}_2 & t_2\mathbf{I}_2 \\ \vdots & \vdots \\ \mathbf{I}_2 & t_n\mathbf{I}_2 \end{bmatrix}, \quad (2.4)$$

we have that $\mathbf{P} = \mathbf{H}\mathbf{X}$. The optimal solution³ $\hat{\mathbf{X}}_{LS} = [\hat{\mathbf{p}}_0^T \ \hat{\mathbf{v}}^T]$ for the cost

³We use the subscript LS to indicate that this is the Linear Squares solution to the problem.

function in Eq. 2.3 is given by:

$$\hat{\mathbf{X}}_{LS} = (\mathbf{H}^T \mathbf{H})^{-1} \mathbf{H}^T \bar{\mathbf{P}}. \quad (2.5)$$

Although Eq. 2.5 is the most used method to estimate the unknowns from Eq. 2.1, it is also possible to obtain solutions that minimize cost functions different from Eq. 2.3.

In particular, one can pursue a solution through Total Least Squares (TLS - also referred to as Orthogonal Least Squares), as opposed to Least Squares (LS). Starting from Eq. 2.1, we have that:

$$x(t) = x_0 + v_x \cdot t \quad (2.6)$$

$$y(t) = y_0 + v_y \cdot t \quad (2.7)$$

Isolating the t term in Eq. 2.6 and substituting it into Eq. 2.7 leads to:

$$y = y_0 + \frac{v_y}{v_x} (x - x_0) = \left(y_0 - \frac{v_y}{v_x} x_0\right) + \frac{v_y}{v_x} x \quad (2.8)$$

Defining $\alpha \triangleq y_0 - \frac{v_y}{v_x} x_0$ and $\beta = \frac{v_y}{v_x}$, then Eq. 2.8 can be written in the compact form:

$$y = \alpha + \beta x, \quad (2.9)$$

and the unknowns to be found are now α and β . The problem can be recast as finding the Cartesian line $L(\mathbf{l}_0, \vec{\mathbf{l}})$ ($\mathbf{l}_0 \in \mathbb{R}^2$ is a point belonging to the line, and $\vec{\mathbf{l}} \in \mathbb{S}^1$ is the line direction) such that the distance squared between the regularized measured points $\bar{\mathbf{p}}_i, i \in \{1, \dots, n\}$ and the line $L(\mathbf{l}_0, \vec{\mathbf{l}})$ are

minimized. The distance function used in TLS is not necessarily the *Euclidian* distance between a point and a line, unless the error covariance is of the form $\mathbf{P}_\epsilon = \sigma^2 \mathbf{I}_2$, where $\sigma \in \mathbb{R}_{>0}$.

For general values of the covariance matrix, we pursue as in LS by covariance-normalizing the measurements $\bar{\mathbf{p}}_i = \mathbf{L}^{-1} \bar{\mathbf{p}}_i^*$, where \mathbf{L} comes from the decomposition of $\mathbf{P}_\epsilon = \mathbf{L}\mathbf{L}^T$. Defining $d(\bar{\mathbf{p}}_i, L)$ as the *Euclidian* distance between $\bar{\mathbf{p}}_i$ and $L(\mathbf{l}_0, \vec{\mathbf{l}})$, the TLS cost function is given by (see Appendix A.1 for a formal definition of the TLS problem):

$$J_{TLS} = \sum_{i=1}^n d(\bar{\mathbf{p}}_i, L)^2. \quad (2.10)$$

The regression problem for the cost of Eq. 2.10 was first proposed and solved in [1] for the special case in which $\mathbf{P}_\epsilon = \sigma^2 \mathbf{I}_2$. Many solution formulations have been presented to this problem for the general case (see [16, 41, 65] for literature review), but here we present the solution presented in [57] due to its connections to the QuateRA problem.

First, we calculate the centroid of all the data-points:

$$\boldsymbol{\mu}_p \triangleq \frac{1}{n} \sum_{i=1}^n \bar{\mathbf{p}}_i. \quad (2.11)$$

It turns out that the optimal line $\hat{L}(\mathbf{l}_0, \vec{\mathbf{l}})$ passes through the centroid $\boldsymbol{\mu}_p$. Since a line is defined as a point and a direction, the solution is complete once the line direction is found. To this purpose, we define the translated vectors $\underline{\mathbf{p}}_i$:

$$\underline{\mathbf{p}}_i \triangleq \bar{\mathbf{p}}_i - \boldsymbol{\mu}_p, \quad \forall i \in \{1, \dots, n\} \quad (2.12)$$

Clearly, the centroid of the set of vectors $\underline{\mathbf{p}}_i, i \in \{1, \dots, n\}$ is at the origin. Then, we define the matrix $\mathbf{B} \in \mathbb{R}^{2 \times n}$ as a concatenation of all translated vectors $\underline{\mathbf{p}}_i$:

$$\mathbf{B} \triangleq [\underline{\mathbf{p}}_1 \quad \underline{\mathbf{p}}_2 \quad \cdots \quad \underline{\mathbf{p}}_n] \quad (2.13)$$

Taking the Singular Value Decomposition (SVD) on the matrix \mathbf{B} , we get $\mathbf{B} = \mathbf{U}\tilde{\Sigma}\mathbf{V}^T$, where $\mathbf{U} = [\mathbf{u}_1 \quad \mathbf{u}_2]$ contains the *left singular vectors* of \mathbf{B} , $\mathbf{V} = [\mathbf{v}_1 \quad \mathbf{v}_2 \quad \cdots \mathbf{v}_n]$ contains the *right singular vectors* of \mathbf{B} , and $\tilde{\Sigma} = [\Sigma \quad \mathbf{0}_{2 \times n-2}]$ contains the singular values of \mathbf{B} within $\Sigma = \text{diag}(\sigma_1, \sigma_2)$.

As shown in Ref. [57], the line that minimizes the cost function of Eq. 2.10 is parameterized as $\hat{L}(\boldsymbol{\mu}_p, \mathbf{u}_1)$, where $\mathbf{u}_1 \in \mathbb{S}^1$ is the first left singular vector of \mathbf{B} , and the optimal cost is given by $\hat{J}_{TLS} = \sigma_2$. The problem can then be mapped back into the original coordinates:

$$\boldsymbol{\mu}_p^* = \begin{bmatrix} \mu_{px}^* \\ \mu_{py}^* \end{bmatrix} = \mathbf{L}\boldsymbol{\mu}_p, \quad \mathbf{u}_1^* = \begin{bmatrix} u_{1x}^* \\ u_{1y}^* \end{bmatrix} = \frac{\mathbf{L}\mathbf{u}_1}{\|\mathbf{L}\mathbf{u}_1\|}. \quad (2.14)$$

Thus, the TLS minimizer that fits the model of Eq. 2.9 given the measurements of Eq. 2.2 and the measurement noise covariance \mathbf{P}_ϵ is given by the line $\hat{L}^*(\boldsymbol{\mu}_p^*, \mathbf{u}_1^*)$. The constants α and β from Eq. 2.9 can be calculated as:

$$\beta = \frac{u_{1y}^*}{u_{1x}^*}, \quad \alpha = \mu_{py}^* - \beta\mu_{px}^*. \quad (2.15)$$

Going back to the original problem of estimating the velocity in Eq. 2.1, the vector \mathbf{u}_1^* is an estimate of the velocity direction $\vec{\mathbf{v}} \triangleq \mathbf{v}/\|\mathbf{v}\|$. In order to

obtain the estimation of the velocity \mathbf{v} , one still needs to estimate the velocity magnitude $\|\mathbf{v}\|$.

We can project the measured points onto the optimal line $\boldsymbol{\mu}_p^*, \mathbf{u}_1^*$, obtaining the TLS estimates for these points along the line. Then, the velocity magnitude can be estimated as an average displacement along the line.

Given that the measurements are distributed as $\bar{\mathbf{p}}_i^* \sim \mathcal{N}(\mathbf{p}_i, \mathbf{P}_\epsilon)$, it is possible to show that the marginal distribution of $\bar{\mathbf{p}}_i^*$ along any line $L(\mathbf{l}_0, \vec{\mathbf{l}})$ is a one-dimensional normally-distributed random variable with mean at \mathbf{p}_{pi}^* and standard deviation σ along the $\vec{\mathbf{l}}$ direction (see Lemmas 4 and 5 of Appendix A.4 for proof), where:

$$\mathbf{p}_{pi}^* = \mathbf{l}_0 + \frac{1}{\sigma^2} \left[(\bar{\mathbf{p}}_i^* - \mathbf{l}_0)^T \mathbf{P}^{-1} \vec{\mathbf{l}} \right] \vec{\mathbf{l}}, \quad \sigma = \frac{1}{\|\mathbf{L}^{-1} \vec{\mathbf{l}}\|} = \frac{1}{\sqrt{\vec{\mathbf{l}}^T \mathbf{P}^{-1} \vec{\mathbf{l}}}}. \quad (2.16)$$

Hence, defining $\bar{S}_i = \mathbf{p}_{pi}^* \mathbf{u}_1^*$ as the displacement along the optimal TLS line, and admitting the distribution $\bar{S}_i \sim \mathcal{N}(S_i, \sigma^2)$, one can use LS to solve for S_0 and $\|\mathbf{v}\|$ in the model:

$$S_i = S_0 + \|\mathbf{v}\| \cdot t_i. \quad (2.17)$$

2.2.1 Analysis

It turns out that the solution obtained through LS (Eq. 2.5) is generally different from the one obtained through TLS (solution of Eq. 2.17 and the first left singular vector of the matrix in Eq. 2.13). The different solutions are expected, given that both estimators employ different cost functions.

For the particular scenario of estimating the planar system's velocity of Eq. 2.1, the LS solution is more advantageous than TLS in many aspects, some of which are described below. Assuming a linear model (as in Eq. 2.1) with additive gaussian measurement noise (as in Eq. 2.2), LS is a maximum likelihood estimator, implying:

- LS is known to be the globally optimal estimator that obtains the Minimum Mean Square Error (MMSE) of the estimate, i.e., it minimizes $MSE = \mathbb{E} \left[(\bar{\mathbf{X}} - \mathbf{X})^T (\bar{\mathbf{X}} - \mathbf{X}) \right]$. This implies that, in average, no other estimator will perform as good as LS for minimization of MSE. In other words, the LS solution will produce smaller squared error more than 50% of the time (in average) when compared with any other estimator.
- LS is well known for being an unbiased estimator given zero-mean additive noise to the measurements. On the other hand, TLS is only guaranteed to be strongly consistent, i.e., the TLS estimate converges to the true value (with probability 1) as the number of measurements n tend to infinity [20, 27], meaning that it is asymptotically unbiased. Monte Carlo analysis suggest that the bias of TLS is statistically appreciable when signal-to-noise ratio is low, and n is small [30, 65].
- The error-covariance for TLS estimates are known for $n \rightarrow \infty$, while the error-covariance of LS is known for any n . However, the Monte Carlo analysis in [30] suggest that the TLS error-covariance estimation

for $n \rightarrow \infty$ is a good approximation for $n < \infty$ provided that $n > 20$. Ref. 20 derives a TLS covariance matrix for large samples.

- The LS estimate of the velocity magnitude $\|\mathbf{v}\|$ using Eq. 2.17 assumes that the velocity direction $\vec{\mathbf{v}}$ is precisely known. However, as already mentioned, TLS provides a biased estimate $\vec{\mathbf{v}} = \mathbf{u}_1$, which can also lead to a biased estimation of $\|\mathbf{v}\|$.

Based on the comparisons above, there is no compelling reason to convert the model of Eq. 2.1 into the form of Eq. 2.9, and then perform TLS. On the other hand, provided that measurement noise is sufficiently small, and the number of measurements are large enough (e.g., say $n > 20$), then then TLS is a competitive algorithm that matches closely the LS solution in the MSE sense (i.e., it outperforms LS in the MSE sense almost 50% of the time).

As a motivational example, assume a system moving on a line with initial position $\mathbf{p}_0 = [1 \ 0]^T$ m and velocity $\mathbf{v} = [2 \ 1]^T$ m. The measurement error standard deviation is given by $\sigma_\epsilon = 0.1$ m. The measurements are taken once every $dt \triangleq t_{i+1} - t_i = 0.1$ s and the regression is made with $n = 20$ measurements. Running a Monte Carlo simulation of 100000 solutions, it turns out that LS outperforms TLS 51.05% of the time in the estimated squared error sense. If the measurement error standard deviation degrades to $\sigma_\epsilon = 0.5$ m, then LS outperforms TLS 55.44% of the time. By taking $n = 50$ measurements with $\sigma_\epsilon = 0.1$ m, LS outperforms TLS 50.34% of the time.

Despite the possible limitations of TLS, we employ the TLS cost func-

tion in the development of QuateRA. This choice is made because it is then possible to decouple the estimation of the angular velocity axis of rotation from its magnitude, whereas the estimation of the coupled problem (which would be the LS counterpart) is substantially more complex. When estimating a fixed axis of rotation among sequential quaternion measurements, the estimation problem can be posed as a plane fitting problem (special case of TLS), as will be shown in Section 2.4.

2.3 Attitude Kinematics and Measurement Model

2.3.1 Attitude Kinematics

We adopt the notation \mathbf{q}_A^B to represent the relative orientation quaternion between frames A and B . A quaternion is written in the form:

$$\mathbf{q}_A^B = \begin{bmatrix} q_{As}^B \\ \mathbf{q}_{Av}^B \end{bmatrix},$$

where \mathbf{q}_{Av}^B and q_{As}^B are the vector and scalar components of the quaternion \mathbf{q}_A^B , respectively. Also, quaternions satisfy the norm constraint $\|\mathbf{q}_A^B\| = 1$.

We denote the quaternion inverse rotation as $(\mathbf{q}_A^B)^{-1} = \mathbf{q}_B^A$, which is given by:

$$\mathbf{q}_B^A = \begin{bmatrix} q_{As}^B \\ -\mathbf{q}_{Av}^B \end{bmatrix}.$$

The quaternion composition rule is denoted as:

$$\mathbf{q}_A^C = \mathbf{q}_B^C \otimes \mathbf{q}_A^B,$$

in which:

$$\mathbf{q}_B^C \otimes = \begin{bmatrix} q_{Bs}^C & -(\mathbf{q}_{Bv}^C)^T \\ \mathbf{q}_{Bv}^C & q_{Bs}^C \mathbf{I} - [\mathbf{q}_{Bv \times}^C] \end{bmatrix}, \quad (2.18)$$

where \mathbf{I} is the 3×3 identity matrix, and $[\mathbf{v}_\times]$ is the skew-symmetric cross product matrix associated with a vector $\mathbf{v} \in \mathbb{R}^3$. The matrix $\mathbf{q}_B^C \otimes$ is a 4D rotation matrix, implying orthogonality, i.e., it satisfies $\mathbf{q}_B^C \otimes (\mathbf{q}_B^C \otimes)^T = (\mathbf{q}_B^C \otimes)^T \mathbf{q}_B^C \otimes = \mathbf{I}_4$. Also, we denote the *identity quaternion*:

$$\mathbf{q}_I \triangleq (\mathbf{q}_A^B)^{-1} \otimes \mathbf{q}_A^B = \mathbf{q}_A^B \otimes (\mathbf{q}_A^B)^{-1} = [1 \ 0 \ 0 \ 0]^T \quad (2.19)$$

Given a vector $\mathbf{v} \in \mathbb{R}^3$, then we define $\mathbf{v} \otimes \in \mathbb{R}^{4 \times 4}$ as:

$$\mathbf{v} \otimes \triangleq \begin{bmatrix} 0 & -\mathbf{v}^T \\ \mathbf{v} & -[\mathbf{v}_\times] \end{bmatrix}. \quad (2.20)$$

With some slight abuse of notation, we define the composition of a quaternion $\mathbf{q} \in \mathbb{S}^3$ with a vector $\mathbf{v} \in \mathbb{R}^3$ as:

$$\mathbf{q} \otimes \mathbf{v} \triangleq \mathbf{q} \otimes \begin{bmatrix} 0 \\ \mathbf{v} \end{bmatrix}.$$

Given a vector $\mathbf{v}^A \in \mathbb{R}^3$ expressed in frame A , its representation in frame B can be obtained as:

$$\begin{bmatrix} 0 \\ \mathbf{v}^B \end{bmatrix} = \mathbf{q}_A^B \otimes \mathbf{v}^A \otimes (\mathbf{q}_A^B)^{-1}.$$

Alternatively, \mathbf{v}^B can be calculated from \mathbf{v}^A using the expression $\mathbf{v}^B = \mathbf{C}_A^B \mathbf{v}^A$, where \mathbf{C}_A^B is the direction cosine matrix respective to \mathbf{q}_A^B :

$$\mathbf{C}_A^B = \mathbf{I} - 2q_{As}^B [\mathbf{q}_{Av \times}^B] + 2[\mathbf{q}_{Av \times}^B]^2. \quad (2.21)$$

Denote $\boldsymbol{\omega}_{B/A}^C \in \mathbb{R}^3$ as the angular velocity of frame B w.r.t. frame A expressed in frame C . Then, the rotational kinematics for \mathbf{q}_A^B is given by:

$$\dot{\mathbf{q}}_A^B = \frac{1}{2} \boldsymbol{\omega}_{B/A}^B \otimes \mathbf{q}_A^B. \quad (2.22)$$

For an angular velocity $\boldsymbol{\omega}_{B/A}^B$, we denote its magnitude $\Omega_{B/A}$ and its direction $\vec{\boldsymbol{\omega}}_{B/A}^B$, such that:

$$\Omega_{B/A} \triangleq \|\boldsymbol{\omega}_{B/A}^B\|, \quad \vec{\boldsymbol{\omega}}_{B/A}^B \triangleq \frac{\boldsymbol{\omega}_{B/A}^B}{\Omega_{B/A}}.$$

Assuming a constant angular velocity $\boldsymbol{\omega}_{B/A}^B$ throughout a period $\Delta t = t_f - t_0$, then the solution to the kinematic differential equation in Eq. 2.22 is given by $\mathbf{q}_A^B(t_f) = \mathbf{F}(\boldsymbol{\omega}_{B/A}^B) \cdot \mathbf{q}_A^B(t_0)$, where:

$$\mathbf{F}(\boldsymbol{\omega}_{B/A}^B) = \exp\left[\frac{\Delta t}{2} \boldsymbol{\omega}_{B/A}^B \otimes\right] = \cos\frac{\Omega_{B/A} \Delta t}{2} \cdot \mathbf{I}_4 + \sin\frac{\Omega_{B/A} \Delta t}{2} \cdot \vec{\boldsymbol{\omega}}_{B/A}^B \otimes. \quad (2.23)$$

Using the subscript I to denote inertial frame and O for the frame of the object of interest, the remainder of this paper will denote $\mathbf{q}_i \triangleq \mathbf{q}_I^O(t_i)$, $\boldsymbol{\omega} \triangleq \boldsymbol{\omega}_{O/I}^O$, $\vec{\boldsymbol{\omega}} \triangleq \vec{\boldsymbol{\omega}}_{O/I}^O$, and $\Omega \triangleq \Omega_{O/I}$.

2.3.2 Measurement Model

In this section, we present the assumed measurement model for the problem. The assumptions and derivations herein presented are crucial for posing and solving the AOR optimal estimation within QuateRA.

We employ the quaternion measurement model given by:

$$\bar{\mathbf{q}}_i = \mathbf{q}_i \otimes \mathbf{q}_{Ni}, \quad (2.24)$$

where $\mathbf{q}_i = [q_{si} \ \mathbf{q}_{vi}^T]^T$ is the true quaternion and \mathbf{q}_{Ni} is the noise quaternion:

$$\mathbf{q}_{Ni} \triangleq \begin{bmatrix} \cos \frac{\theta_i}{2} \\ \mathbf{e}_{Ni} \sin \frac{\theta_i}{2} \end{bmatrix}, \quad (2.25)$$

in which θ_i and \mathbf{e}_{Ni} are independent random variables. We assume that θ_i is Gaussian (Although it might be unrealistic to assume that angles are distributed as Gaussian, Ref. [43] has shown that this is a reasonable approximation for double-precision machines as long as $\sigma_\theta \leq 22$ deg) such that $\theta_i \sim \mathcal{N}(0, \sigma_\theta^2)$, and $\mathbf{e}_{Ni} \in \mathbb{S}^2$ is a unit-norm random vector uniformly distributed⁴ in $\mathbb{S}^2 = \{\mathbf{x} \in \mathbb{R}^3 : \|\mathbf{x}\| = 1\}$ and has the characteristics $\mathbb{E}[\mathbf{e}_{Ni}] = \mathbf{0}$ and $\mathbb{E}[\mathbf{e}_{Ni}\mathbf{e}_{Ni}^T] = \frac{1}{3}\mathbf{I}$ (see Appendix A.3).

Assuming that all \mathbf{q}_{Ni} , $i \in \{1, \dots, n\}$ are independent and identically distributed, we define the quantities $\boldsymbol{\mu}_N$ and \mathbf{P}_N as the mean and covariance for the noise quaternion, respectively:

$$\begin{aligned} \boldsymbol{\mu}_N &\triangleq \mathbb{E}[\mathbf{q}_{Ni}] = \mathbb{E} \begin{bmatrix} \cos \frac{\theta_i}{2} \\ \mathbf{e}_{Ni} \sin \frac{\theta_i}{2} \end{bmatrix} = \begin{bmatrix} \mathbb{E}[\cos \frac{\theta_i}{2}] \\ \mathbb{E}[\mathbf{e}_{Ni} \sin \frac{\theta_i}{2}] \end{bmatrix} = \begin{bmatrix} \mathbb{E}[\cos \frac{\theta_i}{2}] \\ \mathbb{E}[\mathbf{e}_{Ni}] \mathbb{E}[\sin \frac{\theta_i}{2}] \end{bmatrix} \\ &= \mathbb{E}[\cos \frac{\theta_i}{2}] \begin{bmatrix} 1 \\ \mathbf{0} \end{bmatrix} \\ \mathbf{P}_N &\triangleq \mathbb{E}[(\mathbf{q}_{Ni} - \boldsymbol{\mu}_N)(\mathbf{q}_{Ni} - \boldsymbol{\mu}_N)^T] = \mathbb{E}[\mathbf{q}_{Ni}\mathbf{q}_{Ni}^T] - \boldsymbol{\mu}_N\boldsymbol{\mu}_N^T \\ &= \begin{bmatrix} \mathbb{E}[\cos^2 \frac{\theta_i}{2}] - \mathbb{E}^2[\cos \frac{\theta_i}{2}] & \mathbb{E}[\mathbf{e}_{Ni}^T \cos \frac{\theta_i}{2} \sin \frac{\theta_i}{2}] \\ \mathbb{E}[\mathbf{e}_{Ni} \cos \frac{\theta_i}{2} \sin \frac{\theta_i}{2}] & \mathbb{E}[\mathbf{e}_{Ni}\mathbf{e}_{Ni}^T] \mathbb{E}[\sin^2 \frac{\theta_i}{2}] \end{bmatrix} \\ &= \begin{bmatrix} \mathbb{E}[\cos^2 \frac{\theta_i}{2}] - \mathbb{E}^2[\cos \frac{\theta_i}{2}] & \mathbf{0} \\ \mathbf{0} & \frac{1}{3}\mathbb{E}[\sin^2 \frac{\theta_i}{2}] \mathbf{I}_3 \end{bmatrix} \end{aligned}$$

⁴The reader should note that this is a simplification, given that it is not always true that the angle randomness is as likely in any direction. For instance, star trackers tend to have different noise characteristics in the boresight direction and the ones perpendicular to it.

The expected values above can be calculated according with Ref. [43]:
 $\mathbb{E} [\cos \frac{\theta_i}{2}] = e^{-\sigma_\theta^2/8}$, $\mathbb{E} [\cos^2 \frac{\theta_i}{2}] = \frac{1}{2} (1 + e^{-\sigma_\theta^2/2})$, and $\mathbb{E} [\sin^2 \frac{\theta_i}{2}] = \frac{1}{2} (1 - e^{-\sigma_\theta^2/2})$. Defining $\sigma_s^2 \triangleq \mathbb{E} [\cos^2 \frac{\theta_i}{2}] - \mathbb{E}^2 [\cos \frac{\theta_i}{2}]$ and $\sigma_v^2 \triangleq \frac{1}{3} \mathbb{E} [\sin^2 \frac{\theta_i}{2}]$, then the noise covariance matrix takes the form:

$$\mathbf{P}_N = \begin{bmatrix} \sigma_s^2 & \mathbf{0} \\ \mathbf{0} & \sigma_v^2 \mathbf{I}_3 \end{bmatrix}. \quad (2.26)$$

We define the covariance for the measured quaternion as:

$$\begin{aligned} \mathbf{P}_q &\triangleq \mathbb{E} [(\bar{\mathbf{q}}_i - \mathbb{E} [\bar{\mathbf{q}}_i]) (\bar{\mathbf{q}}_i - \mathbb{E} [\bar{\mathbf{q}}_i])^T] = \mathbb{E} [\bar{\mathbf{q}}_i \bar{\mathbf{q}}_i^T] - \mathbb{E} [\bar{\mathbf{q}}_i] \mathbb{E} [\bar{\mathbf{q}}_i]^T \\ &= (\mathbf{q}_i \otimes) \mathbb{E} [\mathbf{q}_{N_i} \mathbf{q}_{N_i}^T] (\mathbf{q}_i \otimes)^T - (\mathbf{q}_i \otimes) \boldsymbol{\mu}_N \boldsymbol{\mu}_N^T (\mathbf{q}_i \otimes)^T \\ &= (\mathbf{q}_i \otimes) [\mathbb{E} [\mathbf{q}_{N_i} \mathbf{q}_{N_i}^T] - \boldsymbol{\mu}_N \boldsymbol{\mu}_N^T] (\mathbf{q}_i \otimes)^T = (\mathbf{q}_i \otimes) \mathbf{P}_N (\mathbf{q}_i \otimes)^T. \end{aligned}$$

If we make the notation relaxation $\mathbf{q}_i = [q_s \ \mathbf{q}_v^T]^T$, and use Eqs. 2.18 and 2.26, we can further expand \mathbf{P}_q as:

$$\mathbf{P}_q = \begin{bmatrix} \sigma_s^2 q_s^2 + \sigma_v^2 \mathbf{q}_v^T \mathbf{q}_v & \sigma_s^2 q_s \mathbf{q}_v^T - \sigma_v^2 q_s \mathbf{q}_v^T \\ \sigma_s^2 q_s \mathbf{q}_v - \sigma_v^2 q_s \mathbf{q}_v & \sigma_s^2 \mathbf{q}_v \mathbf{q}_v^T - \sigma_v^2 (q_s^2 \mathbf{I}_3 - [\mathbf{q}_{v \times}]^2) \end{bmatrix}.$$

Using the properties $[\mathbf{q}_{v \times}]^2 = \mathbf{q}_v \mathbf{q}_v^T - \mathbf{q}_v^T \mathbf{q}_v \mathbf{I}_3$, and $q_s^2 + \mathbf{q}_v^T \mathbf{q}_v = 1$, we have that:

$$\mathbf{P}_q = \begin{bmatrix} \sigma_v^2 + (\sigma_s^2 - \sigma_v^2) q_s^2 & (\sigma_s^2 - \sigma_v^2) q_s \mathbf{q}_v^T \\ (\sigma_s^2 - \sigma_v^2) q_s \mathbf{q}_v & \sigma_v^2 \mathbf{I}_3 + (\sigma_s^2 - \sigma_v^2) \mathbf{q}_v \mathbf{q}_v^T \end{bmatrix} = \sigma_v^2 \mathbf{I}_4 + (\sigma_s^2 - \sigma_v^2) \mathbf{q}_i \mathbf{q}_i^T. \quad (2.27)$$

Using the statistics above, if one desires to perform a quaternion measurement normalization, it is necessary to decompose the covariance matrix in

the form $\mathbf{P}_q = \mathbf{L}_q \mathbf{L}_q^T$. There are multiple ways of proceeding with the decomposition, but here we derive the *square root* decomposition, i.e., $\mathbf{P}_q = \mathbf{L}_q \mathbf{L}_q$, where $\mathbf{L}_q = \mathbf{L}_q^T$. Starting from Eq. 2.27, we add and subtract $2\sigma_v^2 \mathbf{q}_i \mathbf{q}_i^T$ and $2\sigma_v \sigma_s \mathbf{q}_i \mathbf{q}_i^T$ on the right-hand side of the equation:

$$\begin{aligned} \mathbf{P}_q &= \sigma_v^2 \mathbf{I}_4 - 2\sigma_v^2 \mathbf{q}_i \mathbf{q}_i^T + 2\sigma_v \sigma_s \mathbf{q}_i \mathbf{q}_i^T + (\sigma_s^2 - 2\sigma_v \sigma_s + \sigma_v^2) \mathbf{q}_i \mathbf{q}_i^T \\ &= \sigma_v^2 \mathbf{I}_4 - 2\sigma_v (\sigma_v - \sigma_s) \mathbf{q}_i \mathbf{q}_i^T + (\sigma_v - \sigma_s)^2 \mathbf{q}_i \mathbf{q}_i^T. \end{aligned}$$

Defining $\sigma_q \triangleq \sigma_v - \sigma_s$ and using the property $\mathbf{q}_i \mathbf{q}_i^T = \mathbf{q}_i \mathbf{q}_i^T \mathbf{q}_i \mathbf{q}_i^T$ then:

$$\begin{aligned} \mathbf{P}_q &= \sigma_v^2 \mathbf{I}_4 - 2\sigma_v \sigma_q \mathbf{q}_i \mathbf{q}_i^T + \sigma_q^2 \mathbf{q}_i \mathbf{q}_i^T \mathbf{q}_i \mathbf{q}_i^T = \sigma_v^2 \mathbf{I}_4 - 2\sigma_v \sigma_q \mathbf{q}_i \mathbf{q}_i^T + \sigma_q^2 (\mathbf{q}_i \mathbf{q}_i^T)^2 \\ &= (\sigma_v \mathbf{I}_4 - \sigma_q \mathbf{q}_i \mathbf{q}_i^T)^2 \end{aligned} \quad (2.28)$$

Therefore, the matrix square-root of \mathbf{P}_q is given by $\mathbf{L}_q = \sigma_v \mathbf{I}_4 - \sigma_q \mathbf{q}_i \mathbf{q}_i^T$, where $\sigma_q = \sigma_v - \sigma_s$. The inverse of the square-root matrix is given by:

$$\mathbf{L}_q^{-1} = \frac{1}{\sigma_s \sigma_v} (\sigma_s \mathbf{I}_4 + \sigma_q \mathbf{q}_i \mathbf{q}_i^T).$$

Post-multiplying \mathbf{L}_q^{-1} by \mathbf{q}_i , we get that:

$$\mathbf{L}_q^{-1} \mathbf{q}_i = \frac{1}{\sigma_s \sigma_v} (\sigma_s \mathbf{q}_i + \sigma_q \mathbf{q}_i) = \frac{\sigma_v}{\sigma_s \sigma_v} \mathbf{q}_i = \frac{1}{\sigma_s} \mathbf{q}_i.$$

Therefore, \mathbf{q}_i is an eigenvector of \mathbf{L}_q^{-1} , and the corresponding eigenvalue is given by $\lambda_q = 1/\sigma_s$. Having that in mind, if we perform a Taylor Expansion on Eq. 2.24 around $\theta_i = 0$, and pre-multiply by \mathbf{L}_q^{-1} , we get that:

$$\begin{aligned} \mathbf{L}_q^{-1} \bar{\mathbf{q}}_i &= \mathbf{L}_q^{-1} \mathbf{q}_i \otimes \mathbf{q}_{Ni} = \mathbf{L}_q^{-1} (\mathbf{q}_i \otimes) \left(\mathbf{q}_I + \left. \frac{\partial \mathbf{q}_{Ni}}{\partial \theta_i} \right|_0 \theta_i + \left. \frac{\partial^2 \mathbf{q}_{Ni}}{\partial \theta_i^2} \right|_0 \theta_i^2 + \dots \right) \\ &= \mathbf{L}_q^{-1} \mathbf{q}_i + \mathbf{L}_q^{-1} (\mathbf{q}_i \otimes) \left(\left. \frac{\partial \mathbf{q}_{Ni}}{\partial \theta_i} \right|_0 \theta_i + \left. \frac{\partial^2 \mathbf{q}_{Ni}}{\partial \theta_i^2} \right|_0 \theta_i^2 + \dots \right) \\ &= \frac{1}{\sigma_s} \mathbf{q}_i + \mathbf{L}_q^{-1} (\mathbf{q}_i \otimes) \left(\left. \frac{\partial \mathbf{q}_{Ni}}{\partial \theta_i} \right|_0 \theta_i + \left. \frac{\partial^2 \mathbf{q}_{Ni}}{\partial \theta_i^2} \right|_0 \theta_i^2 + \dots \right), \end{aligned}$$

where \mathbf{q}_I is the identity quaternion defined in Eq. 2.19.

Therefore, if we consider only the *zero-th* order approximation for the measurement normalization performed by the operation $\mathbf{L}_q^{-1}\bar{\mathbf{q}}_k$, then this operation is just a scaling operation on the true quaternion. In practice, it is impossible to perform the measurement normalization $\mathbf{L}_q^{-1}\bar{\mathbf{q}}_i$ because \mathbf{L}_q is a function of the true quaternion \mathbf{q}_i (not the measured one), which is unknown. Alternatively, if we make the practical approximation [20]:

$$\mathbf{P}_q \approx (\sigma_v \mathbf{I}_4 - \sigma_q \bar{\mathbf{q}}_i \bar{\mathbf{q}}_i^T)^2 \quad \Longrightarrow \quad \mathbf{L}_q^{-1} \approx \frac{1}{\sigma_s \sigma_v} (\sigma_s \mathbf{I}_4 + \sigma_q \bar{\mathbf{q}}_i \bar{\mathbf{q}}_i^T), \quad (2.29)$$

then the measurement normalization leads to $\mathbf{L}_q^{-1}\bar{\mathbf{q}}_i = \lambda_q \bar{\mathbf{q}}_i$.

2.4 Problem Formulation

This section poses the problem that we solve with QuateRA. Let $\bar{\mathbf{q}}_i$ be a quaternion measurement at time t_i , and assume that we have n measurements. Defining $\hat{\mathbf{q}}_i \in \mathbb{S}^3$ as the quaternion estimate at time t_i , we want to minimize the cost function:

$$\begin{aligned} J_{LS} &= \frac{1}{2} \sum_{i=1}^n (\hat{\mathbf{q}}_i - \bar{\mathbf{q}}_i)^T \mathbf{P}_q^{-1} (\hat{\mathbf{q}}_i - \bar{\mathbf{q}}_i) = \frac{1}{2} \sum_{i=1}^n (\hat{\mathbf{q}}_i - \bar{\mathbf{q}}_i)^T \mathbf{L}_q^{-T} \mathbf{L}_q^{-1} (\hat{\mathbf{q}}_i - \bar{\mathbf{q}}_i) \\ &= \frac{1}{2} \sum_{i=1}^n (\mathbf{L}_q^{-1} \hat{\mathbf{q}}_i - \mathbf{L}_q^{-1} \bar{\mathbf{q}}_i)^T (\mathbf{L}_q^{-1} \hat{\mathbf{q}}_i - \mathbf{L}_q^{-1} \bar{\mathbf{q}}_i). \end{aligned}$$

Making the practical approximations $\mathbf{L}_q^{-1}\bar{\mathbf{q}}_i \approx \lambda_q \bar{\mathbf{q}}_i$ and $\mathbf{L}_q^{-1}\hat{\mathbf{q}}_i \approx \lambda_q \hat{\mathbf{q}}_i$, then:

$$J_{LS} \approx \frac{1}{2} \lambda_q^2 \sum_{i=1}^n \|\hat{\mathbf{q}}_i - \bar{\mathbf{q}}_i\|_2^2. \quad (2.30)$$

Dropping the constant gain λ_q from the cost function (as it shouldn't impact the optimal solution), and using the property $\bar{\mathbf{q}}_i^T \bar{\mathbf{q}}_i = \hat{\mathbf{q}}_i^T \hat{\mathbf{q}}_i = 1$, then J_{LS} can be further simplified as:

$$\begin{aligned} J_{LS} &= \frac{1}{2} \sum_{i=1}^n \|\hat{\mathbf{q}}_i - \bar{\mathbf{q}}_i\|_2^2 = \frac{1}{2} \sum_{i=1}^n (\hat{\mathbf{q}}_i - \bar{\mathbf{q}}_i)^T (\hat{\mathbf{q}}_i - \bar{\mathbf{q}}_i) = \frac{1}{2} \sum_{i=1}^n (2 - 2\hat{\mathbf{q}}_i^T \bar{\mathbf{q}}_i) \\ &= n - \sum_{i=1}^n \hat{\mathbf{q}}_i^T \bar{\mathbf{q}}_i. \end{aligned} \quad (2.31)$$

Additionally, the optimal estimation problem has to be subject to the quaternion kinematic equation of Eq. 2.22:

$$\dot{\mathbf{q}} = \frac{1}{2} \boldsymbol{\omega} \otimes \mathbf{q}.$$

Assuming that $\boldsymbol{\omega} = \Omega \vec{\boldsymbol{\omega}}$ is constant, the rotational kinematics evolves as described by the state transition matrix of Eq. 2.23:

$$\mathbf{q}(t) = \left[\cos \frac{\Omega \Delta t}{2} \cdot \mathbf{I}_4 + \sin \frac{\Omega \Delta t}{2} \cdot \vec{\boldsymbol{\omega}} \otimes \right] \mathbf{q}_0 = \cos \frac{\Omega \Delta t}{2} \cdot \mathbf{q}_0 + \sin \frac{\Omega \Delta t}{2} \cdot \vec{\boldsymbol{\omega}} \otimes \mathbf{q}_0, \quad (2.32)$$

where $\Delta t \triangleq t - t_0$. In summary, we are searching for estimates of $\hat{\boldsymbol{\omega}} = \hat{\Omega} \hat{\vec{\boldsymbol{\omega}}}$, and $\hat{\mathbf{q}}_i$ satisfying:

$$\begin{cases} \min_{\hat{\boldsymbol{\omega}}, \hat{\mathbf{q}}_i} & J_{LS} = n - \sum_{i=1}^n \hat{\mathbf{q}}_i^T \bar{\mathbf{q}}_i \\ s.t. & \hat{\mathbf{q}}_{i+1} = \cos \frac{\hat{\Omega} \delta_i}{2} \cdot \hat{\mathbf{q}}_i + \sin \frac{\hat{\Omega} \delta_i}{2} \cdot \hat{\vec{\boldsymbol{\omega}}} \otimes \hat{\mathbf{q}}_i, \quad \forall i \in \{1, \dots, n-1\} \\ & \|\hat{\mathbf{q}}_i\| = 1, \quad \forall i \in \{1, \dots, n\} \end{cases}, \quad (2.33)$$

where $\delta_i \triangleq t_{i+1} - t_i$.

As mentioned in the Introduction, QuateRA is a two step algorithm: it first estimates the AOR $\hat{\vec{\omega}}$, and then uses its knowledge to estimate for the AVM $\hat{\Omega}$. In order to estimate the AOR, QuateRA uses a geometric interpretation based on the solution to the quaternion kinematic equation of Eq. 2.32.

Defining the vectors $\mathbf{u}_1 \in \mathbb{S}^3 = \mathbf{q}_0$ and $\mathbf{u}_2 \in \mathbb{S}^3 = \vec{\omega} \otimes \mathbf{q}_0$, we have that $\mathbf{u}_1^T \mathbf{u}_2 = \mathbf{q}_0 \cdot \vec{\omega} \otimes \mathbf{q}_0$. Since $\vec{\omega} \otimes$ is a skew-symmetric matrix (see Eq. 2.20) then $\mathbf{u}_1^T \mathbf{u}_2 = 0$, i.e., $\mathbf{u}_1 \perp \mathbf{u}_2$. Defining $\alpha \triangleq \frac{\Omega \Delta t}{2}$, we can write Eq. 2.32 as:

$$\mathbf{q}(t) = \cos \alpha \cdot \mathbf{u}_1 + \sin \alpha \cdot \mathbf{u}_2. \quad (2.34)$$

Clearly, any $\mathbf{q}(t)$ described by Eq. 2.34 is a linear combination of \mathbf{u}_1 and \mathbf{u}_2 , for all $t \in \mathbb{R}$. Hence, if we define the 4D hyperplane $\mathbb{P}(\mathbf{u}_1, \mathbf{u}_2) = \text{span}\{\mathbf{u}_1, \mathbf{u}_2\}$, then $\mathbf{q}(t) \in \mathbb{P}(\mathbf{u}_1, \mathbf{u}_2), \forall t \in \mathbb{R}$. Thus, the optimally estimated quaternions should belong to a single plane of rotation: $\hat{\mathbf{q}}_i \in \mathbb{P}(\mathbf{u}_1, \mathbf{u}_2), \forall i \in \{1, \dots, n\}$. In addition, we have that $\boldsymbol{\omega} = \mathbf{u}_2 \otimes \mathbf{u}_1^{-1}$.

Therefore, if we have a sequence of measurements $\bar{\mathbf{q}}_i, i \in \{1, \dots, n\}$, with $n \in \mathbb{N}_{\geq 2}$ (\mathbb{N} is the set of natural numbers), then we can estimate the axis of rotation by finding the optimal hyperplane that fits the measured quaternions. Classically speaking, plane-fitting is a Total Least Squares (TLS) problem [65]. We define $\hat{\mathbf{q}}_i^{TLS}$ as the TLS best in-plane estimate for the i -th measurement. Defining the matrices $\bar{\mathbf{Q}}$ and $\hat{\mathbf{Q}}^{TLS}$ as:

$$\bar{\mathbf{Q}} \triangleq [\bar{\mathbf{q}}_1 \quad \bar{\mathbf{q}}_2 \quad \dots \quad \bar{\mathbf{q}}_n], \quad \hat{\mathbf{Q}}^{TLS} \triangleq [\hat{\mathbf{q}}_1^{TLS} \quad \hat{\mathbf{q}}_2^{TLS} \quad \dots \quad \hat{\mathbf{q}}_n^{TLS}], \quad (2.35)$$

then our plane-fitting problem can be cast in the following TLS form:

$$\begin{cases} \min_{\hat{\mathbf{u}}_1, \hat{\mathbf{u}}_2, \hat{\mathbf{q}}_i} & J_{TLS} = \left\| \hat{\mathbf{Q}}^{TLS} - \bar{\mathbf{Q}} \right\|_F^2 \\ s.t. & \hat{\mathbf{q}}_i^{TLS} \in \mathbb{P}(\hat{\mathbf{u}}_1, \hat{\mathbf{u}}_2), \quad \forall i \in \{1, \dots, n\} \\ & \|\hat{\mathbf{q}}_i^{TLS}\| = 1, \quad \forall i \in \{1, \dots, n\} \end{cases}, \quad (2.36)$$

where the $\|\cdot\|_F$ denotes the *Frobenius norm*. Notice that the optimization problem of Eq. 2.36 stems from the classical TLS problem, except for the unit norm constraint $\|\hat{\mathbf{q}}_i^{TLS}\| = 1$. Hence, although we start from a TLS cost function for estimating the quaternion plane of rotation, the solution is not related to the textbook solutions on TLS.

Once we solve the optimization problem of Eq. 2.36, we are able to obtain estimates for the axis of rotation $\hat{\vec{\omega}}$, the plane of rotation $\mathbb{P}(\hat{\mathbf{u}}_1, \hat{\mathbf{u}}_2)$, and the quaternion estimates $\hat{\mathbf{q}}_i^{TLS} \in \mathbb{P}(\hat{\mathbf{u}}_1, \hat{\mathbf{u}}_2)$. Given those estimates, we recast the optimization problem of Eq. 2.33 as:

$$\begin{cases} \min_{\hat{\Omega}, \hat{\mathbf{q}}_i} & J_{LS} = n - \sum_{i=1}^n \hat{\mathbf{q}}_i^T \hat{\mathbf{q}}_i^{TLS} \\ s.t. & \hat{\mathbf{q}}_{i+1} = \cos \frac{\hat{\Omega} \delta_i}{2} \cdot \hat{\mathbf{q}}_i + \sin \frac{\hat{\Omega} \delta_i}{2} \cdot \hat{\vec{\omega}} \otimes \hat{\mathbf{q}}_i, \quad \forall i \in \{1, \dots, n-1\} \\ & \|\hat{\mathbf{q}}_i\| = 1, \quad \forall i \in \{1, \dots, n\} \\ & \hat{\mathbf{q}}_i \in \mathbb{P}(\hat{\mathbf{u}}_1, \hat{\mathbf{u}}_2), \quad \forall i \in \{1, \dots, n\} \end{cases}, \quad (2.37)$$

In a nutshell, the problem of Eq. 2.36 is solved by taking the Singular Value Decomposition on $\mathbf{Z} \triangleq \bar{\mathbf{Q}}\bar{\mathbf{Q}}^T$, whose two first left singular vectors determine the quaternion plane of rotation. The AOR direction is uniquely identified from the plane of rotation. In order to solve the problem of Eq. 2.37, we observe that a unit quaternion \mathbf{q}_i on a plane can be uniquely identified by a single angle Φ_i . Hence, if we assume that this angle is evolving linearly as

in $\Phi_i = \Phi_1 + \Omega\Delta t$, we can perform least squares to solve for optimal $\hat{\Phi}_1$ and $\hat{\Omega}$ that determine the quaternion evolution on that plane. QuateRA's algorithm is summarized in Section 2.5.4.

2.5 The Quaternion Regression Algorithm

In this section, we develop the QuateRA algorithm. The remainder of this section is structured as follows: Section 2.5.1 derives the AOR estimation algorithm, while Section 2.5.2 derives the AVM estimator. A method for estimating the covariance matrix is given in Section 2.5.3. Section 2.5.4 summarizes QuateRA into a few steps, and Section 2.5.5 presents some insights and analysis to the overall algorithm.

2.5.1 Estimation of the Axis of Rotation

In order to estimate the AOR, the goal is to find a plane $\hat{\mathbb{P}}(\hat{\mathbf{u}}_1, \hat{\mathbf{u}}_2) = \text{span}\{\hat{\mathbf{u}}_1, \hat{\mathbf{u}}_2\}$ and a set of estimated quaternions $\hat{\mathbf{q}}_i \in \hat{\mathbb{P}}(\hat{\mathbf{u}}_1, \hat{\mathbf{u}}_2)$, $i \in \{1, \dots, n\}$ that minimizes the TLS cost function:

$$J_1 = \frac{1}{2} \|\bar{\mathbf{Q}} - \hat{\mathbf{Q}}^{TLS}\|_F^2. \quad (2.38)$$

In order to reduce heavy notation, the remainder of this subsection will denote $\hat{\mathbf{Q}} \equiv \hat{\mathbf{Q}}^{TLS}$ and $\hat{\mathbf{q}}_i \equiv \hat{\mathbf{q}}_i^{TLS}$.

Starting from the definition of $\bar{\mathbf{Q}}$ in Eq. 2.35, we can derive the following

property:

$$\text{tr}(\bar{\mathbf{Q}}\bar{\mathbf{Q}}^T) = \text{tr}\left(\sum_{i=1}^n \bar{\mathbf{q}}_i \bar{\mathbf{q}}_i^T\right) = \sum_{i=1}^n \text{tr}(\bar{\mathbf{q}}_i \bar{\mathbf{q}}_i^T) = \sum_{i=1}^n \|\bar{\mathbf{q}}_i\|^2 = n \quad (2.39)$$

From the Frobenius norm definition, we have that:

$$\begin{aligned} J_1 &= \frac{1}{2} \text{tr} \left[(\bar{\mathbf{Q}} - \hat{\mathbf{Q}}) (\bar{\mathbf{Q}} - \hat{\mathbf{Q}})^T \right] = \frac{1}{2} \text{tr} [\bar{\mathbf{Q}}\bar{\mathbf{Q}}^T - \bar{\mathbf{Q}}\hat{\mathbf{Q}}^T - \hat{\mathbf{Q}}\bar{\mathbf{Q}}^T + \hat{\mathbf{Q}}\hat{\mathbf{Q}}^T] \\ &= \frac{1}{2} \text{tr}(\bar{\mathbf{Q}}\bar{\mathbf{Q}}^T) - \frac{1}{2} \text{tr}(\bar{\mathbf{Q}}\hat{\mathbf{Q}}^T) - \frac{1}{2} \text{tr}(\hat{\mathbf{Q}}\bar{\mathbf{Q}}^T) + \frac{1}{2} \text{tr}(\hat{\mathbf{Q}}\hat{\mathbf{Q}}^T). \end{aligned} \quad (2.40)$$

Using the trace property $\text{tr}(\mathbf{AB}) = \text{tr}(\mathbf{BA})$, and the property of Eq. 2.39, we have that:

$$J_1 = n - \text{tr}(\bar{\mathbf{Q}}\hat{\mathbf{Q}}^T) = n - \text{tr}\left(\sum_{i=1}^n \bar{\mathbf{q}}_i \hat{\mathbf{q}}_i^T\right) = n - \sum_{i=1}^n \text{tr}(\bar{\mathbf{q}}_i \hat{\mathbf{q}}_i^T) = n - \sum_{i=1}^n \bar{\mathbf{q}}_i^T \hat{\mathbf{q}}_i. \quad (2.41)$$

Minimizing the cost function of Eq. 2.41 is equivalent to *maximizing* the following cost function:

$$J_2 = \sum_{i=1}^k \bar{\mathbf{q}}_i^T \hat{\mathbf{q}}_i. \quad (2.42)$$

Theorem 1. *Given a quaternion $\mathbf{q} \in \mathbb{S}^3$ and a plane spanned by the unit vectors $\mathbf{u}_1 \in \mathbb{S}^3$ and $\mathbf{u}_2 \in \mathbb{S}^3$ such that $\mathbf{u}_1^T \mathbf{u}_2 = 0$. Denoting this plane as $\mathbb{P}(\mathbf{u}_1, \mathbf{u}_2)$, the quaternion $\mathbf{q}_p \in \mathbb{S}^3$ that belongs to the plane $\mathbb{P}(\mathbf{u}_1, \mathbf{u}_2)$ and minimizes the cost function:*

$$J_0 = \frac{1}{2} \|\mathbf{q} - \mathbf{q}_p\|_2^2 = \frac{1}{2} \|\mathbf{q} - \mathbf{q}_p\|_F^2 \quad (2.43)$$

is given by:

$$\mathbf{q}_p = \frac{1}{\sqrt{(\mathbf{q}^T \mathbf{u}_1)^2 + (\mathbf{q}^T \mathbf{u}_2)^2}} [(\mathbf{q}^T \mathbf{u}_1) \mathbf{u}_1 + (\mathbf{q}^T \mathbf{u}_2) \mathbf{u}_2] \quad (2.44)$$

Proof. The cost function of Eq. 2.43 can be written as:

$$J_0 = \frac{1}{2} \|\mathbf{q} - \mathbf{q}_p\|_2^2 = \frac{1}{2} (\mathbf{q}^T \mathbf{q} - 2\mathbf{q}^T \mathbf{q}_p + \mathbf{q}_p^T \mathbf{q}_p) = 1 - \mathbf{q}^T \mathbf{q}_p. \quad (2.45)$$

Minimizing the cost function of Eq. 2.45 is the same as maximizing the following cost function:

$$J_1 = \mathbf{q}^T \mathbf{q}_p. \quad (2.46)$$

Every quaternion that belongs to the plane $\mathbb{P}(\mathbf{u}_1, \mathbf{u}_2)$ can be written as a linear combination of \mathbf{u}_1 and \mathbf{u}_2 :

$$\mathbf{q}_p = a\mathbf{u}_1 + b\mathbf{u}_2. \quad (2.47)$$

In order to satisfy the norm condition for $\|\mathbf{q}_p\| = 1$, the following holds:

$$\|\mathbf{q}_p\| = \mathbf{q}_p^T \mathbf{q}_p = a^2 \mathbf{u}_1^T \mathbf{u}_1 + 2ab \mathbf{u}_1^T \mathbf{u}_2 + b^2 \mathbf{u}_2^T \mathbf{u}_2 = a^2 + b^2 = 1$$

Hence, the coefficients a and b from Eq. 2.47 are constrained such that $a^2 + b^2 = 1$. We rewrite the optimization problem as:

$$\begin{cases} \max_{a,b} J_1 = \mathbf{q}^T \mathbf{q}_p = a\mathbf{q}^T \mathbf{u}_1 + b\mathbf{q}^T \mathbf{u}_2 \\ \text{s.t.} \quad a^2 + b^2 = 1. \end{cases} \quad (2.48)$$

Introducing the Lagrange multiplier λ , the Lagrangian related to the problem above is written as:

$$\mathcal{L} = a\mathbf{q}^T \mathbf{u}_1 + b\mathbf{q}^T \mathbf{u}_2 + \frac{1}{2}\lambda(a^2 + b^2 - 1) \quad \Longrightarrow \quad \begin{cases} \frac{\partial \mathcal{L}}{\partial a} = \mathbf{q}^T \mathbf{u}_1 + \lambda a \\ \frac{\partial \mathcal{L}}{\partial b} = \mathbf{q}^T \mathbf{u}_2 + \lambda b \end{cases} .$$

From the first-order necessary optimality conditions, we get that:

$$\begin{cases} \mathbf{q}^T \mathbf{u}_1 + \lambda a = 0 & \implies a = -\frac{\mathbf{q}^T \mathbf{u}_1}{\lambda} \\ \mathbf{q}^T \mathbf{u}_2 + \lambda b = 0 & \implies b = -\frac{\mathbf{q}^T \mathbf{u}_2}{\lambda} \end{cases}. \quad (2.49)$$

Substituting a and b from Eq. 2.49 into $a^2 + b^2 = 1$, we get that:

$$\frac{(\mathbf{q}^T \mathbf{u}_1)^2}{\lambda^2} + \frac{(\mathbf{q}^T \mathbf{u}_2)^2}{\lambda^2} = 1 \implies \lambda = \pm \sqrt{(\mathbf{q}^T \mathbf{u}_1)^2 + (\mathbf{q}^T \mathbf{u}_2)^2}. \quad (2.50)$$

Therefore, we have that:

$$a = -\frac{\mathbf{q}^T \mathbf{u}_1}{\lambda} = \pm \frac{1}{\sqrt{(\mathbf{q}^T \mathbf{u}_1)^2 + (\mathbf{q}^T \mathbf{u}_2)^2}} \mathbf{q}^T \mathbf{u}_1, \quad (2.51)$$

$$b = -\frac{\mathbf{q}^T \mathbf{u}_2}{\lambda} = \pm \frac{1}{\sqrt{(\mathbf{q}^T \mathbf{u}_1)^2 + (\mathbf{q}^T \mathbf{u}_2)^2}} \mathbf{q}^T \mathbf{u}_2. \quad (2.52)$$

We can notice that this problem has two extremum points: a maximizing solution and a minimizing one. By inspecting the cost function in Eq. 2.48, the maximizing solution has to be the one given by:

$$a = \frac{1}{\sqrt{(\mathbf{q}^T \mathbf{u}_1)^2 + (\mathbf{q}^T \mathbf{u}_2)^2}} \mathbf{q}^T \mathbf{u}_1, \quad b = \frac{1}{\sqrt{(\mathbf{q}^T \mathbf{u}_1)^2 + (\mathbf{q}^T \mathbf{u}_2)^2}} \mathbf{q}^T \mathbf{u}_2, \quad (2.53)$$

leading to the solution of Eq. 2.44.

□

Using Theorem 1, then $\hat{\mathbf{q}}$ can be written as a linear combination of the optimal plane vectors $\hat{\mathbf{u}}_1$ and $\hat{\mathbf{u}}_2$. Hence, the cost function J_2 from Eq. 2.42

can be written as:

$$\begin{aligned}
J_2 &= \sum_{i=1}^n \frac{1}{\sqrt{(\bar{\mathbf{q}}_i^T \hat{\mathbf{u}}_1)^2 + (\bar{\mathbf{q}}_i^T \hat{\mathbf{u}}_2)^2}} \bar{\mathbf{q}}_i^T [(\bar{\mathbf{q}}_i^T \hat{\mathbf{u}}_1) \hat{\mathbf{u}}_1 + (\bar{\mathbf{q}}_i^T \hat{\mathbf{u}}_2) \hat{\mathbf{u}}_2] \\
&= \sum_{i=1}^n \frac{1}{\sqrt{(\bar{\mathbf{q}}_i^T \hat{\mathbf{u}}_1)^2 + (\bar{\mathbf{q}}_i^T \hat{\mathbf{u}}_2)^2}} [(\bar{\mathbf{q}}_i^T \hat{\mathbf{u}}_1)^2 + (\bar{\mathbf{q}}_i^T \hat{\mathbf{u}}_2)^2] \\
&= \sum_{i=1}^n \sqrt{(\bar{\mathbf{q}}_i^T \hat{\mathbf{u}}_1)^2 + (\bar{\mathbf{q}}_i^T \hat{\mathbf{u}}_2)^2} \tag{2.54}
\end{aligned}$$

Note that in the total absence of measurement noise, and assuming $\hat{\mathbf{u}}_1 \in \text{span}\{\mathbf{u}_1, \mathbf{u}_2\}$, $\hat{\mathbf{u}}_2 \in \text{span}\{\mathbf{u}_1, \mathbf{u}_2\}$ with $\hat{\mathbf{u}}_1^T \hat{\mathbf{u}}_2 = 0$, the following holds:

$$\sqrt{(\bar{\mathbf{q}}_i^T \hat{\mathbf{u}}_1)^2 + (\bar{\mathbf{q}}_i^T \hat{\mathbf{u}}_2)^2} = 1, \quad \forall i \in \{1, \dots, n\}.$$

Defining the variable $x \triangleq (\bar{\mathbf{q}}_i^T \hat{\mathbf{u}}_1)^2 + (\bar{\mathbf{q}}_i^T \hat{\mathbf{u}}_2)^2$, the First order Taylor Expansion of \sqrt{x} around $x = 1$ is given by:

$$\sqrt{x} \approx \frac{1}{2} + \frac{x}{2} \quad \Longrightarrow \quad \sqrt{(\bar{\mathbf{q}}_i^T \hat{\mathbf{u}}_1)^2 + (\bar{\mathbf{q}}_i^T \hat{\mathbf{u}}_2)^2} \approx \frac{1}{2} + \frac{1}{2} (\bar{\mathbf{q}}_i^T \hat{\mathbf{u}}_1)^2 + \frac{1}{2} (\bar{\mathbf{q}}_i^T \hat{\mathbf{u}}_2)^2$$

Therefore, under the small angle approximation for the measurement noise, we have that the cost function J_2 can be approximated to:

$$J_2 \approx \frac{n}{2} + \frac{1}{2} \sum_{i=1}^n [(\bar{\mathbf{q}}_i^T \hat{\mathbf{u}}_1)^2 + (\bar{\mathbf{q}}_i^T \hat{\mathbf{u}}_2)^2] \tag{2.55}$$

For simplicity of notation, we define a new cost function whose maximization is equivalent to the maximization of Eq. 2.55:

$$J = \sum_{i=1}^n [(\bar{\mathbf{q}}_i^T \hat{\mathbf{u}}_1)^2 + (\bar{\mathbf{q}}_i^T \hat{\mathbf{u}}_2)^2] = \sum_{i=1}^n [\hat{\mathbf{u}}_1^T \bar{\mathbf{q}}_i \bar{\mathbf{q}}_i^T \hat{\mathbf{u}}_1 + \hat{\mathbf{u}}_2^T \bar{\mathbf{q}}_i \bar{\mathbf{q}}_i^T \hat{\mathbf{u}}_2] \tag{2.56}$$

$$= \hat{\mathbf{u}}_1^T \sum_{i=1}^n \bar{\mathbf{q}}_i \bar{\mathbf{q}}_i^T \hat{\mathbf{u}}_1 + \hat{\mathbf{u}}_2^T \sum_{i=1}^n \bar{\mathbf{q}}_i \bar{\mathbf{q}}_i^T \hat{\mathbf{u}}_2 = \hat{\mathbf{u}}_1^T \bar{\mathbf{Q}} \bar{\mathbf{Q}}^T \hat{\mathbf{u}}_1 + \hat{\mathbf{u}}_2^T \bar{\mathbf{Q}} \bar{\mathbf{Q}}^T \hat{\mathbf{u}}_2 \tag{2.57}$$

Defining $\bar{\mathbf{Z}} \triangleq \bar{\mathbf{Q}}\bar{\mathbf{Q}}^T$, the optimization problem can be stated in the following form:

$$\begin{cases} \max_{\hat{\mathbf{u}}_1 \in \mathbb{S}^3, \hat{\mathbf{u}}_2 \in \mathbb{S}^3} & \hat{\mathbf{u}}_1^T \bar{\mathbf{Z}} \hat{\mathbf{u}}_1 + \hat{\mathbf{u}}_2^T \bar{\mathbf{Z}} \hat{\mathbf{u}}_2 \\ \text{s.t.} & \hat{\mathbf{u}}_1^T \hat{\mathbf{u}}_2 = 0 \end{cases} . \quad (2.58)$$

The optimization problem of Eq. 2.58 does not admit a unique solution. This should be an obvious statement, since there are infinitely many pairs of orthogonal vectors that define a plane. Still, this is not an issue for QuateRA, since the axis of rotation direction can be uniquely determined from the hyperplane, regardless of which particular optimal solution has been obtained for $\hat{\mathbf{u}}_1$ and $\hat{\mathbf{u}}_2$. Lemma 1 introduces a particular optimal solution to the problem above.

Lemma 1. *A solution to the optimization problem in Eq. 2.58 can be obtained from the Singular Value Decomposition (SVD) of $\bar{\mathbf{Z}} = \hat{\mathbf{U}}\hat{\Sigma}\hat{\mathbf{U}}^T$, where $\hat{\mathbf{U}} \in \mathbb{R}^{4 \times 4} = [\hat{\mathbf{u}}_1 \ \hat{\mathbf{u}}_2 \ \hat{\mathbf{u}}_3 \ \hat{\mathbf{u}}_4]$ contains the singular vectors of $\bar{\mathbf{Z}}$, and $\hat{\Sigma} = \text{diag}(\hat{\sigma}_1, \hat{\sigma}_2, \hat{\sigma}_3, \hat{\sigma}_4)$ contains the singular values of $\bar{\mathbf{Z}}$, wherein $\hat{\sigma}_1 \geq \hat{\sigma}_2 \geq \hat{\sigma}_3 \geq \hat{\sigma}_4 \geq 0$. If $\hat{\sigma}_2 > \hat{\sigma}_3$, then $\hat{\mathbf{u}}_1$ and $\hat{\mathbf{u}}_2$ compose a solution to the optimization problem in Eq. 2.58 and the optimal cost is given by $J^*(\hat{\mathbf{u}}_1, \hat{\mathbf{u}}_2) = \hat{\sigma}_1 + \hat{\sigma}_2$, with $\hat{\sigma}_1 = \hat{\mathbf{u}}_1^T \bar{\mathbf{Z}} \hat{\mathbf{u}}_1$ and $\hat{\sigma}_2 = \hat{\mathbf{u}}_2^T \bar{\mathbf{Z}} \hat{\mathbf{u}}_2$.*

Proof. This follows from common knowledge in SVD, as the best-fit k -dimensional subspace for a matrix is the subspace spanned by the first k singular vectors [61]. As we are looking for a 2-dimensional subspace that best approximates $\bar{\mathbf{Z}}$, then the solution to the optimization problem of Eq. 2.58 is given by the first two left singular vectors of $\bar{\mathbf{Z}}$. \square

Having the optimal hyperplane estimate $\hat{\mathbb{P}}(\hat{\mathbf{u}}_1, \hat{\mathbf{u}}_2)$, we still need to calculate the AOR $\hat{\vec{\omega}}$ that leads to rotation on that plane. As previously observed in Eq. 2.32, the optimal hyperplane can be written as $\hat{\mathbb{P}}(\hat{\mathbf{u}}_1, \hat{\mathbf{u}}_2) = \hat{\mathbb{P}}(\hat{\mathbf{u}}_1, \hat{\vec{\omega}} \otimes \hat{\mathbf{u}}_1)$. This implies that $\hat{\mathbf{u}}_2 = \hat{\vec{\omega}} \otimes \hat{\mathbf{u}}_1$. Therefore, the optimal estimate for the AOR is given by:

$$\hat{\vec{\omega}} = \hat{\mathbf{u}}_2 \otimes \hat{\mathbf{u}}_1^{-1}. \quad (2.59)$$

An important observation is that $\hat{\vec{\omega}}$ is an ambiguous estimate of $\vec{\omega}$ up to a sign error, i.e, it estimates the direction of $\vec{\omega}$, but the sense might be wrong. This ambiguity is eliminated when estimating the AVM Ω , whose estimate $\hat{\Omega}$ will be negative when $\hat{\vec{\omega}}$ is an estimate of $-\vec{\omega}$. In any case, the product $\hat{\omega} = \hat{\Omega} \hat{\vec{\omega}}$ is consistent with $\omega = \Omega \vec{\omega}$.

Using the result from Theorem 1, the optimally estimated quaternions on the plane $\hat{\mathbb{P}}(\hat{\mathbf{u}}_1, \hat{\mathbf{u}}_2)$ are given by:

$$\hat{q}_i^{TLS} = \frac{1}{\sqrt{(\bar{q}_i^T \hat{\mathbf{u}}_1)^2 + (\bar{q}_i^T \hat{\mathbf{u}}_2)^2}} [(\bar{q}_i^T \hat{\mathbf{u}}_1) \hat{\mathbf{u}}_1 + (\bar{q}_i^T \hat{\mathbf{u}}_2) \hat{\mathbf{u}}_2]. \quad (2.60)$$

2.5.2 Estimation of the Angular Velocity Magnitude

In this section, we use the estimated in-plane quaternions $\hat{q}_i^{TLS} \in \mathbb{P}(\hat{\mathbf{u}}_1, \hat{\mathbf{u}}_2)$ to solve the optimization problem of Eq. 2.37, where \hat{q}_i^{TLS} is given by Eq. 2.60.

We make the observation that a unit quaternion belonging to a plane $\mathbb{P}(\hat{\mathbf{u}}_1, \hat{\mathbf{u}}_2)$ can be fully specified simply by an angle on that plane. We define

the quaternion angle on $\mathbb{P}(\hat{\mathbf{u}}_1, \hat{\mathbf{u}}_2)$ as having a zero-angle when aligned with \mathbf{u}_1 , and it grows positive as the quaternion rotates from \mathbf{u}_1 towards \mathbf{u}_2 . We make the definitions:

$$\hat{\Phi}_i = 2 \cdot \text{atan2}(\hat{\mathbf{u}}_2^T \hat{\mathbf{q}}_i, \hat{\mathbf{u}}_1^T \hat{\mathbf{q}}_i), \quad \bar{\Phi}_i = 2 \cdot \text{atan2}(\hat{\mathbf{u}}_2^T \hat{\mathbf{q}}_i^{TLS}, \hat{\mathbf{u}}_1^T \hat{\mathbf{q}}_i^{TLS}), \quad (2.61)$$

where $\bar{\Phi}_i$ is the respective angle of the quaternion $\hat{\mathbf{q}}_i^{TLS}$, and $\hat{\Phi}_i$ is the angle of the quaternion that we are estimating $\hat{\mathbf{q}}_i$.

If we define $\psi_i \triangleq \hat{\Phi}_i - \bar{\Phi}_i$, then we have that $\hat{\mathbf{q}}_i^T \hat{\mathbf{q}}_i^{TLS} = \cos \frac{|\psi|}{2}$. Using Taylor series around the origin, we can approximate $\hat{\mathbf{q}}_i^T \hat{\mathbf{q}}_i^{TLS} \approx 1 - \frac{\psi^2}{8}$. Hence, for sufficiently small ψ (i.e. low noise characteristics), the cost function of Eq. 2.37 can be approximated as:

$$J_{LS} = n - \sum_{i=1}^n \hat{\mathbf{q}}_i^T \hat{\mathbf{q}}_i^{TLS} \approx n - n + \frac{1}{8} \sum_{i=1}^n \psi^2 = \frac{1}{8} \sum_{i=1}^n (\hat{\Phi}_i - \bar{\Phi}_i)^2. \quad (2.62)$$

If we assume the system model:

$$\Phi_i = \Phi_1 + \Omega \Delta t_i = \begin{bmatrix} 1 & \Delta t_i \end{bmatrix} \begin{bmatrix} \Phi_1 \\ \Omega \end{bmatrix},$$

and the measurement model:

$$\hat{\Phi}_i = \Phi_i + \nu_i,$$

where ν_i is the measurement noise such that $\mathbb{E}[\nu_i] = 0$, $\mathbb{E}[\nu_i \nu_j] = 0$, $i \neq j$, and $\mathbb{E}[\nu_i^2] = P_\nu$, then we can use least squares to estimate for $\hat{\Phi}_1$ and $\hat{\Omega}$:

$$\hat{\mathbf{X}} \triangleq \begin{bmatrix} \hat{\Phi}_1 \\ \hat{\Omega} \end{bmatrix} = (\mathbf{H}^T \mathbf{H})^{-1} \mathbf{H}^T \hat{\Phi}, \quad (2.63)$$

where:

$$\mathbf{H} \triangleq \begin{bmatrix} 1 & \cdots & 1 \\ \Delta t_1 & \cdots & \Delta t_n \end{bmatrix}^T, \quad \hat{\Phi} \triangleq [\hat{\Phi}_1 \quad \cdots \quad \hat{\Phi}_n]^T. \quad (2.64)$$

Given that the measurement noise is assumed to be uncorrelated between two measurements ($\mathbb{E}[\nu_i \nu_j] = 0, i \neq j$), then the covariance matrix of the estimate $\hat{\mathbf{X}}$ is given by $\text{cov}[\hat{\mathbf{X}}] = P_\nu (\mathbf{H}^T \mathbf{H})^{-1}$.

The optimally estimated quaternions $\hat{\mathbf{q}}_i \in \mathbb{P}(\hat{\mathbf{u}}_1, \hat{\mathbf{u}}_2)$ can be retrieved as:

$$\hat{\mathbf{q}}_{i+1} = \cos \frac{\hat{\Omega} \delta_i}{2} \cdot \hat{\mathbf{q}}_i + \sin \frac{\hat{\Omega} \delta_i}{2} \cdot \hat{\boldsymbol{\omega}} \otimes \hat{\mathbf{q}}_i, \quad \forall i \in \{1, \dots, n-1\}. \quad (2.65)$$

Note that the quaternion estimates in Eq. 2.65 satisfies all the constraints of the optimization problem in Eq. 2.37.

Theorem 2 below proves that the noise ν_i is actually zero mean and that $P_\nu = \frac{1}{3} \sigma_\theta^2$, where σ_θ is the noise standard deviation for the measurement noise as defined in Eqs. 2.24 and 2.25.

Theorem 2. *Assume that $\mathbf{q}_N = [\cos \frac{\theta}{2} \quad \mathbf{e}_N^T \sin \frac{\theta}{2}]^T$ is a noise quaternion, where θ is a zero-mean gaussian random variable with $\mathbb{E}[\theta^2] = \sigma_\theta^2$, and $\mathbf{e}_N \in \mathbb{R}^2$ is a unit vector uniformly distributed in the 3D sphere. Also, define a plane $\mathbb{P}(\mathbf{q}_I, \mathbf{q}_v)$ as the hyperplane spanned by the unit vectors \mathbf{q}_I (identity quaternion) and $\mathbf{q}_v \triangleq [0 \quad \mathbf{v}^T]^T$ with $\mathbf{v} \in \mathbb{S}^2$ such that $\mathbf{q}_v^T \mathbf{q}_I = 0$. Now, assume that $\mathbf{q}_{Np} \in \mathbb{P}(\mathbf{q}_I, \mathbf{q}_v)$ is the quaternion that belongs to $\mathbb{P}(\mathbf{q}_I, \mathbf{q}_v)$ and is closest to \mathbf{q}_N such as in Theorem 1. Then, if we assume the small angle approximation on*

$\theta = 0$, the quaternion \mathbf{q}_{Np} has the form:

$$\mathbf{q}_{Np} = \begin{bmatrix} \cos \frac{\Phi}{2} \\ \mathbf{v} \sin \frac{\Phi}{2} \end{bmatrix}, \quad (2.66)$$

where Φ has the approximate statistics $\mathbb{E}[\Phi] = 0$, and $\sigma_\Phi^2 \triangleq \mathbb{E}[\Phi^2] = \frac{1}{3}\sigma_\theta^2$.

Proof. According with Theorem 1, \mathbf{q}_{Np} is given by:

$$\begin{aligned} \hat{\mathbf{q}}_{Np} &= \frac{1}{\sqrt{(\mathbf{q}_N^T \mathbf{q}_I)^2 + (\mathbf{q}_N^T \mathbf{q}_v)^2}} [(\mathbf{q}_N^T \mathbf{q}_I) \mathbf{q}_I + (\mathbf{q}_N^T \mathbf{q}_v) \mathbf{q}_v] \\ &= \frac{1}{\sqrt{(\mathbf{q}_N^T \mathbf{q}_I)^2 + (\mathbf{q}_N^T \mathbf{q}_v)^2}} \begin{bmatrix} \mathbf{q}_N^T \mathbf{q}_I \\ \mathbf{v} \cdot \mathbf{q}_N^T \mathbf{q}_v \end{bmatrix} \end{aligned} \quad (2.67)$$

Comparing Eq. 2.67 with Eq. 2.66, we get that:

$$\cos \frac{\Phi}{2} = \frac{\mathbf{q}_N^T \mathbf{q}_I}{\sqrt{(\mathbf{q}_N^T \mathbf{q}_I)^2 + (\mathbf{q}_N^T \mathbf{q}_v)^2}} \quad (2.68)$$

From the definition of the identity quaternion (Eq. 2.19), we get that $\mathbf{q}_N^T \mathbf{q}_I = \cos \frac{\theta}{2}$. In addition, we have that $\mathbf{q}_N^T \mathbf{q}_v = \mathbf{e}_N^T \mathbf{v} \sin \frac{\theta}{2}$. Defining γ as the angle between the vectors \mathbf{e}_N^T and \mathbf{v} , then we can define $\cos \gamma \triangleq \mathbf{e}_N^T \mathbf{v}$. Given that \mathbf{e}_N is uniformly distributed in a 3D sphere, then Appendix A.3 shows that $\cos \gamma \sim \mathcal{U}[-1, 1]$. Therefore, we have that $\mathbf{q}_N^T \mathbf{q}_v = \cos \gamma \sin \frac{\theta}{2}$. Plugging these values into Eq. 2.68, and performing Taylor series expansion on both sides around $\Phi = 0$ and $\theta = 0$, we get to:

$$\begin{aligned} \cos \frac{\Phi}{2} &= \frac{\cos \frac{\theta}{2}}{\sqrt{\cos^2 \frac{\theta}{2} + \cos^2 \gamma \sin^2 \frac{\theta}{2}}} \quad (\text{Taylor Series on both sides}) \\ 1 - \frac{\Phi^2}{8} &\approx 1 - \cos^2 \gamma \frac{\theta^2}{8} \end{aligned} \quad (2.69)$$

Inspecting Eq. 2.69, we can approximate $\Phi \approx \theta \cdot \cos \gamma$. Therefore, we have that $\mathbb{E}[\Phi] = \mathbb{E}[\theta]\mathbb{E}[\cos \gamma] = 0$ and $\mathbb{E}[\Phi^2] = \mathbb{E}[\theta^2]\mathbb{E}[\cos^2 \gamma] = \frac{1}{3}\sigma_\theta^2$. \square

2.5.3 Covariance Estimate

This section presents a covariance estimate for the estimated angular velocity through a Fisher Information approach. We compute how much information is added to the estimates when a new orientation measurement is processed. We base our Information propagation on the MEKF equations derived in Appendix A.4.

Assuming that the attitude error is in the Gibbs vector format (see Eq. A.28), we define the estimation error vector as $\mathbf{X} = [\delta \mathbf{g}^T \quad \delta \boldsymbol{\omega}^T]^T$, where $\delta \boldsymbol{\omega} \triangleq \hat{\boldsymbol{\omega}} - \boldsymbol{\omega}$. Each orientation measurement has the error covariance $R = \frac{1}{3}\sigma_\theta^2 \mathbf{I}_3$. Defining the covariance matrix $\mathbf{P}_X = \mathbb{E}[\mathbf{X}\mathbf{X}^T]$, the related Fisher information matrix is given by $\mathbb{I} = \mathbf{P}_X^{-1}$.

Assuming that one orientation measurement has been already processed, the information matrix can be initialized as:

$$\mathbb{I}_1 = \begin{pmatrix} \mathbf{R}^{-1} & \mathbf{0}_3 \\ \mathbf{0}_3 & \mathbf{0}_3 \end{pmatrix}. \quad (2.70)$$

The information for all subsequent measurement updates can be processed iteratively as:

$$\mathbb{I}_{k+1} = \boldsymbol{\Gamma}_k^T \mathbb{I}_k \boldsymbol{\Gamma}_k + \mathbf{H}_k \mathbf{R} \mathbf{H}_k^T, \quad \forall k \in \{1, \dots, n-1\}, \quad (2.71)$$

where $\mathbf{H}_k = [\mathbf{I}_3 \quad \mathbf{0}_3]$, $\mathbf{\Gamma}_k \triangleq e^{-A\delta_k}$, $\delta_k \triangleq t_{k+1} - t_k$, and:

$$\mathbf{A} = \begin{bmatrix} -[\boldsymbol{\omega}_\times] & \mathbf{I}_3 \\ \mathbf{0}_3 & \mathbf{0}_3 \end{bmatrix}.$$

Finally, the estimated final covariance matrix is given by $\hat{\mathbf{P}}_X = \mathbb{I}_n^{-1}$.

2.5.4 Algorithm Summary

In this section, we summarize the algorithm steps for QuateRA.

1. Construct the measurement matrix $\bar{\mathbf{Q}}$ as in Eq. 2.35 and calculate $\bar{\mathbf{Z}} = \bar{\mathbf{Q}}\bar{\mathbf{Q}}^T$.
2. Compute the SVD $\bar{\mathbf{Z}} = \hat{\mathbf{U}}\hat{\boldsymbol{\Sigma}}\hat{\mathbf{U}}^T$. The plane of rotation is defined by the first two columns of $\hat{\mathbf{U}} = [\hat{\mathbf{u}}_1 \quad \hat{\mathbf{u}}_2 \quad \hat{\mathbf{u}}_3 \quad \hat{\mathbf{u}}_4]$.
3. The optimal axis of rotation is defined as in Eq. 2.59: $\hat{\boldsymbol{\omega}} = \hat{\mathbf{u}}_2 \otimes \hat{\mathbf{u}}_1^{-1}$.
4. Compute the optimally estimated quaternions $\hat{\mathbf{q}}_i, i \in \{1, \dots, n\}$ on the plane $\hat{\mathbb{P}}(\hat{\mathbf{u}}_1, \hat{\mathbf{u}}_2)$ using Eq. 2.60.
5. For each quaternion $\hat{\mathbf{q}}_i$ on the plane $\hat{\mathbb{P}}(\hat{\mathbf{u}}_1, \hat{\mathbf{u}}_2)$, compute the quaternion angle within the plane $\hat{\Phi}_i$ using Eq. 2.61.
6. Estimate the angular velocity $\hat{\boldsymbol{\Omega}}$ and its associated covariance using Eqs. 2.63 and 2.64. Note that the angles $\bar{\Phi}$ need to be unwrapped before performing the least squares estimation.
7. Initialize the Fisher information matrix as in Eq. 2.70, and update through Eq. 2.71. Compute the final covariance as $\hat{\mathbf{P}}_X = \mathbb{I}_n^{-1}$.

2.5.5 QuateRA Analysis

In this section, we provide some critical analysis and insights about the derivation of QuateRA.

We have converted the initial optimization problem of Eq. 2.33 into two subproblems: one that estimates the AOR by estimating the quaternion plane of rotation (Eq. 2.36), and then we use the plane of rotation knowledge to estimate for the AVM (Eq. 2.37). The items below provide a critical view on our derivations and solutions:

- Although we have employed the TLS cost function, the optimization problem is not a classical TLS problem, as we constrain the optimized variables to be unit norm. Hence, we cannot affirm that all TLS statistical properties are transferred to QuateRA.
- The Least Squares estimate of the AVM $||\mathbf{\Omega}||$ assumes that the velocity direction $\vec{\omega}$ is precisely known. However, as already mentioned, TLS can provide a biased estimate, which can also imply on a biased estimation of $||\mathbf{\Omega}||$.
- Many portions of our derivations assume sufficiently small measurement noise. This implies that QuateRA might not be a reasonable estimator for problems with too large orientation measurement noise.

Given the concerns above, Section 2.6 presents a Monte Carlo analysis of QuateRA, comparing its results with a Multiplicative Extended Kalman

Filter. The Monte Carlo results indicate that QuateRA carries the *strong consistency* property of classical TLS, and it even outperforms MEKF in some situations, especially for situations with large angular velocities and low sampling frequency. On the other hand, MEKF seems to be a slightly better estimator for high sampling frequencies and small angular velocities. Note, however, that the average discrepancy between QuateRA and MEKF disappear as the number of measurements increase.

A few important remarks that should be noted on QuateRA are highlighted below:

- When $n = 2$, QuateRA computes the solution that leads to $J_{LS} = 0$, i.e., $n = 2$ leads to a perfect fit of the data.
- It doesn't matter if $\bar{\mathbf{Q}}$ is constructed with \mathbf{q}_i or $-\mathbf{q}_i$. Plane-fitting is agnostic to the quaternion direction, and the AVM estimation is not affected as long as the angles are unwrapped prior to solving the LS problem.
- The quaternion averaging problem described in Ref. [37] is a special solution for the problem herein presented. Note the similarity between the cost function in Eq. 2.56 with respect to Eq. 12 within Ref. [37] when all the weights are unity. This implies that $\hat{\mathbf{u}}_1$ has the geometric meaning of an *average quaternion* among all the measurements.

2.6 QuateRA Monte Carlo Analysis

This section provides a Monte Carlo analysis of QuateRA, confirming the statistical properties derived in the previous sections, as well as providing a comparison with an MEKF (see Appendix A.4 for referencing the used formulation). We perform extensive simulations for multiple values of n (number of measurements) and σ_θ (standard deviation for the angle in the noise quaternion).

In all simulations, we used an angular velocity with direction $\vec{\omega} = \frac{1}{\sqrt{14}} [1 \ 2 \ 3]^T$. The standard deviation for the measurement noise are chosen as $\sigma_\theta = 1^\circ$, $\sigma_\theta = 2^\circ$, $\sigma_\theta = 3^\circ$, $\sigma_\theta = 4^\circ$, and $\sigma_\theta = 5^\circ$ (large values, when compared to star-tracker technology). The analysis of this section would be quite uninteresting for σ_θ values expected for Star Trackers, since QuateRA's performance would not change much as a function of the number of measurements n). In the simulations that follow, the number of measurements range from $n = 5$ to $n = 50$ in increments of 5. Each Monte Carlo result is obtained after $n_{MC} = 10000$ executions. We denote $\vec{\omega}_\perp \in \mathbb{S}^2$ as an arbitrary unit vector perpendicular to $\vec{\omega}$, i.e., $\vec{\omega}^T \vec{\omega}_\perp = 0$.

In order to evaluate the AOR estimation, we calculate the mean and standard deviation of the estimated AOR $\hat{\vec{\omega}}$ along $\vec{\omega}_\perp$. Defining $\hat{\vec{\omega}}_i^T$ as the estimation of $\vec{\omega}$ at the i^{th} Monte Carlo trial, and $e_{i\perp} \triangleq \hat{\vec{\omega}}_i^T \vec{\omega}_\perp$ as the respective projected error, then the mean μ_\perp and variance σ_\perp^2 for $e_{i\perp}$ is calculated

as:

$$\mu_{\perp} \triangleq \frac{1}{n_{MC}} \sum_{i=1}^{n_{MC}} e_{i\perp}, \quad \sigma_{\perp}^2 \triangleq \frac{1}{n_{MC} - 1} \sum_{i=1}^{n_{MC}} (e_{i\perp} - \mu_{\perp})^2. \quad (2.72)$$

A sample mean around $\mu_{\perp} = 0$ indicates that the AOR is an unbiased estimator. The standard deviation has to belong to the range $0 < \sigma_{\perp} \leq 1/\sqrt{3} \approx 0.5774$, where $\sigma_{\perp} \rightarrow 1/\sqrt{3}$ indicates that the estimator is obtaining solutions uniformly distributed in the unit sphere (see Appendix A.3). In our experience, the AOR estimator provides acceptable estimates when $\sigma_{\perp} \leq 0.1$.

In order to evaluate the AVM estimation, we define the AVM error as $e_{i\Omega} \triangleq \hat{\Omega}_i - \Omega$, where $\hat{\Omega}_i$ is the estimated AVM for the i^{th} Monte Carlo execution. We calculate the mean μ_{Ω} and variance σ_{Ω}^2 of $e_{i\Omega}$ as:

$$\mu_{\Omega} \triangleq \frac{1}{n_{MC}} \sum_{i=1}^{n_{MC}} e_{i\Omega}, \quad \sigma_{\Omega}^2 \triangleq \frac{1}{n_{MC} - 1} \sum_{i=1}^{n_{MC}} (e_{i\Omega} - \mu_{\Omega})^2. \quad (2.73)$$

First, we evaluate QuateRA's performance in a degenerate scenario. We start with measurements taken at 10hz, with an AVM of $\Omega = 0.1\text{rad/s}$. Notice that when the measurement is as high as $5^{\circ} = 0.0873\text{rad}$ and the number of measurements are as low as $n = 5$, the change in orientation throughout that period is of 0.05rad , and hence the signal to noise ratio is extremely low for accurately estimating the angular velocity. Figure 2.1 presents the Monte Carlo results for the AOR estimation, indicating that the estimator is asymptotically unbiased and that the standard deviations decrease as the number of measurements increase. Figure 2.2 shows that the mean error μ_{Ω} converges to zero as the number of measurements n increase. The standard deviation also

decreases as n increases. One should be aware that these solutions only make sense if the AOR make sense, i.e., if σ_{\perp} is small enough.

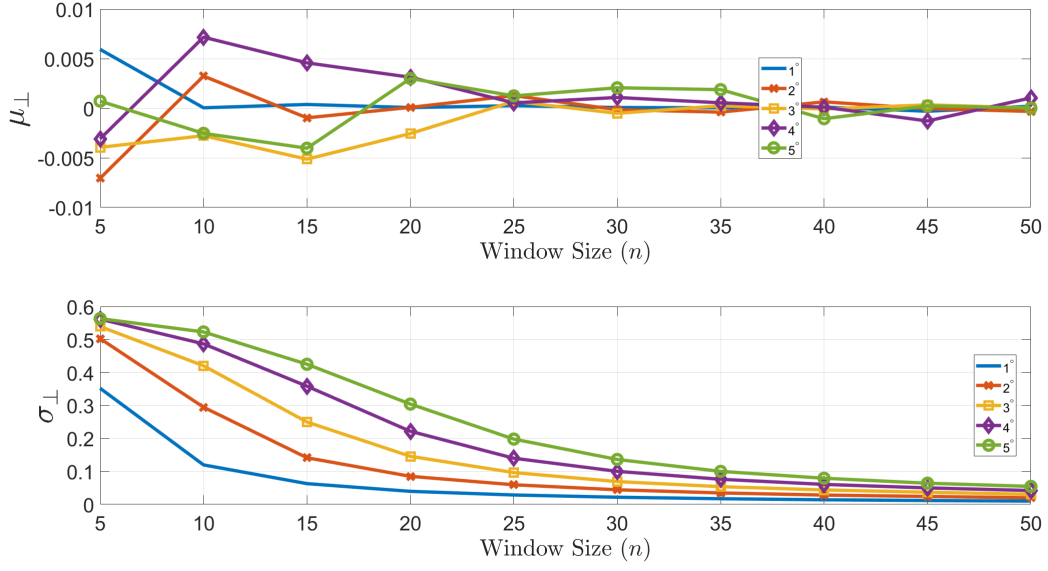


Figure 2.1: Sample Mean and Standard Deviation of the projection of the estimated AOR along a direction perpendicular to the true AOR. Measurements taken at 10Hz, with an AVM of $\Omega = 0.1\text{rad/s}$. Results are shown as a function of the number of measurements (x axis) and the standard deviations σ_{θ} (different plots).

Given the estimate error for the i -th Monte Carlo execution as $\omega_{ei} = \hat{\omega} - \omega$, we compute the sample standard deviation on ω_{ei} , defined as $\sigma_{\omega} = [\sigma_{\omega x} \ \sigma_{\omega y} \ \sigma_{\omega z}]^T$. We compare σ_{ω} with the standard deviations estimated in Section 2.5.3, denoted as $\hat{\sigma}_{\omega} = [\hat{\sigma}_{\omega x} \ \hat{\sigma}_{\omega y} \ \hat{\sigma}_{\omega z}]^T$. We compare both in a

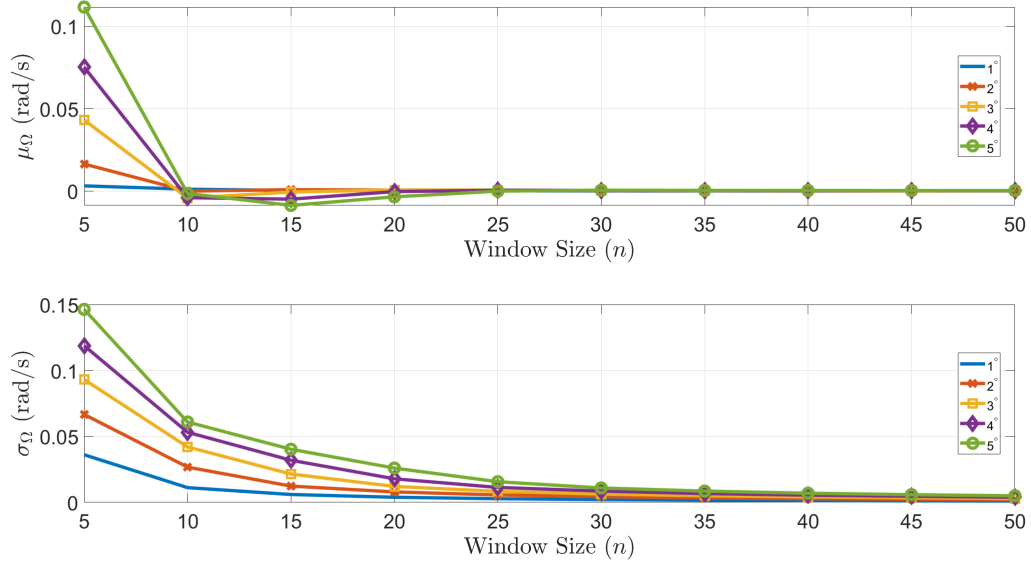


Figure 2.2: Sample Mean and Standard Deviation of the estimated AVM error for measurements taken at 10Hz, and an AVM of $\Omega = 0.1\text{rad/s}$. Results are shown as a function of the number of measurements (x axis) and the standard deviations σ_θ (different plots).

Percent Deviation sense:

$$\begin{aligned}
 PD_{\sigma_x} &\triangleq 100 \cdot \frac{\hat{\sigma}_{\omega x} - \sigma_{\omega x}}{\sigma_{\omega x}}, & PD_{\sigma_y} &\triangleq 100 \cdot \frac{\hat{\sigma}_{\omega y} - \sigma_{\omega y}}{\sigma_{\omega y}}, & (2.74) \\
 PD_{\sigma_z} &\triangleq 100 \cdot \frac{\hat{\sigma}_{\omega z} - \sigma_{\omega z}}{\sigma_{\omega z}}.
 \end{aligned}$$

Figure 2.3 shows how the covariance estimates are biased for a small number of measurements, but the bias diminishes as the number of measurements increase.

QuateRA's performance is improved drastically (compared to the example from before) in a scenario for which measurements are taken at 1Hz, still

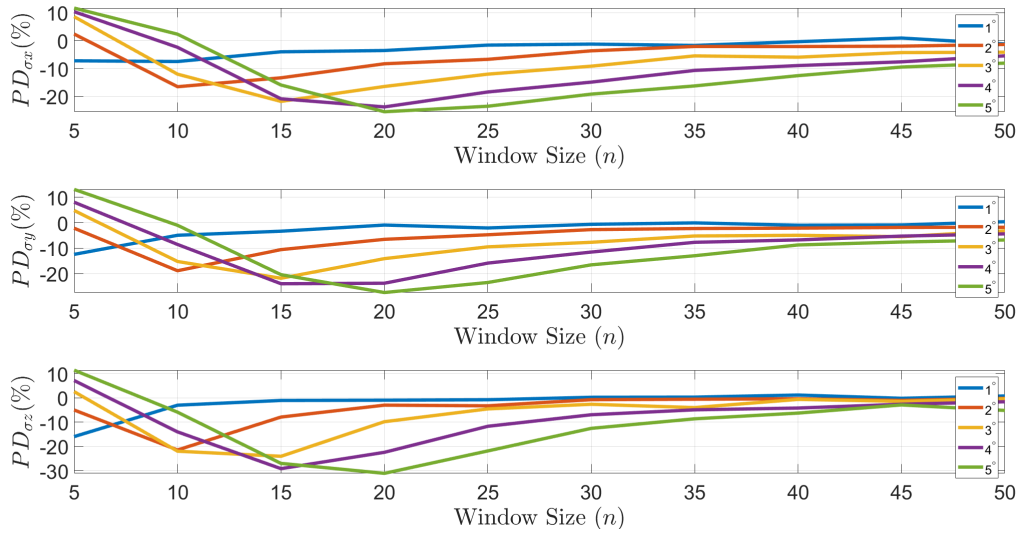


Figure 2.3: Percentual deviation of the average estimated standard deviation for $\hat{\sigma}_\omega$ w.r.t. the sample standard deviation σ_ω , assuming sampling frequency of 10Hz, and an AVM of $\Omega = 0.1\text{rad/s}$. Results are shown as a function of the number of measurements (x axis) and the measurement noise standard deviations σ_θ (different plots).

with an AVM of $\Omega = 0.1\text{rad/s}$. We can see that both the bias and the standard deviations (Figures 2.4 and 2.5) are reduced compared with the previous scenario, and the estimated covariance is very close to the sample covariance (Figure 2.6). Our reasoning for improvement is based upon the fact that TLS can provide better planar estimates when the quaternion measurements are more sparsely distributed along the plane, whereas the previous scenario had many quaternions close to each other, making it harder to determine the plane of rotation from the given measurements.

In order to compare QuateRA with the MEKF, we will analyze varying values for sampling frequency δt and angular velocity magnitude. We com-

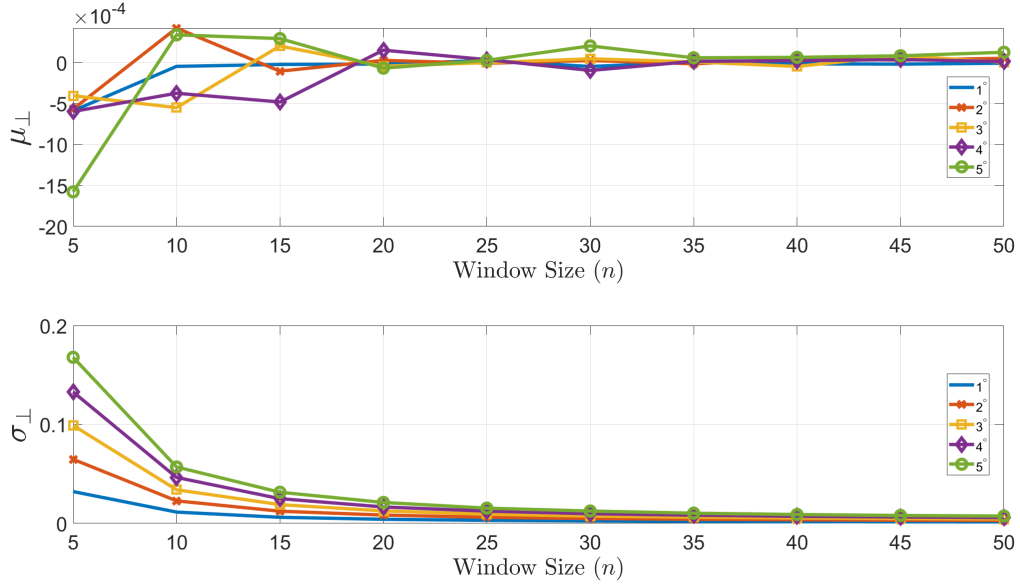


Figure 2.4: Sample Mean and Standard Deviation of the projection of the estimated AOR along a direction perpendicular to the true AOR. Measurements taken at 1Hz, with an AVM of $\Omega = 0.1\text{rad/s}$. Results are shown as a function of the number of measurements (x axis) and the standard deviations σ_θ (different plots).

pare both estimators by evaluating the Least Squares cost function of Eq. 2.33 $J_{LS} = n - \sum \hat{\mathbf{q}}_i^T \bar{\mathbf{q}}_i$. In order to obtain the MEKF quaternion estimates $\hat{\mathbf{q}}$, we first execute the MEKF algorithm - processing all orientation measurements - and then we use the estimated angular velocity to propagate the final orientation backwards in time to obtain previous orientations (smoothing procedure). We compare Quatera with MEKF as a percent deviation:

$$PD(\%) = 100 \cdot \frac{J_{LS}(MEKF) - J_{LS}(QuateRA)}{J_{LS}(MEKF)}, \quad (2.75)$$

where MEKF outperforms QuateRA when $PD(\%) < 0$ and QuateRA outperforms MEKF otherwise.

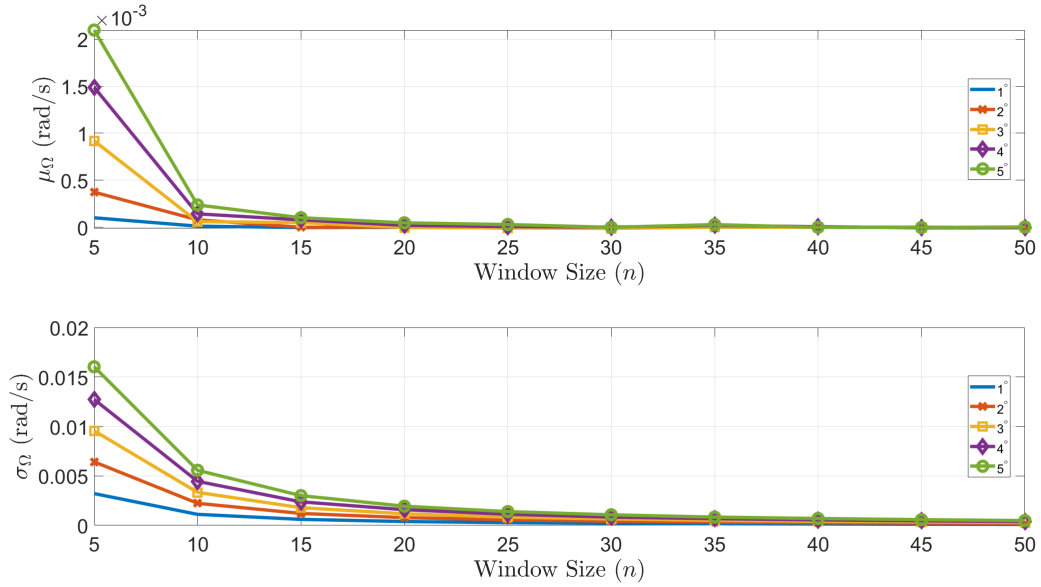


Figure 2.5: Sample Mean and Standard Deviation of the estimated AVM error for measurements taken at 10Hz, and an AVM of $\Omega = 0.1\text{rad/s}$. Results are shown as a function of the number of measurements (x axis) and the standard deviations σ_{θ} (different plots).

Table 2.1 presents the average percent deviation for $dt = 0.1\text{s}$ and $\Omega = 0.1\text{rad}$. We notice that MEKF outperforms QuateRA most of the time for this scenario. The performance between both is quite similar when the number of measurements is in the range $n \geq 25$. Table 2.2 presents the percent deviation for $dt = 1\text{s}$ and $\Omega = 0.1\text{rad}$, and we notice that there is no clear winner when comparing both in this scenario. In contrast, QuateRA outperforms MEKF largely when $dt = 1\text{s}$ and $\Omega = 1\text{rad}$, as shown in Table 2.3. We attribute the poor performance of MEKF in this last scenario due to the fact that MEKF is just a first order filter, and its performance degrades when nonlinearities become dominant when measurements are taken sparsely.

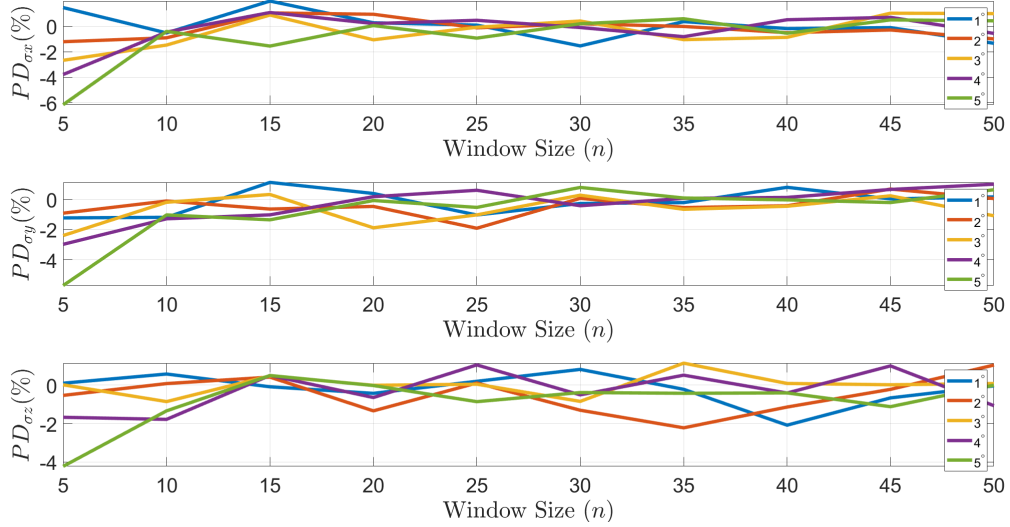


Figure 2.6: Percentual deviation of the average estimated standard deviation for $\hat{\sigma}_\omega$ w.r.t. the sample standard deviation σ_ω , assuming sampling frequency of 10Hz, and an AVM of $\Omega = 0.1\text{rad/s}$. Results are shown as a function of the number of measurements (x axis) and the measurement noise standard deviations σ_θ (different plots).

Finally, QuateRA is compared with a solution obtained from a nonlinear solver for the optimization problem of Eq. 2.33. The optimization problem is initialized with an initial guess for the angular velocity that is obtained from the quaternion kinematic equation of Eq. 2.22. Assuming the approximations $\dot{\mathbf{q}} \approx \frac{\bar{\mathbf{q}}_2 - \bar{\mathbf{q}}_1}{t_2 - t_1}$ and $\dot{\mathbf{q}} \approx \frac{1}{2}\boldsymbol{\omega} \otimes \bar{\mathbf{q}}_1$, then we initialize the nonlinear solver with the estimates $\hat{\boldsymbol{\omega}} = 2\frac{\bar{\mathbf{q}}_2 - \bar{\mathbf{q}}_1}{t_2 - t_1} \otimes \bar{\mathbf{q}}_1^{-1}$ and $\hat{\mathbf{q}}_1 = \bar{\mathbf{q}}_1$. We have used Matlab's [40] function *fmincon* [39] using the *interior-point* algorithm with constraint tolerance of 10^{-6} , maximum of 1000 iterations and optimality tolerance of 10^{-6} . Again, we perform 10000 Monte Carlo executions for the same scenarios as in the previous comparison: first with $dt = 0.1\text{s}$ and $\Omega = 0.1\text{rad}$, then $dt = 1\text{s}$ and

$\Omega = 0.1\text{rad}$, and $dt = 1\text{s}$ and $\Omega = 1\text{rad}$.

Tables 2.4-2.6 show the number of times that *Fmincon* converged for each scenario over 10000 executions. We see that *Fmincon* always had trouble to converge when the number of input measurements were $n = 5$. When $n \neq 5$, we see some variability for the number of convergences depending on the scenario for the sampling frequency and angular velocity. This hints at the idea that a nonlinear optimizer won't always converge, and we see a particular case in which it converged only 83.8% of the time.

We use the following equation for comparing the performance between *Fmincon* and QuateRA:

$$PD(\%) = 100 \cdot \frac{J_{LS}(Fmincon) - J_{LS}(QuateRA)}{J_{LS}(Fmincon)}, \quad (2.76)$$

where *Fmincon* outperforms QuateRA when $PD(\%) < 0$ and QuateRA outperforms *Fmincon* otherwise. In principle, *Fmincon* should always outperform QuateRA, and this analysis helps us in understanding how far is QuateRA from the optimal solution. Note that the analysis hereinafter is done only for *Fmincon's* converged solutions, and the non-converged ones are discarded.

Tables 2.7-2.9 show the percent deviation between both methods. Just as in the comparison with the MEKF, QuateRA is outperformed when n is low, $dt = 0.1\text{s}$ and $\Omega = 0.1\text{rad}$.

A surprising outcome can be seen in Tables 2.8 and 2.9, in which QuateRA largely outperforms *Fmincon* for large number of input measurements

(and performs similarly for a low number of measurements). Although *Fmincon* believes to have converged for most of these optimization problems, the numerical solution quality deteriorates as n increases for this particular scenario.

2.7 Conclusions

This work presented a batch estimation procedure for the determination of a constant angular velocity from quaternion measurements. In the constant angular velocity scenario, we show that the orientation quaternion evolves without departing from a fixed plane of rotation. With this insight, we are able to estimate the axis of rotation. Given the plane of rotation, the quaternions can be reprojected onto this plane, being parametrized as a single evolving angle on the plane. The angular velocity magnitude is then estimated from the evolution of the quaternion angle on the plane.

As we show in our Monte Carlo section, the performance of the Quaternion Regression Algorithm (QuateRA) is a function of n and the expected amplitude of the measurement noise. Our results indicate asymptotic unbiasedness of QuateRA, and we are able to accurately determine the standard deviation of the angular velocity estimation for sufficiently large sample sets. We show that QuateRA performs very close to a Multiplicative Extended Kalman Filter (MEKF), even outperforming the latter when nonlinearities are dominant (as is typically the case with large angular rates), as MEKF is a first order estimator. When compared with a nonlinear optimization solver,

QuateRA performs very close to *Fmincon* when the number of measurements are low. For large measurement sample sets, QuateRA outperforms *Fmincon*, which fails to converge appropriately.

Our earlier contributions have already demonstrated the application of preliminary versions of QuateRA for estimating a non-constant angular velocity. These works introduced tuning parameters for adapting the size of the sliding window and for tuning the Angular Velocity Magnitude (AVM) estimator. In contrast, the current work presents a method for estimating the AVM that is free of tuning parameters, and it does produce a consistent covariance estimate for the estimate (provided a sufficiently large sample set). These contributions are relevant for the overall problem of estimating a time-varying Axis of Rotation (AOR) without the need for heuristic tuning. In the case of non-constant angular velocity with unknown torques and inertia matrix, filtering techniques as an MEKF are not appropriate solutions because the dynamics are not fully modeled. On the other hand, a self-tuning algorithm such as a QuateRA-based sliding window with statistically adaptive window size can figure out how many measurements can be taken without violating the assumption that the angular velocity is approximately constant. Hence, QuateRA is applicable not only for constant angular velocity (the pure-spin case), but also in the presence of unmodeled attitude dynamics (large uncertainties in the inertial properties and possible presence of unknown external disturbance torques). This problem is treated in the chapter that follows.

An interesting path of future work would be to determine a covariance

estimate associated with the estimated AOR. Classically, it is possible to estimate asymptotic covariances for TLS solutions provided that the solution is unique. As shown in Section 2.5, the TLS solution for this problem is not unique and we cannot determine the covariance of $\hat{\mathbf{u}}_1$ and $\hat{\mathbf{u}}_2$ using classical methods in TLS. Since the AOR estimate is determined from $\hat{\mathbf{u}}_1$ and $\hat{\mathbf{u}}_2$, computing the covariance of the estimated AOR is not trivial. Therefore, establishing the AOR covariance would be a meaningful contribution for future work.

Another interesting path for future research would be to expand QuateRA for non-constant measurement covariance over multiple measurements. Additionally, we have assumed that the axis of the noise quaternion is distributed in a uniform spherical distribution, whereas this is not always true in practice. For instance, star trackers typically have different covariances associated with the roll, pitch and yaw directions. Hence, it would also be meaningful to adapt QuateRA to accommodate for a more accurate measurement model.

Table 2.1: Percent deviation between MEKF and QuateRA for $dt = 0.1s$ and $\Omega = 0.1rad$.

	$n = 5$	$n = 10$	$n = 15$	$n = 20$	$n = 25$	$n = 30$	$n = 35$	$n = 40$	$n = 45$	$n = 50$
$\sigma = 1^\circ$	-9.91	-1.18	-0.41	-0.15	-0.06	0.04	0.07	-0.35	0.11	-0.31
$\sigma = 2^\circ$	-9.56	-6.65	-1.71	-0.35	-0.80	-0.85	-0.08	0.08	-0.31	0.14
$\sigma = 3^\circ$	-10.50	-8.27	-4.73	-2.83	-1.49	-0.95	-0.26	0.08	-0.40	-0.12
$\sigma = 4^\circ$	-9.62	-9.04	-7.19	-3.53	-1.35	-1.04	-0.79	-0.16	-0.19	-0.36
$\sigma = 5^\circ$	-9.04	-7.49	-7.08	-5.32	-2.93	-1.67	-0.86	-0.29	-0.20	-0.52

Table 2.2: Percent deviation between MEKF and QuateRA for $dt = 1s$ and $\Omega = 0.1rad$.

	$n = 5$	$n = 10$	$n = 15$	$n = 20$	$n = 25$	$n = 30$	$n = 35$	$n = 40$	$n = 45$	$n = 50$
$\sigma = 1^\circ$	1.18	-0.65	0.10	-0.59	0.09	-0.67	0.22	-0.80	-0.07	-0.22
$\sigma = 2^\circ$	-0.61	-0.66	0.10	0.25	0.22	0.47	-0.04	0.01	0.05	-0.39
$\sigma = 3^\circ$	0.81	-0.10	0.96	-0.35	-0.66	-0.33	-0.14	-0.58	0.13	-0.31
$\sigma = 4^\circ$	-0.02	-0.32	0.35	0.55	-0.09	0.13	-0.39	-0.28	0.21	0.08
$\sigma = 5^\circ$	-2.09	-0.66	-0.80	-0.15	0.03	0.56	0.38	-0.12	0.15	-0.25

Table 2.3: Percent deviation between MEKF and QuateRA for $dt = 1s$ and $\Omega = 1rad$.

	$n = 5$	$n = 10$	$n = 15$	$n = 20$	$n = 25$	$n = 30$	$n = 35$	$n = 40$	$n = 45$	$n = 50$
$\sigma = 1^\circ$	92.60	77.54	61.35	47.93	37.35	29.31	23.73	19.12	16.20	13.15
$\sigma = 2^\circ$	76.43	47.19	29.11	19.51	13.79	10.08	7.66	5.74	5.26	4.27
$\sigma = 3^\circ$	60.81	29.69	16.15	10.18	7.26	5.23	4.43	3.11	2.41	2.11
$\sigma = 4^\circ$	47.12	20.07	10.47	6.75	4.95	3.35	2.47	1.93	1.67	1.45
$\sigma = 5^\circ$	37.31	14.65	7.94	5.20	4.09	1.62	1.79	1.22	1.27	0.79

Table 2.4: Number of times that F_{mincon} converged for $dt = 0.1s$ and $\Omega = 0.1rad$.

	$n = 5$	$n = 10$	$n = 15$	$n = 20$	$n = 25$	$n = 30$	$n = 35$	$n = 40$	$n = 45$	$n = 50$
$\sigma = 1^\circ$	0	10000	10000	10000	10000	10000	10000	10000	10000	10000
$\sigma = 2^\circ$	0	10000	10000	10000	10000	10000	10000	10000	10000	10000
$\sigma = 3^\circ$	0	10000	10000	10000	10000	10000	10000	10000	10000	10000
$\sigma = 4^\circ$	0	10000	10000	10000	10000	10000	10000	10000	10000	10000
$\sigma = 5^\circ$	0	10000	10000	10000	10000	10000	10000	10000	10000	10000

Table 2.5: Number of times that F_{mincon} converged for $dt = 1s$ and $\Omega = 0.1rad$.

	$n = 5$	$n = 10$	$n = 15$	$n = 20$	$n = 25$	$n = 30$	$n = 35$	$n = 40$	$n = 45$	$n = 50$
$\sigma = 1^\circ$	0	10000	9984	9200	8544	8545	8837	8664	8455	8384
$\sigma = 2^\circ$	0	10000	9982	9216	8619	8663	8795	8827	8946	9005
$\sigma = 3^\circ$	0	10000	9964	9327	8847	8835	8973	9088	9231	9326
$\sigma = 4^\circ$	0	10000	9974	9448	8961	8984	9057	9198	9354	9518
$\sigma = 5^\circ$	0	10000	9972	9519	9138	9116	9185	9296	9454	9568

Table 2.6: Number of times that F_{mincon} converged for $dt = 1s$ and $\Omega = 1rad$.

	$n = 5$	$n = 10$	$n = 15$	$n = 20$	$n = 25$	$n = 30$	$n = 35$	$n = 40$	$n = 45$	$n = 50$
$\sigma = 1^\circ$	0	10000	10000	10000	9998	9998	9999	9997	9996	9991
$\sigma = 2^\circ$	0	10000	10000	10000	10000	9997	9998	9997	9995	9990
$\sigma = 3^\circ$	0	10000	10000	9998	10000	9999	9997	9993	9991	9987
$\sigma = 4^\circ$	0	10000	10000	9999	9998	9995	9994	9990	9992	9985
$\sigma = 5^\circ$	0	10000	9999	10000	10000	9999	9997	9996	9987	9991

Table 2.7: Percent deviation between *Fmincon* and *QuateRA* for $dt = 0.1s$ and $\Omega = 0.1rad$ (there is no data for $n = 5$).

	$n = 5$	$n = 10$	$n = 15$	$n = 20$	$n = 25$	$n = 30$	$n = 35$	$n = 40$	$n = 45$	$n = 50$
$\sigma = 1^\circ$	x	-0.54	-0.76	-0.72	-0.97	0.15	-0.51	-0.10	0.04	0.29
$\sigma = 2^\circ$	x	-7.35	-1.17	-1.34	-0.18	0.20	0.25	-0.12	-0.32	-0.24
$\sigma = 3^\circ$	x	-9.42	-4.97	-2.05	-0.58	-0.19	-0.25	0.36	-0.24	0.22
$\sigma = 4^\circ$	x	-7.34	-7.54	-4.40	-1.87	-0.51	-0.32	-0.36	-0.24	-0.25
$\sigma = 5^\circ$	x	-6.61	-6.49	-4.87	-2.42	-0.65	-1.53	-0.57	-0.76	-0.63

Table 2.8: Percent deviation between *Fmincon* and *QuateRA* for $dt = 1s$ and $\Omega = 0.1rad$ (there is no data for $n = 5$).

	$n = 5$	$n = 10$	$n = 15$	$n = 20$	$n = 25$	$n = 30$	$n = 35$	$n = 40$	$n = 45$	$n = 50$
$\sigma = 1^\circ$	x	-0.64	-0.43	0.23	0.20	-0.06	-0.43	0.10	0.03	0.10
$\sigma = 2^\circ$	x	-0.46	1.21	0.74	0.28	0.82	0.13	21.77	21.42	62.82
$\sigma = 3^\circ$	x	0.49	0.11	0.04	-0.72	19.72	19.32	77.92	81.65	92.21
$\sigma = 4^\circ$	x	-0.43	0.49	-0.51	29.00	66.02	74.48	89.94	93.99	96.35
$\sigma = 5^\circ$	x	0.63	0.49	7.79	64.48	85.36	88.25	95.41	96.64	97.49

Table 2.9: Percent deviation between *Fmincon* and *QuateRA* for $dt = 1s$ and $\Omega = 1rad$ (there is no data for $n = 5$).

	$n = 5$	$n = 10$	$n = 15$	$n = 20$	$n = 25$	$n = 30$	$n = 35$	$n = 40$	$n = 45$	$n = 50$
$\sigma = 1^\circ$	x	0.97	0.06	0.47	-0.15	0.09	0.03	0.41	0.23	47.83
$\sigma = 2^\circ$	x	0.53	-0.11	0.20	0.36	0.37	-0.39	0.39	31.96	18.91
$\sigma = 3^\circ$	x	-0.65	-0.50	-0.23	-0.19	-0.06	0.18	12.43	16.98	65.44
$\sigma = 4^\circ$	x	-0.21	0.16	-0.34	-0.20	-0.04	12.63	35.66	52.67	71.67
$\sigma = 5^\circ$	x	-0.20	-0.31	-0.17	9.34	14.84	32.94	58.70	65.84	81.74

Chapter 3

Real-time Angular Velocity Estimation of Non-cooperative Space Objects Using Camera Measurements

3.1 Introduction

This chapter¹ presents a solution to the problem of estimating the relative angular velocity (RAV) between a camera (onboard a chaser spacecraft) and an object in space (the target spacecraft or celestial object) using camera measurements only. The work presented in this chapter is a natural step as an application of QuateRA [6] as a generalized angular velocity estimator. Our approach assumes no prior knowledge of the inertial characteristics of the target space object such as shape, size, and mass distribution, making it seamlessly applicable to different applications. If we assume that the angular velocity of the chaser is known, then our approach provides the absolute angular velocity of the target object.

Using camera measurements, the relative pose between the chaser and the target can be estimated by tracking known features (assuming a known target) or through Simultaneous Localization and Mapping (SLAM) algorithms [25]. Previous works show that SLAM algorithms can be used for resolving the relative pose problem in space applications. More specifically, in Ref. [22], the authors use images obtained from NASA’s STS-125 Service Mission 4² in tandem with the ORB-SLAM package [44], demonstrating that it tracked closely the estimated relative pose during the mission [45]. In Ref. [46],

¹“Marcelino Almeida, Renato Zanetti, Daniele Mortari, and Maruthi Akella. Real-time angular velocity estimation of non-cooperative space objects using camera measurements. *2018 AAS/AIAA Astrodynamics Specialist Conference in Snowbird, UT*, 167(18-420), Aug. 2018.” (Marcelino Almeida conducted the problem formulation and solution, simulation and analyses, and wrote the paper.)

²Service Mission to the Hubble Space Telescope carried out in May-2009.

the authors use data from the Rosetta mission³ to feed an EKF-SLAM algorithm, which estimates Rosetta’s spin state, mass, and moments, as well as the chaser’s position and velocity.

The main issue with using EKF-based algorithms for estimating the RAV of a non-cooperative target is that the external torques upon the same might be unknown. In this case, any perturbing external torques have to be estimated by extending the states (assuming smooth torques with bounded derivatives) or by using a sufficiently large process noise in the angular velocity covariance propagation. The problem becomes even harder when the target’s inertia matrix is unknown, since it is barely observable at long distances [46].

The lack of precise knowledge of a system’s inertia matrix and torque vector also poses a challenge to non Kalman-filtering techniques. Many of the existing angular velocity estimators [9, 47, 53] rely on the knowledge of the target’s specific inertia and torque parameters. An exception can be made for the *derivative approach* described in Ref. [9], but as the author acknowledges, the angular velocity estimator can produce considerable error due to the presence of measurement noise. In Ref. [10], the authors present the Pseudolinear Kalman Filter (PSELIKA), which does not depend on knowledge of inertia matrix or input torques. However, PSELIKA is developed with the goal of “simplicity rather than accuracy” [10], serving as a crude angular velocity estimator for control loop damping purposes.

³<https://www.aerosociety.com/news/lecture-report-rosetta-how-we-landed-on-a-comet/>

An alternative solution to the RAV problem is to use methods based on the Multiplicative Extended Kalman Filter (MEKF) [24,34,36], since these rely on kinematics only. Still, one needs to have tight bounds upon how fast the angular velocity of the target might be changing with time, and use the process noise covariance as a tuning parameter (i.e., a forgetting factor). If the target is being actuated or it is tumbling (e.g., the Toutatis asteroid⁴), then the rate at which the target’s angular velocity varies with time is not necessarily constant. In this scenario, properly tuning the forgetting factor becomes a formidable task, thereby providing a strong motivation for the need to resort to adaptive estimators.

In this context, the Angular Velocity Adaptive Estimation (AVAst) algorithm [42] is an attractive option for real-time applications, since it is adaptive, is based on kinematics, and is not computationally expensive. The AVAst algorithm builds upon the Quaternion Regression Algorithm (QuateRA) [6], which uses *sequential orientation measurements* for estimating *constant angular velocity* (pure spin) through a batch procedure. In order to prevent confusion throughout the text, we refer to QuateRA as an estimator for *constant angular velocity*, while AVAst estimates a *dynamic angular velocity*, but the reader should keep in mind that AVAst still employs QuateRA internally. QuateRA is divided in two parts: one that estimates the axis of rotation (AOR), and another that estimates the angular velocity’s magnitude

⁴https://science.nasa.gov/science-news/science-at-nasa/2012/12dec_toutatis/

(AVM). In order to calculate the AOR, QuateRA estimates the average plane of rotation for the given sequence of rotations, then uses AOR information to estimate for the AVM. AVAst distinguishes from QuateRA by adaptively changing the set of input measurements that are used in QuateRA such that the angular velocity estimates are statistically consistent.

The main contribution of this work concerns in presenting a strategy in how to employ QuateRA as a generalized estimator for angular velocity. In addition, we demonstrate how AVAst can be engaged with ORB-SLAM for estimating the angular velocity of a non-cooperative target. Simulation results are shown for ratifying the proposed pipeline. In terms of the overall algorithm implementation, our approach uses camera images to feed into a SLAM algorithm, which is able to determine the relative pose between the target and the chaser. Towards this goal, we employ the ORB-SLAM algorithm that was also used earlier in Ref. [22]. As already shown in Ref. [22], ORB-SLAM is capable of running in real time (no need for post-processing), and it has been documented to produce satisfactory results in numerous applications. Then, AVAst is used for estimating the angular velocity of the given target.

The remainder of this paper is organized as follows: Section 3.2 poses the problem of estimating the angular velocity of a target object using camera measurements, also introducing the assumed statistics of the measurement noise. Section 3.3 introduces QuateRA, and Section 3.4 presents the consistency test used in AVAst. Section 3.5 presents simulation results, along with a comparison with an estimation algorithm inspired from Ref. [10]. Finally,

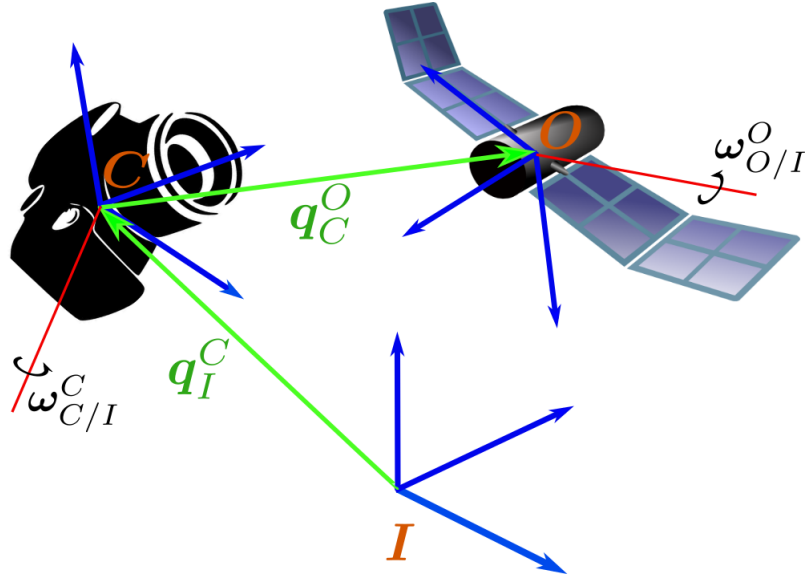


Figure 3.1: Reference frames and rotational transformations.

conclusions are presented in Section 3.6.

3.2 Problem Formulation

The various reference frames adopted for this problem is displayed in Fig. 3.1. We assume a chaser camera (frame C) with known orientation \mathbf{q}_I^C w.r.t. a star tracker inertial frame of reference (frame I). We assume that the chaser angular velocity $\boldsymbol{\omega}_{C/I}^C$ is known. Also, we assume a target object (frame O) with unknown relative angular velocity $\boldsymbol{\omega}_{O/C}^O$, but within the field of view of the chaser's camera. In addition, we do not assume knowledge of the target's inertia matrix or actuation torques.

The objective of this work is to obtain the target's angular velocity $\boldsymbol{\omega}_{O/I}^O$ through visual inspection. We use ORB-SLAM [44] to measure the rel-

ative orientation between the chaser and the target. The measured relative orientation between C and O at time t_i is denoted as the quaternion $\mathbf{q}_C^O(t_i)$. The quaternion parameterizing the absolute pose of the target at time t_i is then calculated as:

$$\mathbf{q}_I^O(t_i) = \mathbf{q}_C^O(t_i) \otimes \mathbf{q}_I^C(t_i) \quad (3.1)$$

We use the target's pose measurements $\mathbf{q}_I^O(t_i)$ as inputs to QuateRA, which separately estimates the target's axis of rotation (denoted as $\vec{\omega}_{O/I}^O$), and the angular velocity magnitude (denoted as $\Omega_{O/I}^O$). The target's estimated angular velocity is then:

$$\boldsymbol{\omega}_{O/I}^O = \Omega_{O/I}^O \vec{\omega}_{O/I}^O \quad (3.2)$$

For simplicity of notation, the remainder of this chapter will denote $\mathbf{q}(t) \triangleq \mathbf{q}_I^O(t)$, $\mathbf{q}_i \triangleq \mathbf{q}_I^O(t_i)$, $\boldsymbol{\omega} \triangleq \boldsymbol{\omega}_{O/I}^O$, $\vec{\omega} \triangleq \vec{\omega}_{O/I}^O$, and $\Omega \triangleq \Omega_{O/I}^O$. We denote $\hat{\mathbf{x}}$ as an estimate of the variable \mathbf{x} , and we use the notation $\bar{\mathbf{x}}_i$ to denote a measurement of the variable \mathbf{x} at instant i . Specifically, the quaternion measurement model is assumed to be:

$$\bar{\mathbf{q}}_i = \mathbf{q}_{N_i} \otimes \mathbf{q}_i, \quad (3.3)$$

where \mathbf{q}_N is the noise quaternion:

$$\mathbf{q}_{N_k} \triangleq \begin{bmatrix} \cos \frac{\theta_i}{2} \\ \mathbf{e}_{N_i} \sin \frac{\theta_i}{2} \end{bmatrix}, \quad (3.4)$$

in which θ_i and \mathbf{e}_{N_i} are independent random variables. Just like in Ref. [6], the measurement model assumes that θ_i is Gaussian such that $\theta_i \sim \mathcal{N}(0, \sigma_\theta^2)$,

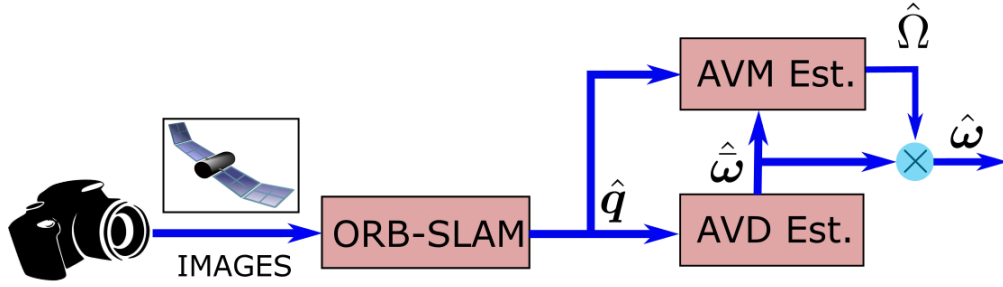


Figure 3.2: Proposed Algorithm Pipeline.

and $\mathbf{e}_{N_i} \in \mathbb{S}^2$ is a unit-norm random vector uniformly distributed in $\mathbb{S}^2 = \{\mathbf{x} \in \mathbb{R}^3 : \|\mathbf{x}\| = 1\}$ and has the characteristics $\mathbb{E}[\mathbf{e}_{N_i}] = \mathbf{0}$ and $\mathbb{E}[\mathbf{e}_{N_i} \mathbf{e}_{N_i}^T] = \frac{1}{3} \mathbf{I}$.

The target's kinematics is described as:

$$\dot{\mathbf{q}}(t) = \frac{1}{2} \boldsymbol{\omega} \otimes \mathbf{q}(t). \quad (3.5)$$

Assuming that the target's angular velocity $\boldsymbol{\omega}(t_i)$ is approximately constant during the period $t = [t_i, t_{i+1}]$, then the solution to Eq. 3.5 is $\mathbf{q}_{k+1} = \mathbf{F}(\boldsymbol{\omega}) \cdot \mathbf{q}_i$, where:

$$\mathbf{F}(\boldsymbol{\omega}) = \exp \left[\frac{\delta t}{2} \boldsymbol{\omega} \otimes \right] = \cos \frac{\Omega \delta t}{2} \cdot \mathbf{I} + \sin \frac{\Omega \delta t}{2} \cdot \vec{\boldsymbol{\omega}} \otimes, \quad (3.6)$$

where $\delta t = t_{i+1} - t_i$.

Figure 3.2 depicts the suggested pipeline utilized in this work: images are fed to ORB-SLAM, which in turn produces a relative orientation. The relative orientation is used in QuateRA to estimate the AVD $\hat{\boldsymbol{\omega}}$, which is then used to estimate for the AVM $\hat{\Omega}$.

3.3 The Quaternion Regression Algorithm

This section presents QuateRA, as well as some crucial aspects used in its derivation, herein presented as a summary of Section 2.5 with some slight changes in notation. QuateRA assumes constant $\boldsymbol{\omega}$ to first estimate the AOR $\hat{\boldsymbol{\omega}}$, then uses its knowledge to estimate for the AVM $\hat{\Omega}$. Finally, the estimated angular velocity is given by $\hat{\boldsymbol{\omega}} = \hat{\Omega}\hat{\boldsymbol{\omega}}$.

In order to estimate the AOR, QuateRA uses a geometric interpretation based on the solution to the quaternion kinematic equation for constant $\boldsymbol{\omega}$:

$$\mathbf{q}(t) = \left[\cos \frac{\Omega \delta t}{2} \cdot \mathbf{I} + \sin \frac{\Omega \delta t}{2} \cdot \vec{\boldsymbol{\omega}} \otimes \right] \mathbf{q}_0, \quad (3.7)$$

with $\delta t \triangleq t - t_0$. Defining the vectors $\mathbf{u}_1 \in \mathbb{S}^3 = \mathbf{q}_0$ and $\mathbf{u}_2 \in \mathbb{S}^3 = \vec{\boldsymbol{\omega}} \otimes \mathbf{q}_0$, we have that $\mathbf{u}_1^T \mathbf{u}_2 = \mathbf{q}_0 \cdot \vec{\boldsymbol{\omega}} \otimes \mathbf{q}_0$. Since $\vec{\boldsymbol{\omega}} \otimes$ is a skew-symmetric matrix (see Eq. 2.20) then $\mathbf{u}_1^T \mathbf{u}_2 = 0$, i.e., $\mathbf{u}_1 \perp \mathbf{u}_2$. Clearly, any $\mathbf{q}(t)$ described by Eq. 3.7 is a linear combination of \mathbf{u}_1 and \mathbf{u}_2 , for all $t \in \mathbb{R}$. Hence, if we define the 4D hyperplane $\mathbb{P}(\mathbf{u}_1, \mathbf{u}_2) = \text{span}\{\mathbf{u}_1, \mathbf{u}_2\}$, then $\mathbf{q}(t) \in \mathbb{P}(\mathbf{u}_1, \mathbf{u}_2), \forall t \in \mathbb{R}$. In addition, there exists a perpendicular plane $\mathbb{P}(\mathbf{u}_3, \mathbf{u}_4) = \text{span}\{\mathbf{u}_3, \mathbf{u}_4\}$, with $\mathbf{u}_3, \mathbf{u}_4 \in \mathbb{S}^3$ such that $\mathbf{u}_4 = \vec{\boldsymbol{\omega}} \otimes \mathbf{u}_3$, where $\mathbf{u}_3^T \mathbf{q}(t) = \mathbf{u}_4^T \mathbf{q}(t) = 0, \forall t \in \mathbb{R}$.

Therefore, given a sequence of measurements $\bar{\mathbf{q}}_i, i \in \{1, \dots, n\}$, with $n \in \mathbb{N}_{\geq 2}$, QuateRA estimates the AOR by finding the optimal hyperplane that minimizes the distance to the measured quaternions.

At a given time t_k , QuateRA constructs the measurement matrix with n measurements $\bar{\mathbf{Q}}_{k,n}$ as:

$$\bar{\mathbf{Q}}_{k,n} \triangleq \begin{bmatrix} \bar{\mathbf{q}}_{k-n+1} & \bar{\mathbf{q}}_{k-n+2} & \cdots & \bar{\mathbf{q}}_k \end{bmatrix}. \quad (3.8)$$

Similarly, we define the window matrix of estimated quaternions as:

$$\hat{\mathbf{Q}}_{k,n} \triangleq [\hat{\mathbf{q}}_{k-n+1} \quad \hat{\mathbf{q}}_{k-n+2} \quad \cdots \quad \hat{\mathbf{q}}_k]. \quad (3.9)$$

Note that the quaternions in each column of $\hat{\mathbf{Q}}_{k,n}$ should belong to the estimated plane of rotation: $\hat{\mathbf{q}}_i \in \mathbb{P}(\hat{\mathbf{u}}_1, \hat{\mathbf{u}}_2)$, $i \in \{k-n+1, \dots, k\}$. The quaternions $\hat{\mathbf{q}}_i$ are estimated to minimize the Total Least Squares cost function:

$$J_0 = \frac{1}{2} \|\bar{\mathbf{Q}}_{k,n} - \hat{\mathbf{Q}}_{k,n}\|_F^2, \quad (3.10)$$

subject to $\hat{\mathbf{q}}_i \in \mathbb{P}(\hat{\mathbf{u}}_1, \hat{\mathbf{u}}_2)$, $\forall i \in \{k-n+1, \dots, k\}$, where $\hat{\mathbf{u}}_1$ and $\hat{\mathbf{u}}_2$ define the optimally estimated plane of rotation.

Assuming small angle approximation for the noise quaternion (see Eq. 3.4), Ref. [6] shows that the optimization problem above is approximately equivalent to finding the unit-norm vectors $\hat{\mathbf{u}}_1 \in \mathbb{S}^3$, $\hat{\mathbf{u}}_2 \in \mathbb{S}^3$ such that $\hat{\mathbf{u}}_1^T \hat{\mathbf{u}}_2 = 0$, that maximizes the following cost function:

$$J = \sum_{i=1}^n \left[(\bar{\mathbf{q}}_i^T \hat{\mathbf{u}}_1)^2 + (\bar{\mathbf{q}}_i^T \hat{\mathbf{u}}_2)^2 \right] = \hat{\mathbf{u}}_1^T \bar{\mathbf{Z}} \hat{\mathbf{u}}_1 + \hat{\mathbf{u}}_2^T \bar{\mathbf{Z}} \hat{\mathbf{u}}_2, \quad (3.11)$$

where $\bar{\mathbf{Z}} \triangleq \bar{\mathbf{Q}}_{k,n} \bar{\mathbf{Q}}_{k,n}^T$. Given $\hat{\mathbf{u}}_1$, $\hat{\mathbf{u}}_2$, the optimally estimated quaternions within $\hat{\mathbf{Q}}$ are given by:

$$\hat{\mathbf{q}}_i = \frac{1}{\sqrt{(\bar{\mathbf{q}}_i^T \hat{\mathbf{u}}_1)^2 + (\bar{\mathbf{q}}_i^T \hat{\mathbf{u}}_2)^2}} [(\bar{\mathbf{q}}_i^T \hat{\mathbf{u}}_1) \hat{\mathbf{u}}_1 + (\bar{\mathbf{q}}_i^T \hat{\mathbf{u}}_2) \hat{\mathbf{u}}_2]. \quad (3.12)$$

Ref. [6] proves non-uniqueness of the solution $\hat{\mathbf{u}}_1$, $\hat{\mathbf{u}}_2$ that maximizes Eq. 3.11. This holds because the solution can also be described by any other pair of vectors $\hat{\mathbf{v}}_1 \in \mathbb{S}^3$, $\hat{\mathbf{v}}_2 \in \mathbb{S}^3$ that satisfy $\hat{\mathbf{v}}_1^T \hat{\mathbf{v}}_2 = 0$ and $\hat{\mathbf{v}}_1, \hat{\mathbf{v}}_2 \in \mathbb{P}(\hat{\mathbf{u}}_1, \hat{\mathbf{u}}_2)$.

A particular solution to the plane-fitting problem can be obtained through Singular Value Decomposition (SVD) of $\bar{\mathbf{Z}} = \hat{\mathbf{U}}\hat{\mathbf{\Sigma}}\hat{\mathbf{U}}^T$, where $\hat{\mathbf{U}} \in \mathbb{R}^{4 \times 4} = [\hat{\mathbf{u}}_1 \ \hat{\mathbf{u}}_2 \ \hat{\mathbf{u}}_3 \ \hat{\mathbf{u}}_4]$ contains the *singular vectors* of $\bar{\mathbf{Z}}$, and $\hat{\mathbf{\Sigma}} = \text{diag}(\hat{\sigma}_1, \hat{\sigma}_2, \hat{\sigma}_3, \hat{\sigma}_4)$ contains the *singular values* of $\bar{\mathbf{Z}}$, wherein $\hat{\sigma}_1 \geq \hat{\sigma}_2 \geq \hat{\sigma}_3 \geq \hat{\sigma}_4 \geq 0$. If $\hat{\sigma}_2 > \hat{\sigma}_3$, then $\hat{\mathbf{u}}_1$ and $\hat{\mathbf{u}}_2$ compose a solution to the optimization problem in Eq. 3.11 and the optimal cost is given by $J^*(\hat{\mathbf{u}}_1, \hat{\mathbf{u}}_2) = \hat{\sigma}_1 + \hat{\sigma}_2$, with $\hat{\sigma}_1 = \hat{\mathbf{u}}_1^T \bar{\mathbf{Z}} \hat{\mathbf{u}}_1$ and $\hat{\sigma}_2 = \hat{\mathbf{u}}_2^T \bar{\mathbf{Z}} \hat{\mathbf{u}}_2$. It is also true that $\hat{\sigma}_3 = \hat{\mathbf{u}}_3^T \bar{\mathbf{Z}} \hat{\mathbf{u}}_3$ and $\hat{\sigma}_4 = \hat{\mathbf{u}}_4^T \bar{\mathbf{Z}} \hat{\mathbf{u}}_4$.

Having the optimal hyperplane estimate $\hat{\mathbb{P}}(\hat{\mathbf{u}}_1, \hat{\mathbf{u}}_2)$, the optimal estimate for the AOR is given by:

$$\hat{\omega} = \hat{\mathbf{u}}_2 \otimes \hat{\mathbf{u}}_1^{-1}. \quad (3.13)$$

The optimal quaternion estimates $\hat{\mathbf{q}}_i \in \mathbb{P}(\hat{\mathbf{u}}_1, \hat{\mathbf{u}}_2)$, $i \in \{k-n+1, \dots, k\}$ can be re-parameterized as just an angle on the plane $\mathbb{P}(\hat{\mathbf{u}}_1, \hat{\mathbf{u}}_2)$. Taking $\hat{\mathbf{u}}_1$ as a reference vector, the angle $\hat{\Phi}_i$ of any quaternion $\hat{\mathbf{q}}_i$ w.r.t. $\hat{\mathbf{u}}_1$ is given by:

$$\hat{\Phi}_i = 2 \cdot \text{atan2}(\hat{\mathbf{q}}_i^T \hat{\mathbf{u}}_2, \hat{\mathbf{q}}_i^T \hat{\mathbf{u}}_1), \quad i \in \{k-n+1, \dots, k\}. \quad (3.14)$$

Then, assuming the model:

$$\Phi_i = \Phi_0 + \Omega t_i = [1 \ t_i] \begin{bmatrix} \Phi_0 \\ \Omega \end{bmatrix}, \quad (3.15)$$

we can perform the least squares estimation:

$$\hat{\mathbf{X}} \triangleq \begin{bmatrix} \hat{\Phi}_0 \\ \hat{\Omega} \end{bmatrix} = (\mathbf{H}^T \mathbf{H})^{-1} \mathbf{H}^T \hat{\Phi}, \quad (3.16)$$

where:

$$\mathbf{H} \triangleq \begin{bmatrix} 1 & \cdots & 1 \\ t_{k-n+1} & \cdots & t_k \end{bmatrix}^T, \quad \hat{\Phi} \triangleq [\hat{\Phi}_{k-n+1} \quad \cdots \quad \hat{\Phi}_k]^T. \quad (3.17)$$

The estimated covariance matrix of $\hat{\mathbf{X}}$ is given by $\text{cov}[\hat{\mathbf{X}}] = \frac{1}{3}\sigma_\theta^2 (\mathbf{H}^T \mathbf{H})^{-1}$.

3.4 Consistency Test

Since QuateRA assume pure-spin motion, it is not suitable to be used as an angular velocity estimator for a tumbling (or an actuated) system. However, if the sampling frequency is high enough (or the tumbling rate is slow enough), then a sufficiently small sequence of orientation measurements can be approximated as close to pure spin for that sequence of measurements. AVast's objective is to determine the number of sequential orientation measurements that can be used by QuateRA in a way such that the measurements are progressing approximately as in pure spin motion. This can be attained through consistency tests, which is accomplished in this work through residual analysis [13, 19, 67].

Different possibilities can occur when the angular velocity of a body is changing:

1. Only the AVM is changing: as an example, this possibility can occur on a satellite that is in an elliptical orbit around a primary body, but is oriented with an axis that is always pointing towards the center of the primary.

2. Only the AOR is changing: this is an uncommon occurrence, but a controlled satellite could possibly be in a regime like this.
3. Both the AVM and the AOR are changing: can occur on a naturally-tumbling body (such as an asteroid) or on an actuated spacecraft.

AVAst needs to handle all cases above. To do that, it needs to determine if either the AVM or AOR is changing, or both. Remembering the measurement windows of length n at time t_k :

$$\bar{\mathbf{Q}}_{k,n} = [\bar{\mathbf{q}}_{k-n+1} \quad \bar{\mathbf{q}}_{k-n+2} \quad \cdots \quad \bar{\mathbf{q}}_k], \quad \hat{\Phi}_{k,n} = [\hat{\Phi}_{k-n+1} \quad \hat{\Phi}_{k-n+2} \quad \cdots \quad \hat{\Phi}_k]^T. \quad (3.18)$$

We implement AVAst such that $n_{min} \leq n \leq n_{max}$, where n_{max} is a user-specified upper bound on the window size, and $n_{min} \geq 3$ (we need at least two measurements to obtain a solution, and at least three to be able to perform a consistency test). If the measurement windows seem to be consistent, we allow the windows to increase ($n = n + 1$), and we decrease the window size otherwise ($n = n - 1$).

A straightforward consistency test (and the one exploited in Ref. [7]) is to test for residual autocorrelation. We define the Φ -residuals $\hat{\boldsymbol{\epsilon}} \triangleq \hat{\Phi} - \mathbf{H}\hat{\mathbf{X}}$ and the AOR residuals as the projection of the quaternion measurements onto the third singular vector $\hat{\mathbf{u}}_3$:

$$\hat{\epsilon}_i \triangleq \bar{\mathbf{q}}_i^T \hat{\mathbf{u}}_3, \quad i \in \{k-n+1, \dots, k\} \quad \implies \quad \hat{\boldsymbol{\epsilon}} \triangleq [\hat{\epsilon}_{k-n+1} \quad \cdots \quad \hat{\epsilon}_k]^T = \bar{\mathbf{Q}}_{k,n}^T \hat{\mathbf{u}}_3.$$

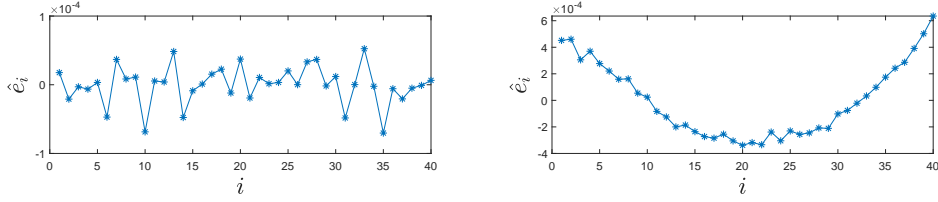


Figure 3.3: Residual plot for planar motion (left) and quaternion motion with out-of-plane component (right). The index i represents the subscript for $\hat{e}_i \triangleq \hat{\mathbf{q}}_i^T \hat{\mathbf{u}}_3$.

The covariace of a residual sequence ($\mathbf{P}_e \triangleq \mathbb{E}[\hat{\mathbf{e}}\hat{\mathbf{e}}^T]$ or $\mathbf{P}_\epsilon \triangleq \mathbb{E}[\hat{\epsilon}\hat{\epsilon}^T]$) is typically a non-diagonal matrix, implying that residuals are commonly auto-correlated sequences [19]. However, this correlation is generally unimportant (weakly autocorrelated), as discussed in Ref. [67, p. 171]. Figure 3.3 depicts a typical simulated scenario displaying the residual sequence \hat{e}_i , $i \in \{1, \dots, 40\}$ corresponding to the case when all quaternions within a window $\bar{\mathbf{Q}}_{k,n}$ of length $n = 40$ stem from planar motion measurements (left plot) and when they do not (right plot). Visually inspecting, the right-hand plot in Figure 3.3 is, qualitatively speaking, *more autocorrelated* than the plot on the left.

In order to quantify autocorrelation in a sequence $\hat{\mathbf{e}}$ (or $\hat{\epsilon}$), we use the following one-lag autocorrelation formulas [13, p. 31]:

$$r_e = \frac{1}{n \cdot r_{0e}} \sum_{i=k-n+1}^{k-1} (\hat{e}_i - \mu_e)(\hat{e}_{i+1} - \mu_e), \quad (3.19)$$

$$r_\epsilon = \frac{1}{n \cdot r_{0\epsilon}} \sum_{i=k-n+1}^{k-1} (\hat{\epsilon}_i - \mu_\epsilon)(\hat{\epsilon}_{i+1} - \mu_\epsilon), \quad (3.20)$$

where μ_e , μ_ϵ , r_{0e} and $r_{0\epsilon}$ are, the mean and zero-lag autocorrelation of the

residual sequences:

$$\begin{aligned} \mu_e &= \frac{1}{n} \sum_{i=k-n+1}^k \hat{e}_i, & r_{0e} &= \frac{1}{n} \sum_{i=k-n+1}^k (\hat{e}_i - \mu_e)^2, \\ \mu_\epsilon &= \frac{1}{n} \sum_{i=k-n+1}^k \hat{\epsilon}_i, & r_{0\epsilon} &= \frac{1}{n} \sum_{i=k-n+1}^k (\hat{\epsilon}_i - \mu_\epsilon)^2. \end{aligned} \quad (3.21)$$

The one-lag autocorrelation signals as defined in Eq. 3.19 satisfies $-1 \leq r_e \leq 1$ and $-1 \leq r_\epsilon \leq 1$, where the signal is one-lag perfectly correlated when $r_e \rightarrow 1$ or $r_\epsilon \rightarrow 1$, and is one-lag uncorrelated when $|r_e| \rightarrow 0$ or $r_\epsilon \rightarrow 0$. In addition, our experience suggests that one-lag autocorrelation of residuals are typically negative when the model fits the data (i.e., neighboring residuals tend to have opposite signs), while we expect positive autocorrelation when the model does not fit the data as in the right plot of Figure 3.3. For instance, the residuals in Figure 3.3 present one-lag autocorrelation of $r_e = -0.15$ (left plot) and $r_e = 0.8705$ (right plot).

In order to obtain confidence bounds on whether a sequence is auto-correlated, we need to estimate the autocorrelation covariance. To that end, we use the following expression [13, p. 188]:

$$\sigma_{r_e}^2 \triangleq \text{var}[r_e] = \frac{1}{n} (1 + 2r_e^2), \quad \sigma_{r_\epsilon}^2 \triangleq \text{var}[r_\epsilon] = \frac{1}{n} (1 + 2r_\epsilon^2). \quad (3.22)$$

The consistency test is made by performing the comparison of r_e (r_ϵ) with a tuning threshold r_e^* (r_ϵ^*). Whenever the motion is close to pure spin, i.e. $r_e < r_e^*$ ($r_\epsilon < r_\epsilon^*$), the consistency test is satisfied, otherwise whenever $r_e \geq r_e^*$ ($r_\epsilon \geq r_\epsilon^*$), the consistency test fails. Driven by extensive numerical simulations

of this algorithm, we found that a reasonable choice for the threshold is $r_e^* = \sigma_{re}$ ($r_\epsilon^* = \sigma_{r\epsilon}$), where σ_{re} and $\sigma_{r\epsilon}$ are defined in Eq. 3.22.

3.5 Simulation Results

In order to numerically test our proposed algorithm pipeline, we have developed a simulator that can obtain visual feed of a tumbling object⁵. The simulator is able to obtain rendered images in either monocular or stereo modes from 3D CAD models. The simulator is able to display the 3D model in any pose, as well as set the camera at any pose as well, allowing us to have a truth baseline. In addition, one can prescribe any desired values for the camera’s resolution, focal lengths, and stereo baseline. Figure 3.4 shows some examples of renderings that were obtained with the simulator using a 3D model⁶ for the Itokawa asteroid [56], assuming a camera with resolution of 720p. The images in Figure 3.4 (from left to right) display the asteroid with frontal light source, lateral light source, and a fading lateral light source (near eclipse).

In order to test AVAst as outlined in this paper, we set the Itokawa asteroid to tumble according with unperturbed attitude dynamics, assuming a normalized inertia matrix (inertia matrix divided by the asteroid’s mass) \mathbf{J}_I

⁵The simulator is open source and can be downloaded from https://github.com/marcelinomalmeidan/view_asteroid.

⁶<https://nasa3d.arc.nasa.gov/detail/itokawa>

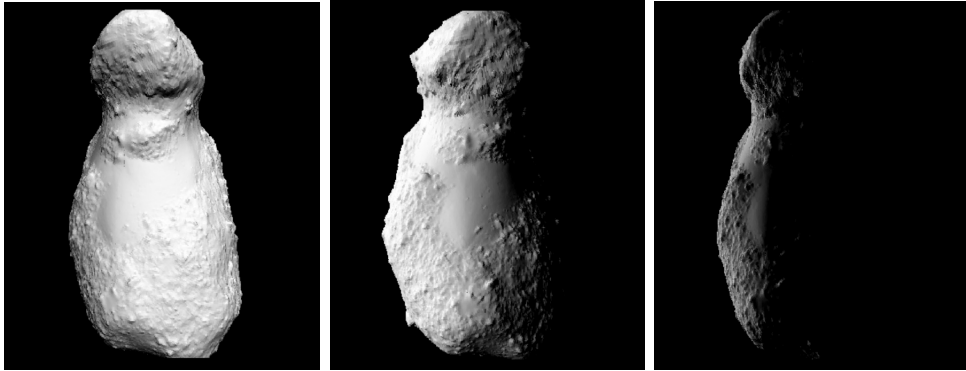


Figure 3.4: Itokawa rendering with different light sources.

given by Ref. 56:

$$\mathbf{J}_I = \begin{bmatrix} 0.00673 & 0 & 0 \\ 0 & 0.02122 & 0 \\ 0 & 0 & 0.02235 \end{bmatrix} \text{ km}^2. \quad (3.23)$$

We have simulated Itokawa’s attitude dynamics in different hypothetical tumbling and lighting conditions. Each experiment is recorded for 20 minutes and the camera pose is assumed stationary, without loss of generality. For each scenario, ORB-SLAM is executed to determine the relative pose of the camera with respect to the asteroid. An example of the camera’s relative trajectory w.r.t. the tumbling asteroid is shown in Figure 3.5-(left), while 3.5-(right) displays a sample of tracked Orb features in one frame. The ORB-SLAM algorithm is able to produce a sequence of relative poses at a rate of approximately 10Hz⁷, hence $\delta_k \approx 0.1\text{s}$. According with the data we’ve obtained, ORB-SLAM is able to produce orientation measurements with an

⁷These results were obtained in a computer with an Intel Core i5-4690K CPU (Quad Core 3.50GHz).

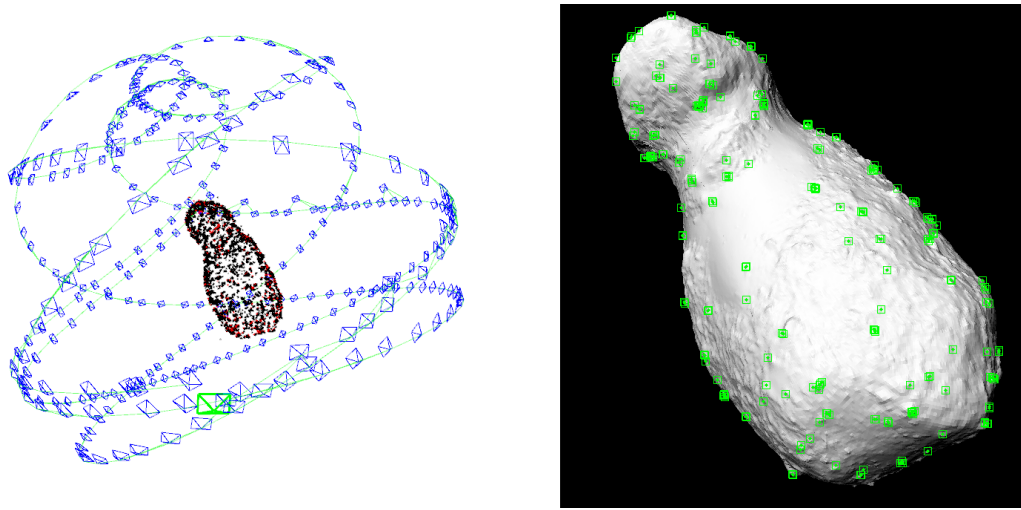


Figure 3.5: Left: History of the camera's pose with respect to the asteroid's fixed frame determined from running the ORB-SLAM algorithm. The red and black dots are features on the asteroid surface. Right: Example of features taken from one frame in the image plane.

approximate accuracy of $\sigma_\theta \approx 0.002\text{rad} = 412.5\text{arcsec}$. These orientation measurements are fed incrementally to AVAst algorithm to estimate the target's RAV. The algorithm parameters for all simulations were chosen as $n_{max} = 200$, and $r_1^* = \sigma_{r1}$ (as defined in Eq. 3.22).

Figure 3.6 shows the results for a simulation in which Itokawa's initial angular velocity is given by $\boldsymbol{\omega}(0) = [0.025, 0.01, 0.005]^T$. Figure 3.6(a) shows the sliding window length for $\hat{\mathbf{Q}}$, Figure 3.6(b) shows the angular velocity magnitude error, Figure 3.6(c) superimposes the true axis of rotation with the estimated one, and Figure 3.6(d) superimposes the true angular velocity with the estimated one. Figure 3.7 shows the results for a simulation with initial angular velocity $\boldsymbol{\omega}(0) = [0.01, 0.02, -0.005]^T$ (higher angular

velocity in the unstable axis of rotation), but with fading lateral light source (near eclipse - see Figure 3.4). We do not observe any algorithm performance degradation on these results when compared to the previous one, which had better lighting conditions.

We have also executed some simulations using a 3D model⁸ of the Cassini spacecraft (see Figure 3.8), assuming the inertia tensor [32]:

$$\mathbf{J}_c = \begin{bmatrix} 8810 & -136.8 & 115.3 \\ -136.8 & 7922.7 & 192.1 \\ 115.3 & 192.1 & 4586.2 \end{bmatrix} \quad (3.24)$$

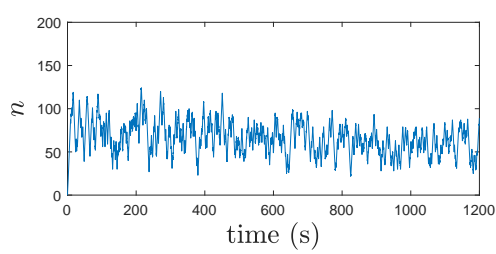
Figure 3.9 shows the results for a tumbling motion of Cassini with initial angular velocity $\boldsymbol{\omega}_2 \triangleq \boldsymbol{\omega}(0) = [0.01, 0.02, 0.005]^T$ (again, principal motion is around the unstable axis of rotation). Similarly, Figure 3.10 shows the results for a perturbed tumbling motion of Cassini, with perturbation given by:

$$\boldsymbol{\tau}^B(t) = 10 \cdot \begin{bmatrix} \sin(0.01t) \\ \sin(0.01t + \frac{2\pi}{3}) \\ \sin(0.01t + \frac{4\pi}{3}) \end{bmatrix} \quad (3.25)$$

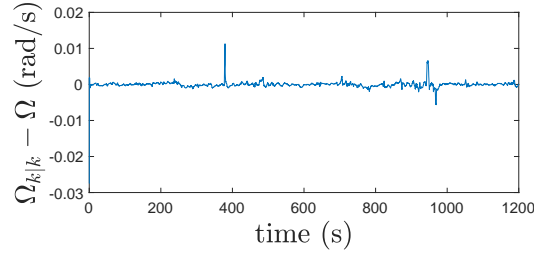
3.5.1 Metrics for Analysis of Simulation Results

The simulation results in Figures 3.6-3.10 show that AVAst is able to closely track the angular velocities of the non-cooperative targets. Here we make a performance evaluation of the algorithm performance for the different simulation situations.

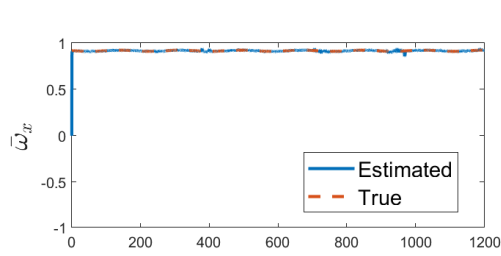
⁸<https://nasa3d.arc.nasa.gov/detail/jpl-vtad-cassini>



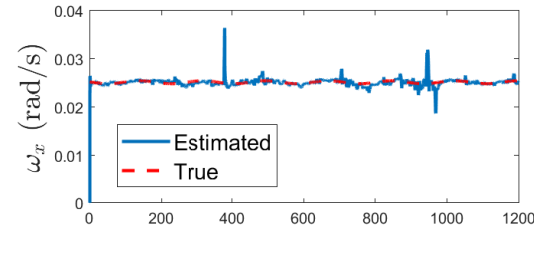
(a) Sliding Window Length



(b) Angular Velocity Magnitude Error



(c) Axis of Rotation



(d) Angular Velocity

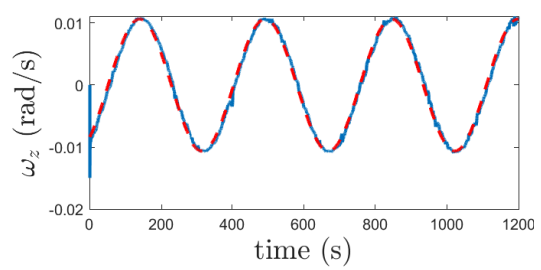
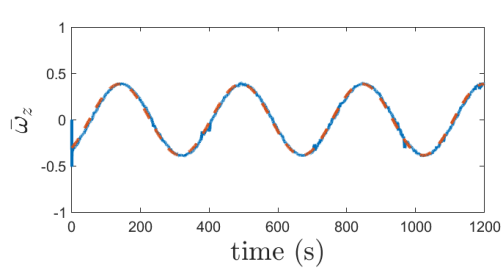
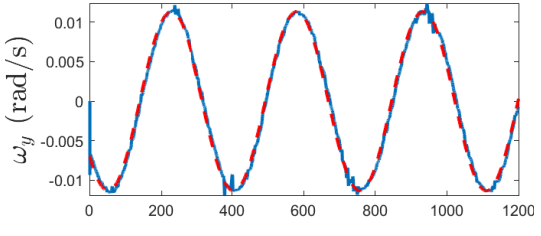
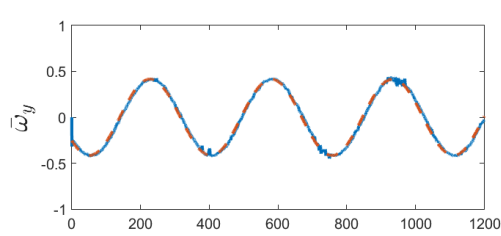
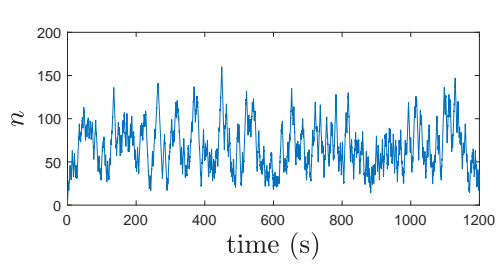
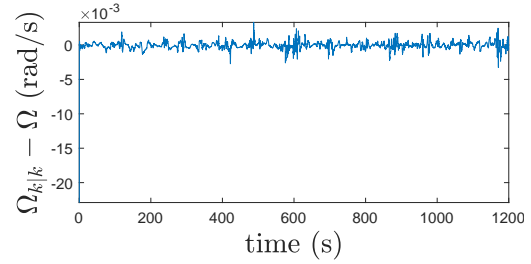


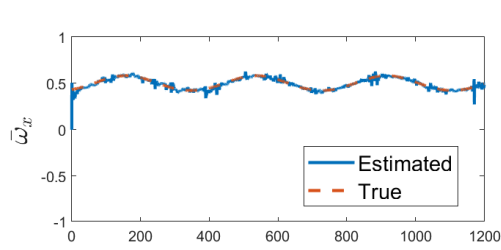
Figure 3.6: Simulation results for Itokawa's tumbling motion assuming initial angular velocity of $\boldsymbol{\omega}(0) = [0.025, 0.01, 0.005]^T$



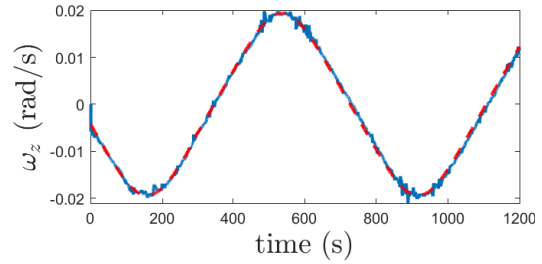
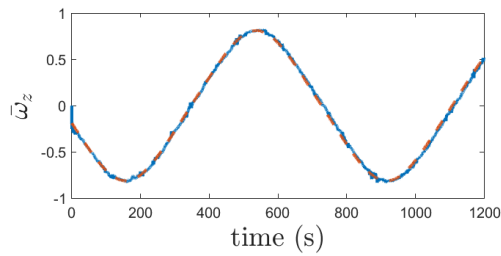
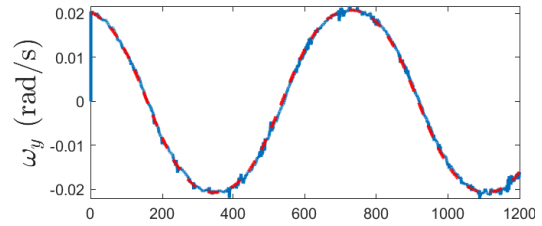
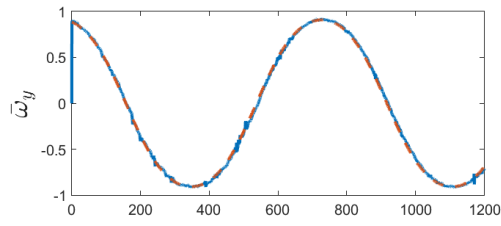
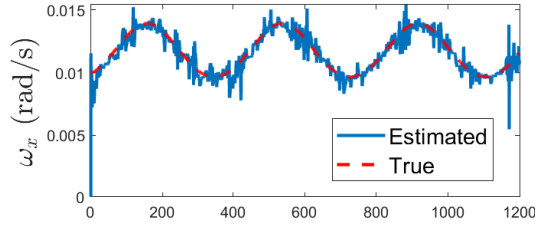
(a) Sliding Window Length



(b) Angular Velocity Magnitude Error



(c) Axis of Rotation



(d) Angular Velocity

Figure 3.7: Simulation results for Itokawa's tumbling motion with poor lighting conditions assuming initial angular velocity of $\boldsymbol{\omega}(0) = [0.01, 0.02, -0.005]^T$

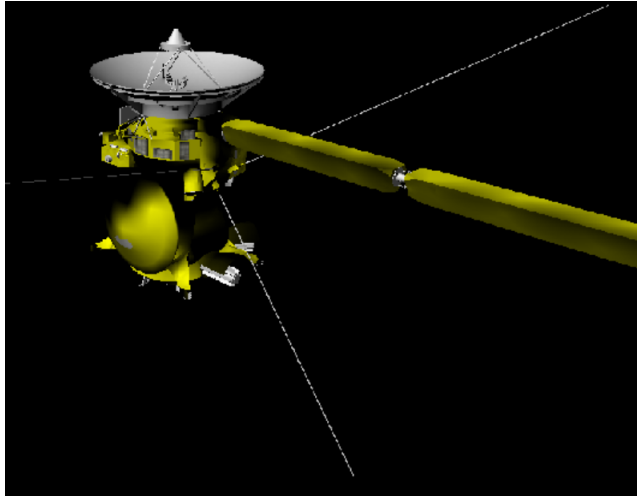


Figure 3.8: Simulated view of the Cassini spacecraft.

We define $\bar{\omega}_{ek} \triangleq \bar{\omega}_{k\perp}^T \hat{\omega}_k$ as the axis estimated pointing error for the angular velocity vector, where $\bar{\omega}_{k\perp}^T$ is any vector in the plane perpendicular to $\hat{\omega}_k^T$. Also, we define $\bar{e}_{\Omega k} \triangleq \Omega_k - \Omega_{k|k}$ as the AVM estimation error. The mean and standard deviation error metrics are computed as:

$$\bar{e}_{\bar{\omega}} = \frac{1}{N} \sum \bar{\omega}_{ek}, \quad (3.26)$$

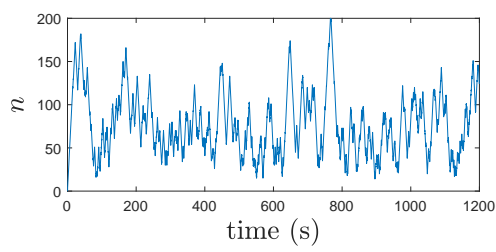
$$\sigma_{\bar{\omega}} = \frac{1}{N-1} \sum (\bar{\omega}_{ek} - \bar{e}_{\bar{\omega}})^2, \quad (3.27)$$

$$\bar{e}_{\Omega} \triangleq \frac{1}{N} \sum \bar{e}_{\Omega k}, \quad (3.28)$$

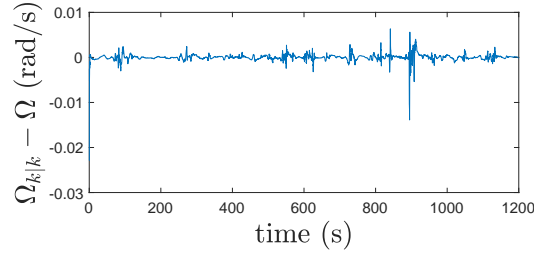
$$\sigma_{\Omega} \triangleq \frac{1}{N-1} \sum (\bar{e}_{\Omega k} - \bar{e}_{\Omega})^2, \quad (3.29)$$

where N is the number of measurements. Additionally, we define the mean window length as:

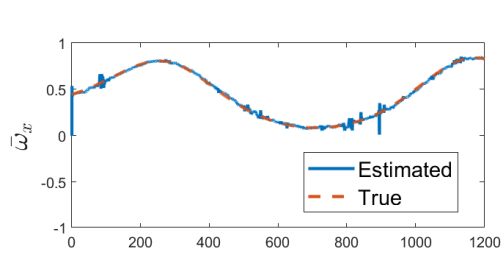
$$\mu_L \triangleq \frac{1}{N} \sum n_k, \quad (3.30)$$



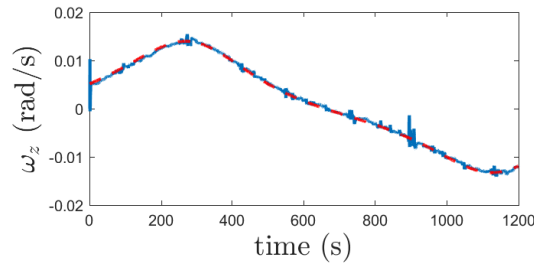
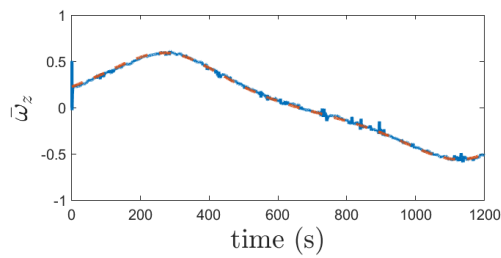
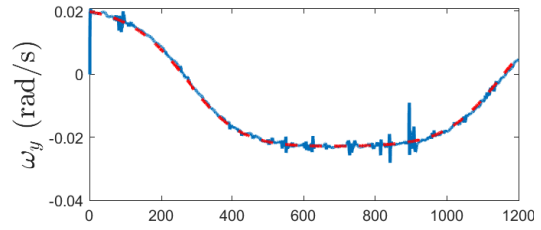
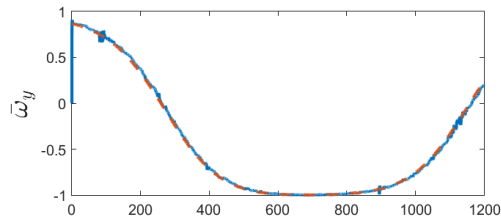
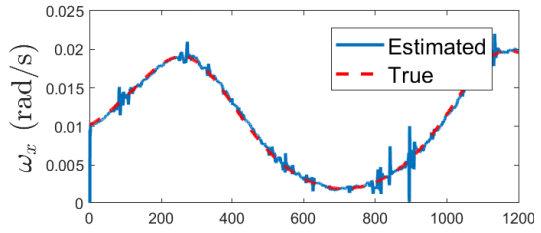
(a) Sliding Window Length



(b) Angular Velocity Magnitude Error

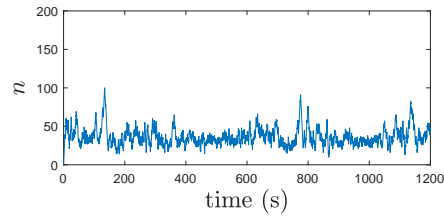


(c) Axis of Rotation

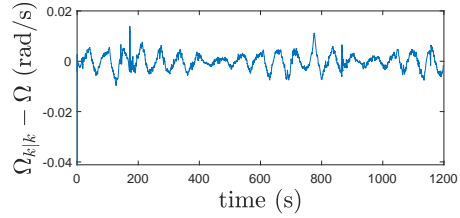


(d) Angular Velocity

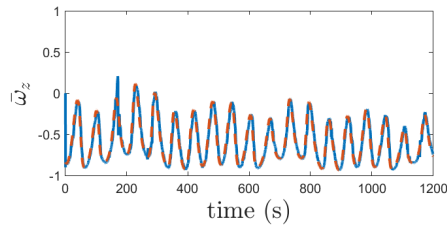
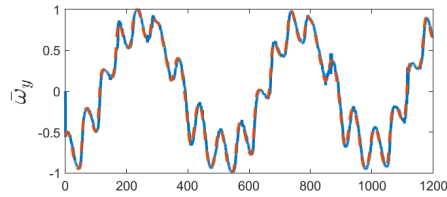
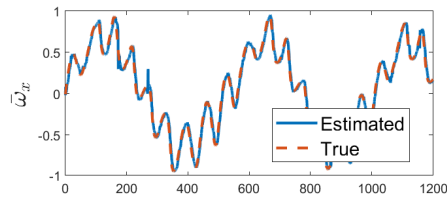
Figure 3.9: Simulation results for Cassini's tumbling motion assuming initial angular velocity of $\boldsymbol{\omega}(0) = [0.01, 0.02, 0.005]^T$



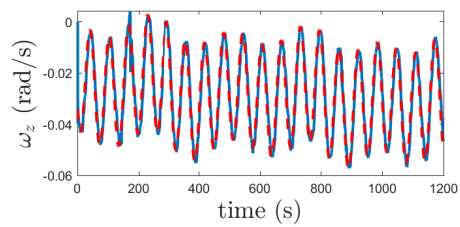
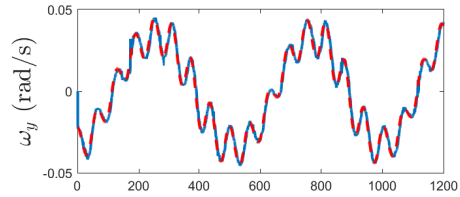
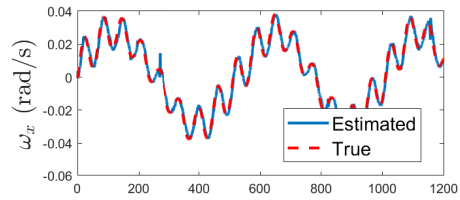
(a) Sliding Window Length



(b) Angular Velocity Magnitude Error



(c) Axis of Rotation



(d) Angular Velocity

Figure 3.10: Simulation results for Cassini's tumbling perturbed motion assuming initial angular velocity of $\boldsymbol{\omega}(0) = [0.0, -0.02, -0.035]^T$

where n_k is the window length of $\hat{\mathbf{Q}}_{k,n}$ at the $k - th$ iteration of the algorithm.

Using the definitions above, Table 3.1 presents a performance comparison among the various simulation results. All simulation results indicate nearly identical performance, except for the actuated Cassini case, which performed worse. This is expected, since all other simulations present only tumbling motions, while the last one had the spacecraft being actuated. This led to a quickly changing motion (see Fig. 3.10), which substantially reduced the average window length n . An immediate consequence of a reduced window length n is higher variance in the axis estimation error $\bar{\omega}_{ek}$, which can also be potentially biased. Since the angular velocity axis estimation performs worse, then it follows that the estimation of $\Omega_{k|k}$ also performs worse.

	Itokawa	Itokawa Dark	Cassini	Cassini Actuated
μ_L	66.75	67.74	76.16	36.59
$\bar{e}_{\bar{\omega}}$	$9.81 \cdot 10^{-5}$	$-1.34 \cdot 10^{-4}$	$-3.06 \cdot 10^{-4}$	$5.48 \cdot 10^{-4}$
$\sigma_{\bar{\omega}}$	$2.22 \cdot 10^{-2}$	$2.40 \cdot 10^{-2}$	$2.11 \cdot 10^{-2}$	$6.20 \cdot 10^{-2}$
\bar{e}_{Ω} (rad/s)	$-2.57 \cdot 10^{-5}$	$-5.38 \cdot 10^{-5}$	$1.19 \cdot 10^{-5}$	$-1.08 \cdot 10^{-4}$
σ_{Ω} (rad/s)	$8.50 \cdot 10^{-4}$	$5.89 \cdot 10^{-4}$	$8.21 \cdot 10^{-4}$	$3.2 \cdot 10^{-3}$

Table 3.1: Performance comparison for the multiple simulations.

It is important to point out that even though the Itokawa simulation with poor lighting conditions performed nearly on par with the simulation that used fair lighting conditions, one should not jump to conclusions that light source quality does not play an important role. Whereas the performance deterioration has not been captured in the simulated environment presented in this paper, one would need to further validate these results with carefully

conducted experiments using a real camera in a real space mission. An interesting avenue for further work would be to improve the camera model of the simulator to make it more realistic (i.e., add measurement noise, image blur, radiation noise).

The algorithm presented in this work has one tuning parameter, the autocorrelation threshold r_1^* . All our simulations were executed with $r_1^* = \sigma_{r1}$. Regarding this choice for r_1^* , we are satisfied with the given choice, and we believe that this is appropriate for the problem at hand. However, there could be other settings wherein one could desire to be less conservative by choosing $r_1^* = 2 \cdot \sigma_{r1}$ or $r_1^* = 3 \cdot \sigma_{r1}$. This would imply that the window length would only decrease when there is more evidence that the motion is not in pure spin. This leads to a higher average window size n , and consequently adds more lag to the estimation of $\bar{\omega}$ (not to mention having larger requirements for the memory buffer). Instead, we prefer to choose $r_1^* = \sigma_{r1}$ because this is a conservative choice, preventing the window from growing too much.

3.5.2 Algorithm Comparison

In order to compare AVAst with a traditional filtering method, we have extended the MEKF presented in Appendix A.4 by assuming a markov process as the propagation for the angular velocity [10, 48]:

$$\dot{\omega} = -\alpha\omega + \nu_\omega, \quad (3.31)$$

where α is an inverted time constant and ν_ω is assumed to be a zero-mean Gaussian process noise vector with covariance $\mathbb{E}[\nu_\omega \nu_\omega^T] = \sigma_\omega^2 \mathbf{I}$.

A drawback in using such a method is that that α and σ_ω are tuning knobs, and the use of such an algorithm involves tuning of those parameters for a given application (i.e., optimal choices for those parameters are application-dependent). We execute this extended MEKF within the same SLAM scenarios as the ones for which we used QuateRA. After some trial and error, we reached $\alpha = 0.1$ and $\sigma_\omega = 10^{-3}$ as reasonable values for those parameters.

Table 3.2 shows the performance of the MEKF using the same metrics as the ones described in Section 3.5.1. When compared with Table 3.1, we can see that the performance of both methods are reasonably similar. We point out, however, that AVast does not need any tuning, except for the simple parameter r_1^* , whereas the MEKF had to be tuned for the range of motions that we expect within the given simulations.

	Itokawa	Itokawa Dark	Cassini	Cassini Actuated
\bar{e}_ω	$1.12 \cdot 10^{-4}$	$-4.18 \cdot 10^{-4}$	$-3.20 \cdot 10^{-4}$	$-3.43 \cdot 10^{-4}$
σ_ω	$2.37 \cdot 10^{-2}$	$2.96 \cdot 10^{-2}$	$3.76 \cdot 10^{-2}$	$4.14 \cdot 10^{-2}$
\bar{e}_Ω (rad/s)	$1.32 \cdot 10^{-5}$	$-3.12 \cdot 10^{-5}$	$1.94 \cdot 10^{-5}$	$-2.52 \cdot 10^{-6}$
σ_Ω (rad/s)	$1.42 \cdot 10^{-3}$	$8.84 \cdot 10^{-4}$	$1.39 \cdot 10^{-3}$	$1.65 \cdot 10^{-3}$

Table 3.2: Performance comparison for the multiple simulations using linear Markov extension for the MEKF.

3.6 Conclusions

In this chapter, we have introduced and analyzed the performance of the AVast algorithm for the angular velocity of a non-cooperative target through visual inspection. The relative pose between the chaser and the target is

estimated using ORB-SLAM, and this information is used to get the relative angular velocity through QuateRA.

Simulation results demonstrate that the algorithm is successful in tracking the true angular velocity of the target without much need for tuning. The same tuning parameters were used throughout all the simulations, showing robustness of the algorithm to different scenarios. When compared with an application-tuned filter approach, AVAst compares similar to the presented method, with the advantage that AVAst does not require any fine tuning.

A surprising result that we had was that the algorithm did not perform differently when lighting conditions were not favorable. However, we believe that we need to improve our camera models to make it more realistic in order to have a more thorough analysis of the algorithm deterioration in the face of poor lighting conditions.

An interesting path of future work would be to use the proposed algorithm using real imagery from space missions such as the ones obtained by the Seeker spacecraft in future missions [49, 62]. Validation could be performed if Seeker estimates the angular velocity of a spacecraft that has its own gyroscopes.

Part II

Finite-time Attitude Controllers

Chapter 4

New Class of Attitude Controllers Guaranteed to Converge within Specified Finite-Time

4.1 Introduction

This chapter¹ introduces a finite-time feedback controller for fully actuated rigid-body attitude dynamics. We make use of Lyapunov’s Direct Method to design a feedback law that regulates the configuration from an arbitrary initial state to any final state within a desired finite transfer-time t_f . The control synthesis is explicit, i.e., given the transfer-time time t_f , the feedback-gains are explicitly calculated to satisfy the convergence specifications, even in the presence of bounded disturbances.

Several recent papers in literature address finite-time regulation problems for fully-controllable systems that are diffeomorphic to the so-called normal form representation. Some of these methods stem from non-smooth feedback, such as bang-bang [8], and/or sliding-mode controllers. These methods usually introduce discontinuous dynamics through feedback, which can lead

¹“Marcelino Almeida and Maruthi Akella. New class of attitude controllers guaranteed to converge within specified finite-time. *The Journal of the Astronautical Sciences*, pages 1-19, 2019.” (Marcelino Almeida conducted the problem formulation and solution, simulation and analyses, and wrote the paper.)

to chattering and excitation of undesired frequencies [59]. Other methods are built on top of the “Lyapunov differential inequality” [12], and many recent results stem from this methodology (see Ref. 60 and references therein). Whereas many of existing methods provide existence results for finite-time control algorithms, the explicit synthesis of such feedback schemes is far from being fully resolved, especially when applied to nonlinear systems such as the attitude control problem.

In this chapter, we introduce a feedback control law whose feedback gains are time-varying and grow unbounded towards the terminal time t_f . Although the notion of using unbounded feedback gains can be unsettling at a first glance, such an approach has certain strong theoretical underpinnings that are based upon variational calculus. Specifically, finite-horizon optimal control problems with terminal state constraints are known to produce unbounded feedback gains [14].

The major contributions of this chapter are as follows. Our formulation introduces a feedback structure that is closely related to Ref. 60. However, a major contrast is that our work does not seek to arbitrarily cancel out nonlinearities including those associated with the rotational kinematics. Thus, instead of resorting to the traditional approach of feedback-linearization, our approach utilizes the unbounded gains in conjunction with the logarithmic Lyapunov function presented by Ref. 64 for the attitude kinematics based on the Modified Rodrigues Parameters (MRPs) representation.

This chapter is structured along these following lines: Section 4.2

presents our control design for attitude stabilization around the origin, while Section 4.3 extends the result for trajectory tracking problems (such as slew maneuvers). Section 4.4 introduces some practical considerations for the implementation of the designed controller. Section 4.5 presents numerical simulation results and Section 4.6 summarizes the chapter by drawing some concluding remarks.

4.2 Control Design

Assume a rotation of an angle $\psi \in (-2\pi, 2\pi)$ around a unit-norm axis $\hat{e} \in \mathbb{R}^3$. The three-parameter MRP (Modified Rodrigues Parameters) representation $\boldsymbol{\sigma} \in \mathbb{R}^3$ for the same rotation is defined as:

$$\boldsymbol{\sigma} \triangleq \hat{e} \tan \frac{\psi}{4}. \quad (4.1)$$

The kinematics of MRPs [29] is given by

$$\dot{\boldsymbol{\sigma}}(t) = \frac{1}{4} \mathbf{B}(\boldsymbol{\sigma}(t)) \boldsymbol{\omega}(t), \quad (4.2)$$

where $\boldsymbol{\omega}(t) \in \mathbb{R}^3$ is the angular velocity expressed in a body-fixed frame, and

$$\mathbf{B}(\boldsymbol{\sigma}(t)) = (1 - \boldsymbol{\sigma}^T \boldsymbol{\sigma}) \mathbf{I}_3 + 2\boldsymbol{\sigma}^* + 2\boldsymbol{\sigma} \boldsymbol{\sigma}^T, \quad (4.3)$$

where we denote \mathbf{v}^* as the skew-symmetric matrix associated with a vector $\mathbf{v} \in \mathbb{R}^3$.

It should be noticed that the product $\boldsymbol{\sigma}^T \mathbf{B}(\boldsymbol{\sigma})$ satisfies the property:

$$\boldsymbol{\sigma}^T \mathbf{B}(\boldsymbol{\sigma}) = (1 - \boldsymbol{\sigma}^T \boldsymbol{\sigma}) \boldsymbol{\sigma}^T + 2\boldsymbol{\sigma}^T \boldsymbol{\sigma} \boldsymbol{\sigma}^T = (1 + \boldsymbol{\sigma}^T \boldsymbol{\sigma}) \boldsymbol{\sigma}^T = b(\boldsymbol{\sigma}) \boldsymbol{\sigma}^T, \quad (4.4)$$

where $b(\boldsymbol{\sigma}) \in \mathbb{R}_{\geq 1}$ is a scalar defined as $b(\boldsymbol{\sigma}) \triangleq (1 + \boldsymbol{\sigma}^T \boldsymbol{\sigma})$, and satisfies the property $2\|\boldsymbol{\sigma}\| \leq b(\boldsymbol{\sigma})$. In addition, the matrix $\mathbf{B}(\boldsymbol{\sigma})$ satisfies the norm property [55]:

$$\|\mathbf{B}(\boldsymbol{\sigma})\| = b(\boldsymbol{\sigma}). \quad (4.5)$$

The composition rule between the MRPs $\boldsymbol{\sigma}_1$ and $\boldsymbol{\sigma}_2$ is given by [58]:

$$\boldsymbol{\sigma}_3 \triangleq \boldsymbol{\sigma}_1 \otimes \boldsymbol{\sigma}_2 = \frac{(1 - \|\boldsymbol{\sigma}_1\|^2)\boldsymbol{\sigma}_2 + (1 - \|\boldsymbol{\sigma}_2\|^2)\boldsymbol{\sigma}_1 + 2\boldsymbol{\sigma}_2^* \boldsymbol{\sigma}_1}{1 + \|\boldsymbol{\sigma}_1\|^2 \|\boldsymbol{\sigma}_2\|^2 - 2\boldsymbol{\sigma}_1^T \boldsymbol{\sigma}_2}. \quad (4.6)$$

The direction cosine matrix associated with an MRP $\boldsymbol{\sigma}$ can be obtained by:

$$\mathbf{C}(\boldsymbol{\sigma}) = \mathbf{I} + \frac{8(\boldsymbol{\sigma}^*)^2 - 4(1 - \boldsymbol{\sigma}^T \boldsymbol{\sigma})\boldsymbol{\sigma}^*}{(1 + \boldsymbol{\sigma}^T \boldsymbol{\sigma})^2} \quad (4.7)$$

Defining the MRP inverse $\boldsymbol{\sigma}^{-1}$ as the parameterization for the rotation matrix $\mathbf{C}(\boldsymbol{\sigma}^{-1}) = \mathbf{C}^T(\boldsymbol{\sigma})$, then the relation between $\boldsymbol{\sigma}^{-1}$ and $\boldsymbol{\sigma}$ is given by:

$$\boldsymbol{\sigma}^{-1} = -\boldsymbol{\sigma}. \quad (4.8)$$

The body angular velocity $\boldsymbol{\omega}(t)$ evolves according with Euler's rotation equation:

$$\mathbf{J}\dot{\boldsymbol{\omega}}(t) = -\boldsymbol{\omega}^*(t)\mathbf{J}\boldsymbol{\omega}(t) + \mathbf{u}(t) + \mathbf{d}(t), \quad (4.9)$$

where $\mathbf{J} = \mathbf{J}^T > 0$ is the inertia tensor expressed in the body-fixed frame, $\mathbf{u}(t)$ is an input torque. The torque $\mathbf{d}(t)$ is an unknown bounded disturbance

torque, meaning that there exists $\bar{d} \in \mathbb{R}_{\geq 0}$ such that $\|d(t)\| \leq \bar{d}, \forall t \in [0, t_f)$.

We define \underline{J} and \bar{J} as the smallest and largest eigenvalues of \mathbf{J} , respectively.

The goal of this work is to find a control law $\mathbf{u}(t), t \in [0, t_f)$, such that $\boldsymbol{\sigma}(t_f) = \boldsymbol{\omega}(t_f) = 0$, for some specified final time $0 < t_f < \infty$, even in the presence of non-zero disturbance torques. We accomplish this through a backstepping design: first, we assume that $\boldsymbol{\omega}(t) = \boldsymbol{\omega}_r(t)$ is an “input” to Eq. 4.2. We find a Lyapunov candidate function that stabilizes the MRP in finite time (i.e., $\boldsymbol{\sigma}(t_f) = 0$) by applying the control law $\boldsymbol{\omega}_r(t), t \in [0, t_f)$. Then, we use $\boldsymbol{\omega}_r(t)$ to find a new control law \mathbf{u} that stabilizes both $\boldsymbol{\sigma}(t)$ and $\boldsymbol{\omega}(t)$.

Subsection 4.2.1 presents the procedure for stabilizing Eq. 4.2 assuming input $\boldsymbol{\omega}(t) = \boldsymbol{\omega}_r(t)$. Subsection 4.2.2 presents the backstepping formulation for designing the feedback law $\mathbf{u}(t)$ that stabilizes both Eqs. 4.2 and 4.9.

4.2.1 MRP Stabilization

Assume that $\boldsymbol{\omega}_r(t)$ is the input to

$$\dot{\boldsymbol{\sigma}}(t) = \frac{1}{4} \mathbf{B}(\boldsymbol{\sigma}(t)) \boldsymbol{\omega}_r(t), \quad t \in [0, t_f). \quad (4.10)$$

Next, define the function $\mu(t)$ as:

$$\mu(t) \triangleq \frac{t_f}{t_f - t}, \quad t \in [0, t_f). \quad (4.11)$$

One should note that $\mu(0) = 1, \mu(t) > 1, \forall t \in (0, t_f)$, and $\lim_{t \rightarrow t_f} \mu(t) = \infty$. In addition, the derivative of $\mu(t)$ with respect to time is given by:

$$\dot{\mu}(t) = \frac{t_f}{(t_f - t)^2} = \frac{1}{t_f} \left(\frac{t_f}{t_f - t} \right)^2 = \frac{1}{t_f} \mu^2(t), \quad t \in [0, t_f). \quad (4.12)$$

The integral of $\mu^2(t)$ with respect to time is given by:

$$\int_0^t \mu^2(\beta) d\beta = \frac{t_f^2}{t_f - t} \Big|_0^t = t_f \mu(t) \Big|_0^t = t_f(\mu(t) - 1) = t_f \bar{\mu}(t), \quad (4.13)$$

where $\bar{\mu}(t) \triangleq \mu(t) - 1$. The signal $\bar{\mu}(t)$ satisfies the properties $\bar{\mu}(0) = 0$, $\bar{\mu}(t) > 0, \forall t \in (0, t_f)$, $\lim_{t \rightarrow t_f} \bar{\mu}(t) = \infty$, and $\dot{\bar{\mu}}(t) = \dot{\mu}(t)$.

We define the following Lyapunov candidate function:

$$V_0(t) = \mu^\lambda(t) \ln(1 + \boldsymbol{\sigma}^T(t)\boldsymbol{\sigma}(t)), \quad t \in [0, t_f], \quad (4.14)$$

for some $\lambda \in \mathbb{R}_{>0}$. Clearly, $V_0(t) = 0 \iff \|\boldsymbol{\sigma}(t)\| = 0$, and $V_0(t) > 0, \forall t \in [0, t_f)$, if $\|\boldsymbol{\sigma}(t)\| \neq 0$.

The time derivative of Eq. 4.14 is given by:

$$\begin{aligned} \dot{V}_0(t) &= \frac{\partial V_0}{\partial \mu} \dot{\mu}(t) + \frac{\partial V_0}{\partial \boldsymbol{\sigma}} \dot{\boldsymbol{\sigma}}(t) \\ &= \lambda \mu^{\lambda-1} \dot{\mu}(t) \ln(1 + \boldsymbol{\sigma}^T(t)\boldsymbol{\sigma}(t)) + \frac{1}{4} \frac{\partial V_0}{\partial \boldsymbol{\sigma}} \mathbf{B}(\boldsymbol{\sigma}(t)) \boldsymbol{\omega}_r(t) \\ &= \frac{\lambda}{t_f} \mu^{\lambda+1}(t) \ln(1 + \boldsymbol{\sigma}^T(t)\boldsymbol{\sigma}(t)) + \frac{\mu^\lambda(t)}{2} \cdot \frac{\boldsymbol{\sigma}^T(t)}{1 + \boldsymbol{\sigma}^T(t)\boldsymbol{\sigma}(t)} \mathbf{B}(\boldsymbol{\sigma}(t)) \boldsymbol{\omega}_r(t) \\ &= \frac{\lambda}{t_f} \mu^{\lambda+1}(t) \ln(1 + \boldsymbol{\sigma}^T(t)\boldsymbol{\sigma}(t)) + \frac{\mu^\lambda(t)}{2} \cdot \frac{\boldsymbol{\sigma}^T(t) \mathbf{B}(\boldsymbol{\sigma}(t))}{1 + \boldsymbol{\sigma}^T(t)\boldsymbol{\sigma}(t)} \boldsymbol{\omega}_r(t). \end{aligned} \quad (4.15)$$

Using the property from Eq. 4.4 into Eq. 4.15 leads to:

$$\dot{V}_0(t) = \frac{\lambda}{t_f} \mu^{\lambda+1}(t) \ln(1 + \boldsymbol{\sigma}^T(t)\boldsymbol{\sigma}(t)) + \frac{\mu^\lambda(t)}{2} \boldsymbol{\sigma}^T(t) \boldsymbol{\omega}_r(t). \quad (4.16)$$

Since $\ln(1 + \eta) \leq \eta, \forall \eta \geq 0$, then:

$$\dot{V}_0(t) \leq \frac{\lambda}{t_f} \mu^{\lambda+1}(t) \boldsymbol{\sigma}^T(t)\boldsymbol{\sigma}(t) + \frac{\mu^\lambda(t)}{2} \boldsymbol{\sigma}^T(t) \boldsymbol{\omega}_r(t) \quad (4.17)$$

In addition, $\mu^{\lambda+1}(t)\boldsymbol{\sigma}^T(t)\boldsymbol{\sigma}(t) \leq \mu^{\lambda+2}(t)\boldsymbol{\sigma}^T(t)\boldsymbol{\sigma}(t)$, $t \in [0, t_f]$, leading to:

$$\begin{aligned}\dot{V}_0(t) &\leq \frac{\lambda}{t_f}\mu^{\lambda+2}(t)\boldsymbol{\sigma}^T(t)\boldsymbol{\sigma}(t) + \frac{\mu^\lambda(t)}{2}\boldsymbol{\sigma}^T(t)\boldsymbol{\omega}_r(t) \\ &= \mu^\lambda(t)\boldsymbol{\sigma}^T(t) \left(\frac{\lambda}{t_f}\mu^2(t)\boldsymbol{\sigma}(t) + \frac{1}{2}\boldsymbol{\omega}_r(t) \right)\end{aligned}\quad (4.18)$$

We can choose the control law:

$$\boldsymbol{\omega}_r(t) = -2 \left(\frac{\lambda}{t_f}\mu^2(t)\boldsymbol{\sigma}(t) + k\mu^2(t)\boldsymbol{\sigma}(t) \right) \quad (4.19)$$

$$= -2 \left(\frac{\lambda}{t_f} + k \right) \mu^2(t)\boldsymbol{\sigma}(t), \quad (4.20)$$

$$= -\phi\mu^2(t)\boldsymbol{\sigma}(t), \quad (4.21)$$

for some constant gain $k > 0$, $\phi \triangleq 2 \left(\frac{\lambda}{t_f} + k \right) > 0$ and $t \in [0, t_f]$, leading to:

$$\dot{V}_0(t) \leq -k\mu^{\lambda+2}(t)\boldsymbol{\sigma}^T(t)\boldsymbol{\sigma}(t). \quad (4.22)$$

Noticing again that $-\ln(1 + \eta) \geq -\eta$, $\forall \eta \geq 0$, then:

$$\begin{aligned}\dot{V}_0(t) &\leq -k\mu^{\lambda+2}(t) \ln(1 + \boldsymbol{\sigma}^T(t)\boldsymbol{\sigma}(t)) \\ &= -k\mu^2(t)V_0.\end{aligned}\quad (4.23)$$

Invoking the Comparison Lemma [31], we have that:

$$V_0(t) \leq V_0(0) \exp \left[-k \int_0^t \mu^2(\gamma) d\gamma \right]. \quad (4.24)$$

Using Eq. 4.13, we get:

$$\begin{aligned}V_0(t) &\leq V_0(0) \exp \left[-kt_f \cdot \bar{\mu}(t) \right] \\ \mu^\lambda(t) \ln(1 + \boldsymbol{\sigma}^T(t)\boldsymbol{\sigma}(t)) &\leq V_0(0) \exp \left[-kt_f \cdot \bar{\mu}(t) \right].\end{aligned}\quad (4.25)$$

Observing that $\lim_{t \rightarrow t_f} \exp[-kt_f \cdot \bar{\mu}(t)] = 0$, then:

$$\lim_{t \rightarrow t_f} V_0(t) \leq 0 \implies \lim_{t \rightarrow t_f} V_0(t) = 0 \implies \lim_{t \rightarrow t_f} \boldsymbol{\sigma}(t) = 0. \quad (4.26)$$

Therefore, if the control law in Eq. 4.21 is realizable (i.e. $\boldsymbol{\omega}_r \in L_\infty$), then we have finite time convergence of $\boldsymbol{\sigma}$ to the origin. Also, it is desirable that $\lim_{t \rightarrow t_f} \boldsymbol{\omega}_r(t) = 0$, which would imply that once the state $\boldsymbol{\sigma}$ reaches zero at $t = t_f$, it will remain there for $t > t_f$ (i.e., soft-landing).

Taking the two-norm of the control law from Eq. 4.21, we get that:

$$\|\boldsymbol{\omega}_r(t)\| = \phi \|\mu^2(t)\boldsymbol{\sigma}(t)\| \quad (4.27)$$

Therefore, it is sufficient to say that if the product $\mu^2\boldsymbol{\sigma} \in L_\infty$, then $\boldsymbol{\omega}_r \in L_\infty$, implying that the control law is realizable. Appendix A.3 proves that if Eq. 4.25 holds true, then $\mu^{\alpha_1}\boldsymbol{\sigma} \in L_\infty, \forall \alpha_1 \in \mathbb{R}$, implying that:

$$\exists \alpha_2 \in \mathbb{R} \text{ s.t. } \|\mu^{\alpha_1}(t)\boldsymbol{\sigma}(t)\| \leq \alpha_2, \forall t \in [0, t_f], \quad (4.28)$$

which leads to:

$$\|\mu^{\alpha_1-1}(t)\boldsymbol{\sigma}(t)\| \leq \frac{\alpha_2}{\mu(t)}, \forall t \in [0, t_f]. \quad (4.29)$$

Choosing $\alpha_1 = 3$, we have that:

$$\lim_{t \rightarrow t_f} \|\mu^2(t)\boldsymbol{\sigma}(t)\| \leq \lim_{t \rightarrow t_f} \frac{\alpha_2}{\mu(t)} = 0. \quad (4.30)$$

Therefore, from Eq. 4.27 we get that $\lim_{t \rightarrow t_f} \|\mu^2(t)\boldsymbol{\sigma}(t)\| = 0 \implies \lim_{t \rightarrow t_f} \|\boldsymbol{\omega}_r(t)\| = 0$.

4.2.2 Attitude Stabilization

In the previous subsection, the variable $\omega(t) = \omega_r(t)$ was assumed to be a control variable. Now, we employ a backstepping design to stabilize $\sigma(t)$ and $\omega(t)$ in finite time. The equations of motion are given by:

$$\begin{cases} \dot{\sigma}(t) = \mathbf{g}(\sigma)\omega(t) \\ \mathbf{J}\dot{\omega}(t) = -\omega^*(t)\mathbf{J}\omega(t) + \mathbf{u}(t) + \mathbf{d}(t) \end{cases}, \quad (4.31)$$

where $\mathbf{g}(\sigma) \triangleq \frac{1}{4}\mathbf{B}(\sigma(t))$, and $\mathbf{d}(t)$ is a bounded disturbance input with $\|\mathbf{d}(t)\| \leq \bar{d}$.

The goal is to design $\mathbf{u}(t)$ such that $\mathbf{u} \in L_\infty$ and $\lim_{t \rightarrow t_f} [\sigma(t), \omega(t)] = 0$.

We rewrite Eq. 4.2 as:

$$\begin{aligned} \dot{\sigma}(t) &= \mathbf{g}(\sigma)\omega(t) + \mathbf{g}(\sigma)\omega_r(t) - \mathbf{g}(\sigma)\omega_r(t) \\ &= \mathbf{g}(\sigma)\omega_r(t) + \mathbf{g}(\sigma)(\omega(t) - \omega_r(t)) \\ &= \mathbf{g}(\sigma)\omega_r(t) + \mathbf{g}(\sigma)\omega_e(t), \end{aligned} \quad (4.32)$$

where $\omega_e(t) \triangleq \omega(t) - \omega_r(t)$.

Then, we construct a new Lyapunov candidate function $V : [0, t_f) \rightarrow \mathbb{R}^+$:

$$\begin{aligned} V(t) &= V_0(t) + \frac{1}{2}\mu^4(t)\omega_e^T(t)\mathbf{J}\omega_e(t), \\ &= \mu^\lambda(t) \ln(1 + \sigma^T(t)\sigma(t)) + \frac{1}{2}\mu^4(t)\omega_e^T(t)\mathbf{J}\omega_e(t). \end{aligned} \quad (4.33)$$

The time derivative of Eq. 4.33 is given by:

$$\begin{aligned}
\dot{V}(t) &= \frac{\partial V_0}{\partial \boldsymbol{\mu}} \dot{\boldsymbol{\mu}}(t) + \frac{\partial V_0}{\partial \boldsymbol{\sigma}} \dot{\boldsymbol{\sigma}}(t) + 2\mu^3(t) \dot{\mu}(t) \boldsymbol{\omega}_e^T(t) \mathbf{J} \boldsymbol{\omega}_e(t) + \mu^4(t) \boldsymbol{\omega}_e^T(t) \mathbf{J} \dot{\boldsymbol{\omega}}_e \\
&= \frac{\partial V_0}{\partial \boldsymbol{\mu}} \dot{\boldsymbol{\mu}}(t) + \frac{\partial V_0}{\partial \boldsymbol{\sigma}} \mathbf{g}(\boldsymbol{\sigma}) \boldsymbol{\omega}_r(t) + \frac{\partial V_0}{\partial \boldsymbol{\sigma}} \mathbf{g}(\boldsymbol{\sigma}) \boldsymbol{\omega}_e(t) + \frac{2}{t_f} \mu^5(t) \boldsymbol{\omega}_e^T(t) \mathbf{J} \boldsymbol{\omega}_e(t) \\
&\quad + \mu^4(t) \boldsymbol{\omega}_e^T(t) [\mathbf{u}(t) + \mathbf{d}(t) - \boldsymbol{\omega}^*(t) \mathbf{J} \boldsymbol{\omega}(t) - \mathbf{J} \dot{\boldsymbol{\omega}}_r(t)].
\end{aligned}$$

From Eqs. 4.15-4.23 in the previous section, it follows that:

$$\frac{\partial V_0}{\partial \boldsymbol{\mu}} \dot{\boldsymbol{\mu}}(t) + \frac{\partial V_0}{\partial \boldsymbol{\sigma}} \mathbf{g}(\boldsymbol{\sigma}) \boldsymbol{\omega}_r(t) \leq -k\mu^2(t)V_0(t), \quad (4.34)$$

for some $k > 0$ and $\boldsymbol{\omega}_r(t)$ given by Eq. 4.21. Using Eq. 4.34 together with the property from Eq. 4.4, we get:

$$\begin{aligned}
\dot{V}(t) &\leq -k\mu^2(t)V_0(t) + \frac{\mu^\lambda(t)}{2} \boldsymbol{\sigma}^T(t) \boldsymbol{\omega}_e(t) + \frac{2}{t_f} \mu^5(t) \boldsymbol{\omega}_e^T(t) \mathbf{J} \boldsymbol{\omega}_e(t) \\
&\quad + \mu^4(t) \boldsymbol{\omega}_e^T(t) [\mathbf{u}(t) - \boldsymbol{\omega}^*(t) \mathbf{J} \boldsymbol{\omega}(t) - \mathbf{J} \dot{\boldsymbol{\omega}}_r(t)] + \mu^4(t) \boldsymbol{\omega}_e^T(t) \mathbf{d}(t).
\end{aligned}$$

Focusing on the disturbance term, we have that²:

$$\begin{aligned}
\mu^4(t) \boldsymbol{\omega}_e^T(t) \mathbf{d}(t) &= \mu^2(t) (\mu^2(t) \boldsymbol{\omega}_e^T(t)) \mathbf{d}(t) \\
&\leq \frac{1}{2} \mu^2(t) [\mu^4(t) \|\boldsymbol{\omega}_e(t)\|^2 + \|\mathbf{d}(t)\|^2] \\
&\leq \frac{1}{2} \mu^6(t) \|\boldsymbol{\omega}_e(t)\|^2 + \frac{1}{2} \mu^2(t) \bar{d}^2, \quad (4.35)
\end{aligned}$$

where \bar{d} is an upper bound on the disturbance $\|\mathbf{d}(t)\| \leq \bar{d}$.

²We use the property $\mathbf{a} \mathbf{b}^T \mathbf{c} \leq \frac{1}{2} (a^2 \|\mathbf{b}\|^2 + \|\mathbf{c}\|^2)$, $\forall a \in \mathbb{R}_{>0}, \mathbf{b} \in \mathbb{R}^n, \mathbf{c} \in \mathbb{R}^n, n \in \mathbb{Z}_{>0}$.

In addition, using the fact $\mu^5(t)\omega_e^T(t)\mathbf{J}\omega_e(t) \leq \mu^6(t)\omega_e^T(t)\mathbf{J}\omega_e(t)$, we get that:

$$\begin{aligned}\dot{V}(t) &\leq -k\mu^2(t)V_0(t) + \frac{\mu^\lambda(t)}{2}\boldsymbol{\sigma}^T(t)\omega_e(t) + \frac{2}{t_f}\mu^6(t)\omega_e^T(t)\mathbf{J}\omega_e(t) \\ &\quad + \mu^4(t)\omega_e^T(t) \left[\mathbf{u}(t) + \frac{\mu^2(t)}{2}\omega_e(t) - \omega^*(t)\mathbf{J}\omega(t) - \mathbf{J}\dot{\omega}_r(t) \right] + \frac{1}{2}\mu^2(t)\bar{d}^2 \\ &\leq -k\mu^2(t)V_0(t) + \frac{1}{2}\mu^2(t)\bar{d}^2 + \mu^4(t)\omega_e^T(t)\zeta(t),\end{aligned}\quad (4.36)$$

where:

$$\zeta(t) \triangleq \mathbf{u}(t) + \mu^2(t) \left(\frac{1}{2}\mathbf{I} + \frac{2}{t_f}\mathbf{J} \right) \omega_e(t) - \omega^*(t)\mathbf{J}\omega(t) - \mathbf{J}\dot{\omega}_r(t) + \frac{1}{2}\mu^{\lambda-4}(t)\boldsymbol{\sigma}(t).$$

We can choose the control law:

$$\begin{aligned}\mathbf{u}(t) &= - \left(\frac{1}{2}k\mathbf{J} + \frac{2}{t_f}\mathbf{J} + \frac{1}{2}\mathbf{I} \right) \mu^2(t)\omega_e(t) - \frac{1}{2}\mu^{\lambda-4}(t)\boldsymbol{\sigma}(t) \\ &\quad + \omega^*(t)\mathbf{J}\omega(t) + \mathbf{J}\dot{\omega}_r(t),\end{aligned}\quad (4.37)$$

where $\dot{\omega}_r(t)$ can be obtained by differentiating Eq. 4.21:

$$\begin{aligned}\dot{\omega}_r(t) &= -\phi\mu^2(t) \left[\frac{2}{t_f}\mu(t)\boldsymbol{\sigma}(t) + \mathbf{g}(\boldsymbol{\sigma})\omega(t) \right] \\ &= -\frac{2}{t_f}\phi\mu^3(t)\boldsymbol{\sigma}(t) - \phi\mathbf{g}(\boldsymbol{\sigma})\mu^2(t)\omega_e(t) - \phi\mathbf{g}(\boldsymbol{\sigma})\mu^2(t)\omega_r(t) \\ &= -\frac{2}{t_f}\phi\mu^3(t)\boldsymbol{\sigma}(t) - \phi\mathbf{g}(\boldsymbol{\sigma})\mu^2(t)\omega_e(t) + \phi^2\mathbf{g}(\boldsymbol{\sigma})\mu^4(t)\boldsymbol{\sigma}(t).\end{aligned}\quad (4.38)$$

Substituting Eq. 4.37 into Eq. 4.36 leads to:

$$\begin{aligned}\dot{V}(t) &\leq -k\mu^2(t)V_0(t) - \frac{1}{2}k\mu^6(t)\omega_e^T(t)\mathbf{J}\omega_e(t) + \frac{1}{2}\mu^2(t)\bar{d}^2 \\ &\leq -k\mu^2(t) \left(V_0(t) + \frac{1}{2}\mu^4(t)\omega_e^T(t)\mathbf{J}\omega_e(t) \right) + \frac{1}{2}\mu^2(t)\bar{d}^2 \\ &\leq -k\mu^2(t)V(t) + \frac{1}{2}\mu^2(t)\bar{d}^2.\end{aligned}\quad (4.39)$$

Once again, invoking the Comparison lemma leads to:

$$V(t) \leq \Phi(t, 0)V(0) + \Phi(t, 0) \int_0^t \Phi(0, \tau) \frac{1}{2} \mu^2(t) \bar{d}^2 d\tau, \quad (4.40)$$

where $\Phi(t_1, t_2) = \exp[-kt_f(\mu(t_1) - \mu(t_2))]$. Solving the integral in Eq. 4.40, we can show that:

$$V(t) \leq V(0) \exp[-kt_f \cdot \bar{\mu}(t)] + \frac{\bar{d}^2}{2k} (1 - \exp[-kt_f \cdot \bar{\mu}(t)]) \quad (4.41)$$

We provide the analysis for the disturbance free case in Section 4.2.2.1 and the analysis for the case with non-zero disturbance torques in Section 4.2.2.2. We demonstrate that the control objectives are reached in the disturbance-free case for any $\lambda > 0$, while we require $\lambda = 8$ to satisfy complete disturbance rejection at terminal time t_f .

4.2.2.1 Disturbance-Free Analysis

In the absence of disturbances, $\bar{d} = 0$ and the following holds:

$$V(t) \leq V(0) \exp[-kt_f \cdot \bar{\mu}(t)], \quad (4.42)$$

which implies:

$$\begin{cases} \frac{1}{2} \mu^4(t) \boldsymbol{\omega}_e^T(t) \mathbf{J} \boldsymbol{\omega}_e(t) \leq V(0) \exp[-kt_f \cdot \bar{\mu}(t)] \\ \mu^\lambda \ln(1 + \boldsymbol{\sigma}^T \boldsymbol{\sigma}) \leq V(0) \exp[-kt_f \cdot \bar{\mu}(t)] \end{cases}. \quad (4.43)$$

We also have that:

$$\lim_{t \rightarrow t_f} V(t) \leq 0 \implies \lim_{t \rightarrow t_f} V(t) = 0 \implies \begin{cases} \lim_{t \rightarrow t_f} \|\mu^2(t) \boldsymbol{\omega}_e(t)\|^2 = 0 \\ \lim_{t \rightarrow t_f} \|\boldsymbol{\sigma}(t)\|^2 = 0 \end{cases}. \quad (4.44)$$

Since $\lim_{t \rightarrow t_f} \boldsymbol{\omega}_e(t) = 0$ and $\lim_{t \rightarrow t_f} \boldsymbol{\omega}_r(t) = 0$ (See Eqs. 4.27 and 4.30), then $\lim_{t \rightarrow t_f} \boldsymbol{\omega}(t) = 0$. Also, the right-hand side of Eq. 4.41 is a bounded function, for $t \in [0, t_f)$, implying that:

$$V \in L_\infty \implies \boldsymbol{\omega}_e \in L_\infty \implies \boldsymbol{\omega} \in L_\infty, \quad (4.45)$$

where the last implication above holds true given that $\boldsymbol{\omega}_r = -\phi\mu^2\boldsymbol{\sigma} \in L_\infty$ (See Appendix A.3).

We need to ensure that the control torque $\mathbf{u}(t)$ is bounded. According with Eqs. 4.43 and 4.44, $\mu^2\boldsymbol{\omega}_e \in L_\infty$, $\boldsymbol{\sigma} \in L_\infty$, $\lim_{t \rightarrow t_f} \|\mu^2(t)\boldsymbol{\omega}_e(t)\| = 0$, and $\lim_{t \rightarrow t_f} \|\boldsymbol{\sigma}(t)\| = 0$. Given that Eq. 4.43 holds, Appendix A shows that $\mu^3\boldsymbol{\sigma} \in L_\infty$, $\lim_{t \rightarrow t_f} \|\mu^3(t)\boldsymbol{\sigma}(t)\| = 0$, $\mu^4\boldsymbol{\sigma} \in L_\infty$, $\lim_{t \rightarrow t_f} \|\mu^4(t)\boldsymbol{\sigma}(t)\| = 0$. Since $\boldsymbol{\sigma} \in L_\infty$, then $\mathbf{g}(\boldsymbol{\sigma}) \in L_\infty$.

Therefore, $\mathbf{u}(t)$ is composed as a sum of bounded signals, which implies that $\mathbf{u} \in L_\infty$. In addition, since $\lim_{t \rightarrow t_f} \|\mu^2(t)\boldsymbol{\omega}_e(t)\| = 0$, $\lim_{t \rightarrow t_f} \|\boldsymbol{\sigma}(t)\| = 0$, $\lim_{t \rightarrow t_f} \|\mu^3(t)\boldsymbol{\sigma}(t)\| = 0$ and $\lim_{t \rightarrow t_f} \|\mu^4(t)\boldsymbol{\sigma}(t)\| = 0$, then $\lim_{t \rightarrow t_f} \mathbf{u}(t) = \mathbf{0}$.

4.2.2.2 Disturbance Analysis

Eq. 4.41 can be upper bounded as:

$$V(t) \leq V(0) + \frac{\bar{d}^2}{2k}. \quad (4.46)$$

Defining the constant $\bar{V} \triangleq V(0) + \frac{\bar{d}^2}{2k}$, it follows that:

$$\mu^\lambda(t) \ln(1 + \boldsymbol{\sigma}^T(t)\boldsymbol{\sigma}(t)) \leq \bar{V} \quad (4.47)$$

$$\frac{1}{2}\mu^4(t)\boldsymbol{\omega}_e^T(t)\mathbf{J}\boldsymbol{\omega}_e(t) \leq \bar{V}. \quad (4.48)$$

Starting from Eq. 4.47, it is possible to show that $\mu^{\lambda/2}\boldsymbol{\sigma} \in L_\infty$ and that $\lim_{t \rightarrow t_f} \mu^\rho(t)\boldsymbol{\sigma}(t) = 0, \forall \rho < \lambda/2$ (See Appendix B.2), which implies that $\lim_{t \rightarrow t_f} \boldsymbol{\sigma}(t) = 0$, if $\lambda > 0$.

Given that the control law of Eq. 4.37 is function of $\dot{\boldsymbol{\omega}}_r(t)$, which depends on $\mu^4(t)\boldsymbol{\sigma}(t)$ (see Eq. 4.38), then we need that $\lambda/2 \geq 4 \implies \lambda \geq 8$ to satisfy $\mu^4\boldsymbol{\sigma} \in L_\infty$. Additionally, the control law of Eq. 4.37 depends on $\mu^{\lambda-4}(t)\boldsymbol{\sigma}(t)$, implying that we need $\lambda - 4 \leq \lambda/2 \implies \lambda \leq 8$. Therefore, $\lambda = 8$ satisfies both $\mu^4\boldsymbol{\sigma} \in L_\infty$ and $\mu^{\lambda-4}\boldsymbol{\sigma} \in L_\infty$.

Eq. 4.48 implies that $\mu^2\boldsymbol{\omega}_e \in L_\infty$. Also, since $\boldsymbol{\omega}_e^T(t)\mathbf{J}\boldsymbol{\omega}_e(t) \leq \mu^{-4}(t)\bar{V}$, then $\lim_{t \rightarrow t_f} \boldsymbol{\omega}_e^T(t)\mathbf{J}\boldsymbol{\omega}_e(t) = 0 \implies \lim_{t \rightarrow t_f} \boldsymbol{\omega}_e(t) = 0$.

Given that $\lim_{t \rightarrow t_f} \boldsymbol{\omega}_e(t) = 0$ and $\lim_{t \rightarrow t_f} \boldsymbol{\omega}_r(t) = \lim_{t \rightarrow t_f} -\phi\mu^2(t)\boldsymbol{\sigma}(t) = 0$ (for $\lambda = 8$), then $\lim_{t \rightarrow t_f} \boldsymbol{\omega}(t) = \lim_{t \rightarrow t_f} \boldsymbol{\omega}_e(t) + \lim_{t \rightarrow t_f} \boldsymbol{\omega}_r(t) = 0$.

Therefore, by choosing $\lambda = 8$ we have that the control law of Eq. 4.37 is a sum of bounded terms, implying that $\mathbf{u} \in L_\infty$. In addition, $\lim_{t \rightarrow t_f} \boldsymbol{\sigma}(t) = 0$ and $\lim_{t \rightarrow t_f} \boldsymbol{\omega}(t) = 0$, accomplishing the desired control objectives. One should also note that there are no guarantees that $\lim_{t \rightarrow t_f} \mathbf{u}(t) = 0$, as is the case for the disturbance-free control.

4.3 Tracking Control

In the previous section, we developed a stabilizing controller that takes the system to the origin. In this section, we generalize the solution for tracking

a desired trajectory.

Assume a desired trajectory given by a desired orientation signal $\boldsymbol{\sigma}_d(t)$ and a desired angular velocity signal $\boldsymbol{\omega}_d(t)$. The objective is to reach the desired trajectory at time $t = t_f$, i.e., $\delta\boldsymbol{\sigma}(t_f) = 0$ and $\delta\boldsymbol{\omega}(t_f) = 0$, where $\delta\boldsymbol{\sigma}(t) \triangleq \boldsymbol{\sigma}(t) \otimes \boldsymbol{\sigma}_d^{-1}(t)$ is the reference attitude error and $\delta\boldsymbol{\omega}(t) \triangleq \boldsymbol{\omega}(t) - \mathbf{C}(\delta\boldsymbol{\sigma})\boldsymbol{\omega}_d(t)$ is the angular velocity error expressed in the true orientation's frame of reference. The matrix $\mathbf{C}(\delta\boldsymbol{\sigma})$ is the direction cosine matrix equivalent to the rotation $\delta\boldsymbol{\sigma}$ (see Eq. 4.7) and satisfies $\dot{\mathbf{C}}(\delta\boldsymbol{\sigma}) = -\delta\boldsymbol{\omega}^* \mathbf{C}(\delta\boldsymbol{\sigma})$. We assume that the quantities $\boldsymbol{\sigma}_d(t)$, $\boldsymbol{\omega}_d(t)$, and $\dot{\boldsymbol{\omega}}_d(t)$ are fully specified as part of the tracking control objective.

As in the previous section, we first assume that the error dynamics for $\delta\dot{\boldsymbol{\sigma}}(t)$ is driven by a signal $\delta\boldsymbol{\omega}_r(t)$ as follows:

$$\delta\dot{\boldsymbol{\sigma}}(t) = \mathbf{g}(\delta\boldsymbol{\sigma})\delta\boldsymbol{\omega}_r(t), \quad (4.49)$$

where $\mathbf{g}(\delta\boldsymbol{\sigma}) \triangleq \frac{1}{4}\mathbf{B}(\delta\boldsymbol{\sigma})$.

We can choose the control law

$$\delta\boldsymbol{\omega}_r(t) = -\phi\mu^2(t)\delta\boldsymbol{\sigma}(t), \quad (4.50)$$

which was already shown to lead to $\lim_{t \rightarrow t_f} \delta\boldsymbol{\sigma}(t) = 0$. Also, we've already proven that the control law given by Eq.4.50 is realizable and that $\lim_{t \rightarrow t_f} \delta\boldsymbol{\omega}_r(t) = 0$.

In order to control the tracking error dynamics, we need to stabilize

the equations of motion below:

$$\begin{cases} \delta\dot{\boldsymbol{\sigma}}(t) = \mathbf{g}(\delta\boldsymbol{\sigma})\delta\boldsymbol{\omega}(t) \\ \mathbf{J}\dot{\boldsymbol{\omega}}(t) = -\boldsymbol{\omega}^*(t)\mathbf{J}\boldsymbol{\omega}(t) + \mathbf{u}(t) + \mathbf{d}(t) \end{cases} \quad (4.51)$$

In order to achieve stability, we define the angular velocity error signal $\delta\boldsymbol{\omega}_e(t) \triangleq \delta\boldsymbol{\omega}(t) - \delta\boldsymbol{\omega}_r(t)$. The derivative of $\mathbf{J}\delta\boldsymbol{\omega}_e(t)$ is given by:

$$\begin{aligned} \mathbf{J}\delta\dot{\boldsymbol{\omega}}_e(t) &= \mathbf{J}\delta\dot{\boldsymbol{\omega}}(t) - \mathbf{J}\delta\dot{\boldsymbol{\omega}}_r(t) \\ &= \mathbf{J}\dot{\boldsymbol{\omega}}(t) - \mathbf{J}\dot{\mathbf{C}}(\delta\boldsymbol{\sigma})\boldsymbol{\omega}_d(t) - \mathbf{J}\mathbf{C}(\delta\boldsymbol{\sigma})\dot{\boldsymbol{\omega}}_d(t) - \mathbf{J}\delta\dot{\boldsymbol{\omega}}_r(t) \\ &= -\boldsymbol{\omega}^*(t)\mathbf{J}\boldsymbol{\omega}(t) + \mathbf{u}(t) + \mathbf{d}(t) + \mathbf{J}\delta\boldsymbol{\omega}^*(t)\mathbf{C}(\delta\boldsymbol{\sigma})\boldsymbol{\omega}_d(t) \\ &\quad - \mathbf{J}\mathbf{C}(\delta\boldsymbol{\sigma})\dot{\boldsymbol{\omega}}_d(t) - \mathbf{J}\delta\dot{\boldsymbol{\omega}}_r(t), \end{aligned} \quad (4.52)$$

where $\delta\dot{\boldsymbol{\omega}}_r(t)$ can be obtained by differentiating Eq. 4.50:

$$\delta\dot{\boldsymbol{\omega}}_r(t) = -\phi\mu^2(t) \left[\frac{2}{t_f}\mu(t)\delta\boldsymbol{\sigma}(t) + \mathbf{g}(\delta\boldsymbol{\sigma})\delta\boldsymbol{\omega}(t) \right]. \quad (4.53)$$

We choose the control law:

$$\begin{aligned} \mathbf{u}(t) &= -\left(\frac{1}{2}k\mathbf{J} + \frac{2}{t_f}\mathbf{J} + \frac{1}{2}\mathbf{I}\right)\mu^2(t)\delta\boldsymbol{\omega}_e(t) - \frac{1}{2}\mu^{\lambda-4}(t)\boldsymbol{\sigma}(t) + \boldsymbol{\omega}^*(t)\mathbf{J}\boldsymbol{\omega}(t) \\ &\quad + \mathbf{J}\dot{\boldsymbol{\omega}}_r(t) - \mathbf{J}\delta\boldsymbol{\omega}^*(t)\mathbf{C}(\delta\boldsymbol{\sigma})\boldsymbol{\omega}_d(t) + \mathbf{J}\mathbf{C}(\delta\boldsymbol{\sigma})\dot{\boldsymbol{\omega}}_d(t). \end{aligned} \quad (4.54)$$

Replicating the same analysis as in the stabilization case, it is possible to show that the tracking error converges to zero: $\lim_{t \rightarrow t_f} \delta\boldsymbol{\sigma}(t) = 0$ and $\lim_{t \rightarrow t_f} \delta\boldsymbol{\omega}(t) = 0$. In addition, it is possible to use the same arguments as before to show that the control law from Eq. 4.54 is realizable (both in the presence and absence of disturbances).

4.4 Practical Considerations

We have proven in the previous sections that the control laws Eqs. 4.37 and 4.54 are bounded even in the presence of disturbances. Still, there are some practical aspects that have to be considered when utilizing these controller designs.

An important matter that arises in any real implementation concerns the feedback control using noisy measurements. Assuming a measurement model with zero-mean additive noise, the designed control laws cannot be guaranteed to drive the system to the origin anymore. As t approaches t_f , $\mu(t)$ increases unboundedly and amplifies the measurement noise that is introduced into the system through Eqs. 4.37 or 4.54. Instead of being driven to the origin, the system states converge to a time-varying residual set whose extent changes as a function of $\mu(t)$.

A simple saturation heuristic that can be used to remedy the noise amplification is to bound $\mu(t)$ as follows:

$$\mu(t) = \begin{cases} \frac{t_f}{t_f - t}, & t \in [0, \kappa t_f) \\ \frac{t_f}{t_f - \kappa t_f}, & t \in [\kappa t_f, \infty) \end{cases}, \quad (4.55)$$

for some user-chosen $\kappa \in (0, 1)$. This heuristic avoids $\mu(t)$ from becoming unbounded and thereby eliminating the possibility of increasingly amplifying the measurement noise.

A judicious choice of κ in Eq. 4.55 depends on the measurement noise characteristics, as well as the final time t_f . As κ approaches 0, the risk is

that the system might not reach an acceptably small residual set within the prescribed finite time. Alternatively, as κ approaches 1, the noise amplification might be too high, demanding too much on the actuators. Therefore, a rational choice of κ would be one that caps the signal $\mu(t)$ as soon as the system reaches to within a small enough residual set.

In order to identify whether or not the system trajectories are within the residual set, one can perform a rigorous analysis to characterize the measure of the residual set as a function of noise variance, initial states and final time. Alternatively, our experience based on extensive numerical simulations of the control laws Eqs. 4.37 and 4.54 shows that it is possible to determine whether the system has reached the residual set by analyzing the Fast Fourier Transform (FFT) of the measured angular velocity ω ($\delta\omega$ for the tracking case) and identifying the instant when the high-frequencies (mostly noise) dominates the measured signal.

Finite-time (or even infinite time) convergence to the origin in the presence of noise is unattainable, given that the controller attempts to converge to a measured zero, which is not the true zero. Once the system states reach within a residual set, we cannot really claim that there is any advantage in using the control law from Eqs. 4.37 or 4.54 with respect to other works in the literature, including non-finite controllers. This means that one can run the finite-time controller until the system reaches the residual set, then switch to some other classical control law, such as a Proportional-Derivative controller [18, 64, 69] tuned with optimal feedback gains (minimizing actuation

energy or residual set measure).

4.5 Simulation Results

This section presents some simulation results for the designed control laws. In the absence of measurement noise, we show that the designed control laws drive the system to zero error as expected. Subsection 4.5.1 presents results for the control being applied in the absence of measurement noise, while Subsection 4.5.2 shows the results for the control law with noisy measurements. Our simulations are performed for final time $t_f = 30\text{s}$.

For all simulations, the initial orientation is given by a rotation of $\psi(0) = \pi$ around the axis $\hat{e}(0) = 1/\sqrt{3} [1, 1, 1]^T$, and the initial angular velocity is given by $\boldsymbol{\omega}(0) = [-0.03, 0.04, -0.05]^T$. The inertia matrix is given by:

$$\mathbf{J} = \begin{bmatrix} 95 & -0.69 & 0.18 \\ -0.69 & 190 & 0.12 \\ 0.18 & 0.12 & 142.5 \end{bmatrix} \quad (4.56)$$

4.5.1 Perfect measurements

This section presents simulation results for attitude stabilization using noise-free measurements. We are able to demonstrate that the system converges to arbitrary final configurations for arbitrary initial conditions. We implement $\mu(t)$ with saturation as in Eq. 4.55 with $\kappa = 0.995$, avoiding the singularity at $t = t_f$.

Figure 4.1 shows the result for the stabilization of the system to the

origin using the control law from Eq. 4.37. The plots on the left display the simulation outputs in a linear scale, whereas the plots on the right present the same outputs in logarithmic scale. Values below $2.20 \cdot 10^{-16}$ are considered zero and are not shown on the log plot. We can see that the system is being driven towards the origin increasingly faster until the machine zero is reached. Notice that the states ($\boldsymbol{\omega}(t)$ and $\boldsymbol{\sigma}(t)$) and the inputs ($\mathbf{u}(t)$) all converge to zero. The log plots fade after 20 seconds, but one should have in mind that this is the *double precision zero*, not the *mathematical zero*. The mathematical zero should only happen at exactly $t = t_f$ as per our proofs.

Figure 4.2 shows the result for the stabilization of a perturbed system to the origin using the control law from Eq. 4.37 with $\lambda = 8$. The disturbance is constant and given by $d(t) = [1, 1, 1]^T$. The angular velocity $\boldsymbol{\omega}(t)$ reaches zero before the terminal time, while $\|\boldsymbol{\sigma}(t_f)\| = 3.62 \cdot 10^{-12}$. In steady state, the input torque compensates the disturbance signal $\mathbf{u}(t) \rightarrow [-1, -1, -1]^T$.

Figure 4.3 shows a result for the stabilization of the system to a tumbling configuration, using the control law from Eq 4.54. The desired trajectory follows the differential equation:

$$\begin{cases} \dot{\boldsymbol{\sigma}}_d(t) = \mathbf{g}(\boldsymbol{\sigma}_d)\boldsymbol{\omega}_d(t) \\ \mathbf{J}\dot{\boldsymbol{\omega}}_d(t) = -\boldsymbol{\omega}_d^*(t)\mathbf{J}\boldsymbol{\omega}_d(t) \end{cases}, \quad (4.57)$$

with $\boldsymbol{\sigma}_d(0) = -1/\sqrt{3} [1, 1, 1]^T$, $\boldsymbol{\omega}_d(0) = [0.01, 0.01, 0.01]^T$. We can see that, for this scenario, the states of the error dynamics converge to “machine-zero” sometime after about 20s. The states ($\boldsymbol{\omega}(t)$ and $\boldsymbol{\sigma}(t)$) and the input torques $\mathbf{u}(t)$ all converge to zero.

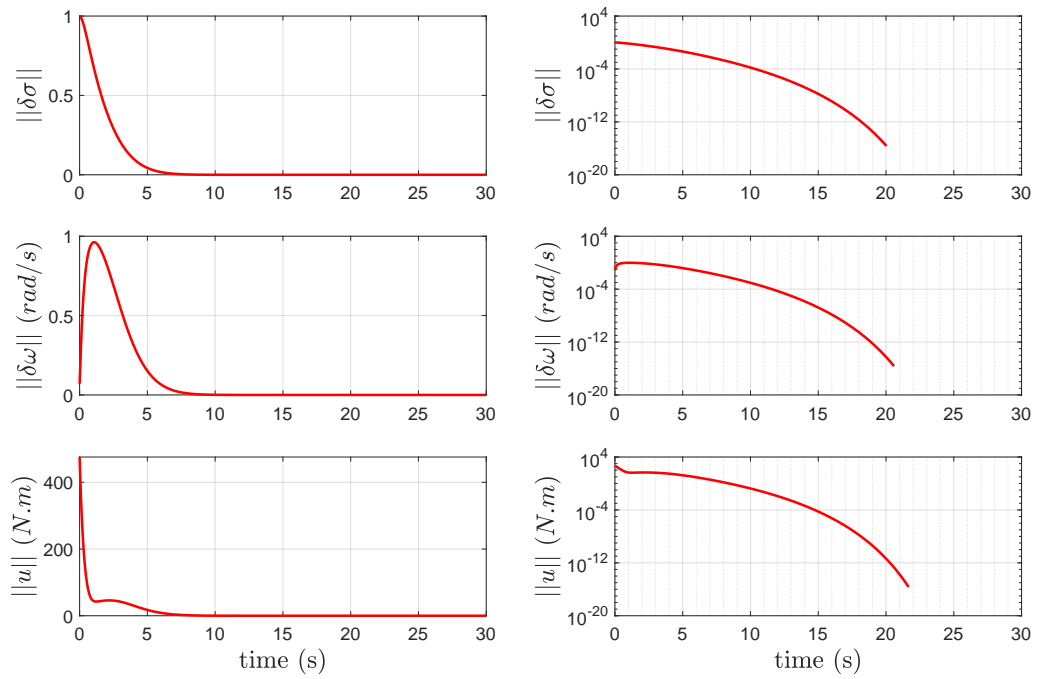


Figure 4.1: Time histories of state trajectories for the set-point regulation case with perfect measurements. The plots on the left display the simulation outputs in a linear scale, whereas the plots on the right present the same outputs in logarithmic scale.

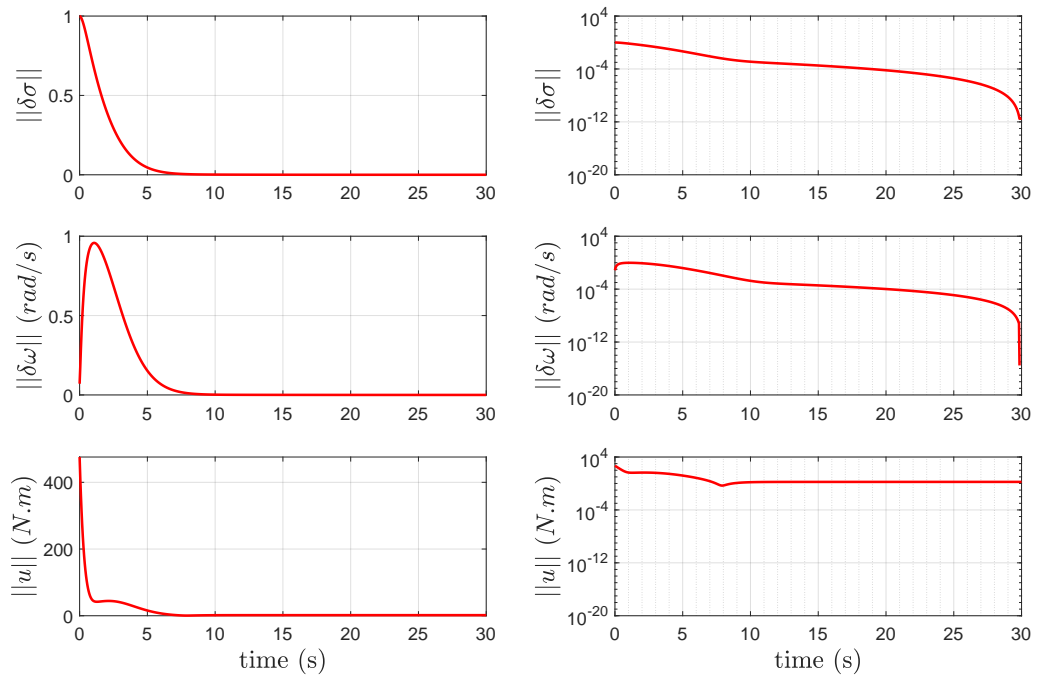


Figure 4.2: Time histories of state trajectories for the set-point regulation case with perfect measurements and applied disturbances. The plots on the left display the simulation outputs in a linear scale, whereas the plots on the right present the same outputs in logarithmic scale.

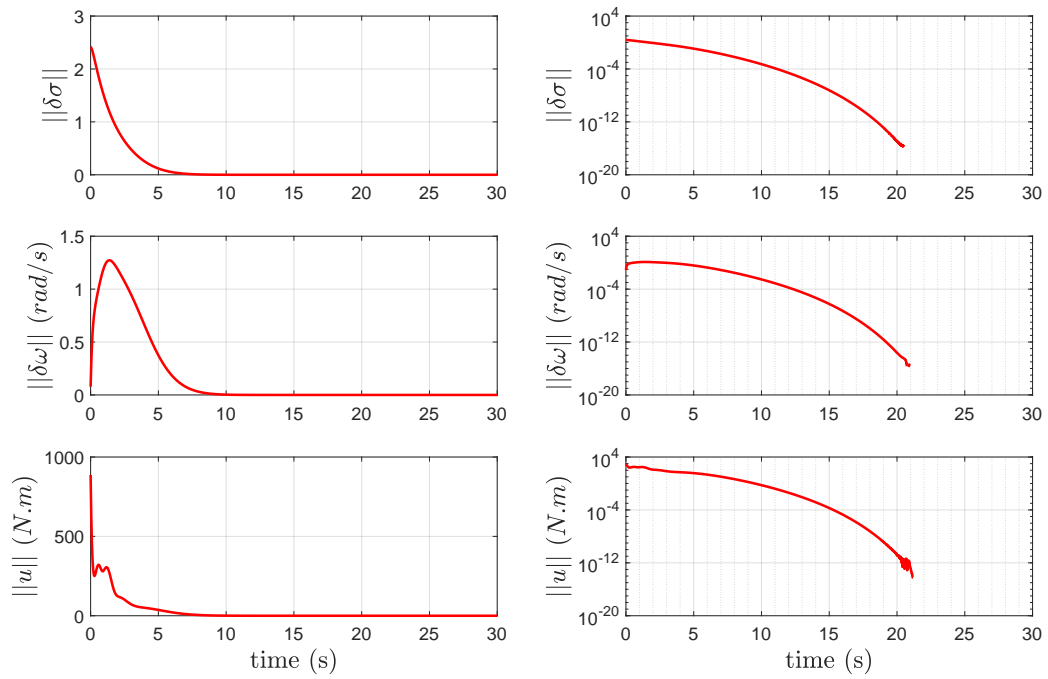


Figure 4.3: Time histories of state trajectory errors for the trajectory tracking case with perfect measurements. The plots on the left display the simulation outputs in a linear scale, whereas the plots on the right present the same outputs in logarithmic scale.

4.5.2 Noise corrupted measurements

In order to test the presented algorithm in presence of noise, we add measurement noise that is typical for a spacecraft with a star tracker, a gyroscope, and is executing an onboard state estimation algorithm. We assume that the state estimator is executing at a rate of 100Hz, and that it produces angular velocity measurements with standard deviation $\sigma_\omega = 0.002\text{rad/s}$ and attitude measurements with angular orientation error having standard deviation of $\sigma_\phi = 2\text{arcsec} = 9.7 \cdot 10^{-6}\text{rad}$ (in fact, commercial star tracker standard deviation is typically below 1.5arcsec [17]).

Figure 4.4 shows a result for the stabilization of the system to the origin using the two heuristics described in Section 4.4 for measurement noise accommodation. The blue plot implements $\mu(t)$ as in Eq. 4.55 with a fixed value of $\kappa = 0.85$ (Fixed Kappa Method - FKM). The red plot implements the FFT heuristic described in Section 4.4 by analyzing the FFT of $\|\omega\|$ over a window of 256 measurements, and tracking the instant at which frequencies above 10Hz dominate over frequencies below 10Hz.

We can see in the blue plot of Figure 4.4 that even though the state errors reach a residual set sometime after 13s, the controller gains keep increasing until $t = 25.5\text{s}$. Because of this, the FKM controller demands more control torque on average than the one using the FFT method, which capped the value of $\mu(t)$ at $t = 12.22\text{s}$. On average, the FKM results get to a narrower residual set for $\delta\sigma$ than the FFT results, but the residual set for $\delta\omega$ is larger in the FKM results than it is in the FFT one.

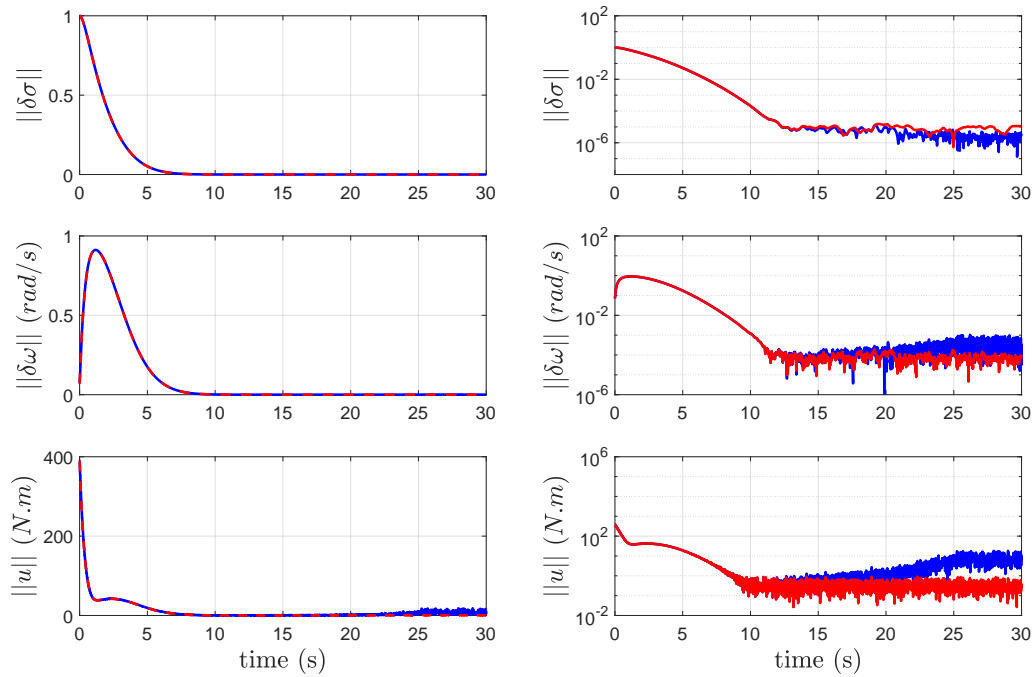


Figure 4.4: System convergence to the origin with noisy measurements. The blue plot shows the controller that caps $\mu(t)$ at $\kappa = 0.85$, while the red plot shows the controller that detects the switching time through the FFT method. The plots on the left display the simulation outputs in a linear scale, whereas the plots on the right present the same outputs in logarithmic scale.

4.6 Conclusion

In this paper, we have introduced a finite-time controller for fully-actuated rigid-body attitude dynamics. The feedback control law is established using Lyapunov’s direct method, regulating the system’s configuration from any arbitrary initial state to any final one within user-specified finite transfer time t_f even in the presence of disturbances. In order to achieve finite-time regulation, the feedback gain grows unbounded as time approaches t_f .

We have presented simulation results, demonstrating the efficacy of the controller in reaching the desired configuration within finite time. In presence of noise, the system trajectories are shown to converge within a residual set and we propose mechanisms to avoid unnecessary amplification of noise.

An interesting avenue for further work would be seeking the design of a finite-time controller for attitude dynamics without going through the backstepping process, as in the current work. An obvious downside of the backstepping design is that the designed control laws (Eqs. 4.37 and 4.54) are algebraically heavy due to the fact that they partially compensate for the “non-working” gyroscopic terms in the attitude dynamics equations (for example, the $\boldsymbol{\omega}^* \mathbf{J} \boldsymbol{\omega}$ term). On the other hand, the literature for asymptotic attitude stabilization (not finite-time) is abundant with control designs that can be obtained without gyroscopic compensation [64, 69].

Chapter 5

Time-varying feedback for attitude regulation in prescribed finite-time

5.1 Introduction

This chapter¹ introduces a finite-time feedback controller for stabilizing the attitude dynamics of a fully actuated rigid-body. The major novelty of this finite-time regulation control law is that it satisfies the self-reduction property, i.e., the feedback law is designed to be independent of the inertia properties of the rigid-body thereby providing stability robustness. We make use of a Lyapunov-like analysis to design this feedback law that regulates the configuration from an arbitrary initial state within a desired finite transfer-time t_f . The control synthesis is explicit, i.e., given the transfer-time time t_f , the feedback-gains are explicitly stated to satisfy the convergence specifications.

Many recent papers in literature address finite-time regulation problems for controllable systems that are diffeomorphic to the so-called normal form representation. Some of these methods derive from non-smooth feedback, such as bang-bang [8] and/or sliding-mode controllers. These methods usually introduce discontinuous dynamics through feedback, which can lead to chattering and excitation of undesired frequencies [59]. Other methods are built on top of the “Lyapunov differential inequality” [12], and many recent results stem from this methodology (see Ref. [60] and references therein). Whereas many of existing methods provide existence results for finite-time control algo-

¹“Marcelino Almeida and Maruthi Akella. Time-varying feedback for attitude regulation in prescribed finite-time. *2019 AAS/AIAA Astrodynamics Specialist Conference in Portland, ME*, (19-653), Aug. 2019.” (Marcelino Almeida conducted the problem formulation and solution, simulation and analyses, and wrote the paper.)

rithms, the explicit synthesis of such feedback schemes is far from being fully resolved, especially when applied to nonlinear systems such as the attitude control problem.

Within our recently reported prior work [2], we derived a control law for finite-time regulation on a fully actuated rigid-body attitude system. We used a backstepping control design to obtain the proposed control law, but the controller derived in that work requires compensation of the non-working terms within Euler's rotational dynamics equations, demanding precise knowledge of the rigid-body's inertia tensor. It is well known that asymptotic attitude stabilization does not need compensation of the rotational gyroscopic terms (i.e., the self-reduction property, see Refs. [64, 69]), motivating us to further pursue a finite-time stabilization feedback control law that does not require cancellation via feedback of the aforementioned terms.

This chapter circumvents the need for the backstepping design used in Ref. [2] by designing a new Lyapunov-like function that demonstrates finite-time stability of the system's attitude dynamics without resorting to cancellation of the non working terms in the Euler's rotational dynamic equations. We introduce a feedback control law whose feedback gains are time-varying and grow unbounded towards the terminal time t_f , while the feedback terms are function of the system's orientation (herein parameterized as the Modified Rodrigues Parameters - MRPs) and angular velocity. We prove that even though the feedback gains grow unbounded as t_f approaches, the product between these gains and the system's states is actually bounded, ensuring bounded

feedback torques. The major contribution of this chapter is to introduce the new control law, along with its respective finite-time stability analysis.

We present simulation results to demonstrate the efficacy of the proposed control law, highlighting the importance of the control gains in the transient trajectory of the controlled system.

Section 5.2 presents an outline for the stability analysis for the prescribed finite-time attitude stabilization feedback law. Section 5.3 presents numerical simulation results that validate the proposed method. Finally, Section 5.4 summarizes the current contribution by drawing some concluding remarks.

5.2 Control Design

The goal of this work is to find a feedback control law $\mathbf{u}(t)$, $t \in [0, t_f)$, such that $\boldsymbol{\sigma}(t_f) = \boldsymbol{\omega}(t_f) = 0$, for some specified final time $0 < t_f < \infty$. The proposed control law is time varying, with feedback gains growing unbounded as time approaches $t = t_f$. We make use of a storage function to prove that the proposed controller achieves the desired finite time stabilization, and that the control input is bounded for all time: $\mathbf{u}(t) \in L_\infty$, $t \in [0, t_f)$. Notation, kinematic and dynamic definitions used in the Chapter are introduced in Section 4.2.

This work makes extensive use of the time-varying function $\mu(t) \in \mathbb{R}_{\geq 1}$

as defined below:

$$\mu(t) \triangleq \frac{t_f}{t_f - t}, \quad t \in [0, t_f). \quad (5.1)$$

One should notice that $\mu(0) = 1$, $\mu(t) > 1, \forall t \in (0, t_f)$ and $\lim_{t \rightarrow t_f} \mu(t) = \infty$. Because $\mu(t) \geq 1$, it also holds that $\mu^\alpha(t) \leq \mu^\beta(t), \forall \alpha \leq \beta$.

The derivative of $\mu(t)$ is given by:

$$\dot{\mu}(t) = \frac{t_f}{(t_f - t)^2} = \frac{1}{t_f} \left(\frac{t_f}{t_f - t} \right)^2 = \frac{1}{t_f} \mu^2(t), \quad t \in [0, t_f). \quad (5.2)$$

Using the property of Eq. 5.2, we have that:

$$\frac{d}{dt} \mu^\alpha(t) = \alpha \mu^{\alpha-1}(t) \dot{\mu}(t) = \frac{\alpha}{t_f} \mu^{\alpha+1}(t). \quad (5.3)$$

The integral of $\mu^2(t)$ with respect to time is given by:

$$\int_{t_0}^t \mu^2(\beta) d\beta = \frac{t_f^2}{t_f - t} \Big|_{t_0}^t = t_f \mu(t) \Big|_{t_0}^t = F t_f (\mu(t) - \mu(t_0)) \quad (5.4)$$

5.2.1 Storage Function

This section defines the storage function used to derive finite-time stability for the attitude problem given the dynamics of Eqs. 4.2 and 4.9, and the control law:

$$\mathbf{u}(t) = -\frac{b(\boldsymbol{\sigma})}{\psi} (k_1 \mu^4(t) \boldsymbol{\sigma}(t) + k_2 \mu^2(t) \boldsymbol{\omega}(t)), \quad (5.5)$$

where $\psi > 0$, $k_1 > 0$, $k_2 > 0$ are constants.

We define the following quantities:

$$V_1 \triangleq 2\nu \mu^{\eta+4} \boldsymbol{\sigma}^T \boldsymbol{\sigma}, \quad V_2 \triangleq \frac{\psi}{2} \mu^\eta \boldsymbol{\omega}^T \mathbf{J} \boldsymbol{\omega}, \quad V_3 \triangleq \lambda \mu^{\eta+2} \boldsymbol{\sigma}^T \mathbf{J} \boldsymbol{\omega}, \quad (5.6)$$

where $\lambda > 0$ and $\nu > 0$ are constant values. The storage function $V \in \mathbb{R}_{\geq 0}$ is defined as $V = V_1 + V_2 + V_3$. In the absence of disturbances, the proofs in this paper actually works for any value of $\eta \in \mathbb{R}_{>0}$. However, we need $\eta \geq 4$ to accommodate disturbance rejection. The remainder of this chapter assumes $\eta = 4$:

$$V_1 = 2\nu\mu^8\boldsymbol{\sigma}^T\boldsymbol{\sigma}, \quad V_2 = \frac{\psi}{2}\mu^4\boldsymbol{\omega}^T\mathbf{J}\boldsymbol{\omega}, \quad V_3 = \lambda\mu^6\boldsymbol{\sigma}^T\mathbf{J}\boldsymbol{\omega}. \quad (5.7)$$

An upper bound on V can be derived as (notice that we use the property $2ab \leq a^2 + b^2$, for $a, b \in \mathbb{R}$):

$$\begin{aligned} V &= 2\nu\mu^8\|\boldsymbol{\sigma}\|^2 + \frac{\psi}{2}\mu^4\boldsymbol{\omega}^T\mathbf{J}\boldsymbol{\omega} + \lambda\mu^6\boldsymbol{\sigma}^T\mathbf{J}\boldsymbol{\omega} \\ &\leq 2\nu\mu^8\|\boldsymbol{\sigma}\|^2 + \frac{\psi}{2}\bar{J}\mu^4\|\boldsymbol{\omega}\|^2 + \lambda\bar{J}(\mu^4\|\boldsymbol{\sigma}\|)(\mu^2\|\boldsymbol{\omega}\|) \\ &\leq 2\nu\mu^8\|\boldsymbol{\sigma}\|^2 + \frac{\psi}{2}\bar{J}\mu^4\|\boldsymbol{\omega}\|^2 + \frac{\lambda\bar{J}}{2}\mu^8\|\boldsymbol{\sigma}\|^2 + \frac{\lambda\bar{J}}{2}\mu^4\|\boldsymbol{\omega}\|^2 \\ &= (2\nu + \frac{\lambda\bar{J}}{2})\mu^8\|\boldsymbol{\sigma}\|^2 + (\psi + \lambda)\frac{\bar{J}}{2}\mu^4\|\boldsymbol{\omega}\|^2 \\ &\leq \bar{\alpha}(\mu^8\|\boldsymbol{\sigma}\|^2 + \mu^4\|\boldsymbol{\omega}\|^2), \end{aligned} \quad (5.8)$$

where $\bar{\alpha} \triangleq \max(2\nu + \frac{\lambda\bar{J}}{2}, \frac{\psi}{2}\bar{J} + \frac{\lambda}{2}\bar{J})$.

Similarly, we can derive a lower bound on V :

$$\begin{aligned} V &= 2\nu\mu^8\|\boldsymbol{\sigma}\|^2 + \frac{\psi}{2}\mu^4\boldsymbol{\omega}^T\mathbf{J}\boldsymbol{\omega} + \lambda\mu^6\boldsymbol{\sigma}^T\mathbf{J}\boldsymbol{\omega} \\ &\geq 2\nu\mu^8\|\boldsymbol{\sigma}\|^2 + \frac{\psi\underline{J}}{2}\mu^4\|\boldsymbol{\omega}\|^2 - (\mu^4\lambda\underline{J}\|\boldsymbol{\sigma}\|)(\mu^2\|\boldsymbol{\omega}\|) \\ &\geq 2\nu\mu^8\|\boldsymbol{\sigma}\|^2 + \frac{\psi\underline{J}}{2}\mu^4\|\boldsymbol{\omega}\|^2 - \frac{\lambda\underline{J}}{2}(\mu^8\|\boldsymbol{\sigma}\|^2 + \mu^4\|\boldsymbol{\omega}\|^2) \\ &= (2\nu - \frac{\lambda}{2}\underline{J})\mu^8\|\boldsymbol{\sigma}\|^2 + (\frac{\psi}{2}\underline{J} - \frac{\lambda}{2}\underline{J})\mu^4\|\boldsymbol{\omega}\|^2 \\ &\geq \underline{\alpha}(\mu^8\|\boldsymbol{\sigma}\|^2 + \mu^4\|\boldsymbol{\omega}\|^2), \end{aligned} \quad (5.9)$$

where $\underline{\alpha} \triangleq \min \left(2\nu - \frac{\lambda\bar{J}}{2}, \frac{\psi}{2}\underline{J} - \frac{\lambda}{2}\bar{J} \right)$.

The following conditions ensure positive definiteness of V :

$$\nu > 0, \quad \psi > 0, \quad \nu > \frac{\lambda\bar{J}}{4}, \quad \frac{\psi}{\lambda} > \frac{\bar{J}}{\underline{J}}. \quad (5.10)$$

Defining the ratio $\frac{\psi}{\lambda} = \beta \frac{\bar{J}}{\underline{J}}$, for some $\beta > 1$, then the last condition in Eq. 5.10 is satisfied. In addition, we have that $\lambda = \frac{J\psi}{\beta\bar{J}}$, leading to the following condition on ν :

$$\frac{\nu}{\psi} > \frac{J}{\beta}. \quad (5.11)$$

5.2.2 Finite Time Proof

This section proves that the system of Eqs. 4.2 and 4.9 stabilizes in finite time by using the controller of Eq. 5.5. We explicitly define $\nu \triangleq k_1 + \frac{\lambda k_2}{\psi}$. First, we take time-derivatives on V_1 :

$$\begin{aligned} \dot{V}_1 &= \frac{16\nu}{t_f} \mu^9 \boldsymbol{\sigma}^T \boldsymbol{\sigma} + 4\nu \mu^8 \boldsymbol{\sigma}^T \dot{\boldsymbol{\sigma}} = \frac{16\nu}{t_f} \mu^9 \|\boldsymbol{\sigma}\|^2 + \nu \mu^8 \boldsymbol{\sigma}^T \mathbf{B}(\boldsymbol{\sigma}) \boldsymbol{\omega} \\ &= \frac{16\nu}{t_f} \mu^9 \|\boldsymbol{\sigma}\|^2 + \left(k_1 + \frac{\lambda k_2}{\psi} \right) \mu^8 b(\boldsymbol{\sigma}) \boldsymbol{\sigma}^T \boldsymbol{\omega}. \end{aligned} \quad (5.12)$$

Now, taking derivative of V_2 :

$$\begin{aligned} \dot{V}_2 &= \frac{2\psi}{t_f} \mu^5 \boldsymbol{\omega}^T \mathbf{J} \boldsymbol{\omega} + \psi \mu^4 \boldsymbol{\omega}^T (-\boldsymbol{\omega}^* \mathbf{J} \boldsymbol{\omega} + \mathbf{u} + \mathbf{d}) \\ &\leq \frac{2\psi\bar{J}}{t_f} \mu^5 \|\boldsymbol{\omega}\|^2 + \psi \mu^4 \boldsymbol{\omega}^T \mathbf{u} + \psi (\delta \mu^3 \boldsymbol{\omega}^T) \left(\frac{1}{\delta} \mu \mathbf{d} \right) \\ &\leq \frac{2\psi\bar{J}}{t_f} \mu^5 \|\boldsymbol{\omega}\|^2 + \psi \mu^4 \boldsymbol{\omega}^T \mathbf{u} + \frac{\psi \delta^2}{2} \mu^6 \|\boldsymbol{\omega}\|^2 + \frac{\psi}{2\delta^2} \mu^2 \bar{d}^2, \end{aligned} \quad (5.13)$$

where $\delta > 0$ is a constant scalar.

Combining \dot{V}_1 with \dot{V}_2 , the control law of Eq. 5.5, and the definition $\nu \triangleq k_1 + \frac{\lambda k_2}{\psi}$, we get:

$$\begin{aligned}
\dot{V}_1 + \dot{V}_2 &\leq \frac{16\nu}{t_f} \mu^9 \|\boldsymbol{\sigma}\|^2 + \frac{2\psi\bar{J}}{t_f} \mu^5 \|\boldsymbol{\omega}\|^2 + \left(\cancel{k_1} + \frac{\lambda k_2}{\psi} \right) \mu^8 b(\boldsymbol{\sigma}) \boldsymbol{\sigma}^T \boldsymbol{\omega} \\
&\quad - \mu^4 b(\boldsymbol{\sigma}) \boldsymbol{\omega}^T (k_1 \mu^4 \boldsymbol{\sigma} + k_2 \mu^2 \boldsymbol{\omega}) + \frac{\psi \delta^2}{2} \mu^8 \|\boldsymbol{\omega}\|^2 + \frac{\psi}{2\delta^2} \bar{d}^2 \\
&= \frac{16\nu}{t_f} \mu^9 \|\boldsymbol{\sigma}\|^2 + \frac{2\psi\bar{J}}{t_f} \mu^5 \|\boldsymbol{\omega}\|^2 - k_2 b(\boldsymbol{\sigma}) \mu^6 \|\boldsymbol{\omega}\|^2 + \frac{\lambda k_2}{\psi} b(\boldsymbol{\sigma}) \mu^8 \boldsymbol{\sigma}^T \boldsymbol{\omega} \\
&\quad + \frac{\psi \delta^2}{2} \mu^6 \|\boldsymbol{\omega}\|^2 + \frac{\psi}{2\delta^2} \mu^2 \bar{d}^2.
\end{aligned} \tag{5.14}$$

Using the definition $b(\boldsymbol{\sigma}) \triangleq (1 + \boldsymbol{\sigma}^T \boldsymbol{\sigma})$ on the third term of Eq. 5.14, it follows that:

$$\begin{aligned}
\dot{V}_1 + \dot{V}_2 &\leq \frac{16\nu}{t_f} \mu^9 \|\boldsymbol{\sigma}\|^2 + \left(\frac{2\psi\bar{J}}{t_f} \mu^{-1} + \frac{\psi \delta^2}{2} - k_2 \right) \mu^6 \|\boldsymbol{\omega}\|^2 \\
&\quad - k_2 \mu^6 \|\boldsymbol{\sigma}\|^2 \|\boldsymbol{\omega}\|^2 + \frac{\lambda k_2}{\psi} b(\boldsymbol{\sigma}) \mu^8 \boldsymbol{\sigma}^T \boldsymbol{\omega} + \frac{\psi}{2\delta^2} \mu^2 \bar{d}^2.
\end{aligned} \tag{5.15}$$

Finally, taking derivative on V_3 :

$$\begin{aligned}
\dot{V}_3 &= \frac{6\lambda}{t_f} \mu^7 \boldsymbol{\sigma}^T \mathbf{J} \boldsymbol{\omega} + \lambda \mu^6 \boldsymbol{\sigma}^T (-\boldsymbol{\omega}^* \mathbf{J} \boldsymbol{\omega} + \mathbf{u} + \mathbf{d}) + \frac{\lambda}{4} \mu^6 \boldsymbol{\omega}^T \mathbf{J} \mathbf{B}(\boldsymbol{\sigma}) \boldsymbol{\omega} \\
&\leq \frac{6\lambda\bar{J}}{t_f} \mu^7 \|\boldsymbol{\sigma}\| \|\boldsymbol{\omega}\| + \lambda \mu^6 \bar{J} \|\boldsymbol{\sigma}\| \|\boldsymbol{\omega}\|^2 + \lambda \mu^6 \boldsymbol{\sigma}^T (\mathbf{u} + \mathbf{d}) + \frac{\lambda\bar{J}}{4} b(\boldsymbol{\sigma}) \mu^6 \|\boldsymbol{\omega}\|^2,
\end{aligned} \tag{5.16}$$

where we used the property of Eq. 4.5 in the last step above. Using the property $\|\boldsymbol{\sigma}\| \leq \frac{1}{2} b(\boldsymbol{\sigma})$ on the second term of Eq. 5.16, and using the relation

$2\mu^7\|\boldsymbol{\sigma}\|\|\boldsymbol{\omega}\| = 2(\mu^4\|\boldsymbol{\sigma}\|)(\mu^3\|\boldsymbol{\omega}\|) \leq \mu^8\|\boldsymbol{\sigma}\|^2 + \mu^6\|\boldsymbol{\omega}\|^2$, we reach:

$$\begin{aligned}
\dot{V}_3 &\leq \frac{3\lambda\bar{J}}{t_f}\mu^8\|\boldsymbol{\sigma}\|^2 + \frac{3\lambda\bar{J}}{t_f}\mu^6\|\boldsymbol{\omega}\|^2 + \frac{\lambda\bar{J}}{2}b(\boldsymbol{\sigma})\mu^6\|\boldsymbol{\omega}\|^2 + \lambda\mu^6\boldsymbol{\sigma}^T\mathbf{u} + \lambda\mu^6\boldsymbol{\sigma}^T\mathbf{d} \\
&\quad + \frac{\lambda\bar{J}}{4}b(\boldsymbol{\sigma})\mu^6\|\boldsymbol{\omega}\|^2 \\
&= \frac{3\lambda\bar{J}}{t_f}\mu^8\|\boldsymbol{\sigma}\|^2 + \frac{3\lambda\bar{J}}{t_f}\mu^6\|\boldsymbol{\omega}\|^2 + \frac{3\lambda\bar{J}}{4}b(\boldsymbol{\sigma})\mu^6\|\boldsymbol{\omega}\|^2 + \lambda\mu^6\boldsymbol{\sigma}^T\mathbf{u} + \lambda\mu^6\boldsymbol{\sigma}^T\mathbf{d} \\
&= \frac{3\lambda\bar{J}}{t_f}\mu^8\|\boldsymbol{\sigma}\|^2 + \frac{3\lambda\bar{J}}{t_f}\mu^6\|\boldsymbol{\omega}\|^2 + \frac{3\lambda\bar{J}}{4}\mu^6\|\boldsymbol{\omega}\|^2 + \frac{3\lambda\bar{J}}{4}\mu^6\|\boldsymbol{\sigma}\|^2\|\boldsymbol{\omega}\|^2 \\
&\quad + \lambda\mu^6\boldsymbol{\sigma}^T\mathbf{u} + \lambda\mu^6\boldsymbol{\sigma}^T\mathbf{d}, \tag{5.17}
\end{aligned}$$

where the last step above used the definition $b(\boldsymbol{\sigma}) \triangleq (1 + \boldsymbol{\sigma}^T\boldsymbol{\sigma})$.

Substituting the control law of Eq. 5.5 on the last term of Eq. 5.17, we get that:

$$\begin{aligned}
\lambda\mu^6\boldsymbol{\sigma}^T\mathbf{u} &= -\frac{\lambda k_1}{\psi}b(\boldsymbol{\sigma})\mu^{10}\|\boldsymbol{\sigma}\|^2 - \frac{\lambda k_2}{\psi}b(\boldsymbol{\sigma})\mu^8\boldsymbol{\sigma}^T\boldsymbol{\omega} \\
&= -\frac{\lambda k_1}{\psi}\mu^{10}\|\boldsymbol{\sigma}\|^2 - \frac{\lambda k_1}{\psi}\mu^{10}\|\boldsymbol{\sigma}\|^4 - \frac{\lambda k_2}{\psi}b(\boldsymbol{\sigma})\mu^8\boldsymbol{\sigma}^T\boldsymbol{\omega}. \tag{5.18}
\end{aligned}$$

In addition, using the relation $\lambda\mu^6\boldsymbol{\sigma}^T\mathbf{d} = \lambda(\delta\mu^5\boldsymbol{\sigma}^T)(\frac{1}{\delta}\mu\mathbf{d}) \leq \frac{\lambda\delta^2}{2}\mu^{10}\|\boldsymbol{\sigma}\|^2 + \frac{\lambda}{2\delta^2}\mu^2\bar{d}^2$ for some $\delta > 0$, we get to the following form for \dot{V}_3 :

$$\begin{aligned}
\dot{V}_3 &\leq \lambda\left(\frac{3\bar{J}}{t_f}\mu^{-2} + \frac{\delta^2}{2} - \frac{k_1}{\psi}\right)\mu^{10}\|\boldsymbol{\sigma}\|^2 - \lambda\frac{k_1}{\psi}\mu^{10}\|\boldsymbol{\sigma}\|^4 + \lambda\left(\frac{3\bar{J}}{t_f} + \frac{3\bar{J}}{4}\right)\mu^6\|\boldsymbol{\omega}\|^2 \\
&\quad + \frac{3\lambda\bar{J}}{4}\mu^6\|\boldsymbol{\sigma}\|^2\|\boldsymbol{\omega}\|^2 - \frac{\lambda k_2}{\psi}b(\boldsymbol{\sigma})\mu^8\boldsymbol{\sigma}^T\boldsymbol{\omega} + \frac{\lambda}{2\delta^2}\mu^2\bar{d}^2. \tag{5.19}
\end{aligned}$$

Combining terms on $\dot{V} = \dot{V}_1 + \dot{V}_2 + \dot{V}_3$, we notice that the last term on Eq. 5.17 cancels with the last term of Eq. 5.15, leading to:

$$\begin{aligned}
\dot{V} &\leq -\lambda\left(\frac{k_1}{\psi} - \frac{16\nu}{\lambda t_f}\mu^{-1} - \frac{3\bar{J}}{t_f}\mu^{-2} - \frac{\delta^2}{2}\right)\mu^{10}\|\boldsymbol{\sigma}\|^2 - \lambda\frac{k_1}{\psi}\mu^{10}\|\boldsymbol{\sigma}\|^4 + \left(\frac{\lambda}{2\delta^2} + \frac{\psi}{2\delta^2}\right)\mu^2\bar{d}^2 \\
&\quad - \left(k_2 - \frac{3\bar{J}\lambda}{t_f} - \frac{3\bar{J}\lambda}{4} - \frac{2\psi\bar{J}}{t_f}\mu^{-1} - \frac{\psi\delta^2}{2}\right)\mu^6\|\boldsymbol{\omega}\|^2 - \left(k_2 - \frac{3\lambda\bar{J}}{4}\right)\mu^6\|\boldsymbol{\sigma}\|^2\|\boldsymbol{\omega}\|^2. \tag{5.20}
\end{aligned}$$

Defining $\phi_1 \triangleq \frac{k_1}{\psi}$, $\phi_2 \triangleq \frac{k_2}{\psi}$, and using the relation $\lambda = \frac{J\psi}{\beta\bar{J}} \implies \lambda\bar{J} = \frac{J\psi}{\beta}$, \dot{V} is rewritten as:

$$\begin{aligned}
\dot{V} &\leq -\lambda \left(\phi_1 - \frac{16\nu}{\lambda t_f} \mu^{-1} - \frac{3\bar{J}}{t_f} \mu^{-2} - \frac{\delta^2}{2} \right) \mu^{10} \|\boldsymbol{\sigma}\|^2 - \lambda \phi_1 \mu^{10} \|\boldsymbol{\sigma}\|^4 + \left(\frac{\lambda}{2\delta^2} + \frac{\psi}{2\delta^2} \right) \mu^2 \bar{d}^2 \\
&\quad - \left(k_2 - \frac{3}{t_f} \frac{J\psi}{\beta} - \frac{3}{4} \frac{J\psi}{\beta} - \frac{2\psi\bar{J}}{t_f} \mu^{-1} - \frac{\psi\delta^2}{2} \right) \mu^6 \|\boldsymbol{\omega}\|^2 - \left(k_2 - \frac{3}{4} \frac{J\psi}{\beta} \right) \mu^6 \|\boldsymbol{\sigma}\|^2 \|\boldsymbol{\omega}\|^2 \\
&= -\lambda \left(\phi_1 - \frac{16\nu}{\lambda t_f} \mu^{-1} - \frac{3\bar{J}}{t_f} \mu^{-2} - \frac{\delta^2}{2} \right) \mu^{10} \|\boldsymbol{\sigma}\|^2 - \lambda \phi_1 \mu^{10} \|\boldsymbol{\sigma}\|^4 + \left(\frac{\lambda}{2\delta^2} + \frac{\psi}{2\delta^2} \right) \mu^2 \bar{d}^2 \\
&\quad - \psi \left(\phi_2 - \frac{3}{t_f} \frac{J}{\beta} - \frac{3}{4} \frac{J}{\beta} - \frac{2\bar{J}}{t_f} \mu^{-1} - \frac{\delta^2}{2} \right) \mu^6 \|\boldsymbol{\omega}\|^2 - \psi \left(\phi_2 - \frac{3}{4} \frac{J}{\beta} \right) \mu^6 \|\boldsymbol{\sigma}\|^2 \|\boldsymbol{\omega}\|^2.
\end{aligned} \tag{5.21}$$

Define $\kappa_1 \triangleq \phi_1 - \frac{\delta^2}{2}$, $\kappa_2 \triangleq \phi_2 - \frac{3}{t_f} \frac{J}{\beta} - \frac{3}{4} \frac{J}{\beta} - \frac{\delta^2}{2}$, $\kappa_3 \triangleq \phi_2 - \frac{3}{4} \frac{J}{\beta}$. Given any value for $\phi_1 > 0$ and $\phi_2 > 0$, it is always possible to come up with β large enough and δ small enough such that $\kappa_1 > 0$, $\kappa_2 > 0$, and $\kappa_3 > 0$. We rewrite Eq. 5.21 as:

$$\begin{aligned}
\dot{V} &\leq -\lambda \overbrace{\left(\kappa_1 - \frac{16\nu}{\lambda t_f} \mu^{-1} - \frac{3\bar{J}}{t_f} \mu^{-2} \right)}^{\triangleq \gamma_1(t)} \mu^{10} \|\boldsymbol{\sigma}\|^2 - \overbrace{\lambda \phi_1}^{\triangleq \gamma_2} \mu^{10} \|\boldsymbol{\sigma}\|^4 \\
&\quad - \underbrace{\psi \left(\kappa_2 - \frac{2\bar{J}}{t_f} \mu^{-1} \right)}_{\triangleq \gamma_3(t)} \mu^6 \|\boldsymbol{\omega}\|^2 - \underbrace{\psi \kappa_3}_{\triangleq \gamma_4} \mu^6 \|\boldsymbol{\sigma}\|^2 \|\boldsymbol{\omega}\|^2 + \underbrace{\left(\frac{\lambda}{2\delta^2} + \frac{\psi}{2\delta^2} \right)}_{\triangleq \gamma_5} \mu^2 \bar{d}^2 \\
&= -\gamma_1(t) \mu^{10} \|\boldsymbol{\sigma}\|^2 - \gamma_2 \mu^{10} \|\boldsymbol{\sigma}\|^4 - \gamma_3(t) \mu^6 \|\boldsymbol{\omega}\|^2 - \gamma_4 \mu^6 \|\boldsymbol{\sigma}\|^2 \|\boldsymbol{\omega}\|^2 + \gamma_5 \mu^2 \bar{d}^2.
\end{aligned} \tag{5.22}$$

Under the assumption that $\kappa_3 > 0$ (β sufficiently large), we have that both $\gamma_2 > 0$ and $\gamma_4 > 0$. Then, we simplify Eq. 5.22 as:

$$\dot{V} \leq -\gamma_1(t) \mu^{10} \|\boldsymbol{\sigma}\|^2 - \gamma_3(t) \mu^6 \|\boldsymbol{\omega}\|^2 + \gamma_5 \mu^2 \bar{d}^2. \tag{5.23}$$

As for $\gamma_1(t)$ and $\gamma_3(t)$, we notice that $\lim_{t \rightarrow t_f} \gamma_1(t) = \lambda \phi_1$ and $\lim_{t \rightarrow t_f} \gamma_3(t) = \psi \kappa_1$. Since $\gamma_1(t)$ and $\gamma_3(t)$ are monotonically increasing functions in the interval $t \in [0, t_f)$, then $\exists t_1 \in [0, t_f)$ s.t. $\gamma_1(t) > 0$ and $\gamma_3(t) > 0$, for any $t \in [t_1, t_f)$.

In the proofs that follow, Lemma 2 demonstrates that the differential equation of Eq. 5.23 does not admit finite-time-escape in the interval $t \in [0, t_1]$. Then, Lemma 3 proves that $V(t)$ is bounded for $t \in [t_1, t_f)$.

Lemma 2. Given the definitions $\gamma_1(t) \triangleq \lambda \left(\kappa_1 - \frac{16\nu}{\lambda t_f} \mu^{-1} - \frac{3\bar{J}}{t_f} \mu^{-2} \right)$, $\gamma_3(t) \triangleq \psi \left(\kappa_2 - \frac{2\bar{J}}{t_f} \mu^{-1} \right)$, and $\gamma_5 \triangleq \frac{\lambda}{2\delta^2} + \frac{\psi}{2\delta^2}$, the differential equation of Eq. 5.23 does not admit finite-time-escape for $t \in [0, t_1]$, $\forall t_1 < t_f$.

Proof. We start the proof by bounding Eq. 5.23 as:

$$\begin{aligned}
\dot{V} &\leq -\gamma_1(t)\mu^{10}\|\boldsymbol{\sigma}\|^2 - \gamma_3(t)\mu^6\|\boldsymbol{\omega}\|^2 + \gamma_5\mu^2\bar{d}^2 \\
&= -\lambda \left(\kappa_1 - \frac{16\nu}{\lambda t_f} \mu^{-1} - \frac{3\bar{J}}{t_f} \mu^{-2} \right) \mu^{10}\|\boldsymbol{\sigma}\|^2 - \psi \left(\kappa_2 - \frac{2\bar{J}}{t_f} \mu^{-1} \right) \mu^6\|\boldsymbol{\omega}\|^2 + \gamma_5\mu^2\bar{d}^2 \\
&\leq \left(\frac{16\nu}{t_f} + \frac{3\lambda\bar{J}}{t_f} \right) \mu^{10}\|\boldsymbol{\sigma}\|^2 + \frac{2\psi\bar{J}}{t_f} \mu^6\|\boldsymbol{\omega}\|^2 + \gamma_5\mu^2\bar{d}^2 \\
&\leq \Gamma\mu^2 (\mu^8\|\boldsymbol{\sigma}\|^2 + \mu^4\|\boldsymbol{\omega}\|^2) + \gamma_5\mu^2\bar{d}^2, \tag{5.24}
\end{aligned}$$

where $\Gamma \triangleq \max \left(\frac{16\nu}{t_f} + \frac{3\lambda\bar{J}}{t_f}, \frac{2\psi\bar{J}}{t_f} \right)$. Using Eq. 5.9 and noticing that $\mu(t) \leq \mu(t_1)$, $\forall t \in [0, t_1]$, for $t_1 < t_f$, then Eq. 5.24 can be bounded as:

$$\dot{V} \leq \frac{\Gamma}{\underline{\alpha}} \mu^2(t_1) V + \gamma_5 \mu^2(t_1) \bar{d}^2. \tag{5.25}$$

Using the Comparison Lemma [31] on Eq. 5.25, we get that:

$$\begin{aligned}
V(t) &\leq V(0) \exp \left(\frac{\Gamma}{\underline{\alpha}} \mu^2(t_1) \cdot t \right) + \frac{\gamma_5 \underline{\alpha} \bar{d}^2}{\Gamma} \left[\exp \left(\frac{\Gamma}{\underline{\alpha}} \mu^2(t_1) \cdot t \right) - 1 \right], \quad t \in [0, t_1] \\
&\leq V(0) \exp \left(\frac{\Gamma}{\underline{\alpha}} \mu^2(t_1) \cdot t_1 \right) + \frac{\gamma_5 \underline{\alpha} \bar{d}^2}{\Gamma} \left[\exp \left(\frac{\Gamma}{\underline{\alpha}} \mu^2(t_1) \cdot t_1 \right) - 1 \right], \quad t \in [0, t_1]. \tag{5.26}
\end{aligned}$$

Hence, $V(t)$ is upper-bounded by a constant in the period $t \in [0, t_1]$, implying that finite-time-escape is not possible for the same period. \square

Lemma 3. Given that $\gamma_1(t_1) > 0$ and $\gamma_1(t_3) > 0$, the solution to the differential equation of Eq. 5.23 is bounded for $t \in [t_1, t_f]$.

Proof. Eq. 5.23 can be written as:

$$\begin{aligned}
\dot{V} &\leq -\gamma_1(t)\mu^{10}\|\boldsymbol{\sigma}\|^2 - \gamma_3(t)\mu^6\|\boldsymbol{\omega}\|^2 + \gamma_5\mu^2\bar{d}^2 \\
&\leq -\gamma_1(t_1)\mu^{10}\|\boldsymbol{\sigma}\|^2 - \gamma_3(t_1)\mu^6\|\boldsymbol{\omega}\|^2 + \gamma_5\mu^2\bar{d}^2 \\
&\leq -L\mu^2 (\mu^8\|\boldsymbol{\sigma}\|^2 + \mu^4\|\boldsymbol{\omega}\|^2) + \gamma_5\mu^2\bar{d}^2, \tag{5.27}
\end{aligned}$$

where $L \triangleq \min(\gamma_1(t_1), \gamma_3(t_1))$. Combining Eq. 5.27 with Eq. 5.8, we get that:

$$\dot{V} \leq -\frac{L}{\bar{\alpha}}\mu^2V + \gamma_5\mu^2\bar{d}^2. \quad (5.28)$$

Once again, invoking the Comparison lemma leads to:

$$V(t) \leq \Phi(t, t_1)V(t_1) + \gamma_5\bar{d}^2\Phi(t, 0) \int_{t_1}^t \Phi(0, \tau)\mu^2(\tau) d\tau, \quad (5.29)$$

where $\Phi(t_1, t_2) = \exp[-\frac{L}{\bar{\alpha}}t_f(\mu(t_1) - \mu(t_2))]$.

As shown in Eq. 5.2, $\frac{d\mu(\tau)}{d\tau} = \frac{1}{t_f}\mu^2(\tau)$, leading to $\mu^2(\tau)d\tau = t_f d\mu$. The integral within Eq. 5.29 can be written as:

$$\begin{aligned} \int_{t_1}^t \Phi(0, \tau)\mu^2(\tau) d\tau &= t_f \int_{\mu(t_1)}^{\mu(t)} \Phi(0, \tau) d\mu = t_f \int_{\mu(t_1)}^{\mu(t)} \exp\left[\frac{L}{\bar{\alpha}}t_f \cdot \mu\right] d\mu \\ &= \frac{\bar{\alpha}}{L} \exp\left[\frac{L}{\bar{\alpha}}t_f \cdot \mu\right] \Big|_{\mu(t_1)}^{\mu(t)} \\ &= \frac{\bar{\alpha}}{L} \exp\left(\frac{L}{\bar{\alpha}}t_f \cdot \mu(t)\right) \left[1 - \exp\left[-\frac{L}{\bar{\alpha}}t_f(\mu(t) - \mu(t_1))\right]\right] \\ &= \frac{\bar{\alpha}}{L} \Phi(0, t) \left[1 - \exp\left[-\frac{L}{\bar{\alpha}}t_f(\mu(t) - \mu(t_1))\right]\right]. \end{aligned} \quad (5.30)$$

Using the fact that $\Phi(t, 0)\Phi(0, t) = \mathbf{I}$, Eq. 5.29 can be written as:

$$\begin{aligned} V(t) &\leq V(t_1) \exp\left[-\frac{L}{\bar{\alpha}}t_f(\mu(t) - \mu(t_1))\right] + \frac{\gamma_5\bar{\alpha}}{L}\bar{d}^2 \left(1 - \exp\left[-\frac{L}{\bar{\alpha}}t_f(\mu(t) - \mu(t_1))\right]\right) \\ &\leq V(t_1) + \frac{\gamma_5\bar{\alpha}}{L}\bar{d}^2. \end{aligned} \quad (5.31)$$

Therefore, $V(t) \in L_\infty$, for $t \in [t_1, t_f]$. \square

We have proven so far that the storage function satisfies $V(t) \in L_\infty, t \in [0, t_f]$. Because $V(t) \in L_\infty$, there exists \bar{V} such that $V(t) \leq \bar{V}$ for $t \in [0, t_f]$. Using this inequality with Eq. 5.9, we get that:

$$\underline{\alpha}\mu^8\|\boldsymbol{\sigma}\|^2 + \underline{\alpha}\mu^4\|\boldsymbol{\omega}\|^2 \leq \bar{V} \implies \begin{cases} \underline{\alpha}\mu^8\|\boldsymbol{\sigma}\|^2 \leq \bar{V} \\ \underline{\alpha}\mu^4\|\boldsymbol{\omega}\|^2 \leq \bar{V} \end{cases} \implies \begin{cases} \mu^4\|\boldsymbol{\sigma}\| \leq \sqrt{\frac{\bar{V}}{\underline{\alpha}}} \\ \mu^2\|\boldsymbol{\omega}\| \leq \sqrt{\frac{\bar{V}}{\underline{\alpha}}} \end{cases} \quad (5.32)$$

Therefore, $\mu^4(t)\|\boldsymbol{\sigma}(t)\| \in L_\infty$ and $\mu^2(t)\|\boldsymbol{\omega}(t)\| \in L_\infty$. Because $\mu^4(t)\|\boldsymbol{\sigma}(t)\| \in L_\infty$, then it must be true that $\|\boldsymbol{\sigma}(t)\| \in L_\infty$ implying that $b(\boldsymbol{\sigma}) = 1 + \|\boldsymbol{\sigma}(t)\|^2 \in L_\infty$. Hence, the control law of Eq. 5.5 is a product of bounded terms, satisfying $\mathbf{u}(t) \in L_\infty$, i.e., it is realizable. In addition, the following can be established from Eq. 5.32:

$$\begin{cases} \mu^4\|\boldsymbol{\sigma}\| \leq \sqrt{\frac{\bar{V}}{\alpha}} \\ \mu^2\|\boldsymbol{\omega}\| \leq \sqrt{\frac{\bar{V}}{\alpha}} \end{cases} \implies \begin{cases} \|\boldsymbol{\sigma}\| \leq \mu^{-4}\sqrt{\frac{\bar{V}}{\alpha}} \\ \|\boldsymbol{\omega}\| \leq \mu^{-2}\sqrt{\frac{\bar{V}}{\alpha}} \end{cases} \implies \begin{cases} \lim_{t \rightarrow t_f} \|\boldsymbol{\sigma}\| \leq 0 \\ \lim_{t \rightarrow t_f} \|\boldsymbol{\omega}\| \leq 0 \end{cases} . \quad (5.33)$$

Therefore, $\lim_{t \rightarrow t_f} \|\boldsymbol{\sigma}\| = 0$ and $\lim_{t \rightarrow t_f} \|\boldsymbol{\omega}\| = 0$, finalizing our proofs.

5.2.3 Summary of the Stability Proof

In this section we summarize all important details used in the stability proof. We have proven that the system below is finite-time stable:

$$\begin{cases} \dot{\boldsymbol{\sigma}}(t) = \frac{1}{4}\mathbf{B}(\boldsymbol{\sigma}(t))\boldsymbol{\omega}(t) \\ \mathbf{J}\dot{\boldsymbol{\omega}}(t) = -\boldsymbol{\omega}^*(t)\mathbf{J}\boldsymbol{\omega}(t) + \mathbf{u}(t) \\ \mathbf{u} = -b(\boldsymbol{\sigma}) \left(\phi_1\mu^4(t)\boldsymbol{\sigma} + \phi_2\mu^2(t)\boldsymbol{\omega} \right) \end{cases} , \quad (5.34)$$

provided that $\phi_1 \triangleq \frac{k_1}{\psi} > 0$ and $\phi_2 \triangleq \frac{k_2}{\psi} > 0$.

Our proof was made based on the storage function:

$$V = 2\nu\mu^8\boldsymbol{\sigma}^T\boldsymbol{\sigma} + \frac{\psi}{2}\mu^4\boldsymbol{\omega}^T\mathbf{J}\boldsymbol{\omega} + \lambda\mu^6\boldsymbol{\sigma}^T\mathbf{J}\boldsymbol{\omega}, \quad (5.35)$$

where $\lambda \triangleq \frac{J\psi}{\beta J}$. The storage function above is positive-definite in the interval $t \in [0, t_f)$ provided that $\nu > 0$, $\psi > 0$, $\lambda > 0$, $\frac{\nu}{\psi} > \frac{J}{\beta}$ and $\beta > 1$. We have defined $\nu \triangleq k_1 + \lambda\phi_2$, so it is sufficient that $\frac{k_1}{\psi} = \phi_1 > \frac{J}{\beta}$ to satisfy $\frac{\nu}{\psi} > \frac{J}{\beta}$, implying that we need $\beta > \frac{J}{\phi_1}$.

In order to guarantee ultimate boundedness of the storage function $V(t)$, $t \in [0, t_f)$, we also made the requirement that β has to be large enough and δ small enough to make $\kappa_1 > 0$, $\kappa_2 > 0$ and $\kappa_3 > 0$ for any given $\phi_1 > 0$ and $\phi_2 > 0$, where $\kappa_1 \triangleq \phi_1 - \frac{\delta^2}{2}$, $\kappa_2 \triangleq \phi_2 - \frac{3J}{t_f\beta} - \frac{3J}{4\beta} - \frac{\delta^2}{2}$, $\kappa_3 \triangleq \phi_2 - \frac{3J}{4\beta}$.

Given β and δ satisfying all previous requirements, we can prove that the storage function satisfies $V(t) \in L_\infty$. The boundedness on the storage function is a sufficient condition to prove that the control law $\mathbf{u} = -b(\boldsymbol{\sigma}) (\phi_1 \mu^4(t) \boldsymbol{\sigma} + \phi_2 \mu^2(t) \boldsymbol{\omega})$ is realizable and that $\lim_{t \rightarrow t_f} \|\boldsymbol{\sigma}\| = 0$ and $\lim_{t \rightarrow t_f} \|\boldsymbol{\omega}\| = 0$.

The control design herein presented can be extended to the trajectory tracking case. The proofs for trajectory tracking and its respective control law can be found in Appendix C.1.

5.3 Simulation Results

This section presents some simulation results for the newly designed control laws. We show that these control laws drive the system to zero error as expected. Simulations are performed for final time $t_f = 30$ s.

For all simulations, the initial orientation is given by a rotation of $\psi(0) = \pi$ around the axis $\hat{\mathbf{e}}(0) = 1/\sqrt{3} [1, 1, 1]^T$, and the initial angular velocity is given by $\boldsymbol{\omega}(0) = [-0.03, 0.04, -0.05]^T$. The inertia matrix is the same as in Ref. [29]:

$$\mathbf{J} = \begin{bmatrix} 95 & -0.69 & 0.18 \\ -0.69 & 190 & 0.12 \\ 0.18 & 0.12 & 142.5 \end{bmatrix} \quad (5.36)$$

Figure 5.1 shows the result for the stabilization of the system to the origin using the control law from Eq. 5.34, with $\phi_1 = \phi_2 = 20$. The left plots are in a linear scale, while the plots on the right are in logarithm scale. Values below $2.20 \cdot 10^{-16}$ are considered zero and are not shown on the log plot. We can see that the system is being driven towards the origin increasingly faster

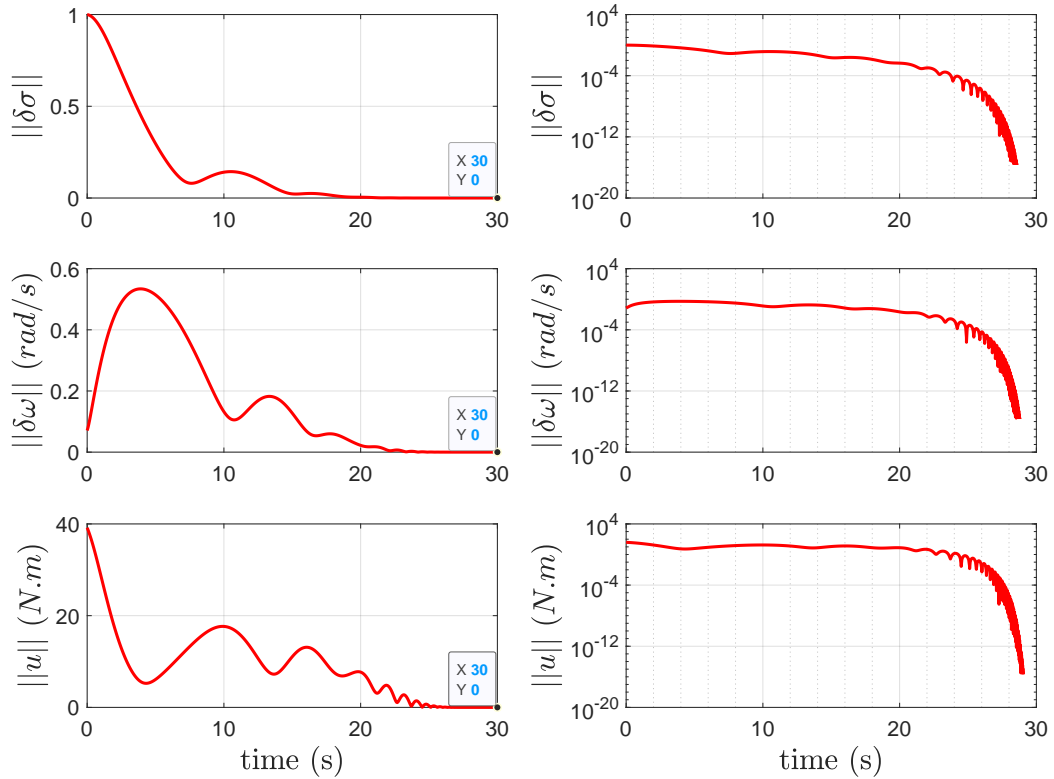


Figure 5.1: Time histories of state trajectories for the set-point regulation case with $\phi_1 = \phi_2 = 20$.

until the machine zero is reached. Notice that the states (ω and σ) and the inputs (\mathbf{u}) all converge to zero. The log plots fade to zero before 30 seconds, but one should have in mind that this is the *double precision zero*, not the *mathematical zero*. The mathematical zero should only happen at exactly $t = t_f$ as per our proofs.

Figure 5.2 has a simulation result that is similar to the last one, except that now we apply a disturbance torque on the system $\mathbf{d} =$

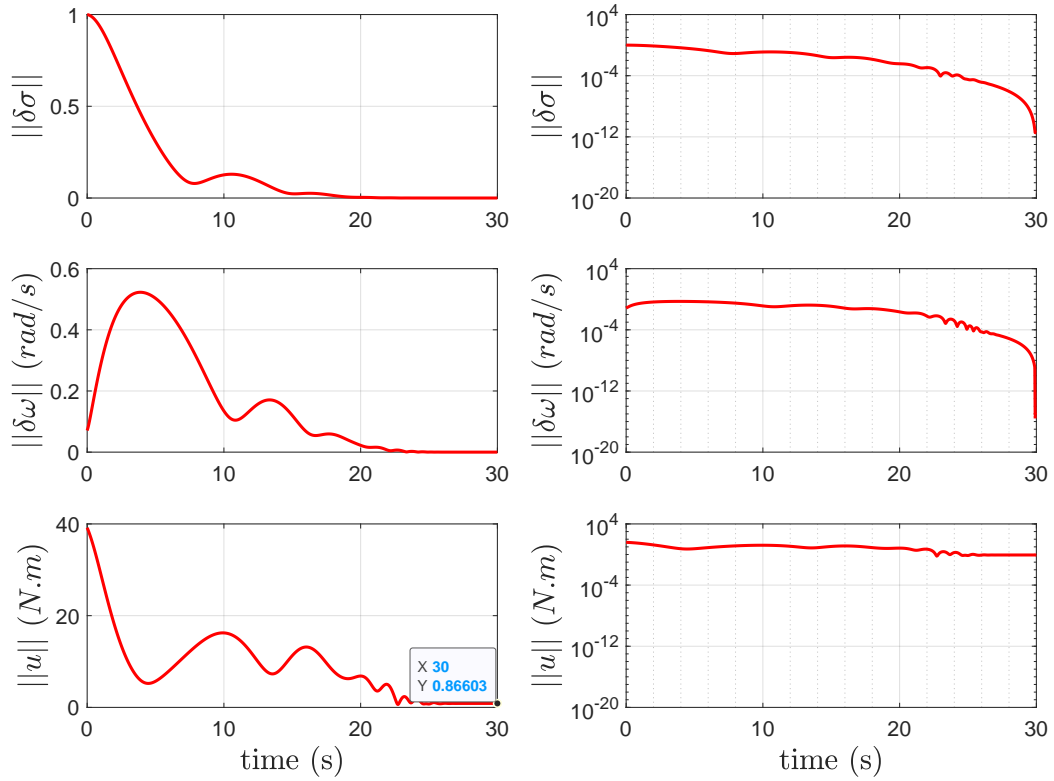


Figure 5.2: Time histories of state trajectories for the disturbed set-point regulation case with $\phi_1 = \phi_2 = 20$, and $\mathbf{d} = [0.5 \ 0.5 \ 0.5]^T \text{N.m}$.

$[0.5 \ 0.5 \ 0.5]^T \text{N.m}$. Note that the states of the system converge to the origin, but the control input converges as $\lim_{t \rightarrow t_f} \|\mathbf{u}\| = \|\mathbf{d}\| = 0.86603 \text{N.m}$.

Figure 5.3 shows another stabilization result without disturbances, except that the control gains are given as $\phi_1 = \phi_2 = 100$. We notice that the system converges faster than in the previous simulations (as one would expect from higher feedback gains), but the control input norm $\|\mathbf{u}\|$ is much higher at the beginning of the simulation. Hence, we can observe a trade-off between

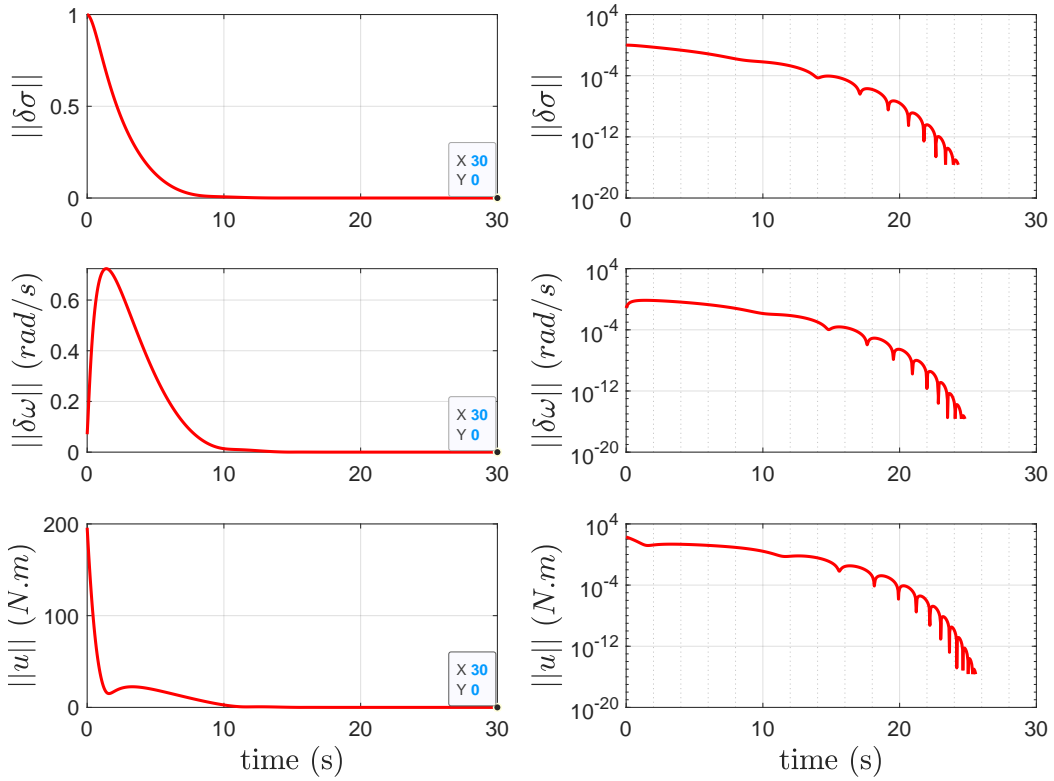


Figure 5.3: Time histories of state trajectories for the disturbed set-point regulation case with $\phi_1 = \phi_2 = 100$.

the norm of the control input and convergence rate as a function of the control gains, and one should avoid too high control gains if the actuators cannot achieve very high torques.

Figure 5.4 shows another stabilization result without disturbances, except that the control gains are much lower compared to the previous simulations, as we choose $\phi_1 = \phi_2 = 1$. We notice that convergence is much slower, and that the control effort is much higher (in terms of the two-norm absolute

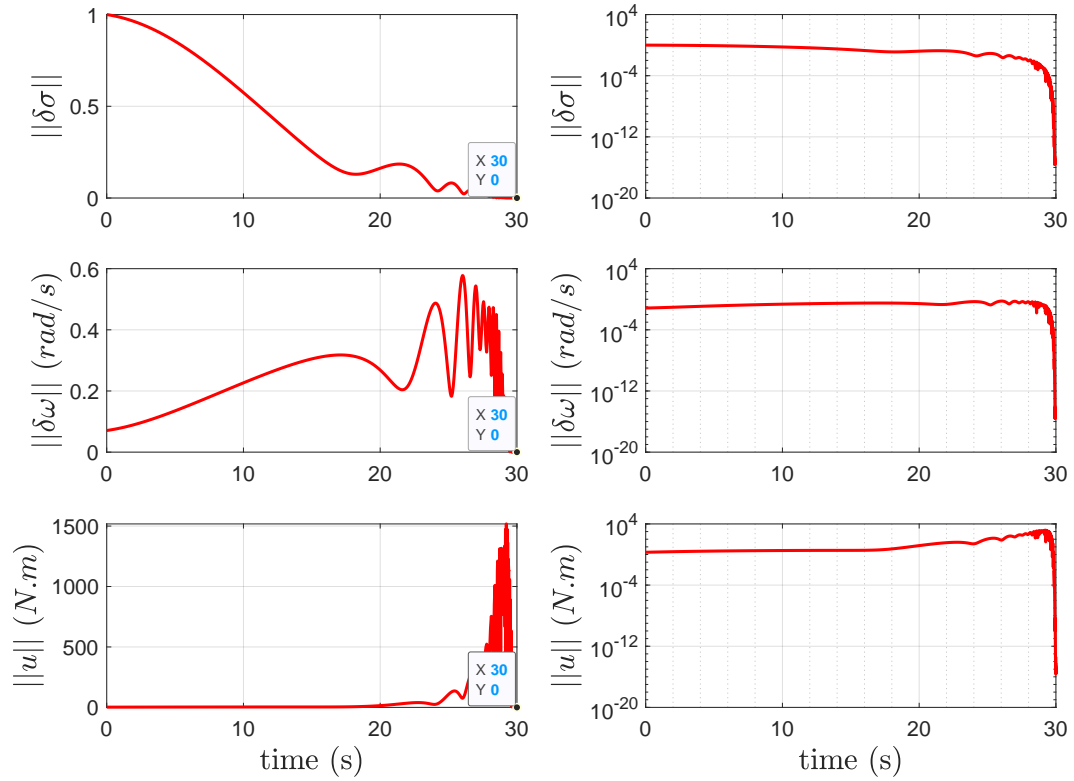


Figure 5.4: Time histories of state trajectories for the disturbed set-point regulation case with $\phi_1 = \phi_2 = 1$.

value) than in any of the previous simulations. Practitioners should avoid too low control gains in order to prevent high bounds on the control effort as time approaches the terminal time.

5.4 Conclusions

This work introduces a feedback control law that is able to regulate the attitude system for a rigid body from any initial configuration to a desired

one in prescribed finite time. This result builds upon recently reported prior work by the authors, using some crucial insights that allow for robustness for the resulting controller albeit the possibility for large-scale uncertainties in the inertia properties. The major distinction from those prior results is that we introduce a new Lyapunov-like function here that enables us to derive a stabilizing feedback control law that does not need to explicitly cancel the rotational gyroscopic terms (fulfilling the well-known self-reduction property of attitude systems). Saliiently, we show that the proposed control law allows the attitude system to converge to the origin even in the presence of unknown bounded disturbances. For the sake of completeness, we also extended this control result for the attitude tracking case through the inclusion of certain carefully formulated feed-forward terms.

An interesting avenue of future work resides in finding bounds on the control effort within the interval $t \in [0, t_f)$ as a function of the control gains ϕ_1 , ϕ_2 and the prescribed final time t_f . This could possibly provide engineering insights that can be used by practitioners to determine whether a desired final time t_f allows finite-time transfer with given torque saturation constraints of the attitude system. In addition, it would be important to determine methods to tune the gains ϕ_1 , ϕ_2 based on desired response. The interested reader might want to refer to Ref. [29] for obtaining a “bang-bang” approximation of minimum bounds for final transfer time given inertial properties and maximum input torque bounds for rest to rest attitude transfers.

Another path of future work would be on the development of a finite-

time rigid-body attitude observer based on attitude measurements only, contrasting with asymptotic attitude observers [63, 72]. Ref. [23] presents a general finite-time observer for linear systems, but the development of finite-time observers for nonlinear systems is still an open problem. Some of the formulations in the present work could serve as guidance for the development of a finite-time observer for attitude systems.

Chapter 6

Conclusions

This dissertation presented developments in the fields of Control and Estimation for attitude systems. The first half of this dissertation treated the problem of estimating the angular velocity of a rotating rigid body, either in pure spin or in tumbling motion. The second half concerned of the derivation of Lyapunov-based finite-time attitude controllers for rigid bodies.

The first main contribution of this work resided in the introduction of the Quaternion Regression Algorithm, a simple batch algorithm that estimates the angular velocity of a rigid body in pure spin by measuring the body's orientation evolution over time using the quaternion parameterization. The performance of the proposed algorithm is analyzed using Monte Carlo simulations, and is further compared with a Multiplicative Extended Kalman Filter. Future work on this subject should include the derivation of the axis of rotation's error-covariance matrix, as well as expanding the algorithm for using measurements with non-constant error-covariance.

The second contribution of this dissertation consisted on adapting the Quaternion Regression Algorithm to deal with tumbling objects. In order to accomplish this, an adaptive algorithm is introduced, which assumes that the

rotating body is in pure-spin for a finite set of measurements. The new algorithm determines by itself whether a sequence of measurements seem to be in pure spin or not, and then adapts itself to use sequences that are close enough to pure spin. The developed method is applied in conjunction with the optical relative navigation technique of Simultaneous Localization and Mapping, and simulation results demonstrate the effectiveness of the proposed approach. Future work on this subject should use data from real space missions, validating the proposed techniques.

The third and fourth contributions within this dissertation lie upon the introduction of two Lyapunov-based finite-time attitude controllers for rigid bodies. The first proposed controller relied on backstepping control techniques to derive the proposed control-law, whereas the second one is based on a single Lyapunov-like function. Simulation results demonstrate the effectiveness of the proposed controllers, and their robustness to measurement noise and unknown bounded disturbances. Future work on this subject should look into understanding the transient response based on the controllers' tuning parameters, as well as understanding control effort magnitudes for different final transfer time and tuning parameters. In addition, the formulations herein presented could possibly be used as guidance for the development of a finite-time attitude observer.

Appendices

Appendix A

Appendices for QuateRA

A.1 Total Least Squares Problem Formulation

The Total Least Squares problem consists of estimating the matrix $\hat{\mathbf{A}}_0 \in \mathbb{R}^{m \times n}$, and the vectors $\hat{\mathbf{B}}_0 \in \mathbb{R}^m$ and $\hat{\mathbf{X}} \in \mathbb{R}^n$ that fits the linear model [65]:

$$\mathbf{A}_0 \mathbf{X} = \mathbf{B}_0, \quad (\text{A.1})$$

where \mathbf{A}_0 is called the *data matrix*, \mathbf{B}_0 is the *measurement vector*, and \mathbf{X} is an unknown vector. In the TLS problem, the measured components are \mathbf{A}_i^* and \mathbf{B}_i^* , which are random variables of the type:

$$\begin{cases} \mathbf{A}_i^* = \mathbf{A}_{0i} + \Delta \mathbf{A}_i \\ \mathbf{B}_i^* = \mathbf{B}_{0i} + \Delta \mathbf{B}_i \end{cases}, \quad (\text{A.2})$$

where \mathbf{A}_{0i} and \mathbf{B}_{0i} are the true (unobservable) variables at the i^{th} measurement, $\Delta \mathbf{A}_i$, $\Delta \mathbf{B}_i$ are their zero-mean respective observation errors, and $i \in \{1, 2, \dots, m\}$, with m being the number of measurements. For the purposes of the current work, we assume \mathbf{A}_i^* as a row vector and \mathbf{B}_i^* as a scalar.

We define the vectors $\mathbf{C}_i^* = [\mathbf{A}_i^* \ \mathbf{B}_i^*]^T$, $\Delta \mathbf{C}_i = [\Delta \mathbf{A}_i \ \Delta \mathbf{B}_i]^T$ and $\mathbf{C}_{0i}^* = [\mathbf{A}_{0i} \ \mathbf{B}_{0i}]^T$. We assume that $\mathbb{E}[\Delta \mathbf{C}_i \Delta \mathbf{C}_j^T] = \mathbf{0}, i \neq j$ and that all $\Delta \mathbf{C}_i$ are identically distributed. Defining the covariance matrix $\mathbf{P}_C \triangleq$

$\mathbb{E}[\Delta\mathbf{C}_i\Delta\mathbf{C}_i^T], \forall i \in \{1, \dots, m\}$, we assume that \mathbf{P}_C is positive definite and known. Taking the Cholesky decomposition $\mathbf{P}_C = \mathbf{L}_C\mathbf{L}_C^T$, we define the matrices $\mathbf{C} \triangleq [\mathbf{L}_C^{-1}\mathbf{C}_1^* \ \dots \ \mathbf{L}_C^{-1}\mathbf{C}_k^*]$ and $\mathbf{C}_0 \triangleq [\mathbf{L}_C^{-1}\mathbf{C}_{01}^* \ \dots \ \mathbf{L}_C^{-1}\mathbf{C}_{0k}^*]$.

Denoting $\hat{\mathbf{C}}_0$ as the estimate of \mathbf{C}_0 , the TLS problem seeks to minimize:

$$J = \|\mathbf{C} - \hat{\mathbf{C}}_0\|_F, \quad (\text{A.3})$$

subject to $\hat{\mathbf{B}}_0 \in \mathcal{R}(\hat{\mathbf{A}}_0)$ ($\hat{\mathbf{B}}_0$ is in the range space of $\hat{\mathbf{A}}_0$).

A.2 Gaussian Marginal Covariance Along a Line

Lemma 4. *Assume a bivariate normally-distributed random variable with mean $\boldsymbol{\mu} = [\mu_x \ \mu_y]^T$ and covariance matrix $\mathbf{P} = \text{diag}(\sigma^2, \sigma^2)$. The Probability Density Function (PDF) for this random variable is given by:*

$$p(x, y) = \frac{1}{2\pi\sigma^2} \exp\left(\frac{1}{2\sigma^2} \left[(x - \mu_x)^2 + (y - \mu_y)^2\right]\right) \quad (\text{A.4})$$

Then the marginal PDF of Eq. A.4 along any line $L(\mathbf{l}_0, \vec{\mathbf{l}})$ is a one-dimensional normally-distributed random variable with mean at \mathbf{l}_0^* and variance σ^2 along the $\vec{\mathbf{l}}$ direction, where $\mathbf{l}_0^* = \text{proj}(\boldsymbol{\mu}, L) = \mathbf{l}_0 + [(\boldsymbol{\mu} - \mathbf{l}_0)^T \vec{\mathbf{l}}] \vec{\mathbf{l}}$ is the point in $L(\mathbf{l}_0, \vec{\mathbf{l}})$ that minimizes the distance between $L(\mathbf{l}_0, \vec{\mathbf{l}})$ and $\boldsymbol{\mu}$.

Proof. To prove this, we refer to Fig. A.1. The circles in Fig. A.1 refer to level sets of the PDF from Eq. A.4, and are centered at $\boldsymbol{\mu} = [\mu_x \ \mu_y]^T$. We define α_n as the distance between $\boldsymbol{\mu}$ and the line $L(\mathbf{l}_0, \vec{\mathbf{l}})$. Also, we define a reference frame LN , which is centered at \mathbf{l}_0 and with basis directions $\vec{\mathbf{l}} \in \mathbb{S}^1$

and $\vec{n} \in \mathbb{S}^1$, where \vec{l} is defined as along the line $L(l_0, \vec{l})$. In addition, we define the rotation matrix $\mathbf{R}_z \in \mathbb{SO}(2)$ such that $\vec{l} = \mathbf{R}_z \vec{x}$ and $\vec{n} = \mathbf{R}_z \vec{y}$, where $\vec{x} \triangleq [1 \ 0]^T$ and $\vec{y} \triangleq [0 \ 1]^T$.

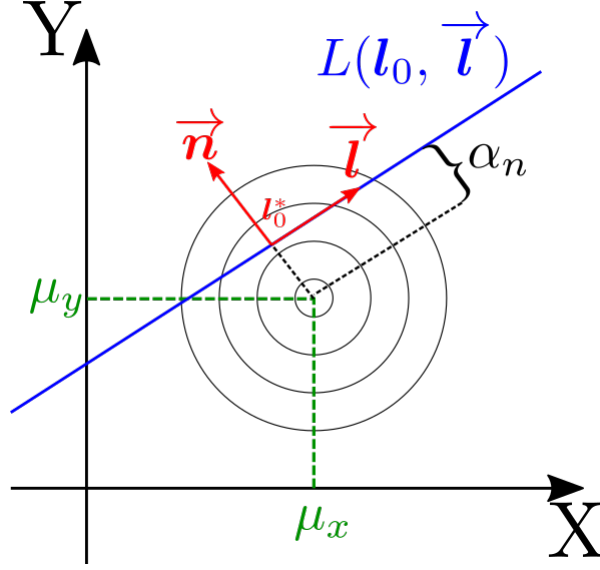


Figure A.1: Illustration for the proof of marginal PDF along a line.

The relation between a point in the LN frame and the XY frame is given by:

$$\begin{bmatrix} l \\ n \end{bmatrix} = \mathbf{R}_z \begin{bmatrix} x - \mu_x \\ y - \mu_y \end{bmatrix} - \begin{bmatrix} 0 \\ \alpha_n \end{bmatrix} \quad (\text{A.5})$$

We define the vector \mathbf{a} as:

$$\mathbf{a} \triangleq \begin{bmatrix} x - \mu_x \\ y - \mu_y \end{bmatrix} = \mathbf{R}_z^T \begin{bmatrix} l \\ n + \alpha_n \end{bmatrix} \quad (\text{A.6})$$

One can see that the PDF of Eq. A.4 can be rewritten as:

$$p(x, y) = \frac{1}{2\pi\sigma^2} \exp\left(\frac{1}{2\sigma^2} \mathbf{a}^T \mathbf{a}\right) \quad (\text{A.7})$$

Calculating $\mathbf{a}^T \mathbf{a}$ on the right-hand-side of Eq. A.6, we have that:

$$\mathbf{a}^T \mathbf{a} = [l \quad n + \alpha_n] \mathbf{R}_z \mathbf{R}_z^T \begin{bmatrix} l \\ n + \alpha_n \end{bmatrix} = [l \quad n + \alpha_n] \begin{bmatrix} l \\ n + \alpha_n \end{bmatrix} = l^2 + (n + \alpha_n)^2 \quad (\text{A.8})$$

Plugging Eq. A.8 into Eq. A.7, we have that:

$$p(l, n) = \frac{1}{2\pi\sigma^2} \exp\left(\frac{1}{2\sigma^2} \left[l^2 + (n + \alpha_n)^2\right]\right) \quad (\text{A.9})$$

Now we calculate the marginal PDF along the direction l . This is accomplished by:

$$p(l) = \int_{-\infty}^{\infty} p(l, n) \, dn = \int_{-\infty}^{\infty} \frac{1}{2\pi\sigma^2} \exp\left(\frac{1}{2\sigma^2} \left[l^2 + (n + \alpha_n)^2\right]\right) \, dn \quad (\text{A.10})$$

$$= \frac{1}{\sqrt{2\pi\sigma^2}} \exp\left(\frac{1}{2\sigma^2} l^2\right) \int_{-\infty}^{\infty} \frac{1}{\sqrt{2\pi\sigma^2}} \exp\left(\frac{1}{2\sigma^2} (n + \alpha_n)^2\right) \, dn \quad (\text{A.11})$$

Making the substitution $N \triangleq n + \alpha_n$, we have that $dn = dN$, implying:

$$p(l) = \frac{1}{\sqrt{2\pi\sigma^2}} \exp\left(\frac{1}{2\sigma^2} l^2\right) \underbrace{\int_{-\infty}^{\infty} \frac{1}{\sqrt{2\pi\sigma^2}} \exp\left(\frac{1}{2\sigma^2} N^2\right) \, dN}_{=1} = \frac{1}{\sqrt{2\pi\sigma^2}} \exp\left(\frac{1}{2\sigma^2} l^2\right) \quad (\text{A.12})$$

Inspecting Eq. A.12, we notice that the random variable l is normally distributed with mean $\mathbb{E}[l] = 0$ and variance $\text{var}[l] = \sigma^2$, i.e., $l \sim \mathcal{N}(0, \sigma^2)$.

□

Lemma 5. *Assume a bivariate normally-distributed random variable $\mathbf{X} \in \mathbb{R}^2$ with mean $\boldsymbol{\mu}$ and covariance matrix \mathbf{P} (not necessarily diagonal), which is*

decomposed in the form $\mathbf{P} = \mathbf{Q}\mathbf{Q}^T$. The Probability Density Function (PDF) for this random variable is given by:

$$p(\mathbf{X}) = \frac{1}{2\pi\sqrt{|\mathbf{P}|}} \exp\left(\frac{1}{2} [(\mathbf{X} - \boldsymbol{\mu})^T \mathbf{P}^{-1} (\mathbf{X} - \boldsymbol{\mu})]\right) \quad (\text{A.13})$$

Then the marginal PDF of Eq. A.4 along any line $L(\mathbf{l}_0, \vec{\mathbf{l}})$ is a one-dimensional normally-distributed random variable with mean at \mathbf{l}_0^* and standard deviation σ along the $\vec{\mathbf{l}}$ direction, where:

$$\mathbf{l}_0^* = \mathbf{l}_0 + \frac{1}{\sigma^2} [(\boldsymbol{\mu} - \mathbf{l}_0)^T \mathbf{P}^{-1} \vec{\mathbf{l}}] \vec{\mathbf{l}}, \quad \sigma = \frac{1}{\|\mathbf{Q}^{-1} \vec{\mathbf{l}}\|} = \frac{1}{\sqrt{\vec{\mathbf{l}}^T \mathbf{P}^{-1} \vec{\mathbf{l}}}}. \quad (\text{A.14})$$

Proof. The random variable \mathbf{X} can be represented as:

$$\mathbf{X} = \boldsymbol{\mu} + \boldsymbol{\epsilon}, \quad (\text{A.15})$$

where $\boldsymbol{\epsilon} \sim \mathcal{N}(\mathbf{0}, \mathbf{P})$. Introducing a state transformation $\mathbf{Y} = \mathbf{Q}^{-1}\mathbf{X}$, we have that:

$$\mathbf{Y} = \mathbf{Q}^{-1}\boldsymbol{\mu} + \mathbf{Q}^{-1}\boldsymbol{\epsilon}. \quad (\text{A.16})$$

Defining the new variables $\boldsymbol{\mu}_Y \triangleq \mathbf{Q}^{-1}\boldsymbol{\mu}$ and $\boldsymbol{\epsilon}_Y = \mathbf{Q}^{-1}\boldsymbol{\epsilon}$, it follows that $\mathbf{Y} \sim \mathcal{N}(\boldsymbol{\mu}_Y, \mathbf{I})$ and $\boldsymbol{\epsilon}_Y \sim \mathcal{N}(\mathbf{0}, \mathbf{I})$. In addition, the line $L(\mathbf{l}_0, \vec{\mathbf{l}})$ gets transformed into the new state-space as $L_Y(\mathbf{l}_{0Y}, \vec{\mathbf{l}}_Y)$, where:

$$\mathbf{l}_{0Y} = \mathbf{Q}^{-1}\mathbf{l}_0, \quad \vec{\mathbf{l}}_Y = \frac{\mathbf{Q}^{-1}\vec{\mathbf{l}}}{\|\mathbf{Q}^{-1}\vec{\mathbf{l}}\|} \quad (\text{A.17})$$

One should notice that any displacement S along the $\vec{\mathbf{l}}$ direction is equivalent to a displacement $S_Y = S \cdot \|\mathbf{Q}^{-1}\vec{\mathbf{l}}\|$ along the $\vec{\mathbf{l}}_Y$ direction.

Using the result from Lemma 4, the marginal distribution of the random variable \mathbf{Y} along the line $L_Y(\mathbf{l}_{0Y}, \vec{\mathbf{l}}_Y)$ is given by $l_Y \sim \mathcal{N}(\mathbf{l}_{0Y}^*, 1)$, where:

$$\mathbf{l}_{0Y}^* = \mathbf{l}_{0Y} + [(\boldsymbol{\mu}_Y - \mathbf{l}_{0Y})^T \vec{\mathbf{l}}_Y] \vec{\mathbf{l}}_Y \quad (\text{A.18})$$

Transforming Eq. A.18 into the original coordinates, and using the transformations $\mathbf{l}_{0Y} = \mathbf{Q}^{-1}\mathbf{l}_0$ and $\boldsymbol{\mu}_Y = \mathbf{Q}^{-1}\boldsymbol{\mu}$, we have that:

$$\begin{aligned} \mathbf{l}_0^* &= \mathbf{Q}\mathbf{l}_{0Y}^* = \mathbf{Q}\mathbf{Q}^{-1}\mathbf{l}_0 + \frac{\mathbf{Q}}{\|\mathbf{Q}^{-1}\vec{\mathbf{l}}\|^2} [(\mathbf{Q}^{-1}\boldsymbol{\mu} - \mathbf{Q}^{-1}\mathbf{l}_0)^T \mathbf{Q}^{-1}\vec{\mathbf{l}}] \mathbf{Q}^{-1}\vec{\mathbf{l}} \\ &= \mathbf{l}_0 + \frac{1}{\vec{\mathbf{l}}^T \mathbf{P}^{-1} \vec{\mathbf{l}}} [(\boldsymbol{\mu} - \mathbf{l}_0)^T \mathbf{Q}^{-T} \mathbf{Q}^{-1} \vec{\mathbf{l}}] \vec{\mathbf{l}} \\ &= \mathbf{l}_0 + \frac{1}{\vec{\mathbf{l}}^T \mathbf{P}^{-1} \vec{\mathbf{l}}} [(\boldsymbol{\mu} - \mathbf{l}_0)^T \mathbf{P}^{-1} \vec{\mathbf{l}}] \vec{\mathbf{l}} \end{aligned} \quad (\text{A.19})$$

Since $l_Y \sim \mathcal{N}(\mathbf{l}_{0Y}^*, 1)$ and any displacement S along the $\vec{\mathbf{l}}$ direction is equivalent to a displacement $S_Y = S \cdot \|\mathbf{Q}^{-1}\vec{\mathbf{l}}\|$ along the $\vec{\mathbf{l}}_Y$ direction, then a standard deviation $\sigma_Y = 1$ in the $\vec{\mathbf{l}}_Y$ direction is equivalent to a standard deviation

$$\sigma = \|\mathbf{Q}^{-1}\vec{\mathbf{l}}\|^{-1} \quad (\text{A.20})$$

in the $\vec{\mathbf{l}}$ direction. □

A.3 Statistics of the Spherical Uniform Distribution

In this section we prove that if $\mathbf{e} \in \mathbb{S}^2$ is a unit vector uniformly distributed in the 3-D unit sphere, then: $\mathbb{E}[\mathbf{e}] = \mathbf{0}$ and $\mathbb{E}[\mathbf{e}\mathbf{e}^T] = \frac{1}{3}\mathbf{I}$.

Assume a unit radius sphere and a cylinder of radius $r = 1$ and height $h = 2$. According with Archimedes' Hat-Box Theorem [21], if we slice both the cylinder and the sphere at the same height as shown on Fig. A.2, then the lateral surface area of the spherical segment (S_1) is equal to the lateral surface area of the cylindrical segment (S_2).

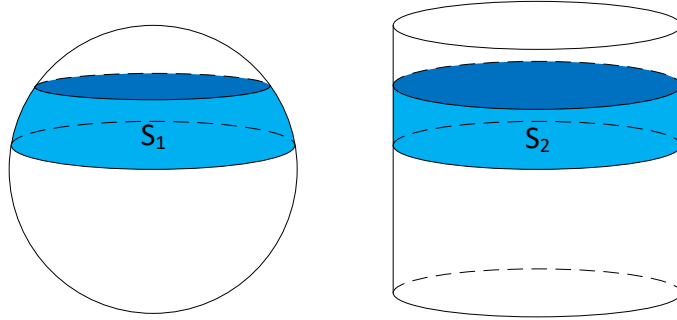


Figure A.2: Illustration of Archimedes' Hat-Box Theorem.

More specifically, the surface area S of the cylinder parametrized with radius $r = 1$ and height $h = 2$ is the same as the unit-radius sphere, i.e., $S = 4\pi$. A commonly used method [68] to generate uniformly distributed samples on a sphere $\mathbf{e} \in \mathbb{S}^2$ is to uniformly sample a point in the cylinder through a height value $z \sim \mathcal{U}[-1, 1]$, and an angle value $\phi \sim \mathcal{U}[-\pi, \pi]$, and then map it to the sphere through the transformation:

$$\mathbf{e} = \begin{bmatrix} \sqrt{1 - z^2} \cos(\phi) \\ \sqrt{1 - z^2} \sin(\phi) \\ z \end{bmatrix}. \quad (\text{A.21})$$

The transformation of Eq. A.21 guarantees that areas in the cylinder are preserved in the sphere after the projection. Therefore, if a random variable

is uniformly distributed in the prior space (cylindrical space), then it should still be uniformly distributed in the posterior space (spherical space).

Denoting $P_z(x)$ and $P_\phi(x)$ as the probability distributions of the scalar variables z and ϕ respectively, then:

$$\begin{aligned}
\mathbb{E}[z] &= \int_{-1}^1 x P_z(x) dx = \frac{1}{2} \int_{-1}^1 x dx = \frac{1}{4} x^2 \Big|_{-1}^1 = 0 \\
\mathbb{E}[z^2] &= \int_{-1}^1 x^2 P_z(x) dx = \frac{1}{2} \int_{-1}^1 x^2 dx = \frac{1}{6} x^3 \Big|_{-1}^1 = \frac{1}{3} \\
\mathbb{E}[1 - z^2] &= 1 - \frac{1}{3} = \frac{2}{3} \\
\mathbb{E}[\cos \phi] &= \int_{-\pi}^{\pi} \cos x P_\phi(x) dx = \frac{1}{2\pi} \int_{-\pi}^{\pi} \cos x dx = \frac{1}{2\pi} \sin x \Big|_{-\pi}^{\pi} = 0 \\
\mathbb{E}[\sin \phi] &= \int_{-\pi}^{\pi} \sin x P_\phi(x) dx = \frac{1}{2\pi} \int_{-\pi}^{\pi} \sin x dx = -\frac{1}{2\pi} \cos x \Big|_{-\pi}^{\pi} = 0 \\
\mathbb{E}[\cos \phi \sin \phi] &= \int_{-\pi}^{\pi} \cos x \sin x P_\phi(x) dx = \frac{1}{2\pi} \int_{-\pi}^{\pi} \cos x \sin x dx = 0 \\
\mathbb{E}[\cos^2 \phi] &= \int_{-\pi}^{\pi} \cos^2 x P_\phi(x) dx = \frac{1}{2\pi} \int_{-\pi}^{\pi} \cos^2 x dx = \frac{1}{2} \\
\mathbb{E}[\sin^2 \phi] &= \int_{-\pi}^{\pi} \sin^2 x P_\phi(x) dx = \frac{1}{2\pi} \int_{-\pi}^{\pi} \sin^2 x dx = \frac{1}{2}
\end{aligned}$$

Therefore, given that z and ϕ are independently distributed, we have that:

$$\mathbb{E}[\mathbf{e}] = \begin{bmatrix} \mathbb{E}[\sqrt{1 - z^2} \cos(\phi)] \\ \mathbb{E}[\sqrt{1 - z^2} \sin(\phi)] \\ \mathbb{E}[z] \end{bmatrix} = \begin{bmatrix} \mathbb{E}[\sqrt{1 - z^2}] \mathbb{E}[\cos(\phi)] \\ \mathbb{E}[\sqrt{1 - z^2}] \mathbb{E}[\sin(\phi)] \\ \mathbb{E}[z] \end{bmatrix} = \begin{bmatrix} 0 \\ 0 \\ 0 \end{bmatrix}. \quad (\text{A.22})$$

Also, we have that:

$$\begin{aligned}\mathbb{E}[\mathbf{e}\mathbf{e}^T] &= \mathbb{E} \left[\begin{bmatrix} (1-z^2)\cos^2\phi & (1-z^2)\cos\phi\sin\phi & (1-z^2)z\cos\phi \\ (1-z^2)\cos\phi\sin\phi & (1-z^2)\sin^2\phi & (1-z^2)z\sin\phi \\ (1-z^2)z\cos\phi & (1-z^2)z\sin\phi & z^2 \end{bmatrix} \right] \\ &= \frac{1}{3}\mathbf{I}.\end{aligned}\tag{A.23}$$

A.4 Multiplicative Extended Kalman Filter Formulation

We present the Multiplicative Extended Kalman Filter (MEKF) formulation for the problem in hand. The filter herein presented is based on the formulations in [34] and [36]. However, our equations differ from the works cited since we do not have gyroscope measurements, and we do not estimate the gyroscope measurement bias. In addition, the assumption that the angular velocity is constant implies no process noise in the dynamics propagation.

We define the reference trajectory kinematics:

$$\dot{\mathbf{q}}_R = \frac{1}{2}\boldsymbol{\omega}_R \otimes \mathbf{q}_R,\tag{A.24}$$

where $\mathbf{q}_R \triangleq [q_{Rs} \quad \mathbf{q}_{Rv}^T]^T$ is the reference quaternion and $\boldsymbol{\omega}_R$ is the reference angular velocity of the reference attitude. The true attitude \mathbf{q} can be represented as:

$$\mathbf{q} = \delta\mathbf{q} \otimes \mathbf{q}_R,\tag{A.25}$$

where $\delta\mathbf{q} \triangleq [\delta q_s \quad \delta \mathbf{q}_v^T]^T$ represents the rotation from \mathbf{q}_R to the true rotation.

Differentiating Eq. A.25, we get:

$$\dot{\mathbf{q}} = \delta\dot{\mathbf{q}} \otimes \mathbf{q}_R + \delta\mathbf{q} \otimes \dot{\mathbf{q}}_R \quad \implies \quad \frac{1}{2}\boldsymbol{\omega} \otimes \mathbf{q} = \delta\dot{\mathbf{q}} \otimes \mathbf{q}_R + \frac{1}{2}\delta\mathbf{q} \otimes \boldsymbol{\omega}_R \otimes \mathbf{q}_R. \quad (\text{A.26})$$

Post-multiplying Eq. A.26 by \mathbf{q}_R^{-1} and isolating $\delta\dot{\mathbf{q}}$, we get:

$$\begin{aligned} \delta\dot{\mathbf{q}} &= \frac{1}{2} (\boldsymbol{\omega} \otimes \mathbf{q} \otimes \mathbf{q}_R^{-1} - \delta\mathbf{q} \otimes \boldsymbol{\omega}_R) = \frac{1}{2} (\boldsymbol{\omega} \otimes \delta\mathbf{q} - \delta\mathbf{q} \otimes \boldsymbol{\omega}_R) \\ &= \frac{1}{2} \left(\begin{bmatrix} 0 & -\boldsymbol{\omega} \\ \boldsymbol{\omega} & -[\boldsymbol{\omega}_\times] \end{bmatrix} \begin{bmatrix} \delta q_s \\ \delta \mathbf{q}_v \end{bmatrix} - \begin{bmatrix} \delta q_s & -\delta \mathbf{q}_v^T \\ \delta \mathbf{q}_v & \delta q_s \mathbf{I} - [\delta \mathbf{q}_v \times] \end{bmatrix} \begin{bmatrix} 0 \\ \boldsymbol{\omega}_R \end{bmatrix} \right) \end{aligned} \quad (\text{A.27})$$

After some algebraic manipulations, we get that:

$$\delta\dot{\mathbf{q}}_s = (\boldsymbol{\omega}_R - \boldsymbol{\omega})^T \delta \mathbf{q}_v, \quad \delta\dot{\mathbf{q}}_v = (\boldsymbol{\omega} - \boldsymbol{\omega}_R) \delta \mathbf{q}_s - (\boldsymbol{\omega} + \boldsymbol{\omega}_R) \times \delta \mathbf{q}_v.$$

We define the scaled attitude error Gibbs vector:

$$\delta \mathbf{g} \triangleq 2 \frac{\delta \mathbf{q}_v}{\delta q_s}, \quad (\text{A.28})$$

The Gibbs vector associated with the noise quaternion of Eq. 2.25 is given by:

$$\mathbf{g}_{Nk} = 2 \mathbf{e}_{Nk} \tan \frac{\theta_k}{2}. \quad (\text{A.29})$$

The transformation from *Gibbs vector* to quaternion is done as follows:

$$\delta q_s = \sqrt{\frac{2}{2 + \|\delta \mathbf{g}\|^2}}, \quad \delta \mathbf{q}_v = \frac{1}{2} \delta q_s \delta \mathbf{g}. \quad (\text{A.30})$$

One should notice that $\mathbb{E}[\mathbf{g}_N] = 0$. In addition, assuming a small angle approximation, then $\tan^2 \frac{\theta_k}{2} \approx \frac{\theta_k^2}{4}$, leading to $\mathbb{E}[\mathbf{g}_N \mathbf{g}_N^T] = \frac{1}{3} \sigma_\theta^2 \mathbf{I}$.

The Gibbs error kinematics is described as:

$$\delta\dot{\mathbf{g}} = 2\frac{\delta\dot{\mathbf{q}}_v}{\delta\mathbf{q}_s} - 2\frac{\delta\mathbf{q}_v}{\delta\mathbf{q}_s}\frac{\delta\dot{\mathbf{q}}_s}{\delta\mathbf{q}_s} = [\mathbf{I} + \frac{1}{4}\delta\mathbf{g}\delta\mathbf{g}^T] (\boldsymbol{\omega} - \boldsymbol{\omega}_R) - \frac{1}{2} (\boldsymbol{\omega} + \boldsymbol{\omega}_R) \times \delta\mathbf{g}.$$

Assuming the first order approximations $\delta\mathbf{g}\delta\mathbf{g}^T \approx 0$, and $\delta\boldsymbol{\omega} \times \delta\mathbf{g} \approx 0$, we get to:

$$\delta\dot{\mathbf{g}} \approx \delta\boldsymbol{\omega} - \boldsymbol{\omega}_R \times \delta\mathbf{g}. \quad (\text{A.31})$$

Defining the state vector $\mathbf{X} \triangleq [\delta\mathbf{g}^T \ \boldsymbol{\omega}^T]^T$ and the dynamics of Eq. A.31, then we have the linearized state dynamics:

$$\dot{\mathbf{X}} = \underbrace{\begin{bmatrix} -[\boldsymbol{\omega} \times] & \mathbf{I}_3 \\ \mathbf{0}_3 & \mathbf{0}_3 \end{bmatrix}}_{\triangleq \mathbf{A}} \mathbf{X}. \quad (\text{A.32})$$

We define the state transition matrix:

$$\mathbf{A}_d[k] \triangleq e^{A\delta_k}, \quad \delta_k \triangleq t_{k+1} - t_k. \quad (\text{A.33})$$

In the propagation step, the following equations are used:

$$\mathbf{q}_{k+1|k} = \mathbf{F}(\boldsymbol{\omega}_{k|k})\mathbf{q}_{k|k},$$

$$\boldsymbol{\omega}_{k+1|k} = \boldsymbol{\omega}_{k|k},$$

$$\mathbf{P}_{k+1|k} = \mathbf{A}_d[k]\mathbf{P}_{k|k}\mathbf{A}_d^T[k],$$

where $\mathbf{P}_{k|k} \triangleq \mathbb{E}[\mathbf{X}_{k|k}\mathbf{X}_{k|k}^T]$, and $\mathbf{P}_{k+1|k} \triangleq \mathbb{E}[\mathbf{X}_{k+1|k}\mathbf{X}_{k+1|k}^T]$, and $\mathbf{F}(\boldsymbol{\omega}_{k|k})$ is defined in Eq. 2.23.

As for the measurement model, only quaternion measurements are available. The innovation term is given by:

$$\boldsymbol{\nu}_k = 2 \frac{\tilde{\mathbf{q}}_v[k]}{\tilde{q}_s[k]}, \quad (\text{A.34})$$

where $\tilde{q}_s[k]$ and $\tilde{\mathbf{q}}_v[k]$ are, respectively, the scalar and vector parts of $\tilde{\mathbf{q}}_k$, defined as:

$$\tilde{\mathbf{q}}_k \triangleq \begin{bmatrix} \tilde{q}_s[k] \\ \tilde{\mathbf{q}}_v[k] \end{bmatrix} \triangleq \hat{\mathbf{q}}_k \otimes \mathbf{q}_{k|k-1}^{-1}.$$

Assuming the measurement noise defined in Eq. A.29, the measurement covariance is given by $\mathbf{R}_k \triangleq \mathbb{E}[\mathbf{g}_N \mathbf{g}_N^T] = \frac{1}{3} \sigma_\theta^2 \mathbf{I}$.

The measurement update step uses the following expressions:

$$\begin{aligned} \mathbf{H}_k &= [\mathbf{I}_3 \quad \mathbf{0}_3], \\ \mathbf{S}_k &= \mathbf{H}_k \mathbf{P}_{k|k-1} \mathbf{H}_k^T + \mathbf{R}_k, \\ \mathbf{K}_k &= \mathbf{P}_{k|k-1} \mathbf{H}_k^T \mathbf{S}_k^{-1}, \\ \Delta \mathbf{x}_{k|k} &= \mathbf{K}_k \boldsymbol{\nu}_k, \\ \mathbf{P}_{k|k} &= (\mathbf{I} - \mathbf{K}_k \mathbf{H}_k) \mathbf{P}_{k|k-1} (\mathbf{I} - \mathbf{K}_k \mathbf{H}_k)^T + \mathbf{K}_k \mathbf{R}_k \mathbf{K}_k^T, \end{aligned}$$

where $\Delta \mathbf{x}_{k|k} \triangleq [\Delta x_1 \quad \Delta x_2 \quad \Delta x_3 \quad \Delta x_4 \quad \Delta x_5 \quad \Delta x_6]^T$ is the incremental state update typical for standard EKF formulations.

The updated state $\delta \mathbf{g}_{k|k}$ can be obtained from $\Delta \mathbf{x}_{k|k}$ as $\delta \mathbf{g}_{k|k} = [\Delta x_1 \quad \Delta x_2 \quad \Delta x_3]^T$. Bearing in mind that $\delta \mathbf{g}_{k|k}$ represents the attitude error respective to $\delta \mathbf{q}_k$ (see Eqs. A.25 and A.28), then $\delta \mathbf{q}_{k|k}$ can be obtained from $\delta \mathbf{g}_{k|k}$ using the transformation in Eq. A.30. Defining $\Delta \boldsymbol{\omega} =$

$[\Delta x_4 \ \Delta x_5 \ \Delta x_6]^T$, the updated states are given by:

$$\mathbf{q}_{k|k} = \delta \mathbf{q}_{k|k} \otimes \mathbf{q}_{k|k-1},$$

$$\boldsymbol{\omega}_{k|k} = \boldsymbol{\omega}_{k|k-1} + \Delta \boldsymbol{\omega}.$$

Appendix B

Appendices for Chapter 4

B.1 Boundedness of $\mu^{\alpha_1} \boldsymbol{\sigma}$

In this section, we prove that if:

$$\mu^\lambda(t) \ln(1 + \boldsymbol{\sigma}^T(t) \boldsymbol{\sigma}(t)) \leq V_0(0) \exp[-kt_f \cdot \bar{\mu}(t)], \quad (\text{B.1})$$

then $\mu^{\alpha_1} \boldsymbol{\sigma} \in L_\infty, \forall \alpha_1 \in \mathbb{R}$.

Starting from Eq. B.1, we use the definition $\bar{\mu}(t) \triangleq \mu(t) - 1$ to get:

$$\begin{aligned} \mu^\lambda(t) \ln(1 + \boldsymbol{\sigma}^T(t) \boldsymbol{\sigma}(t)) &\leq V_0(0) \exp[-kt_f \cdot (\mu(t) - 1)] \\ &= V_0(0) e^{kt_f} \exp[-kt_f \cdot \mu(t)] \\ &= \alpha_2 \exp[-kt_f \cdot \mu(t)], \end{aligned} \quad (\text{B.2})$$

where $\alpha_2 \triangleq V_0(0) e^{kt_f} > 0$.

Defining $\beta(t) \triangleq \exp[-kt_f \cdot \mu(t)]$, it follows that:

$$\begin{aligned}
\mu^\lambda(t) \ln(1 + \boldsymbol{\sigma}^T(t)\boldsymbol{\sigma}(t)) &\leq \alpha_2\beta(t) \\
\ln(1 + \boldsymbol{\sigma}^T(t)\boldsymbol{\sigma}(t)) &\leq \alpha_2\mu^{-\lambda}(t)\beta(t) \\
1 + \boldsymbol{\sigma}^T(t)\boldsymbol{\sigma}(t) &\leq \exp[\alpha_2\mu^{-\lambda}(t)\beta(t)] \\
\boldsymbol{\sigma}^T(t)\boldsymbol{\sigma}(t) &\leq \exp[\alpha_2\mu^{-\lambda}(t)\beta(t)] - 1 \\
\mu^{2\alpha_1}(t)\boldsymbol{\sigma}^T(t)\boldsymbol{\sigma}(t) &\leq \mu^{2\alpha_1}(t) [\exp[\alpha_2\mu^{-\lambda}(t)\beta(t)] - 1] \\
\|\mu^{\alpha_1}(t)\boldsymbol{\sigma}(t)\|^2 &\leq \frac{\exp[\alpha_2\mu^{-\lambda}(t)\beta(t)] - 1}{\mu^{-2\alpha_1}(t)}. \tag{B.3}
\end{aligned}$$

In order to show that the signal $f(t) \triangleq \|\mu^{\alpha_1}(t)\boldsymbol{\sigma}(t)\|^2$ is bounded, we need to evaluate the limit as $t \rightarrow t_f$. Taking the limit on both sides:

$$\lim_{t \rightarrow t_f} f(t) \leq \lim_{t \rightarrow t_f} \frac{\exp[\alpha_2\mu^{-\lambda}(t)\beta(t)] - 1}{\mu^{-2\alpha_1}(t)}. \tag{B.4}$$

The above limit can be rewritten as:

$$\lim_{t \rightarrow t_f} f(t) \leq \lim_{\mu \rightarrow \infty} \frac{\exp[\alpha_2\mu^{-\lambda} \exp[-k \cdot t_f \cdot \mu]] - 1}{\mu^{-2\alpha_1}}. \tag{B.5}$$

Assuming that $\lambda < 2\alpha_1$, Lemmas 6 and 7 are used to prove that the right-hand side of Eq. B.5 is equal to zero, implying that $\|\mu^{\alpha_1}(t)\boldsymbol{\sigma}(t)\|^2 \in L_\infty, \forall \alpha_1 > \lambda/2$. In addition, since $\|\mu^{\eta_1}(t)\boldsymbol{\sigma}(t)\|^2 \leq \|\mu^{\eta_2}(t)\boldsymbol{\sigma}(t)\|^2$, for $\eta_1 \leq \eta_2$, then $\|\mu^{\alpha_1}(t)\boldsymbol{\sigma}(t)\|^2 \in L_\infty, \forall \alpha_1 \in \mathbb{R}$.

Lemma 6. *For any finite real constants $\alpha_1 \neq 0, \alpha_2 > 0, \gamma_1 > 0, \gamma_2 > 0$, then:*

$$\lim_{x \rightarrow 0^+} \alpha_1 x^{-\gamma_1} \exp[-\alpha_2 x^{-\gamma_2}] = 0. \tag{B.6}$$

Proof. Making the substitution $y = x^{-\gamma_2}$, then:

$$\lim_{x \rightarrow 0^+} \alpha_1 x^{-\gamma_1} \exp[-\alpha_2 x^{-\gamma_2}] = \lim_{y \rightarrow \infty} \alpha_1 y^{\gamma_3 + \gamma_4} e^{-\alpha_2 y}, \quad (\text{B.7})$$

where $\gamma_3 \in \mathbb{N} \triangleq \lfloor \gamma_1/\gamma_2 \rfloor$ and $\gamma_4 \in [0, 1) \triangleq \gamma_1/\gamma_2 - \gamma_3$.

One can notice that the limit in Eq. B.7 is a product of zero with ∞ , which can be solved for by using L'Hospital's rule. Defining $\gamma_5 \triangleq \gamma_3 + \gamma_4$, we apply L'Hospital's rule γ_3 times, leading to:

$$\begin{aligned} \lim_{y \rightarrow \infty} \alpha_1 y^{\gamma_5} e^{-\alpha_2 y} &= \lim_{y \rightarrow \infty} -\alpha_1 \alpha_2 \gamma_5 y^{\gamma_5 - 1} e^{-\alpha_2 y} \\ &= \lim_{y \rightarrow \infty} \alpha_1 \alpha_2^2 \gamma_5 (\gamma_5 - 1) y^{\gamma_5 - 2} e^{-\alpha_2 y} \\ &= \dots \\ &= \lim_{y \rightarrow \infty} (-1)^{\gamma_3} \alpha_1 \alpha_2^{\gamma_3} \gamma_5 (\gamma_5 - 1) \dots (\gamma_5 - \gamma_3) y^{\gamma_4} e^{-\alpha_2 y}. \end{aligned} \quad (\text{B.8})$$

If $\gamma_4 = 0$, then the proof is complete. However, if $\gamma_4 \in (0, 1)$, then we need to use L'Hospital's rule one more time:

$$\lim_{y \rightarrow \infty} \alpha_1 y^{\gamma_5} e^{-\alpha_2 y} = \lim_{y \rightarrow \infty} (-1)^{\gamma_3 + 1} \alpha_1 \alpha_2^{\gamma_3 + 1} \gamma_5 (\gamma_5 - 1) \dots (\gamma_5 - \gamma_3) \gamma_4 y^{\gamma_4 - 1} e^{-\alpha_2 y} = 0. \quad (\text{B.9})$$

□

Lemma 7. For any finite real constants $\alpha_1 > 0$, $\alpha_2 > 0$, and $0 < \gamma_1 \leq \gamma_2 < \gamma_3$, then $\lim_{x \rightarrow \infty} f(x) = 0$, where:

$$f(x) = \frac{\exp[\alpha_1 x^{-\gamma_2} \exp[-\alpha_2 x^{\gamma_1}]] - 1}{x^{-\gamma_3}}. \quad (\text{B.10})$$

Proof. Defining $y \triangleq x^{-\gamma_3}$, we have that $y^{-\gamma_4} = x^{\gamma_1}$, and $y^{\gamma_5} = x^{-\gamma_2}$, where $\gamma_4 \triangleq \frac{\gamma_1}{\gamma_3}$ and $\gamma_5 \triangleq \frac{\gamma_2}{\gamma_3}$. Since $0 < \gamma_1 \leq \gamma_2 < \gamma_3$, then $0 < \gamma_4 \leq \gamma_5 < 1$. The limit can be rewritten as:

$$\lim_{x \rightarrow \infty} f(x) = \lim_{y \rightarrow 0^+} f(y) = \frac{\exp[\alpha_1 y^{\gamma_5} \exp[-\alpha_2 y^{-\gamma_4}]] - 1}{y}. \quad (\text{B.11})$$

For notation simplicity, we define $\beta(y) \triangleq \exp[-\alpha_2 y^{-\gamma_4}]$, leading to:

$$\lim_{y \rightarrow 0^+} f(y) = \lim_{y \rightarrow 0^+} \frac{\exp[\alpha_1 y^{\gamma_5} \beta(y)] - 1}{y}. \quad (\text{B.12})$$

It is straightforward to see that $\lim_{y \rightarrow 0^+} \beta(y) = 0$ and that $\lim_{y \rightarrow 0^+} e^{\alpha_1 y^{\gamma_5} \beta(y)} = 1$. Since this limit is a ratio of zero with zero, we can use L'Hospital's rule to show that the right-hand side of Eq. B.12 converges to zero as $y \rightarrow 0^+$. We define the numerator signal as:

$$n(y) \triangleq e^{\alpha_1 y^{\gamma_5} \beta(y)} - 1. \quad (\text{B.13})$$

Clearly, it is sufficient to prove that if $\lim_{y \rightarrow 0^+} \frac{dn(y)}{dy} = 0$, then

$$\lim_{y \rightarrow 0^+} \frac{e^{\alpha_1 y^{\gamma_5} \beta(y)} - 1}{y} = 0, \quad (\text{B.14})$$

implying that $\lim_{y \rightarrow 0^+} f(y) = 0$. Using the notation $f' \triangleq \frac{\partial f}{\partial y}$ the derivative of $n(y)$ is given by:

$$n'(y) = \alpha_1 \left(\frac{\gamma_5}{y^{\gamma_6}} \beta(y) + y^{\gamma_5} \beta'(y) \right) e^{\alpha_1 y^{\gamma_5} \beta(y)}, \quad (\text{B.15})$$

where $\gamma_6 > 0$ is defined as $\gamma_6 \triangleq 1 - \gamma_5$. Given that

$$\beta'(y) = \alpha_2 \gamma_4 y^{-\gamma_4-1} \exp[-\alpha_2 y^{-\gamma_4}] = \frac{\alpha_2 \gamma_4}{y^{\gamma_7}} \beta(y), \quad (\text{B.16})$$

for $\gamma_7 \triangleq 1 + \gamma_4 > 1$, we can substitute Eq. B.16 into Eq. B.15:

$$n'(y) = \alpha_1 \left(\frac{\gamma_5}{y^{\gamma_6}} \beta(y) + \frac{\alpha_2 \gamma_4}{y^{\gamma_7 - \gamma_5}} \beta(y) \right) e^{\alpha_1 y^{\gamma_5} \beta(y)}. \quad (\text{B.17})$$

One should note that since $\gamma_7 > 1$ and $0 < \gamma_5 < 1$, then $\gamma_7 - \gamma_5 > 0$. Using Lemma 6 and the definition $\beta(y) \triangleq \exp[-\alpha_2 y^{-\gamma_4}]$, then:

$$\begin{cases} \lim_{\xi \rightarrow 0^+} \frac{\gamma_5}{y^{\gamma_6}} \beta(y) = 0, \\ \lim_{\xi \rightarrow 0^+} \frac{\alpha_2 \gamma_4}{y^{\gamma_7 - \gamma_5}} \beta(y) = 0 \end{cases}. \quad (\text{B.18})$$

Remembering that $\lim_{y \rightarrow 0^+} \beta(y) = 0$, and that $\lim_{y \rightarrow 0^+} e^{\alpha_1 y^{\gamma_5} \beta(y)} = 1$, then $\lim_{y \rightarrow 0^+} n'(y) = 0$, which implies that $\lim_{x \rightarrow \infty} f(x) = 0$. \square

B.2 Convergence proof for $\mu^\rho(t)\boldsymbol{\sigma}(t)$

In this section, we show that the inequality

$$\mu^\lambda(t) \ln(1 + \boldsymbol{\sigma}^T(t)\boldsymbol{\sigma}(t)) \leq \bar{V}, \quad (\text{B.19})$$

for a constant $\bar{V} > 0$, implies that $\mu^{\lambda/2}\boldsymbol{\sigma} \in L_\infty$ and that $\lim_{t \rightarrow t_f} \mu^\rho(t)\boldsymbol{\sigma}(t) = 0$, $\forall \rho < \lambda/2$.

Starting from Eq. B.19, we have that:

$$\boldsymbol{\sigma}^T(t)\boldsymbol{\sigma}(t) \leq \exp[\bar{V}\mu^{-\lambda}(t)] - 1 \quad (\text{B.20})$$

$$\mu^\lambda(t)\boldsymbol{\sigma}^T(t)\boldsymbol{\sigma}(t) \leq \mu^\lambda(t) [\exp[\bar{V}\mu^{-\lambda}(t)] - 1] \quad (\text{B.21})$$

$$\|\mu^{\lambda/2}(t)\boldsymbol{\sigma}(t)\|^2 \leq \frac{\exp[\bar{V}\mu^{-\lambda}(t)] - 1}{\mu^{-\lambda}(t)}. \quad (\text{B.22})$$

In order to show that the signal $f(t) \triangleq \|\mu^{\lambda/2}(t)\boldsymbol{\sigma}(t)\|^2$ is bounded, we need to evaluate the limit as $t \rightarrow t_f$. Taking the limit on both sides:

$$\lim_{t \rightarrow t_f} f(t) \leq \lim_{t \rightarrow t_f} \frac{\exp[\bar{V}\mu^{-\lambda}(t)] - 1}{\mu^{-\lambda}(t)}. \quad (\text{B.23})$$

Assuming $\lambda > 0$, the above limit can be rewritten as:

$$\lim_{t \rightarrow t_f} f(t) \leq \lim_{\mu \rightarrow \infty} \frac{\exp[\bar{V}\mu^{-\lambda}] - 1}{\mu^{-\lambda}}. \quad (\text{B.24})$$

Defining $\xi(t) \triangleq \mu^{-\lambda}(t)$, we have that:

$$\lim_{t \rightarrow t_f} f(t) \leq \lim_{\xi \rightarrow 0^+} \frac{\exp[\bar{V}\xi] - 1}{\xi}. \quad (\text{B.25})$$

Since the above limit is a ratio of zero with zero, we can use L'Hospital's rule:

$$\lim_{t \rightarrow t_f} f(t) \leq \lim_{\xi \rightarrow 0^+} \frac{\frac{d}{d\xi} [\exp[\bar{V}\xi] - 1]}{\frac{d}{d\xi} \xi} \quad (\text{B.26})$$

$$= \lim_{\xi \rightarrow 0^+} \bar{V} \exp[\bar{V}\xi] \quad (\text{B.27})$$

$$= \bar{V} \quad (\text{B.28})$$

Therefore, $f(t) \triangleq \|\mu^{\lambda/2}(t)\boldsymbol{\sigma}(t)\|^2$ is bounded, i.e., $\mu^{\lambda/2}\boldsymbol{\sigma} \in L_\infty$. Also, since $\|\mu^{\lambda/2}(t)\boldsymbol{\sigma}(t)\|^2 \leq \bar{V}$, then for any $\epsilon > 0$ and constant ρ such that $2\epsilon + \rho = \lambda/2$ we have that $\|\mu^\rho\boldsymbol{\sigma}(t)\|^2 \leq \mu^{-\epsilon}(t)\bar{V}$, implying that $\lim_{t \rightarrow t_f} \|\mu^\rho\boldsymbol{\sigma}(t)\|^2 = 0$.

Appendix C

Appendices for Chapter 5

C.1 Finite Time Tracking Design

Section 5.2 developed a stabilizing controller that takes the system to the origin. In this section, we develop the equivalent controller for tracking a desired trajectory.

Assume a desired trajectory given by a desired orientation signal $\sigma_d(t)$ and a desired angular velocity signal $\omega_d(t)$ such that $\dot{\sigma}_d(t) = \frac{1}{4}\mathbf{B}(\sigma_d(t))\omega_d(t)$. The objective is to reach the desired trajectory at time $t = t_f$, i.e., $\sigma_e(t_f) = 0$ and $\omega_e(t_f) = 0$, where $\sigma_e(t) \triangleq \sigma(t) \otimes \sigma_d^{-1}(t)$ is the reference attitude error and $\omega_e(t) \triangleq \omega(t) - \mathbf{C}(\sigma_e)\omega_d(t)$ is the angular velocity error expressed in the true orientation's frame of reference. The matrix $\mathbf{C}(\sigma_e)$ is the direction cosine matrix equivalent to the rotation σ_e (see Eq. 4.7) and satisfies $\dot{\mathbf{C}}(\sigma_e) = -\omega_e^*\mathbf{C}(\sigma_e)$. We assume that the quantities $\sigma_d(t)$, $\omega_d(t)$, and $\dot{\omega}_d(t)$ are bounded as $\sigma_d(t) \leq \bar{\sigma}_d$, $\omega_d(t) \leq \bar{\omega}_d$, $\dot{\omega}_d(t) \leq \bar{\dot{\omega}}_d$, and are fully specified as part of the tracking control objective. For simplicity of notation, the remainder of this section uses the notation $\omega_d^b \triangleq \mathbf{C}(\sigma_e)\omega_d$ and $\mathbf{C} \triangleq \mathbf{C}(\sigma_e)$.

In order to control the tracking error dynamics, we need to stabilize

the equations of motion below in finite-time:

$$\begin{cases} \dot{\boldsymbol{\sigma}}_e(t) = \mathbf{g}(\boldsymbol{\sigma}_e)\boldsymbol{\omega}_e(t) \\ \mathbf{J}\dot{\boldsymbol{\omega}}(t) = -\boldsymbol{\omega}^*(t)\mathbf{J}\boldsymbol{\omega}(t) + \mathbf{u}(t) + \mathbf{d}(t) \end{cases} \quad (\text{C.1})$$

This can be accomplished with the control law below:

$$\mathbf{u}(t) = \underbrace{-\phi_1\mu^4b(\boldsymbol{\sigma}_e)\boldsymbol{\sigma}_e - \phi_2\mu^2b(\boldsymbol{\sigma}_e)\boldsymbol{\omega}_e}_{\triangleq \mathbf{u}_{fb}} + \underbrace{\mathbf{J}\mathbf{C}\dot{\boldsymbol{\omega}}_d + \boldsymbol{\omega}_d^{b*}\mathbf{J}\boldsymbol{\omega}_d^b}_{\triangleq \mathbf{u}_{ff}}, \quad (\text{C.2})$$

where \mathbf{u}_{fb} contains the feedback terms of the control law and \mathbf{u}_{ff} contains the feed-forward terms.

First, we note that the quantity $\mathbf{J}\boldsymbol{\omega}_d^b$ has the following time-derivative:

$$\mathbf{J}\dot{\boldsymbol{\omega}}_d^b = \mathbf{J}\dot{\mathbf{C}}\boldsymbol{\omega}_d + \mathbf{J}\mathbf{C}\dot{\boldsymbol{\omega}}_d = -\mathbf{J}\boldsymbol{\omega}_e^*\mathbf{C}\boldsymbol{\omega}_d + \mathbf{J}\mathbf{C}\dot{\boldsymbol{\omega}}_d = -\mathbf{J}\boldsymbol{\omega}_e^*\boldsymbol{\omega}_d^b + \mathbf{J}\mathbf{C}\dot{\boldsymbol{\omega}}_d. \quad (\text{C.3})$$

Hence, the time derivative of $\mathbf{J}\boldsymbol{\omega}_e = \mathbf{J}\boldsymbol{\omega} - \mathbf{J}\boldsymbol{\omega}_d^b$ is given by:

$$\mathbf{J}\dot{\boldsymbol{\omega}}_e = -\boldsymbol{\omega}^*\mathbf{J}\boldsymbol{\omega} + \mathbf{u} + \mathbf{J}\boldsymbol{\omega}_e^*\boldsymbol{\omega}_d^b - \mathbf{J}\mathbf{C}\dot{\boldsymbol{\omega}}_d + \mathbf{d}. \quad (\text{C.4})$$

Writing the control input as $\mathbf{u} = \mathbf{u}_{fb} + \mathbf{u}_{ff}$, and explicitly writing the feed-forward term $\mathbf{u}_{ff} = \mathbf{J}\mathbf{C}\dot{\boldsymbol{\omega}}_d + \boldsymbol{\omega}_d^{b*}\mathbf{J}\boldsymbol{\omega}_d^b$, we get to:

$$\begin{aligned} \mathbf{J}\dot{\boldsymbol{\omega}}_e &= \mathbf{u}_{fb} - \boldsymbol{\omega}^*\mathbf{J}\boldsymbol{\omega} + \boldsymbol{\omega}_d^*\mathbf{J}\boldsymbol{\omega}_d + \mathbf{J}\boldsymbol{\omega}_e^*\boldsymbol{\omega}_d^b + \mathbf{d} \\ &= \mathbf{u}_{fb} - \boldsymbol{\omega}^*\mathbf{J}\boldsymbol{\omega} + \boldsymbol{\omega}_d^*\mathbf{J}\boldsymbol{\omega}_d - \mathbf{J}\boldsymbol{\omega}_d^{b*}\boldsymbol{\omega}_e + \mathbf{d}. \end{aligned} \quad (\text{C.5})$$

Using the relation $\boldsymbol{\omega} = \boldsymbol{\omega}_e + \boldsymbol{\omega}_d^b$ on the second term of Eq. C.7, we get that:

$$\boldsymbol{\omega}^*\mathbf{J}\boldsymbol{\omega} = \boldsymbol{\omega}_e^*\mathbf{J}\boldsymbol{\omega} + \boldsymbol{\omega}_d^{b*}\mathbf{J}\boldsymbol{\omega} = \boldsymbol{\omega}_e^*\mathbf{J}\boldsymbol{\omega} + \boldsymbol{\omega}_d^{b*}\mathbf{J}\boldsymbol{\omega}_e + \boldsymbol{\omega}_d^{b*}\mathbf{J}\boldsymbol{\omega}_d^b. \quad (\text{C.6})$$

Combining Eq. C.6 with Eq. C.7, we get:

$$\begin{aligned}
\mathbf{J}\dot{\boldsymbol{\omega}}_e &= \mathbf{u}_{fb} - \boldsymbol{\omega}_e^* \mathbf{J} \boldsymbol{\omega} - \boldsymbol{\omega}_d^{b*} \mathbf{J} \boldsymbol{\omega}_e - \underline{\boldsymbol{\omega}_d^{b*} \mathbf{J} \boldsymbol{\omega}_d^T} + \underline{\boldsymbol{\omega}_d^* \mathbf{J} \boldsymbol{\omega}_d} - \mathbf{J} \boldsymbol{\omega}_d^{b*} \boldsymbol{\omega}_e + \mathbf{d} \\
&= \mathbf{u}_{fb} - \boldsymbol{\omega}_e^* \mathbf{J} \boldsymbol{\omega} - (\boldsymbol{\omega}_d^{b*} \mathbf{J} + \mathbf{J} \boldsymbol{\omega}_d^{b*}) \boldsymbol{\omega}_e + \mathbf{d} \\
&= \mathbf{u}_{fb} - \boldsymbol{\omega}_e^* \mathbf{J} \boldsymbol{\omega} - \mathbf{Q} \boldsymbol{\omega}_e + \mathbf{d},
\end{aligned} \tag{C.7}$$

where $\mathbf{Q} \triangleq \boldsymbol{\omega}_d^{b*} \mathbf{J} + \mathbf{J} \boldsymbol{\omega}_d^{b*}$ is a skew-symmetric, i.e., $\mathbf{Q}^T = -\mathbf{Q}$. This implies that $\boldsymbol{\omega}_e^T \mathbf{Q} \boldsymbol{\omega}_e = 0, \forall \boldsymbol{\omega}_e \in \mathbb{R}^3$. Therefore, we have that:

$$\boldsymbol{\omega}_e^T \mathbf{J} \dot{\boldsymbol{\omega}}_e = \boldsymbol{\omega}_e^T \mathbf{u}_{fb} - \boldsymbol{\omega}_e^T \boldsymbol{\omega}_e^* \mathbf{J} \boldsymbol{\omega} - \boldsymbol{\omega}_e^T \mathbf{Q} \boldsymbol{\omega}_e + \boldsymbol{\omega}_e^T \mathbf{d} = \boldsymbol{\omega}_e^T \mathbf{u}_{fb} + \boldsymbol{\omega}_e^T \mathbf{d}. \tag{C.8}$$

As before, we define our storage function as $V = V_1 + V_2 + V_3$, where:

$$V_1 \triangleq 2\nu\mu^8 \boldsymbol{\sigma}_e^T \boldsymbol{\sigma}_e, \quad V_2 \triangleq \frac{\psi}{2} \mu^4 \boldsymbol{\omega}_e^T \mathbf{J} \boldsymbol{\omega}_e, \quad V_3 \triangleq \lambda \mu^6 \boldsymbol{\sigma}_e^T \mathbf{J} \boldsymbol{\omega}_e, \tag{C.9}$$

where $\lambda > 0, \psi > 0$ and $\nu \triangleq k_1 + \frac{\lambda k_2}{\psi}$ are constant values, and have to satisfy the same conditions as in Eq. 5.10 for positive-definiteness of $V(t)$.

Taking the time-derivative on V_1 , we get:

$$\begin{aligned}
\dot{V}_1 &= \frac{16\nu}{t_f} \mu^9 \boldsymbol{\sigma}_e^T \dot{\boldsymbol{\sigma}}_e + 4\nu\mu^8 \boldsymbol{\sigma}_e^T \dot{\boldsymbol{\sigma}}_e = \frac{16\nu}{t_f} \mu^9 \|\boldsymbol{\sigma}_e\|^2 + \nu\mu^8 \boldsymbol{\sigma}_e^T \mathbf{B}(\boldsymbol{\sigma}_e) \boldsymbol{\omega}_e \\
&= \frac{16\nu}{t_f} \mu^9 \|\boldsymbol{\sigma}_e\|^2 + \left(k_1 + \frac{\lambda k_2}{\psi}\right) \mu^8 b(\boldsymbol{\sigma}_e) \boldsymbol{\sigma}_e^T \boldsymbol{\omega}_e.
\end{aligned} \tag{C.10}$$

Taking the time-derivative on V_2 :

$$\dot{V}_2 = \frac{2\psi}{t_f} \mu^5 \boldsymbol{\omega}_e^T \mathbf{J} \dot{\boldsymbol{\omega}}_e + \psi \mu^4 \boldsymbol{\omega}_e^T \mathbf{J} \dot{\boldsymbol{\omega}}_e. \tag{C.11}$$

Using Eq. C.8, we get:

$$\begin{aligned}
\dot{V}_2 &= \frac{2\psi}{t_f} \mu^5 \boldsymbol{\omega}_e^T \mathbf{J} \boldsymbol{\omega}_e + \psi \mu^4 \boldsymbol{\omega}_e^T \mathbf{u}_{fb} + \psi \mu^4 \boldsymbol{\omega}_e^T \mathbf{d} \\
&\leq \frac{2\psi \bar{J}}{t_f} \mu^5 \|\boldsymbol{\omega}_e\|^2 + \psi \mu^4 \boldsymbol{\omega}_e^T \mathbf{u}_{fb} + \psi (\delta \mu^3 \boldsymbol{\omega}_e^T) \left(\frac{1}{\delta} \mu \mathbf{d} \right) \\
&\leq \frac{2\psi \bar{J}}{t_f} \mu^5 \|\boldsymbol{\omega}_e\|^2 + \psi \mu^4 \boldsymbol{\omega}_e^T \mathbf{u}_{fb} + \frac{\psi \delta^2}{2} \mu^6 \|\boldsymbol{\omega}_e\|^2 + \frac{\psi}{2\delta^2} \mu^2 \bar{d}^2. \tag{C.12}
\end{aligned}$$

Here we use the feedback law:

$$\mathbf{u}_{fb} = -\phi_1 \mu^4 b(\boldsymbol{\sigma}_e) \boldsymbol{\sigma}_e - \phi_2 \mu^2 b(\boldsymbol{\sigma}_e) \boldsymbol{\omega}_e, \tag{C.13}$$

leading to the following on \dot{V}_2 :

$$\begin{aligned}
\dot{V}_2 &\leq \frac{2\psi \bar{J}}{t_f} \mu^5 \|\boldsymbol{\omega}_e\|^2 - \psi \phi_1 \mu^8 b(\boldsymbol{\sigma}_e) \boldsymbol{\omega}_e^T \boldsymbol{\sigma}_e - \psi \phi_2 \mu^6 b(\boldsymbol{\sigma}_e) \|\boldsymbol{\omega}_e\|^2 \\
&\quad + \frac{\psi \delta^2}{2} \mu^6 \|\boldsymbol{\omega}_e\|^2 + \frac{\psi}{2\delta^2} \mu^2 \bar{d}^2. \tag{C.14}
\end{aligned}$$

Using the definitions $\psi \phi_1 = k_1$ and $b(\boldsymbol{\sigma}_e) = 1 + \|\boldsymbol{\sigma}_e\|^2$, we have the following for $\dot{V}_1 + \dot{V}_2$:

$$\begin{aligned}
\dot{V}_1 + \dot{V}_2 &\leq \frac{16\nu}{t_f} \mu^9 \|\boldsymbol{\sigma}_e\|^2 + \frac{\lambda k_2}{\psi} \mu^8 b(\boldsymbol{\sigma}_e) \boldsymbol{\sigma}_e^T \boldsymbol{\omega}_e + \psi \left(\frac{2\bar{J}}{t_f} \mu^{-1} + \frac{\delta^2}{2} - \phi_2 \right) \mu^6 \|\boldsymbol{\omega}_e\|^2 \\
&\quad - \psi \phi_2 \mu^6 \|\boldsymbol{\sigma}_e\|^2 \|\boldsymbol{\omega}_e\|^2 + \frac{\psi}{2\delta^2} \mu^2 \bar{d}^2. \tag{C.15}
\end{aligned}$$

Finally, taking derivative on V_3 :

$$\begin{aligned}
\dot{V}_3 &= \frac{6\lambda}{t_f} \mu^7 \boldsymbol{\sigma}_e^T \mathbf{J} \boldsymbol{\omega}_e + \lambda \mu^6 \boldsymbol{\sigma}_e^T \mathbf{J} \dot{\boldsymbol{\omega}}_e + \frac{\lambda}{4} \mu^6 \boldsymbol{\omega}_e^T \mathbf{J} \mathbf{B}(\boldsymbol{\sigma}_e) \boldsymbol{\omega}_e \\
&\leq \frac{6\lambda \bar{J}}{t_f} \mu^8 \|\boldsymbol{\sigma}_e\|^2 + \frac{6\lambda \bar{J}}{t_f} \mu^6 \|\boldsymbol{\omega}_e\| + \lambda \mu^6 \boldsymbol{\sigma}_e^T \mathbf{J} \dot{\boldsymbol{\omega}}_e + \frac{\lambda \bar{J}}{4} b(\boldsymbol{\sigma}_e) \mu^6 \|\boldsymbol{\omega}_e\|^2 \\
&= \frac{6\lambda \bar{J}}{t_f} \mu^8 \|\boldsymbol{\sigma}_e\|^2 + \lambda \left(\frac{6\bar{J}}{t_f} + \frac{\bar{J}}{4} \right) \mu^6 \|\boldsymbol{\omega}_e\| + \lambda \mu^6 \boldsymbol{\sigma}_e^T \mathbf{J} \dot{\boldsymbol{\omega}}_e + \frac{\lambda \bar{J}}{4} \mu^6 \|\boldsymbol{\sigma}_e\|^2 \|\boldsymbol{\omega}_e\|^2. \tag{C.16}
\end{aligned}$$

Now we expand the term $\mu^6 \boldsymbol{\sigma}^T \mathbf{J} \dot{\boldsymbol{\omega}}_e$ by combining it with Eq. C.7:

$$\begin{aligned}
\mu^6 \boldsymbol{\sigma}_e^T \mathbf{J} \dot{\boldsymbol{\omega}}_e &= \mu^6 [\boldsymbol{\sigma}_e^T \mathbf{u}_{fb} - \boldsymbol{\sigma}_e^T \boldsymbol{\omega}_e^* \mathbf{J} (\boldsymbol{\omega}_e + \boldsymbol{\omega}_d^b) - \boldsymbol{\sigma}_e^T \mathbf{Q} \boldsymbol{\omega}_e + \boldsymbol{\sigma}_e^T \mathbf{d}] \\
&\leq \mu^6 [\boldsymbol{\sigma}_e^T \mathbf{u}_{fb} + \bar{J} \|\boldsymbol{\sigma}_e\| \|\boldsymbol{\omega}_e\|^2 + \bar{\omega}_d \bar{J} \|\boldsymbol{\sigma}_e\| \|\boldsymbol{\omega}_e\| + \bar{Q} \|\boldsymbol{\sigma}_e\| \|\boldsymbol{\omega}_e\| + \bar{d} \|\boldsymbol{\sigma}_e\|] \\
&= \mu^6 [\boldsymbol{\sigma}_e^T \mathbf{u}_{fb} + \bar{J} \|\boldsymbol{\sigma}_e\| \|\boldsymbol{\omega}_e\|^2 + (\bar{\omega}_d \bar{J} + \bar{Q}) \|\boldsymbol{\sigma}_e\| \|\boldsymbol{\omega}_e\| + \bar{d} \|\boldsymbol{\sigma}_e\|] \\
&\leq -\phi_1 b(\boldsymbol{\sigma}_e) \mu^{10} \|\boldsymbol{\sigma}_e\|^2 - \phi_2 b(\boldsymbol{\sigma}_e) \mu^8 \boldsymbol{\sigma}_e^T \boldsymbol{\omega}_e + \frac{\bar{J}}{2} \mu^6 (1 + \|\boldsymbol{\sigma}_e\|^2) \|\boldsymbol{\omega}_e\|^2 + \\
&\quad + \frac{1}{2} (\bar{\omega}_d \bar{J} + \bar{Q}) \mu^8 \|\boldsymbol{\sigma}_e\|^2 + \frac{1}{2} (\bar{\omega}_d \bar{J} + \bar{Q}) \mu^4 \|\boldsymbol{\omega}_e\|^2 + \mu^6 \bar{d} \|\boldsymbol{\sigma}_e\|,
\end{aligned} \tag{C.17}$$

where $\bar{Q} \triangleq \|\check{\mathbf{Q}}\|$, in which $(\check{\cdot})$ is the inverse of the skew-symmetric operator in a vector: $(\check{\mathbf{v}}^*) = \mathbf{v}$.

Given that $\lambda (\frac{1}{\delta} \mu \bar{d}) (\delta \mu^5 \|\boldsymbol{\sigma}_e\|) \leq \frac{\lambda}{2\delta^2} \mu^2 \bar{d}^2 + \frac{\lambda \delta^2}{2} \mu^{10} \|\boldsymbol{\sigma}_e\|^2$ for some $\delta > 0$, we can combine Eq. C.16 with Eq. C.17:

$$\begin{aligned}
\dot{V}_3 &\leq \lambda \left(\frac{6\lambda \bar{J}}{t_f} \mu^{-2} + \frac{\bar{\omega}_d \bar{J}}{2} \mu^{-2} + \frac{\bar{Q}}{2} \mu^{-2} + \frac{\delta^2}{2} - \phi_1 \right) \mu^{10} \|\boldsymbol{\sigma}_e\|^2 - \lambda \phi_1 \mu^{10} \|\boldsymbol{\sigma}_e\|^4 + \frac{\lambda}{2\delta^2} \bar{d}^2 \mu^2 \\
&\quad + \lambda \left(\frac{6\bar{J}}{t_f} + \frac{3\bar{J}}{4} + \frac{\bar{\omega}_d \bar{J}}{2} \mu^{-2} + \frac{\bar{Q}}{2} \mu^{-2} \right) \mu^6 \|\boldsymbol{\omega}_e\| + \frac{3\lambda \bar{J}}{4} \mu^6 \|\boldsymbol{\sigma}_e\|^2 \|\boldsymbol{\omega}_e\|^2 \\
&\quad - \lambda \phi_2 \mu^8 b(\boldsymbol{\sigma}_e) \boldsymbol{\sigma}_e^T \boldsymbol{\omega}_e.
\end{aligned} \tag{C.18}$$

Now we combine Eqs. C.15 and C.18 to obtain \dot{V} :

$$\begin{aligned}
\dot{V} &\leq \lambda \left(\frac{16\nu}{t_f} \mu^{-1} + \frac{6\bar{J}}{t_f} \mu^{-2} + \frac{\bar{\omega}_d \bar{J}}{2} \mu^{-2} + \frac{\bar{Q}}{2} \mu^{-2} + \frac{\delta^2}{2} - \phi_1 \right) \mu^{10} \|\boldsymbol{\sigma}_e\|^2 - \lambda \phi_1 \mu^{10} \|\boldsymbol{\sigma}_e\|^4 \\
&\quad + \left(\frac{6\lambda \bar{J}}{t_f} + \frac{3\lambda \bar{J}}{4} + \frac{\lambda \bar{\omega}_d \bar{J}}{2} \mu^{-2} + \frac{\lambda \bar{Q}}{2} \mu^{-2} + \frac{2\psi \bar{J}}{t_f} \mu^{-1} + \frac{\psi \delta^2}{2} - \psi \phi_2 \right) \mu^6 \|\boldsymbol{\omega}_e\| \\
&\quad + \left(\frac{3\lambda \bar{J}}{4} - \psi \phi_2 \right) \mu^6 \|\boldsymbol{\sigma}_e\|^2 \|\boldsymbol{\omega}_e\|^2 + \left(\frac{\lambda}{2\delta^2} + \frac{\psi}{2\delta^2} \right) \bar{d}^2 \mu^2.
\end{aligned} \tag{C.19}$$

Using the definition $\lambda = \frac{J}{J\beta}\psi$, we get:

$$\begin{aligned}
\dot{V} \leq & -\lambda \left(\phi_1 - \frac{\delta^2}{2} - \frac{16\nu}{t_f}\mu^{-1} - \frac{6\bar{J}}{t_f}\mu^{-2} + \frac{\bar{\omega}_d\bar{J}}{2}\mu^{-2} - \frac{\bar{Q}}{2}\mu^{-2} \right) \mu^{10} \|\sigma_e\|^2 - \lambda \phi_1 \mu^{10} \|\sigma_e\|^4 \\
& - \psi \left(\phi_2 - \frac{\delta^2}{2} - \frac{6}{t_f}\frac{J}{\beta} - \frac{3}{4}\frac{J}{\beta} - \frac{\bar{\omega}_d}{2}\frac{J}{\beta}\mu^{-2} - \frac{\bar{Q}}{2}\frac{J}{J\beta}\mu^{-2} - \frac{2\bar{J}}{t_f}\mu^{-1} \right) \mu^6 \|\omega_e\| \\
& - \psi \left(\phi_2 - \frac{3}{4}\frac{J}{\beta} \right) \mu^6 \|\sigma_e\|^2 \|\omega_e\|^2 + \psi \left(\frac{1}{2\delta^2}\frac{J}{J\beta} + \frac{1}{2\delta^2} \right) \bar{d}^2 \mu^2. \tag{C.20}
\end{aligned}$$

Defining $\kappa_1 \triangleq \phi_1 - \frac{\delta^2}{2}$, $\kappa_2 \triangleq \phi_2 - \frac{\delta^2}{2} - \frac{6}{t_f}\frac{J}{\beta} - \frac{3}{4}\frac{J}{\beta}$, and $\kappa_3 \triangleq \phi_2 - \frac{3}{4}\frac{J}{\beta}$, we can always choose β large enough and δ small enough such that $\kappa_1 > 0$, $\kappa_2 > 0$, and $\kappa_3 > 0$, for any given $\phi_1 > 0$ and $\phi_2 > 0$. We make the definitions:

$$\begin{aligned}
\gamma_1(t) & \triangleq \lambda \left(\kappa_1 - \frac{16\nu}{t_f}\mu^{-1} - \frac{6\bar{J}}{t_f}\mu^{-2} + \frac{\bar{\omega}_d\bar{J}}{2}\mu^{-2} - \frac{\bar{Q}}{2}\mu^{-2} \right), \quad \gamma_2 \triangleq \lambda \phi_1 \\
\gamma_3(t) & \triangleq \psi \left(\kappa_2 - \frac{\bar{\omega}_d}{2}\frac{J}{\beta}\mu^{-2} - \frac{\bar{Q}}{2}\frac{J}{J\beta}\mu^{-2} - \frac{2\bar{J}}{t_f}\mu^{-1} \right), \quad \gamma_4 \triangleq \psi \kappa_3, \\
\gamma_5 & \triangleq \psi \left(\frac{1}{2\delta^2}\frac{J}{J\beta} + \frac{1}{2\delta^2} \right), \tag{C.21}
\end{aligned}$$

such that:

$$\dot{V} \leq -\gamma_1(t)\mu^{10}\|\sigma_e\|^2 - \gamma_2\mu^{10}\|\sigma_e\|^4 - \gamma_3(t)\mu^6\|\omega_e\|^2 - \gamma_4\mu^6\|\sigma_e\|^2\|\omega_e\|^2 + \gamma_5\mu^2\bar{d}^2. \tag{C.22}$$

Because $\gamma_2 > 0$ and $\gamma_4 > 0$, we can simplify Eq. C.22 as:

$$\dot{V} \leq -\gamma_1(t)\mu^{10}\|\sigma_e\|^2 - \gamma_3(t)\mu^6\|\omega_e\|^2 + \gamma_5\mu^2\bar{d}^2. \tag{C.23}$$

Again, we can argue that there exists $t_1 \in [0, t_f)$ such that $\gamma_1(t) > 0$ and $\gamma_2(t) > 0$, for any $t \in [t_1, t_f)$. With this, we can proceed with proofs such as in Lemma 2 and Lemma 3 from Section 5.2.2 to prove that $V(t)$ is bounded for $t \in [0, t_f)$ and that the tracking problem converges in finite-time in the presence of disturbances by use of the control law of Eq. C.2.

Bibliography

- [1] Robert James Adcock. A problem in least squares. *The Analyst*, 5(1):53–54, 1878.
- [2] Marcelino Almeida and Maruthi Akella. New class of attitude controllers guaranteed to converge within specified finite-time. *The Journal of the Astronautical Sciences*, pages 1–19, 2019.
- [3] Marcelino Almeida and Maruthi Akella. Time-varying feedback for attitude regulation in prescribed finite-time. *2019 AAS/AIAA Astrodynamics Specialist Conference in Portland, ME*, (19-653), Aug. 2019.
- [4] Marcelino Almeida and Maruthi Akella. Discrete adaptive angular velocity estimation - an experimental analysis. *2016 AASS/AIAA Space Flight Mechanics Meeting in Napa, CA*, 158(16-374), Feb. 2016.
- [5] Marcelino Almeida and Guilherme V Raffo. Nonlinear control of a tiltrotor uav for load transportation. *IFAC-PapersOnLine*, 48(19):232–237, 2015.
- [6] Marcelino Almeida, Renato Zanetti, Daniele Mortari, and Maruthi Akella. Quatera: The quaternion regression algorithm. *Submitted to the Journal of Guidance, Control, and Dynamics*, 2019.

- [7] Marcelino Almeida, Renato Zanetti, Daniele Mortari, and Maruthi Akella. Real-time angular velocity estimation of non-cooperative space objects using camera measurements. *2018 AAS/AIAA Astrodynamics Specialist Conference in Snowbird, UT*, 167(18-420), Aug. 2018.
- [8] Michael Athans and Peter L. Falb. *Optimal control: an introduction to the theory and its applications*. Courier Corporation, 2013.
- [9] Itzhack Y. Bar-Itzhack. Classification of algorithms for angular velocity estimation. *Journal of Guidance, Control, and Dynamics*, 24(2):214–218, 2001.
- [10] Itzhack Y. Bar-Itzhack, Richard R. Harman, and Julie K. Thienel. Rigid body rate inference from attitude variation. *Journal of guidance, control, and dynamics*, 30(1):275–281, 2007.
- [11] Yaakov Bar-Shalom, X. Rong Li, and Thiagalingam Kirubarajan. *Estimation with applications to tracking and navigation: theory algorithms and software*. John Wiley & Sons, 2004.
- [12] Sanjay P. Bhat and Dennis S. Bernstein. Finite-time stability of continuous autonomous systems. *SIAM Journal on Control and Optimization*, 38(3):751–766, 2000.
- [13] George E. P. Box, Gwilym M Jenkins, Gregory C Reinsel, and Greta M Ljung. *Time series analysis: forecasting and control*. John Wiley & Sons, 2015.

- [14] A. Bryson and Yu-Chi Ho. Applied optimal control: Optimization, estimation, and control (revised edition). *Levittown, Pennsylvania: Taylor & Francis*, 1975.
- [15] Maria Bualat, Trey Smith, Ernest Smith, Terrence Fong, and D. W. Wheeler. Astrobebe: A new tool for iss operations. In *2018 SpaceOps Conference*, page 2517, 2018.
- [16] James R Carr. Orthogonal regression: a teaching perspective. *International Journal of Mathematical Education in Science and Technology*, 43(1):134–143, 2012.
- [17] Joshua Cemenska. *Sensor Modelling and Kalman Filtering Applied to Satellite Attitude Determination*. PhD thesis, University of California at Berkeley, 2004.
- [18] N. A. Chatuverdi, Amit K. Sanyal, and N. Haris McClamroch. Rigid-body attitude control using rotation matrices for continuous, singularity-free control laws. *IEEE Control Systems Magazine*, 31(8):30–51, 2011.
- [19] R. Dennis Cook and Sanford Weisberg. *Residuals and influence in regression*. New York: Chapman and Hall, 1982.
- [20] John L. Crassidis and Yang Cheng. Error-covariance analysis of the total least-squares problem. *Journal of Guidance, Control, and Dynamics*, 37(4):1053–1063, 2014.

- [21] H. Cundy and A. Rollett. Sphere and cylinder: Archimedes theorem. *Mathematical Models*, pages 172–173, 1989.
- [22] Mehregan Dor and Panagiotis Tsiotras. Orb-slam applied to spacecraft non-cooperative rendezvous. In *2018 Space Flight Mechanics Meeting in Kissimmee, FL*, page 1963, Jan. 2018.
- [23] Robert Engel and Gerhard Kreisselmeier. A continuous-time observer which converges in finite time. *IEEE Transactions on Automatic Control*, 47(7):1202–1204, 2002.
- [24] Eliezer Gai, Kevin Daly, James Harrison, and Linda Lemos. Star-sensor-based satellite attitude/attitude rate estimator. *Journal of Guidance, Control, and Dynamics*, 8(5):560–565, 1985.
- [25] Richard Hartley and Andrew Zisserman. *Multiple view geometry in computer vision*. Cambridge university press, 2003.
- [26] Joanna C. Hinks and Mark L. Psiaki. Solution strategies for an extension of wahba’s problem to a spinning spacecraft. *Journal of Guidance, Control, and Dynamics*, 34(6):1734–1745, 2011.
- [27] Sabine Van Huffel and Joos Vandewalle. Analysis and properties of the generalized total least squares problem $ax=b$ when some or all columns in a are subject to error. *SIAM Journal on Matrix Analysis and Applications*, 10(3):294–315, 1989.

- [28] David G. Hull. *Fundamentals of airplane flight mechanics*. Springer, 2007.
- [29] John L. Junkins, Maruthi Akella, and Rush D Robinett. Nonlinear adaptive control of spacecraft maneuvers. *Journal of Guidance, Control, and Dynamics*, 20(6):1104–1110, 1997.
- [30] Ronald H. Ketellapper. The relevance of large sample properties of estimators for the errors-in-variables model: A monte carlo study. *Communications in Statistics-Simulation and Computation*, 11(5):625–634, 1982.
- [31] Hassan K. Khalil. *Nonlinear systems*. New Jersey, Prentice Hall, 2002.
- [32] Allan Y. Lee and Julie A. Wertz. In-flight estimation of the cassini spacecraft’s inertia tensor. *Journal of spacecraft and rockets*, 39(1):153–155, 2002.
- [33] Taeyoung Lee, Melvin Leok, and N Harris McClamroch. Nonlinear robust tracking control of a quadrotor uav on se (3). *Asian Journal of Control*, 15(2):391–408, 2013.
- [34] Ern J. Lefferts, F. Landis Markley, and Malcolm D. Shuster. Kalman filtering for spacecraft attitude estimation. *Journal of Guidance, Control, and Dynamics*, 5(5):417–429, 1982.
- [35] Gerald M. Lerner. Three-axis attitude determination. *Spacecraft Attitude Determination and Control*, 73:420–428, 1978.

- [36] F. Landis Markley. Attitude error representations for kalman filtering. *Journal of guidance, control, and dynamics*, 26(2):311–317, 2003.
- [37] F. Landis Markley, Yang Cheng, John Lucas Crassidis, and Yaakov Oshman. Averaging quaternions. *Journal of Guidance, Control, and Dynamics*, 30(4):1193–1197, 2007.
- [38] F. Landis Markley and Daniele Mortari. Quaternion attitude estimation using vector observations. *Journal of the Astronautical Sciences*, 48(2):359–380, 2000.
- [39] MATLAB. fmincon find minimum of constrained nonlinear multivariable function. <https://www.mathworks.com/help/optim/ug/fmincon.html>. Accessed: 2019-12-04.
- [40] MATLAB. *version 2019a*). The MathWorks Inc., Natick, Massachusetts, 2019.
- [41] Brian J. McCartin. A geometric characterization of linear regression. *Statistics: A Journal of Theoretical and Applied Statistics*, 37(2):101–117, 2003.
- [42] D. Mortari and M. Akella. Discrete and continuous time adaptive angular velocity estimators. *AAS/AIAA Space Flight Mechanics Conference in Williamsburg, VA*, 155(15-254), Jan. 2015.
- [43] Daniele Mortari and Manoranjan Majji. Multiplicative measurement model. *The Journal of the Astronautical Sciences*, 57(1-2):47–60, 2009.

- [44] Raul Mur-Artal, Jose Maria Martinez Montiel, and Juan D. Tardos. Orb-slam: a versatile and accurate monocular slam system. *IEEE Transactions on Robotics*, 31(5):1147–1163, 2015.
- [45] Bo Naasz, John Van Eepoel, Steve Queen, C Michael Southward, and Joel Hannah. Flight results from the hst sm4 relative navigation sensor system. In *33rd Annual AAS Guidance And Control Conference, Guidance and Control 2010, Advances in the Astronautical Sciences*, 2010.
- [46] Corwin Olson, Ryan P. Russell, and Shyam Bhaskaran. Spin state estimation of tumbling small bodies. *The Journal of the Astronautical Sciences*, 63(2):124–157, 2016.
- [47] Yaakov Oshman and Francois Dellus. Spacecraft angular velocity estimation using sequential observations of a single directional vector. *Journal of Spacecraft and Rockets*, 40(2):237–247, 2003.
- [48] Yaakov Oshman and F Landis Markley. Sequential attitude and attitude-rate estimation using integrated-rate parameters. *Journal of Guidance, Control, and Dynamics*, 22(3):385–394, 1999.
- [49] Samuel Pedrotty, Jacob Sullivan, Elisabeth Gambone, and Thomas Kirven. Seeker free-flying inspector overview. In *42nd Annual AAS Guidance and Control Conference*, 2019.
- [50] Mark L. Psiaki. Backward-smoothing extended kalman filter. *Journal of guidance, control, and dynamics*, 28(5):885–894, 2005.

- [51] Mark L. Psiaki. Generalized wahba problems for spinning spacecraft attitude and rate determination. *The Journal of the Astronautical Sciences*, 57(1-2):73–92, 2009.
- [52] Mark L. Psiaki and Joanna C. Hinks. Numerical solution of a generalized wahba problem for a spinning spacecraft. *Journal of Guidance, Control, and Dynamics*, 35(3):764–773, 2012.
- [53] S. Salcudean. A globally convergent angular velocity observer for rigid body motion. *IEEE transactions on Automatic Control*, 36(12):1493–1497, 1991.
- [54] James Saunderson, Pablo A. Parrilo, and Alan S. Willsky. Convex solution to a joint attitude and spin-rate estimation problem. *Journal of Guidance, Control, and Dynamics*, 39(1):118–127, 2015.
- [55] Hanspeter Schaub, Maruthi Akella, and John L. Junkins. Adaptive control of nonlinear attitude motions realizing linear closed loop dynamics. *Journal of Guidance, Control, and Dynamics*, 24(1):95–100, 2001.
- [56] Daniel Scheeres, R. Gaskell, S. Abe, O. Barnouin-Jha, T. Hashimoto, J. Kawaguchi, T. Kubota, J. Saito, M. Yoshikawa, N. Hirata, et al. The actual dynamical environment about itokawa. In *AIAA/AAS Astrodynamics Specialist Conference and Exhibit*, page 6661, 2006.
- [57] Alan Shuchat. Generalized least squares and eigenvalues. *The American Mathematical Monthly*, 92(9):656–659, 1985.

- [58] Malcolm D Shuster. A survey of attitude representations. *Navigation*, 8(9):439–517, 1993.
- [59] Jean-Jacques E. Slotine, Weiping Li, et al. *Applied nonlinear control*, volume 199. Prentice hall Englewood Cliffs, N. J., 1991.
- [60] Yongduan Song, Yujuan Wang, John Holloway, and Miroslav Krstic. Time-varying feedback for regulation of normal-form nonlinear systems in prescribed finite time. *Automatica*, 83:243–251, 2017.
- [61] H. Späth. Orthogonal least squares fitting with linear manifolds. *Numerische Mathematik*, 48(4):441–445, 1986.
- [62] Jacob Sullivan, Elisabeth Gambone, Thomas Kirven, Samuel Pedrotty, and Brandon Wood. Rapid development of the seeker free-flying inspector guidance, navigation, and control system. In *42nd Annual AAS Guidance and Control Conference*, 2019.
- [63] Divya Thakur and Maruthi Akella. Gyro-free rigid-body attitude stabilization using only vector measurements. *Journal of Guidance, Control, and Dynamics*, 38(4):811–818, 2014.
- [64] Panagiotis Tsiotras. New control laws for the attitude stabilization of rigid bodies. In *Automatic Control in Aerospace 1994 (Aerospace Control'94)*, pages 321–326. Elsevier, 1995.
- [65] Sabine Van Huffel and Joos Vandewalle. *The total least squares problem: computational aspects and analysis*, volume 9. Siam, 1991.

- [66] C. Venkatesan. *Fundamentals of helicopter dynamics*. CRC Press, 2014.
- [67] Sanford Weisberg. *Applied linear regression*, volume 528. John Wiley & Sons, 2005.
- [68] Eric W Weisstein. Sphere Point Picking. from mathworld—a wolfram web resource. <http://mathworld.wolfram.com/SpherePointPicking.html>, 2018. Accessed: 2018-08-08.
- [69] JT-Y Wen and Kenneth Kreutz-Delgado. The attitude control problem. *IEEE Transactions on Automatic control*, 36(10):1148–1162, 1991.
- [70] William E. Wiesel. *Spaceflight dynamics*. McGraw-Hill Science Engineering, 1997.
- [71] Stefan B. Williams, Paul Newman, Julio Rosenblatt, Gamini Dissanayake, and Hugh Durrant-Whyte. Autonomous underwater navigation and control. *Robotica*, 19(5):481–496, 2001.
- [72] Sungpil Yang, Maruthi Akella, and Frédéric Mazenc. Immersion and invariance observers for gyro-free attitude control systems. *Journal of Guidance, Control, and Dynamics*, pages 2570–2577, 2016.